



***Microscopic and Spectral
Characterisation of
Optical Fibre Bragg Gratings***

A thesis submitted for the degree of
Doctor of Philosophy
by

Claire M. Rollinson

Centre for Telecommunication and Microelectronics
Faculty of Health, Engineering & Science

Victoria University 2012

Declaration



I, Claire Marice Rollinson, declare that the PhD thesis entitled:

“Microscopic and Spectral Characterisation of Optical Fibre Bragg Gratings”

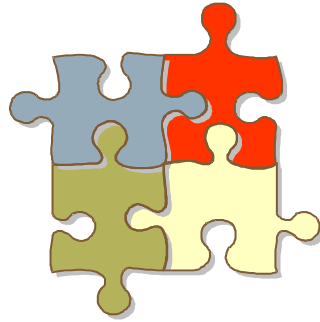
is no more than 100,000 words in length, exclusive of tables, figures, appendices, references and footnotes. This thesis contains no material that has been submitted previously, in whole or in part, for the award of any other academic degree or diploma. Except where otherwise indicated, this thesis is my own work.

Signature:

Date:

*This thesis is dedicated to my husband David.
My Angel, my Saviour;
You are the light that guides me
As I stumble through the darkness.*

Abstract



Microscopic and Spectral Characterisation of Optical Fibre Bragg Gratings

by Claire M. Rollinson

Fibre Bragg gratings (FBGs) have found extensive application in lasers, amplifiers, signal filtering in telecommunications and sensing. The underlying mechanisms and fundamental properties of FBGs are not completely understood, which stands in the way of full exploitation of FBG-based devices across a range of technologies. Differential Interference Contrast (DIC) microscopy was used in this thesis to investigate the internal refractive index structures of FBGs fabricated using various techniques. By measuring the light transmitted through FBGs at various wavelengths, the information gained from spectral measurements has been compared with the DIC images. The sensing capacities of complex structure FBGs were investigated using standard sensor calibration techniques which monitor wavelength shifts with changes in temperature and strain.

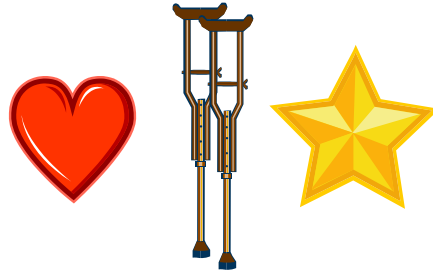
The results show that the fabrication conditions have a significant effect on the induced refractive index structures. For phase-mask-written FBGs, the images revealed interleaving periodic perturbations with a spacing equal to the phase mask period which is inconsistent with the period expected for pure

two-beam interference of the $\pm 1^{\text{st}}$ diffraction orders. The observed complex refractive index structures are instead consistent with the multiple-beam interference patterns. Through the use of a custom-made phase mask, higher than normal contributions of diffraction orders other than the $\pm 1^{\text{st}}$ have been shown to increase the strength of certain harmonic reflections. The images of FBGs written with different phase masks revealed the existence of π phase-shifted gratings with a period equal to that of the phase mask used in fabrication. Consistent with these observations, certain spectral results exhibited split transmission dips under singlemode propagation which were attributed to destructive interference of the forward and backward propagating reflections from the π phase-shifted gratings.

The reflection strengths of spectral features arising from the complex refractive index structures were found to be stronger when propagating under singlemode conditions due to the larger modal overlap between the propagating mode and the index perturbations in the core of the FBG. By investigating the growth of FBG reflectances during fabrication, the origins of spectral features have been shown to vary depending on the wavelength and core size of the fibre. Reflections at the Bragg wavelength were found to be predominantly caused by the second harmonic reflection of the period equal to the phase mask, rather than the first harmonic of a period equal to half the phase mask period.

Unexpected spectral features arising from the observed complex refractive index structures have been found to exhibit the expected responses to axial strain and temperature with potential applications in dual-wavelength simultaneous sensing. Sensing schemes were proposed which exhibit comparable measurement uncertainties to previous work. When combined with the essentially strain independent fluorescence intensity ratio (FIR) technique, the use of two harmonic wavelength shifts in a single rare-earth doped FBG offers potential for simple, co-located detection of two strain and three temperature measurements simultaneously with high precision.

Acknowledgements



There are many people I would like to thank for their contributions and support throughout the duration of this thesis. Thank you to all the past and present staff and students in the Optical Technology Research Laboratory at Victoria University for all of their support and encouragement. In particular, I would like to thank Ass. Prof. Stephen Collins, Dr. Betty Kouskousis and Dr. Daniel Kitcher for valuable contributions, support, kindness and assistance over the years. Thanks to Nicoleta Dragomir and Donald Ermel for the design and construction of the temperature-controlled rotation stage used for imaging. I would also like to thank Bernard Dussardier and his team at The University of Nice, France, and K. T. V. Grattan and his team at City University, London, United Kingdom, for their valuable contributions and support.

My principal supervisor, Prof. Greg Baxter, has been of phenomenal support to me throughout the project. Thank you for your generosity, guidance and valuable contributions. Most of all, I appreciated your never-ending faith and reassurance that I would get there and I always felt that you were not worried in the slightest that I wouldn't. I was fortunate to work with such an inspirational supervisor and I truly admire that your career success was earned through hardwork and by treating people with fairness and kindness.

My co-supervisor, Dr. Scott Wade, was instrumental in the design, development and completion of this thesis. His experimental expertise and innovation were the drivers behind the project. I would like to thank Scott for his generosity and encouragement. His constructive criticisms were carefully considered with the best project outcomes in mind and his support and contributions are greatly appreciated.

I would like to thank my parents, Jennifer and David, and my brother Damien, who have always made me feel as though I make them proud and give me constant inspiration to make them prouder. Thank you especially to my mother, who supported my early education and without whom I would not have felt so loved my whole life.

Finally, I would like to thank my husband Dr. David Simpson for your constant love, support, encouragement and for making me so happy. You are a constant inspiration and an immensely talented scientist. I couldn't possibly have done this without you.

List of Figures



Figure 1-1. Guidance of light in an optical fibre.....	2
Figure 1-2. Typical attenuation of silica optical fibre	2
Figure 1-3. Optical systems for interferometric inscription of FBGs.....	9
Figure 1-4. Optical system for fibre grating fabrication using a typical phase mask	10
Figure 1-5. Typical growth dynamics of the Bragg wavelength peak reflectance during fabrication.....	13
Figure 1-6. Induced refractive index change in a uniform FBG as a function of the distance along the fibre axis	22
Figure 1-7. Optical spectra of an ideal FBG	23
Figure 1-8. Transmission spectrum of a phase-mask-written type II FBG ..	25
Figure 1-9. DIC images of the core region of a type I FBG	28
Figure 2-1. Schematic diagram of the experimental arrangement used for grating fabrication.....	36
Figure 2-2. Schematic diagram of the experimental arrangement used for grating fabrication.....	37
Figure 2-3. Photograph taken during grating fabrication with the custom made phase mask	39
Figure 2-4. Schematic diagram of the experimental arrangement used for grating fabrication.....	40
Figure 2-5. Diffusion of hydrogen molecules into the fibre over time.....	44
Figure 3-1. Predicted intensity distribution at the output face of the prism interferometer due to two-beam interference	47

Figure 3-2. Simulated intensity distributions behind UV irradiated phase masks.....	51
Figure 3-3. Schematic diagram of the modified form of Differential Interference Contrast microscopy used in this work	55
Figure 3-4. Wollaston prism phase bias calibration	57
Figure 3-5. Schematic illustration of sample preparation and positioning used for DIC imaging	58
Figure 3-6. DIC images of the different fibres used in this work.....	60
Figure 3-7. DIC measurements of intensity variation with temperature.....	61
Figure 3-8. Schematic diagram identifying DIC imaging planes and fibre orientations	63
Figure 3-9. DIC images of a type I FBG written with a prism interferometer	67
Figure 3-10. Intensity linescans taken along the fibre axis.....	68
Figure 3-11. DIC images of a type IIA FBG written with a prism interferometer	70
Figure 3-12. DIC images of a type IIA FBG written with a standard phase mask	72
Figure 3-13. Analysis of perpendicular image features of a type II-A FBG ...	73
Figure 3-14. Analysis of parallel image features of a type II-A FBG.....	74
Figure 3-15. DIC images of a type I FBG written with a standard phase mask in standard fibre.....	76
Figure 3-16. Analysis of perpendicular image features of a type I FBG	77
Figure 3-17. Analysis of parallel image features of a type I FBG	78
Figure 3-18. DIC images of a type I FBG written with a standard phase mask in small-core fibre	80
Figure 3-19. Analysis of perpendicular image features of a type I FBG	82
Figure 3-20. Analysis of parallel image features of a type I FBG	83
Figure 3-21. DIC images of a type I FBG written with a custom-made phase mask in standard fibre	85
Figure 3-22. Analysis of perpendicular image features of a type I FBG	86
Figure 3-23. Analysis of parallel image features of a type I FBG.....	87
Figure 3-24. DIC images of a type I FBG written with a custom-made phase mask in small-core fibre	89
Figure 3-25. Analysis of perpendicular image features of a type I FBG	90
Figure 3-26. Analysis of parallel image features of a type I FBG.....	92
Figure 4-1. Schematic diagram of the experimental arrangement used for the measurement of transmission spectra.....	97
Figure 4-2. Spectral behaviour at λ_B of type I and IIA gratings	99

Figure 4-3. Spectral properties at other harmonic reflections.....	102
Figure 4-4. Spectral characteristics of a type I sample prior to type IIA growth	105
Figure 4-5. Growth of sample IIA-1	107
Figure 4-6. Calculated intensity distributions of the LP ₀₁ mode	109
Figure 4-7. Schematic diagram of the experimental arrangement used for the simultaneous measurement of transmission spectra.....	111
Figure 4-8. Spectral properties of multimode and singlemode FBGs fabricated using a standard phase mask.....	113
Figure 4-9. Spectral properties of multimode and singlemode FBGs fabricated using a custom-made phase mask.....	116
Figure 4-10. Evolution of spectral features of sample I-2.....	121
Figure 4-11. Transmission spectra measured after fabrication of samples I-7, I-8 and I-9	122
Figure 4-12. Schematic illustration of harmonic reflections from π phase- shifted Bragg gratings	124
Figure 4-13. Spectral properties of a type I FBG fabricated using a prism interferometer	126
Figure 5-1. The measured and modelled reflectance growth of spectral features at λ_B and $2/3 \lambda_B$ of sample I-1	138
Figure 5-2. The measured and modelled reflectance growth of spectral features at λ_B and $2/3 \lambda_B$ of sample I-2	141
Figure 5-3. The measured and modelled reflectance growth of spectral features at λ_B and $2/3 \lambda_B$ of sample I-3	144
Figure 5-4. The measured and modelled reflectance growth of spectral features at λ_B and $2/3 \lambda_B$ of sample I-4	146
Figure 5-5. DIC images showing the imprinted Talbot diffraction patterns of type I FBGs.....	148
Figure 6-1. Experimental arrangement for axial strain and temperature testing	156
Figure 6-2. Transmission spectra measured after fabrication of type I and IIA gratings	158
Figure 6-3. Responses of transmission dips at $2/3 \lambda_B$ and λ_B for sample I-10	158
Figure 6-4. Transmission spectra measured after fabrication of sample I-11	161
Figure 6-5. Fluorescence spectra of Yb ³⁺	165

List of Tables

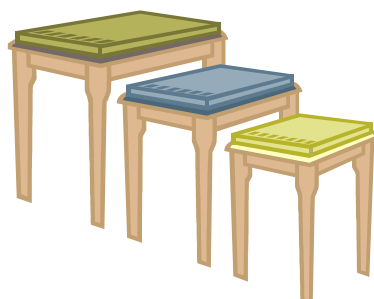
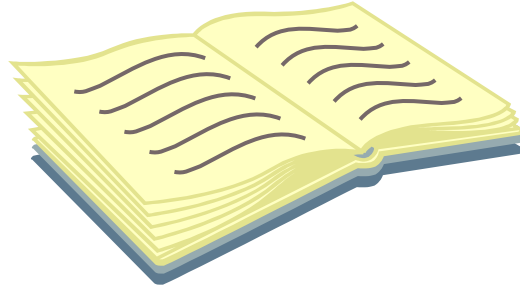


Table 1-1. Applications of fibre Bragg gratings in optical communications	5
Table 1-2. Sellmeier co-efficients for fused silica	19
Table 2-1. UV laser sources used in this work.....	34
Table 2-2. Details of the standard phase masks used in this work.....	34
Table 2-3. Details of the custom-made phase masks used in this work.....	38
Table 2-4. Details of the fibres used in this work	42
Table 2-5. Fabrication details and properties of the FBGs studied in this thesis.....	45
Table 3-1. Spectral components of the simulated diffraction pattern for the standard phase mask SM-2 and custom-made phase mask CM-2	53
Table 3-2. Calculated Talbot lengths of the diffraction patterns produced by the standard phase mask SM-2 and custom-made phase mask CM-2.....	53
Table 3-3. Measured temperature ranges and optimal index-matching temperatures of the fibres used in this work.....	62
Table 3-4. Summary of the prism FBG imaging experiments.....	65
Table 3-5. Periods determined by FFTs of the linescans	69
Table 3-6. Summary of the standard phase mask FBG imaging experiments	71
Table 3-7. Summary of the standard phase mask FBG imaging experiments	84
Table 3-8. Summary of the imaging experiments and results.....	93
Table 4-1. Light sources used for the measurement of optical spectra	97
Table 4-2. Optical spectrum analysers used in this work.....	97

Table 4-3. Approximate values of expected harmonic wavelengths of two grating periods	100
Table 4-4. Reflection peaks in various wavelength regions of type I and type IIA gratings.....	103
Table 4-5. Simulation parameters for large and small core fibres	108
Table 5-1. Measured and calculated parameters of the standard and custom-made phase mask FBGs studied in this work.....	136
Table 5-2. Assessment of Xie <i>et al.</i> model application to measured harmonic reflectance growth of sample I-1.....	139
Table 5-3. Assessment of Xie <i>et al.</i> model application to measured harmonic reflectance growth of sample I-2	141
Table 5-4. Assessment of Xie <i>et al.</i> model application to measured harmonic reflectance growth of sample I-3	144
Table 5-5. Assessment of Xie <i>et al.</i> model application to measured harmonic reflectance growth of sample I-4	146
Table 5-6. Summary of the sample properties and the modelled contributions of spectral components to the observed reflectance growth.....	149
Table 6-1. Axial strain and temperature characteristics of previously reported dual wavelength or dual grating sensors	154
Table 6-2. Axial strain and temperature characteristics of two different wavelengths for various samples	159
Table 6-3. Axial strain and temperature characteristics of two different wavelengths and FIR.....	162

Contents



Declaration.....	i
Abstract	iii
Acknowledgements	v
List of Figures	vii
List of Tables.....	x

Chapter 1: Introduction **1**

1.1 Optical fibres in communications and sensing	1
1.1.1 Optical fibres in telecommunications.....	2
1.1.2 Optical fibre sensing	4
1.2 Fibre Bragg gratings in telecommunications	4
1.3 Fibre Bragg gratings in sensing	5
1.4 Optical fibre Bragg gratings.....	7
1.4.1 Self-organised gratings	7
1.4.2 Interferometric fabrication techniques	8
1.4.3 The phase mask fabrication technique.....	10
1.4.4 Principles of UV-induced refractive index change	12
1.4.5 Grating types.....	13
1.4.6 Enhancing photosensitivity	15
1.5 Characteristics of fibre Bragg gratings	17
1.5.1 The Bragg condition.....	17

1.5.2	Induced Bragg period	20
1.5.3	Induced reflectance.....	20
1.5.4	Induced refractive index change.....	21
1.5.5	Spectral characteristics	23
1.5.6	Microscopic characteristics	26
1.6	Scope of thesis.....	29
Chapter 2: Fibre Bragg Grating Fabrication		32
2.1	Writing fluence	32
2.2	Laser sources.....	34
2.3	Phase mask technique.....	34
2.3.1	Standard phase mask.....	34
2.3.2	Custom-made phase mask.....	38
2.4	Prism interferometer technique	39
2.5	Fibre types.....	42
2.6	Hydrogen loading	42
2.7	Sample details	44
Chapter 3: Microscopic Characterisation		46
3.1	Predicted intensity distributions	46
3.1.1	Prism Interferometer	46
3.1.2	Phase masks and Talbot diffraction	48
3.2	Differential interference contrast microscopy	54
3.2.1	Wollaston prism bias	56
3.2.2	Sample preparation	57
3.2.3	Fibre properties and index-matching.....	58
3.2.4	Rotational analysis.....	62
3.2.5	Analysis of periodic features.....	64
3.3	Prism interferometer FBGs	65
3.3.1	Type I.....	65
3.3.2	Type IIA.....	69
3.4	Standard phase mask FBGs	71
3.4.1	Type IIA.....	71
3.4.2	Standard telecommunications fibre	75
3.4.3	Smaller core fibre.....	79
3.5	Custom-made phase mask FBGs.....	84
3.5.1	Standard telecommunications fibre	84
3.5.2	Smaller core fibre.....	88
3.6	Conclusions.....	93

Chapter 4: Spectral Characterisation	96
4.1 Spectral measurements	96
4.2 Type I and type IIA FBGs	98
4.2.1 The Bragg wavelength.....	98
4.2.2 Other harmonic wavelengths.....	99
4.2.3 Further type IIA results	106
4.3 Multimode versus singlemode conditions.....	107
4.3.1 Predicted modal distributions	108
4.3.2 Simultaneous spectral measurements.....	111
4.3.3 Standard phase mask.....	111
4.3.4 Custom-made phase mask.....	115
4.4 Double-Dip Structure at $2/3 \lambda_B$	119
4.4.1 Phase-shifted FBGs.....	122
4.5 Prism interferometer FBGs	125
4.6 Conclusions	128
Chapter 5: Harmonic Reflectance Growth	131
5.1 The Xie model	132
5.1.1 Data analysis	134
5.1.2 Model parameters	134
5.2 Standard phase mask.....	137
5.2.1 Multimode conditions.....	137
5.2.2 Singlemode conditions.....	140
5.3 Custom-made phase mask.....	143
5.3.1 Multimode conditions.....	143
5.3.2 Singlemode conditions.....	145
5.4 Conclusions	147
Chapter 6: Temperature and Strain Characterisation	151
6.1 Introduction.....	151
6.2 Experimental arrangement.....	156
6.3 Dual wavelength sensing	157
6.4 Dual wavelength sensing with FIR.....	160
6.5 Conclusions	166
Chapter 7: Conclusions	168
7.1 Suggestions for future work.....	174

Bibliography **179**

Appendix: List of Publications **191**

A.1 Book chapters..... 191

A.2 Journal articles 191

A.3 Conference proceedings.....192

Chapter 1:

Introduction

This chapter begins with an introduction to the use of optical fibres in telecommunications and sensing and then discusses the particular importance of fibre Bragg gratings (FBGs) in these fields. The theory relating to the fabrication and optimisation of FBGs is presented followed by a discussion of the spectral and microscopic characteristics of FBGs. The chapter concludes with the scope of this thesis.

1.1 Optical fibres in communications and sensing

Optical fibre technology was first realised in the 1960s and has developed to be an integral part of modern telecommunications and sensing [1, 2]. As shown in Figure 1-1, an optical fibre consists of a core surrounded by a lower refractive index cladding. For certain angles of incidence, light is launched into the allowable modes of propagation and guided along the fibre by the core-cladding boundary. The intrinsic properties of optical fibres such as low loss transmission, immunity to electromagnetic interference, light weight and electrical isolation make them ideal for use in telecommunications and sensing.

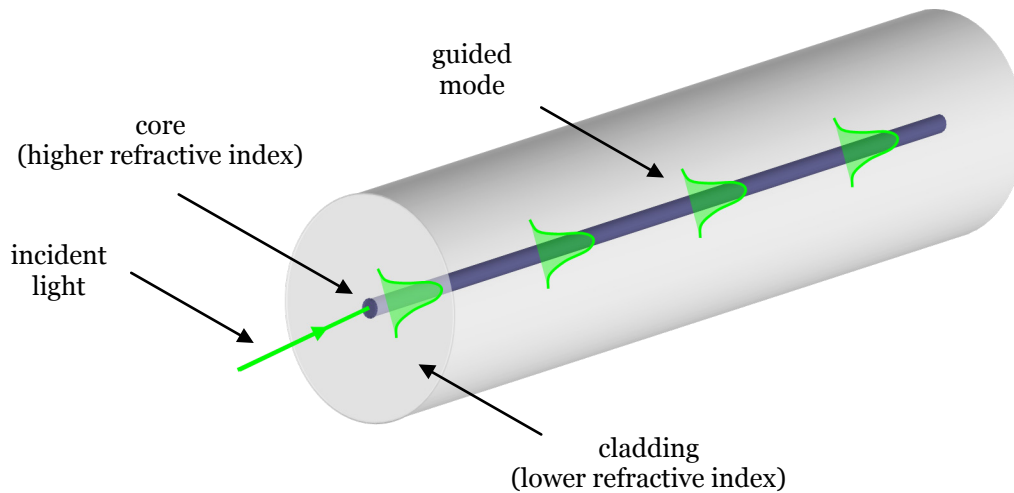


Figure 1-1. Guidance of light in an optical fibre [1].

1.1.1 Optical fibres in telecommunications

Standard telecommunications fibre is generally fabricated using a silica cladding and a silica core doped with germanium to increase the refractive index and form the core-cladding boundary necessary for the guiding of light down the fibre. Silica glass has certain transmission and absorption bands that are critical to telecommunications system design. A number of mechanisms cause signal power attenuation including Rayleigh scattering, loss to absorption and material dispersion. [1]

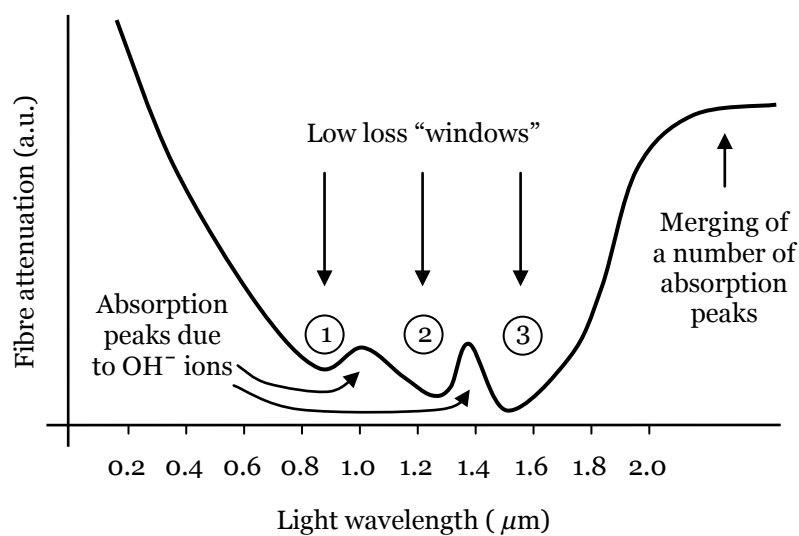


Figure 1-2. Typical attenuation of silica optical fibre over a range of wavelengths [1].

Silica glass is an amorphous material; meaning there is a random configuration of SiO₂ molecules and impurities within the glass. As light travels down a silica optical fibre and interacts with the random molecular structure, shorter wavelengths will be scattered to a greater degree than will longer wavelengths; this is known as Rayleigh scattering. As can be seen in Figure 1-2, the attenuation due to Rayleigh scattering decreases as wavelength increases until just after 0.8 μm when another loss mechanism begins to affect the attenuation spectrum. The attenuation peaks in the 0.8–1.6 μm range in Figure 1-2 are the result of resonance between certain light frequencies and OH⁻ ions in the glass; this is known as absorption loss. The low loss “windows” 1, 2 and 3 in Figure 1-2 correspond to 0.85, 1.30 and 1.55 μm respectively. A number of telecommunications systems have been engineered to operate at 1.3 μm because of the low attenuation and low material dispersion, but the higher dispersive window at 1.55 μm has lower attenuation, which is an important requirement over long distances. Fibre geometry has been designed such that waveguide dispersion can counter the material dispersion and hence opened up the more advantageous 1.55 μm telecommunications window. [1]

Operations such as signal amplification, reflection, diffraction and filtering have, in the past, required light to be coupled in and out of fibre, which was an inherently lossy process that relied on bulk optics. Devices which perform such operations in-fibre have subsequently been developed, including fibre amplifiers, optical switches and fibre Bragg gratings. Such devices work to improve efficiency, transmission speeds and bandwidths of optical telecommunication networks.

Optical fibre technology has become part of the very infrastructure of major communications systems, linking countries around the globe. Long haul transmission speeds of up to 8 Tbit/s have been reported [3] and the field of optical fibres for telecommunications is ever improving.

1.1.2 Optical fibre sensing

The first optical fibre sensors were designed to measure the performance and status of an optical network [4]. Optical networks transmit voice and data around the world and require constant monitoring to ensure signal transmission along the fibres in the network. In addition to telecommunications applications, optical fibre sensors are used in oil and gas services, medical and biomedical engineering, the electrical power industry, structural monitoring, defence and aerospace applications and other specialised industries [2, 4]. Such applications require accurate monitoring of various measurands such as chemical concentration, pH, temperature, pressure, humidity, acceleration and strain. Optical fibre sensors are highly desirable solutions to sensing applications due to their small size, low loss transmission, immunity to electromagnetic interference, light weight and electrical isolation amongst other advantages. Many sensing systems have been proposed and developed which incorporate optical fibre; some which utilise optical fibre both extrinsically and intrinsically. Extrinsic optical fibre sensors use optical fibre to transmit signals from the sensing point to a remote controller to be analysed, whereas intrinsic sensors use the actual fibre as the sensing element [4].

Extrinsic optical fibre sensors can be found in schemes such as Fabry-Perot interferometers which utilise only some of the advantages optical fibres offer over competing technologies. Intrinsic optical fibre sensors such as the fibre optic gyroscope, fibre Bragg gratings, long period gratings, microbend and coated or doped fibre sensors utilise more of the advantages offered by the technology.

1.2 Fibre Bragg gratings in telecommunications

Optical communication networks have enabled the high-capacity transmission and reception of information between most parts of the globe. As the demand for higher transmission speeds and higher capacity increases, so does the necessity for high-speed optical links. Operations with optical fibres such as reflection, diffraction and filtering have, in the past, required light to be

coupled in and out of fibre, which was an inherently lossy process that relied on bulk optics. With the discovery of fibre photosensitivity and the subsequent development of fibre grating devices, such operations can now be performed in fibre. For telecommunications, fibre Bragg gratings have found application in fibre lasers and laser diodes, fibre amplifiers, wavelength division multiplexing and demultiplexing, dispersion compensation, phase conjugation and even temperature sensing in optical networks. Various fibre grating types, linewidths and strengths are required for these different applications and Table 1-1 summarises the typical fabrication characteristics required for various functions in optical communications.

Application	Description	Parameters
Fibre laser	Narrowband reflector	$\Delta\lambda = 0.1-1 \text{ nm}$ $R = 1-100\%$
Laser wavelength stabilisation (980 nm, 1480 nm)	Narrowband reflector	$\Delta\lambda = 0.2-3 \text{ nm}$ $R = 1-10\%$
Pump reflector in fibre amplifiers (1480 nm)	Highly reflective mirror	$\Delta\lambda = 2-25 \text{ nm}$ $R = 100\%$
Raman amplifiers (1300 nm, 1550 nm)	Several highly reflective mirror pairs	$\Delta\lambda = 1 \text{ nm}$ $R = 100\%$
Isolation filters in bidirectional WDM transmission (1550 nm)	Matched sets of WDM gratings	$\Delta\lambda = 0.2-1 \text{ nm}$ $R = 100\%$
Pump reflector in phase conjugator (1550 nm) and isolation filter in wavelength converter	Highly reflective mirror	$\Delta\lambda = 1 \text{ nm}$ $R = 100\%$
WDM demultiplexer (1550 nm)	Multiple high-isolation reflectors	$\Delta\lambda = 0.2-1 \text{ nm}$ Isolation > 50 dB
WDM add/drop filter (1550 nm)	High-isolation reflector	$\Delta\lambda = 0.1-1 \text{ nm}$ Isolation > 30 dB
Optical amplifier gain equaliser (1530-1560 nm)	Blazed Bragg grating or long period grating	$\Delta\lambda = 30 \text{ nm}$ Loss = 0-10 dB
Dispersion compensation for long-haul transmission (1550 nm)	Chirped grating	$\Delta\lambda = 0.1-15 \text{ nm}$ 1600 ps/nm

Table 1-1. Applications of fibre Bragg gratings in optical communications. [5]

1.3 Fibre Bragg gratings in sensing

Fibre Bragg gratings are highly suited as sensor elements for measuring various static and dynamic fields such as temperature, strain and pressure [6]. One of the main advantages of fibre grating sensors over other types of optical fibre sensors is that the measurand information is wavelength encoded,

making the fibre grating sensor self-referencing and rendering it independent of light source fluctuations and system power or connector losses.

Although very attractive as sensors, fibre Bragg gratings suffer an inherent cross-sensitivity between temperature and strain. This creates a problem for sensor systems designed to monitor strain alone for example, as temperature variations along the fibre path can lead to unrepresentative, thermal-induced strain readings [6]. One common method of addressing this cross-sensitivity is by the use of two fibre gratings, one of which is not bonded to the object being measured [7] and hence is not subject to the strain component, but has the disadvantage that the sensors are not co-located. A variety of arrangements of pairs of fibre gratings have been investigated in order to achieve sensor co-location, or at least a compact sensor, in which two gratings are fabricated near each other in a single fibre. Examples of co-located sensors include a pair of Bragg gratings operating at 850 and 1300 nm [8], and a combination of a fibre grating with a long period grating [9, 10]. Other approaches involve the use of both the first- and second-order diffraction wavelengths of a single fibre grating [11-14], a single fibre grating in birefringent fibre [15], the use of two fibre gratings in series but in different fibre types [16], a single fibre grating written across the splice between two different fibres [17], and the combination of two different grating types in the same fibre type [18-23].

Another method of co-located temperature and strain sensing involves writing a fibre grating in rare-earth-doped optical fibre. In this approach rare-earth ions are excited by an optical pulse, in which the resultant fluorescent decay curve has a lifetime that depends strongly upon temperature and weakly upon strain [24]. The related fluorescence intensity ratio (FIR) technique [25], which also relies upon the decay of excited levels in rare-earth ions, has been shown to be essentially strain independent. This scheme has been reported for both Er^{3+} -doped fibre [26] and $\text{Er}^{3+}:\text{Yb}^{3+}$ -co-doped fibre [27].

The bandwidth of optical fibres also allows for more than two parameters to be measured simultaneously. Vibration sensing, in addition to temperature

and strain, has been reported through the use of an interferometer in addition to a fibre grating [28, 29]. Curvature measurement in one axis [30] and two-axes [31] has been reported using gratings written into separate cores of multicore fibre. Simultaneous axial strain, temperature and curvature sensing has been proposed using a single superstructured fibre Bragg grating (SFBG) [32]. Simultaneous refractive index and temperature sensing has been proposed using a non-uniform thinned grating [33], an ultra-long period grating [34] and a slanted multimode fibre grating [35]. Transverse strain measurement has been demonstrated in low-birefringent fibre in which the load causes the Bragg peak to split slightly, with the separation of the peaks increasing linearly with load and was attributed to induced birefringence [36]. Special gratings [37] and long period gratings [38] have also been used for transverse strain sensing. Fibre gratings in highly-birefringent fibre have better sensitivity to transverse strain due to the presence of two closely spaced Bragg wavelengths separated by typically a few nanometres [39-41].

1.4 Optical fibre Bragg gratings

1.4.1 Self-organised gratings

In its most basic form, a fibre Bragg grating consists of a periodic modulation of the refractive index along the optical fibre core that reflects light at wavelengths determined by the Bragg condition (see section 1.5.1) [5, 42]. This refractive index modulation is usually imprinted when a periodic pattern of coherent ultraviolet radiation is formed in the core of certain fibre types. The first fibre Bragg grating was produced as the result of the standing wave interference between incident 488 nm light within the fibre and the 4% Fresnel reflected beam from the cleaved end of the fibre [43]. With prolonged exposure, this weak interference pattern formed a grating along the fibre that gradually enhanced the strength of the back-reflected beam until the reflectivity of the grating reached a saturated level. Gratings produced in this manner were thus called self-organised or self-induced because they formed spontaneously within the optical fibre.

Self-organised gratings were not practical for application in telecommunications due to the Bragg resonance wavelength being limited to the wavelength of the writing beam, which was in the visible part of the spectrum. These gratings also exhibited very small wavelength changes under strain so they were not practical for sensing either. In 1989, following the work by Lam and Garside [44], Meltz *et al.* [45] demonstrated the side-writing technique of producing a fibre grating by transverse holography.

It was found that irradiating the side of an optical fibre with a periodic pattern formed by the intersection of two coherent 244 nm beams in an interferometer resulted in a modulation of the core index of refraction, inducing a periodic grating. Changing the angle between the intersecting beams altered the spacing between interference maxima, whereby the periodicity of the grating was controlled so that operating over a wide range of wavelengths was possible. Side-writing techniques have made it possible to produce gratings at almost any desired Bragg wavelength at the desired location along a fibre and the most common fabrication methods are the interferometric and phase mask techniques.

1.4.2 Interferometric fabrication techniques

Bragg gratings can be written interferometrically by amplitude-splitting or by wavefront-splitting. The former technique includes the transverse holographic method [45] (Figure 1-3(a)) that splits a UV laser beam into two equal intensity beams that subsequently recombine after having undergone a different number of reflections in each optical path, which results in a low-quality fringe pattern for lasers with low spatial coherence. Improvements on this technique involved the addition of a mirror to one of the optical paths to equate the number of reflections and ensure identical interfering beams at the fibre and also the addition of a cylindrical lens for higher intensities at the core and improved grating inscription. The amplitude-splitting interferometric technique offers an important advantage in its ability to inscribe Bragg gratings at any desired wavelength by simply changing the intersection angle of the UV beams, but the method is disadvantageous in its susceptibility to mechanical vibrations. Submicron displacements in the

positions of any system components will cause the interference pattern to drift and wash out the grating. The long optical paths of the laser beams can also be problematic for the stability of the fringe pattern and quality gratings can only be produced with a laser source that has good spatial and temporal coherence and excellent wavelength and output stability. [5]

Examples of wavefront-splitting fabrication techniques include the Lloyd mirror interferometer [46] and the prism interferometer [47, 48] (Figure 1-3(b)). In the Lloyd mirror interferometer fabrication method, the UV beam is centred at the perpendicular intersection of a dielectric mirror and the fibre. The mirror directs half of the beam to the fibre and the overlap of the direct and deviated portions forms a fringe pattern normal to the fibre axis. In the prism interferometer fabrication method, the UV beam is spatially bisected by the edge of a high grade, fused silica prism, and half the beam is spatially reversed by total internal reflection from the prism face. The beam halves are then recombined at the output prism face to produce a fringe pattern parallel to the fibre core.

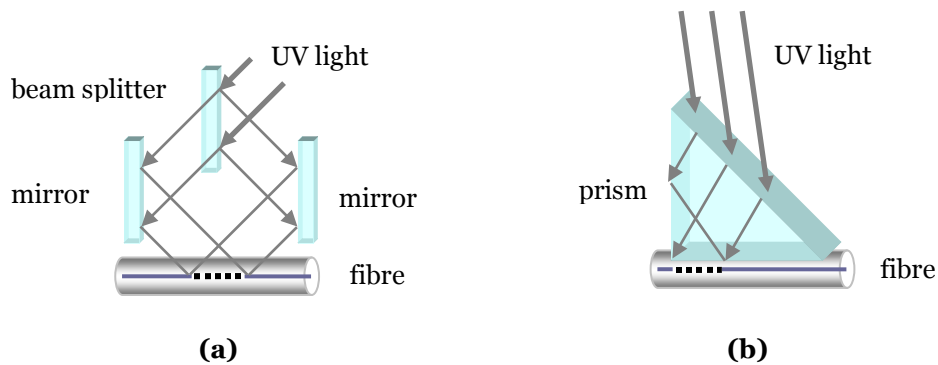


Figure 1-3. Optical systems for interferometric inscription of FBGs: **(a)** transverse holographic and **(b)** prism interferometer techniques.

Both wavefront-splitting methods are intrinsically stable in terms of mechanical vibrations due to the requirement for only one optical component and the short beam separation reduces possible wavefront distortion due to air currents and temperature variations. However, both methods require a highly spatially coherent source as the interference is formed by folding the

beam onto itself and the grating length is restricted to half of the beam width. Wavelength tuning is achieved relatively simply by assembly rotation, but the tuning range is restricted by the physical arrangement of the interferometers and the coherence length of the beam. [5]

1.4.3 The phase mask fabrication technique

Fibre Bragg grating fabrication using a diffractive optical element to produce the UV interference pattern was first reported in 1993 [49, 50]. Using holography or electron-beam lithography, the phase mask is produced as a one-dimensional periodic surface-relief pattern, with period Λ_{pm} etched into fused silica. Phase masks for fibre Bragg grating fabrication are usually designed such that the zeroth-order diffracted beam is suppressed to typically less than 3% of the transmitted power and the diffracted plus and minus first (± 1) orders are maximised to contain typically more than 35%, with the remaining power distributed amongst higher orders [5, 50]. The fibre Bragg grating results from the interference pattern formed by the diffracted orders which overlap coherently in the region of the fibre core.

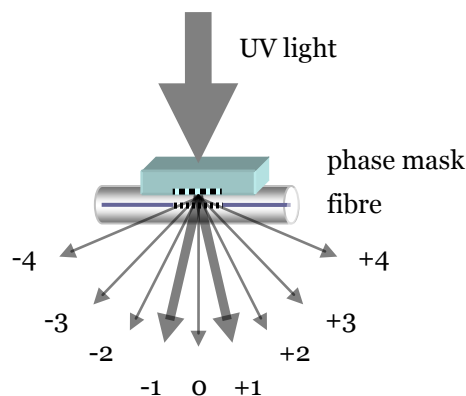


Figure 1-4. Optical system for fibre grating fabrication using a typical phase mask.

The optical arrangement for fabrication of fibre Bragg gratings using a typical phase mask is illustrated in Figure 1-4. The fibre is usually placed as close as possible to the phase mask and the interference pattern formed behind the mask (between the orders which are coherent) is imprinted in the core, if the

laser fluence is sufficient and if the fibre is sufficiently photosensitive (see section 1.4.4).

The phase mask technique greatly reduces the complexity of system alignment in a fibre grating fabrication as it uses only one optical element. The technique also minimises sensitivity to mechanical vibrations and due to the system geometry, a low temporal coherence of the UV source does not affect writing capability as opposed to interferometric techniques. Good spatial coherence is still critical in the phase mask technique, but good quality gratings can still be produced using low spatially coherent sources by optimising the spacing between fibre and mask [5].

While robust and easily employable, the phase mask technique produces multiple beams with varying relative diffraction strengths, whereas interferometric techniques form fringe patterns with only two beams. The multiple beams present behind the phase mask during fabrication may have a measurable effect on the imprinted grating but little information has been reported on the effect of light in orders of phase masks other than the $\pm 1^{\text{st}}$.

Malo *et al.* reported that at low writing intensities, the period of the FBG is half the phase mask period, but at high intensities, even a small zeroth-order contribution can interfere with the $\pm 1^{\text{st}}$ orders to create a grating of the same period as the phase mask [51]. In other work, analysis of grating formation with excimer laser irradiated phase masks for varying efficiencies in each of the diffracted orders demonstrated that even small contributions from the 0^{th} and/or 2^{nd} orders lead to alternating zones with grating periodicities equal to the phase mask, Λ_{pm} , such that this period was dominant over the $\Lambda_{pm}/2$ period which occurs for pure 1^{st} order interference [52]. The alternating zones were found to give rise to a period of $\Lambda_{pm}/2$ as a result of averaging over the fibre core diameter and it was found that in general, the in-fibre index modulation will be composed of a mixture of Λ_{pm} and $\Lambda_{pm}/2$ gratings. In particular, simulations using efficiencies for a typical 0^{th} -order suppressed phase mask in the 0^{th} , 1^{st} , 2^{nd} , 3^{rd} and 4^{th} diffracted orders of 5, 37, 1, 0 and

0%, respectively, produced patterns with alternating zones of Λ_{pm} spaced field perturbations.

1.4.4 Principles of UV-induced refractive index change

The phenomenon of fibre photosensitivity, whereby UV light permanently changes the refractive index, was an exciting discovery that has revolutionised optical fibre technology. It was initially thought to be only associated with highly germanium doped optical fibre that is exposed to 240–250 nm UV light. However, with the realisation that most fibre types can exhibit photosensitivity, it became apparent that the phenomenon is a function of various mechanisms (including photochemical, photomechanical, and thermochemical) and the relative contribution to index change will be dependent on the fibre type, radiation intensity and writing wavelength. The precise mechanisms underlying photosensitivity are not fully understood but a number of theories have been presented. [5, 53]

The transverse (side) writing technique of grating fabrication demonstrated by Meltz *et al.* [45] used a direct excitation wavelength of 240 nm. The absorption band centred on this excitation (240 nm) has been related to defect centres in germanosilicate glass [54, 55]. The following theories, including the Kramers-Kronig [56], dipole [57] and compaction models [58, 59], have been proposed for the formation of fibre Bragg gratings and relate to the breakage of germanium-silicon (Ge-Si) bonds by the UV light.

The Kramers-Kronig [56] model of photosensitivity reasons that UV light causes the breakage of the Ge-Si bond and in doing so creates a GeE' centre, \equiv Si⁺ hole and a released electron. The released electron is captured at Ge(1) or Ge(2) and forms negatively charged colour centres Ge⁻(1) or Ge⁻(2) inducing the refractive index change and a change in the absorption spectra. In the dipole model [57], a GeE' centre is created by the Ge-Si bond breakage and a dipole moment is formed between GeE' and Ge-(1), Ge-(2) that is oriented along the axis of the light-electric field. This orientation causes an electric field in the glass resulting in a refractive index change caused by the electro-optical

effect. The compaction model [58, 59] reasons that the UV radiation breaks bonds in the glass network causing the glass structure to compress and its density to increase, producing the refractive index change. The general consensus on photosensitivity is that colour-centres form as a result of the incident radiation and give way to compaction of the glass [5].

1.4.5 Grating types

Despite the fact there are many fibre types, different UV radiation bands and laser powers available, the growth dynamics of fibre Bragg gratings can be classified into four distinct formation regimes: type I, IIA, II [5] and type IA [60]. Type I fibre gratings are generally formed in most photosensitive fibre types when exposed to continuous wave (CW) or relatively low pulse fluence UV radiation and are characterised by a monotonic increase in the amplitude of the refractive index modulation with UV exposure, as indicated in Figure 1-5(a) by the nature of the typical peak reflectance growth during fabrication. This classification generally refers to gratings written with relatively low power densities (sometimes referred to as fluences) compared to the other formation regimes. The process depends strongly on the photosensitivity of the fibre and results in a positive index change ($\Delta n > 0$) with an accompanying positive shift in peak wavelength.

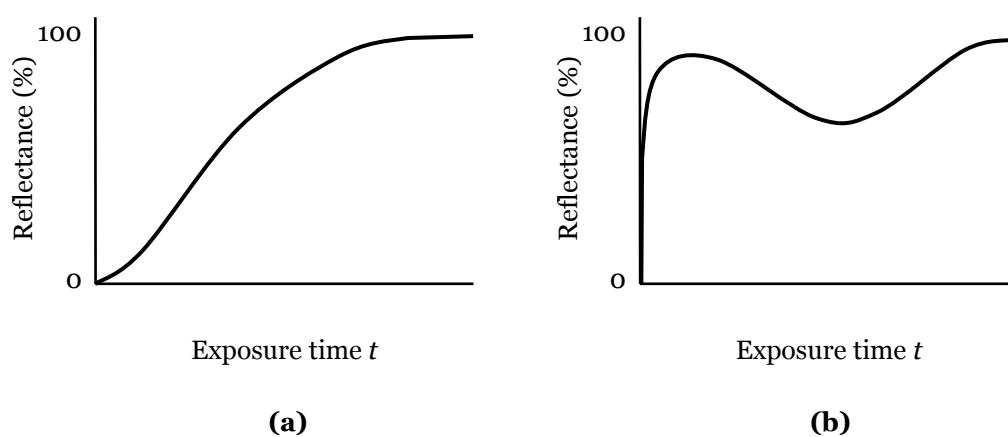


Figure 1-5. Typical growth dynamics of the Bragg wavelength peak reflectance during fabrication of **(a)** type I and **(b)** IIA fibre gratings.

In some fibre types, prolonged exposure of type I fibre gratings can result in partial or complete grating erasure, followed by a new spectral formation, known as a type IIA fibre grating (or sometimes referred to as type III) as shown in Figure 1-5(b). Type IIA gratings are written with fluences that are typically higher than those used for type I gratings. Type IIA grating formation is associated with a negative Δn and an accompanying decrease in the Bragg wavelength. Type IIA [61] growth characteristics are almost certainly always possible in fibres with any concentration of germanium, but are more easily observed in fibre that has been doped with higher than normal levels of germanium. Germanosilicate fibres co-doped with boron (Ge:B) require higher levels of germanium because boron actually lowers the refractive index, so it is possible that enhanced photosensitivity in Ge:B fibres is due to the higher germanium content [42].

It is almost certain that the mechanisms responsible for type I and type IIA gratings are different. Proposed models [5] for the formation of type IIA gratings usually assume that the refractive index evolution with exposure time results from two local reactions. The first reaction which erases and produces some defects or chemical species that lead to a positive index change, while the second, a reaction slower than the first, produces a negative change through structural reorganisation. In 2002, a new fibre grating type was observed in hydrogenated Ge:B doped fibres and was designated type IA [18]. Type IA fibre gratings are similar to type IIA in terms of formation except, during the prolonged exposure after the initial grating erasure, the Bragg wavelength, λ_B , undergoes a red shift in the case of type IA fibre gratings whereas λ_B of type IIA fibre gratings undergoes a blue shift.

At irradiation energy levels greater than 1 J/cm^2 , a single excimer light pulse can photoinduce large refractive changes in small localised regions at the core/cladding boundary. Gratings formed in such a way are known as type II gratings and are the result of physical damage to the core glass having refractive index modulations as high as 10^{-2} . Such high refractive index modulation in the core allows for direct observation with a phase contrast

microscope of the induced changes, which appear to constitute direct physical damage of the fibre through localised fusion.

Apart from standard, uniform gratings, there is also a wide range of other fibre grating types such as blazed, long period, chirped and phase-shifted. Blazed gratings are those which have been fabricated using a tilted fringe pattern resulting in tilted grating planes in the fibre; long period gratings are fabricated using interference patterns with periods typically ranging in hundreds of micrometres; and chirped gratings are those written with a non-uniform or monotonically varying period. Phase-shifted gratings have been produced via superposition of two interference patterns with dissimilar periods to form moiré gratings [62, 63], by laser trimming [64], via phase-shifted phase masks [65] or phase plates [66, 67]. Gratings with a π phase-shift are characterised by a notch centred in the reflection peak/transmission dip due to destructive interference. Phase-shifted Bragg gratings were initially used in surface acoustic wave resonators [68] and later found important applications in semiconductor lasers [69] and in wavelength demultiplexing [70].

1.4.6 Enhancing photosensitivity

The photosensitivity of an optical fibre refers to its capacity to undergo refractive index changes when exposed to UV radiation. Although initially thought to be associated only with highly germanium doped optical fibre that is exposed to 240–250 nm UV light, research over the following years has shown that photosensitivity is exhibited by a wide range of different fibres exposed to different UV wavelengths, that contain dopants other than germanium and some which contained no germanium at all. In 1993, Lemaire *et al.* [71] discovered that photosensitivity could be improved by up to two orders of magnitude by hydrogen loading the fibre before photoinscription of the grating.

Standard singlemode telecommunications fibre, doped with 3% germania, displays typical index changes of $\sim 3 \times 10^{-5}$. Larger indices of $\sim 5 \times 10^{-4}$ can result from increasing the dopant level or subjecting the fibre preform to

reducing conditions at high temperatures. However, for compatibility with existing systems, it is desirable to fabricate gratings in standard optical fibre. Photoinduced refractive index modulations have been increased to values of the order of 10^{-3} and higher via hydrogenation as mentioned above or by flame brushing [72].

In the hydrogen loading (hydrogenation) method of photosensitivity enhancement, fibres are soaked in hydrogen gas for varying lengths of time at temperatures ranging from 20–80 °C and pressures from ~20 atm to more than 750 atm (typically 150 atm). Hydrogen loading results in the diffusion of hydrogen molecules into the fibre core. In this process, hydrogen is used in a chemical reaction with germanosilicate glass to form germanium oxygen-deficient centres (GODCs) [5] that are responsible for the enhanced photosensitivity.

Hydrogen loading allows the fabrication of gratings in most germanosilicate and germanium-free fibres and also has the benefit that the hydrogen will diffuse out of unexposed fibre sections so as to leave negligible absorption losses at the important optical communication windows. Absorption bands produced by hydrogenation introduce losses that are often unacceptable in telecommunications network systems. However, loading the fibre with deuterium rather than hydrogen shifts the UV-induced absorption peak to longer wavelengths, out of the erbium amplifier band of 1.55 μm .

The flame brushing technique [72] involves brushing the fibre repeatedly with a flame fuelled with hydrogen and a small amount of oxygen, reaching temperatures of ~1700 °C for approximately 20 minutes to achieve photosensitisation. At these temperatures, the hydrogen is diffused into the core very quickly and reacts with the germanosilicate glass to produce GODCs, creating a strong absorption band at 240 nm making the fibre highly photosensitive. The flame brushing technique has been used to increase the photosensitivity of standard optical fibre by a factor greater than 10, achieving index changes of $>10^{-3}$.

The flame brushing technique has an advantage over hydrogen loading in that the increased photosensitivity is permanent when the fibre has been flame brushed, whereas hydrogen loaded fibre loses photosensitivity as the hydrogen diffuses out. However, due to the high temperature flames used, flame brushed fibre is weaker, which has serious implications for the long-term stability of any device fabricated by this method.

The addition of various co-dopants in germanosilicate fibre has also been found to enhance photosensitivity. Studies have shown that fibres doped with europium [73], cerium [48] and erbium:germanium [74] exhibit varying degrees of photosensitivity but none induce as much photosensitivity as germania. Dopants such as tin [75] and antimony [76] have also been found to induce photosensitivity. Photosensitivity has been observed in a fluorozirconate fibre doped with cerium:erbium [77] when exposed to 246 nm radiation and germanium-boron co-doping [78] produces highly photosensitive fibre.

Co-doping with boron, in particular, can result in an increase in index change of ~ 4 times larger than that obtained in pure germanosilicate fibre [78]. Studies have shown fibre co-doped with boron to be much more photosensitive than fibre with higher germanium concentration and without boron co-doping. Absorption measurements of the studied fibre suggested that boron co-doping does not enhance photosensitivity through the production of GODCs as in the cases of hydrogenation and flame brushing. On the contrary, it is believed that boron co-doping increases the photosensitivity of the fibre by allowing photoinduced stress relaxation to occur, which seems likely to be initiated by the breakage of bonds by UV light.

1.5 Characteristics of fibre Bragg gratings

1.5.1 The Bragg condition

A fibre Bragg grating, in its simplest form, can be thought of as a uniformly periodic modulation of the refractive index in the core of an optical fibre. Each grating plane scatters a fraction of the light propagating along the fibre and if

the Bragg condition is not satisfied, the reflected light from each of the subsequent planes becomes progressively out of phase and will eventually cancel out. Light that is not resonant with the Bragg wavelength will be partially reflected by each of the grating planes because of the index mismatch. When the Bragg condition is satisfied, each fraction of light reflected from each grating plane adds constructively in the backward direction to form a back-reflected peak with a centre wavelength defined by the grating characteristics.

The induced fibre grating can be described as an optical diffraction grating in the core of the optical fibre and therefore its effect on an incident light wave can be described by the equation [79]:

$$n_{co} \sin \theta_2 = n_{co} \sin \theta_1 + m \frac{\lambda_m}{\Lambda}, \quad \text{Equation 1-1}$$

where n_{co} is the refractive index of the fibre core, θ_1 is the angle of the incident wave, the integer m determines the diffraction order and Λ is the grating period. θ_2 is the angle of the diffracted wave, i.e. the direction into which constructive interference occurs, that can be used to determine the wavelength, λ_m , at which a fibre grating most efficiently couples light between the reflected and transmitted modes.

Since the mode propagation constant is given by $\beta = 2\pi n_{eff} / \lambda_m$ where $n_{eff} = n_{co} \sin \theta$ is the effective mode index of the fibre, Equation 1-1 may be rewritten for guided modes as [80]:

$$\beta_2 = \beta_1 + m \frac{2\pi}{\Lambda}. \quad \text{Equation 1-2}$$

Since the reflected and transmitted modes propagate in opposite directions such that $\beta_2 = -\beta_1$, Equation 1-2 simplifies to the general Bragg condition given by:

$$\lambda_m = \frac{2}{m} n_{eff} \Lambda \quad \text{Equation 1-3}$$

where λ_m is the reflected wavelength of order $m = 1, 2, 3, \dots$, and n_{eff} is the effective index of the LP_{01} mode which is approximately equal to the refractive index of the core at λ_m . The main reflection from the grating is known as the Bragg wavelength, λ_B , and is generally considered to be given by the first-order Bragg condition:

$$\lambda_B = 2 n_{eff} \Lambda. \quad \text{Equation 1-4}$$

Since standard optical fibres consist of a silica cladding surrounding a core with a refractive index difference Δn_{co} , the refractive index of the core is given by:

$$n_{co}(\lambda_m) = n_{silica}(\lambda_m) + \Delta n_{co} \quad \text{Equation 1-5}$$

where $n_{silica}(\lambda_m)$ can be calculated using the Sellmeier co-efficients for fused silica [81] given in Table 1-2 and the Sellmeier equation for refractive index as a function of wavelength [82]:

$$n_{silica}(\lambda_m) = \sqrt{1 + \frac{a_1 \lambda_m^2}{\lambda_m^2 - l_1^2} + \frac{a_2 \lambda_m^2}{\lambda_m^2 - l_2^2} + \frac{a_3 \lambda_m^2}{\lambda_m^2 - l_3^2}}. \quad \text{Equation 1-6}$$

Co-efficient	Value
a_1	0.6961663
a_2	0.4079426
a_3	0.8974794
l_1	0.0684043
l_2	0.1162414
l_3	9.896161

Table 1-2. Sellmeier co-efficients for fused silica [81].

1.5.2 Induced Bragg period

For interferometric fabrication techniques, the fibre grating period Λ is given by the period of the fringe pattern formed by the two interfering beams. For fibre Bragg gratings fabricated using the phase mask technique, the interference pattern behind the mask, of period Λ_{pm} , is generally considered to be formed only by the $\pm 1^{\text{st}}$ order diffracted beams. In this case, the intensity parallel to the surface of the mask would vary with a period equal to half that of the phase mask, i.e. $\Lambda = \Lambda_{pm}/2$. The effect of the higher order diffracted beams of the phase mask on the induced Bragg period will be discussed further in Chapters 2, 4 and 5.

1.5.3 Induced reflectance

Using the coupled mode theory of Lam and Garside [44], a grating of constant modulation amplitude and period has a reflectance given by:

$$R(l, \lambda) = \frac{\Omega^2 \sinh^2(sl)}{\Delta\beta^2 \sinh^2(sl) + s^2 \cosh^2(sl)} \quad \text{Equation 1-7}$$

where $R(l, \lambda)$ is a fraction between 0 and 1 of the propagating optical power reflected by a grating of length l at a given wavelength λ . $\Delta\beta = \beta - \pi / \Lambda$ is the detuning wavevector, $\beta = 2\pi n_{eff} / \lambda$ is the propagation constant and $s^2 = \Omega^2 - \Delta\beta^2$. The coupling coefficient, Ω , for a sinusoidally varying index modulation along the fibre axis is given by:

$$\Omega = \frac{\pi \Delta n}{\lambda} \eta \quad \text{Equation 1-8}$$

where Δn is the amplitude of the induced refractive index at a given wavelength λ . The parameter η is the overlap between the fundamental mode and the index modulation which can be approximated for λ_m in conventional singlemode fibres using:

$$\eta(\lambda_m) \approx 1 - (V(\lambda_m))^{-2} \quad \text{Equation 1-9}$$

when the grating has been written uniformly through the core [45]. V is the normalised frequency at harmonic Bragg wavelengths λ_m given by:

$$V(\lambda_m) = \left(\frac{2\pi}{\lambda_m} \right) a \left(n_{co}^2 - n_{cl}^2 \right)^{1/2} \quad \text{Equation 1-10}$$

where a is the core radius, and n_{co} and n_{cl} are the core and cladding indices, respectively. The fibre is singlemode at wavelengths for which $V \leq 2.405$ [45].

At resonant Bragg wavelengths, λ_m of order m , there is no wavevector detuning, i.e. $\Delta\beta = 0$, so that the expression for reflectance of order m then becomes:

$$R_m(l, \lambda_m) = \tanh^2 \left(\frac{\pi \Delta n_m l \eta(\lambda_m)}{\lambda_m} \right) \quad \text{Equation 1-11}$$

where Δn_m is the amplitude of the induced refractive index at λ_m .

1.5.4 Induced refractive index change

If the refractive index change profile in a uniform fibre Bragg grating with a constant period Λ is assumed to be only a function of z , the profile can be expressed as [83]:

$$\Delta n(z) = \Delta n_o + \Delta n \cos \left(\frac{2\pi z}{\Lambda} \right) \quad \text{Equation 1-12}$$

where Δn_o is the mean refractive index change along the length of the grating, Δn is the amplitude of the photoinduced index modulation, Λ is the period and z is the distance along the length of the grating as shown in Figure 1-6.

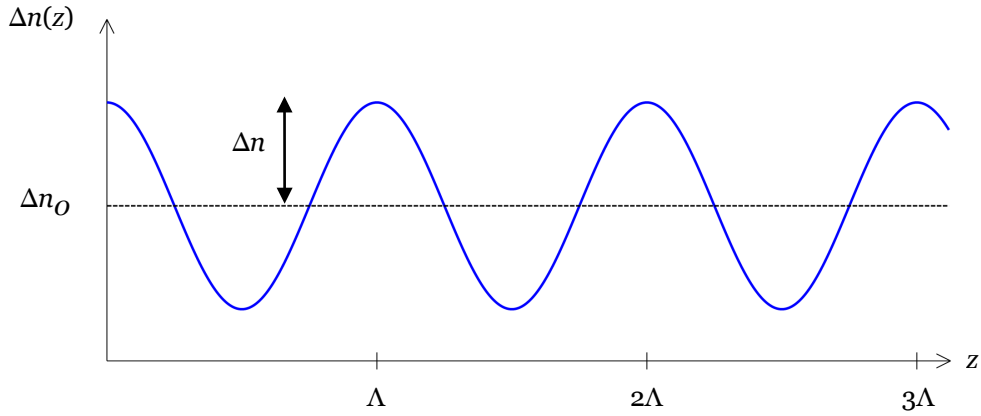


Figure 1-6. Induced refractive index change in a uniform FBG as a function of the distance along the fibre axis, z .

The induced mean index change along the length of the grating, Δn_o , can be inferred from the wavelength shift ($\Delta\lambda_m$) in the reflectance peak (or transmission dip) during fabrication at λ_m . By differentiating the Bragg condition (Equation 1-3) and assuming a constant period, the change of the effective index at λ_m can be written as $\partial n_{eff} = n_{eff} (\partial\lambda_m / \lambda_m)$. The mean index change, Δn_o at λ_m , is equal to ∂n_{eff} divided by the overlap between the fundamental mode and the index modulation $\eta(\lambda_m)$ so that [58, 84]:

$$\Delta n_o(\lambda_m) = \frac{n_{eff}(\lambda_m) \Delta\lambda_m}{\eta(\lambda_m) \lambda_m}. \quad \text{Equation 1-13}$$

Assuming that the index change profile has a constant period and is only a function of z , Equation 1-12 can be expanded as a Fourier series to describe the contributions of higher order components to the induced refractive index profile [83]:

$$\begin{aligned} \Delta n(z) = & \Delta n_o + \Delta n_1 \cos\left(\frac{2\pi z}{\Lambda} + \varphi_1\right) + \Delta n_2 \cos\left(\frac{4\pi z}{\Lambda} + \varphi_2\right) \\ & + \Delta n_3 \cos\left(\frac{6\pi z}{\Lambda} + \varphi_3\right) \dots, \quad 0 \leq z \leq l, \end{aligned}$$

$$\Delta n(z) = 0, \quad z > l \text{ and } z < 0, \quad \text{Equation 1-14}$$

where l is the grating length and $(\varphi_1, \varphi_2, \varphi_3)$ and $(\Delta n_1, \Delta n_2, \Delta n_3)$ represent the first three terms of the Fourier phase and amplitude spectra, respectively. Using coupled mode theory [44], it can be shown that the first periodic term in Equation 1-14 is responsible for the coupling between the forward and backward propagating fundamental modes at λ_1 . Likewise, the second and third periodic terms are responsible for the coupling of the two contradirectional fundamental modes at λ_2 and λ_3 , respectively, and so on.

1.5.5 Spectral characteristics

The induced periodic refractive index change in a fibre Bragg grating causes back-reflection of wavelengths which satisfy the Bragg condition (Equation 1-3). The result is a peak in the reflection spectra or a dip in the transmission spectra at λ_m when broadband light propagates down the fibre, as shown in Figure 1-7. For an ideal fibre Bragg grating, a narrow peak is observed in the reflection spectrum which corresponds to a reflectance R equal to 1 (or 100%) at λ_m . Conversely, an ideal fibre Bragg grating would have a narrow dip in the transmission spectrum corresponding to a transmittance T equal to 0 at λ_m . The grating spectral width, λ_{sw} , is commonly defined as the full width at half maximum (FWHM) of the reflectance peak or transmission dip at λ_m .

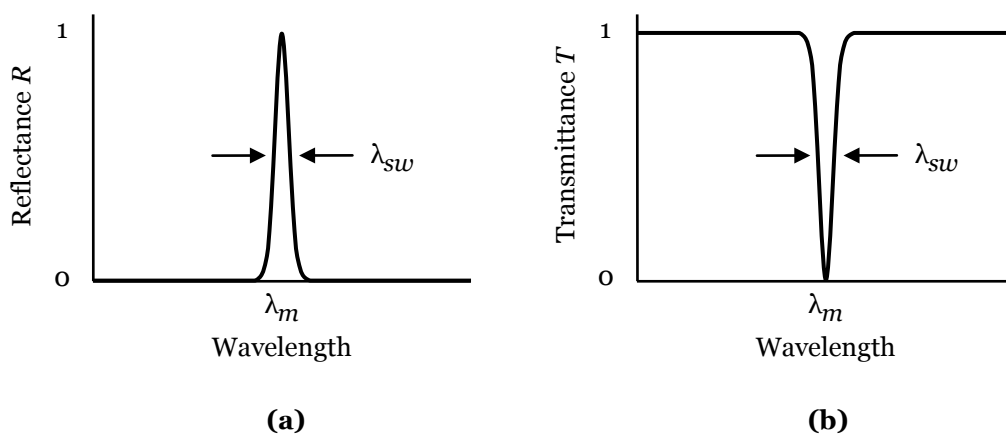


Figure 1-7. Optical spectra of an ideal FBG measured in **(a)** reflection and **(b)** transmission.

In practice, fibre grating spectra exhibit losses on the short wavelength side of reflectance peaks known as side lobes or cladding mode losses [80] that are due to inefficient back-reflections from the grating. These losses can be undesirable in certain applications and can be minimised by using fibres with a depressed cladding region surrounding the core [85].

As can be noted in the Bragg condition in Equation 1-3, different harmonic wavelengths of order m will be back-reflected from a Bragg grating. In 1993, Xie *et al.* [83] reported the first observation of second-order diffraction ($\sim 1/2 \lambda_B$) from fibre Bragg gratings written in germanosilicate fibres doped with various photosensitivity enhancing elements. The tested samples were evidently type I and IIA gratings, fabricated using a prism interferometer (see section 1.4.2) and a frequency doubled XeCl pumped dye laser operating at 243 nm. Xie *et al.* correlated the growth of the second-order reflectance peaks with the saturation of the Bragg reflectance peak growth. Hill and Meltz [86] reported the observation of second-order Bragg reflection lines at about one-half the fundamental Bragg wavelength and at other shorter wavelengths for higher order modes. These observations were attributed to strongly saturated gratings whose refractive index variations are no longer sinusoidal along the length of the fibre. In such a case, the peak index regions would be flattened, whereas the valleys in the perturbation index distribution would be sharpened, giving rise to the new harmonics in the Fourier spatial spectrum of the grating. Hill and Meltz did not give details of the fabrication conditions of the fibre grating in which the higher-order reflection lines were observed.

Malo *et al.* [51] reported the observation of sharp transmission dips in the spectrum of a fibre grating that occurred at 1535, 1030, 770 and 620 nm (see Figure 1-8). The fibre grating was produced using a phase mask of period $\Lambda_{pm} = 1.06 \mu\text{m}$ and single high fluence pulse from a KrF excimer laser operating at 249 nm. The phase mask was reportedly designed to suppress the zeroth-order to $< 5\%$ so that $\sim 80\%$ of the diffracted light was contained in the ± 1 order diffracted beams.

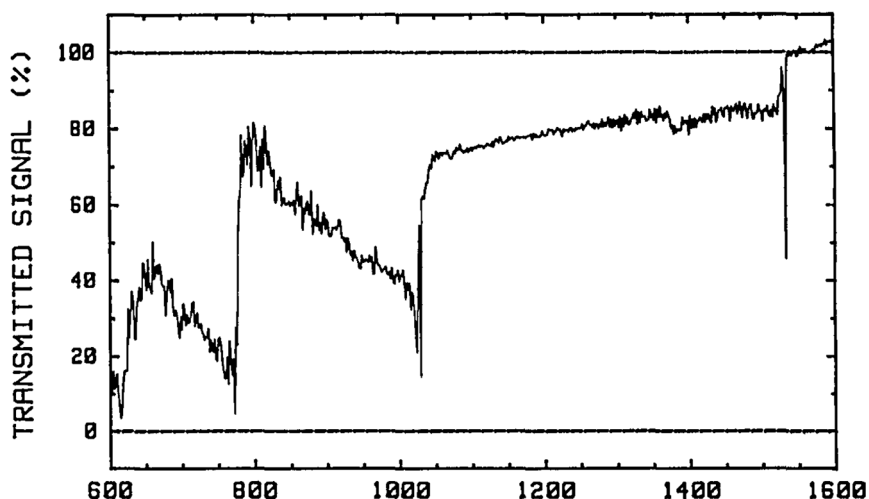


Figure 1-8. Transmission spectrum of a phase-mask-written type II FBG measured over the range 600 to 1600 nm (after [51]).

As discussed in section 1.5.2, the period of a fibre grating written only by the ± 1 orders of a phase mask is equal to half the period of the phase mask. Since a grating with a period $\Lambda_{pm}/2$ cannot efficiently reflect light at wavelengths 1030 and 620 nm, Malo *et al.* attributed all the reflections to a photoimprinted grating with a period Λ_{pm} , equal to the period of the phase mask. This attribution was supported by the observation, using an optical microscope, of refractive index perturbations that were highly localised on the core-cladding boundary and had a period equal to the phase mask inside the core of a type II fibre grating. The authors reasoned that fibre gratings produced using a phase mask and low-fluence multiple-pulses have a period $\Lambda_{pm}/2$ but single, high-fluence pulse exposure conditions result in gratings with a period Λ_{pm} . It was also suggested that a weak grating with period $\Lambda_{pm}/2$ may exist but was not detected since the spatial resolution of the microscope viewing system was near its limit.

Mihailov *et al.* reported the production of fibre gratings in standard SMF-28 and all-silica-core fibre using an ultrafast femtosecond and picosecond infrared (IR) source at 800 nm [87, 88]. Researchers in the same group have analysed the interference patterns formed behind different phase masks using a pulsed IR source and in 2004 reported spatial separation of the $\pm 1^{\text{st}}$

diffracted orders from the zeroth and $\pm 2^{\text{nd}}$ at positions greater than 1.3 mm from a $\Lambda_{pm} = 3.213 \mu\text{m}$ phase mask when using a femtosecond pulsed IR source [89]. When the fibre is placed several millimetres behind the phase mask, the time of arrival at the fibre of each diffracted order pair is different causing a spatial separation of the order pairs, defined as group velocity walk-off [90]. Two-beam interference patterns with a pitch half that of the phase mask can be produced by exploiting the short pulse duration of a femtosecond laser source and the group velocity walk-off of the diffracted phase mask orders along an axis perpendicular to the phase mask. This is not possible for longer pulse sources because the pulse duration is such that there would be much more overlap at large distances from the phase mask.

When the fibre is placed at distances greater than 1.3 mm from a $\Lambda_{pm} = 3.213 \mu\text{m}$ phase mask and it is irradiated with a femtosecond pulsed IR source, the resultant gratings are formed by the interference of only the $\pm 1^{\text{st}}$ orders with a period equal to half that of the phase mask, i.e. $\Lambda = 1.6065 \mu\text{m}$. Referring to Equation 1-3, a reflection at 1550 nm corresponds to the third harmonic reflection from such a grating. Gratings fabricated using this technique reportedly exhibit high reflectivity and strong cladding mode suppression at 1550 nm [91].

1.5.6 Microscopic characteristics

Various procedures have been developed to examine the properties of fibre Bragg gratings. These procedures include the analysis of the reflected and transmitted components of light from the grating or mathematical modelling using methods such as coupled mode theory [44] (as discussed in section 1.5.3) or transfer matrix [92]. These operations, however, give little information about the detailed refractive index structure of a fibre Bragg grating.

Standard microscopes are unable to detect the small refractive index changes in the transparent core of a fibre Bragg grating. In terms of actually visualising the structure of a fibre Bragg grating, a number of techniques have been

developed that reveal more detail. The photoinduced refractive index perturbations inside a fibre grating have been imaged using a diffraction limited photographic technique [51]. Scanning near-field optical microscopy [93] (SNOM) has been used to examine both the structure and internal field distribution of a polished fibre Bragg grating by accessing its evanescent field. A side-diffraction interference [94] technique has been used for the non-destructive analysis of refractive index modulation and period of a grating by forming an interference pattern behind it. The SNOM technique has been used to image the field distributions in free space behind an illuminated phase mask [95] and revealed the existence of Talbot diffraction patterns which will be discussed further in section 3.1.2.

A desirable technique for optical fibre imaging is one that is non-destructive and detects the physical variations inside the core, not simply field variations due to the grating outside the fibre. The Differential Interference Contrast (DIC) [96] imaging technique is non-destructive, and by way of two interfering laser beams, detects refractive index changes present in the sample. This technique allows the acquisition of high resolution images of optical fibre and, based on the well known optical sectioning properties of DIC imaging, 3-dimensional information is also attainable. This technique will be discussed further in Chapter 3.

By the use of a modified form of Differential Interference Contrast microscopy, a complex refractive index structure with a distinct Talbot diffraction pattern has been observed to exist in the core of a phase-mask-written fibre grating; an example of which is shown in Figure 1-9 [97]. The intensity variations in the images in Figure 1-9(a) and (b) are due to refractive index variations in the core of the fibre.

The DIC images in Figure 1-9(a) and (b) each represent an optical slice through the fibre centre with the sample oriented at 0° and 90° , respectively. Consequently, the planes of the two images are orthogonal to one another as illustrated in Figure 1-9(c). As will be discussed in section 3.1.2, the phase mask fabrication technique can result in the formation of a Talbot diffraction

pattern which is periodic in the direction extending out from the phase mask, i.e. parallel to the writing beam. Consequently, the imaged structure in Figure 1-9(a) is consistent with an optical slice recorded in the plane perpendicular to the UV writing beam and the imaged structure in Figure 1-9(b) is consistent with an optical slice recorded in the plane parallel to the UV writing beam.

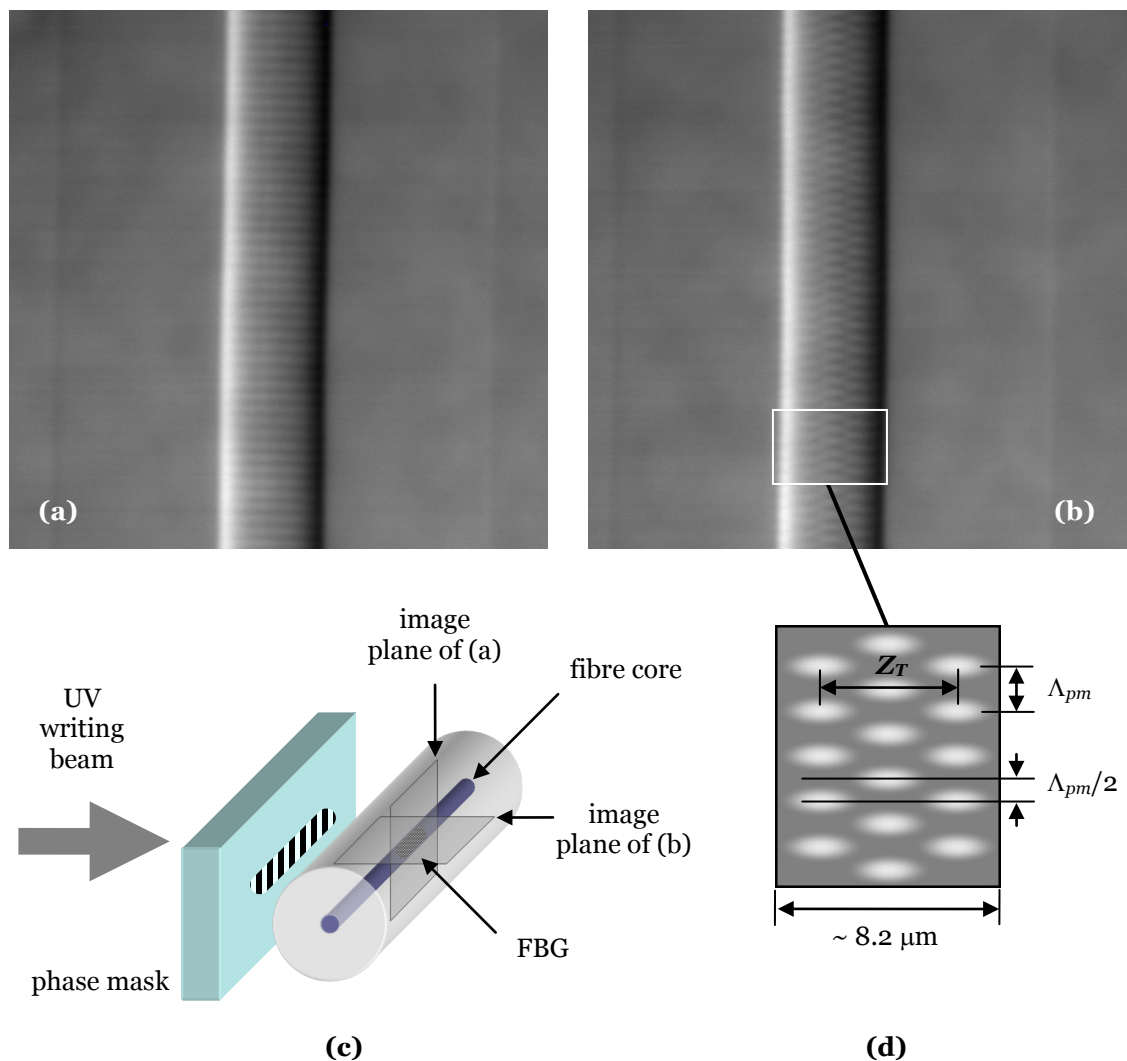


Figure 1-9. DIC images of the core region of a type I FBG covering $47 \times 47 \mu\text{m}$: **(a)** fibre orientation and image plane corresponding to perpendicular to the writing beam and **(b)** the same sample rotated by 90° , i.e. fibre orientation and image plane corresponding to the direction parallel to the writing beam. **(c)** Schematic diagram identifying the planes of the images shown in (a) and (b). **(d)** Schematic diagram illustrating the key features of the image in (b): interleaving planes of refractive index modulation exhibiting two periods, namely Δ_{pm} and $\Delta_{pm}/2$.

The observed complex structure in Figure 1-9(b) was reported to arise as a result of beating between higher diffraction orders of the phase mask. The

observed repeat length of the periodic Talbot diffraction pattern, Z_T , formed across the fibre image in Figure 1-9(b) was consistent with the calculated value of $\sim 4.65 \mu\text{m}$ for beating between the 1st and 2nd diffraction orders of the phase mask used in fabrication. The Bragg wavelength of the imaged fibre grating was $\sim 1535 \text{ nm}$, resulting from a phase mask period of $\Lambda_{pm} = 1.059 \mu\text{m}$. The image in Figure 1-9(b) reveals planes of interleaving fringes indicating that the grating has features representative of a periodicity of both $\sim 0.53 \mu\text{m}$ and $\sim 1.06 \mu\text{m}$, corresponding to $\Lambda_{pm}/2$ and Λ_{pm} respectively.

As discussed in section 1.5.5, a fibre grating fabrication technique has been reported in which the fibre is placed at a fibre-mask distance such that it is produced using pure two-beam interference using a femtosecond pulsed IR source [91]. Indeed, images of such gratings revealed uniform periodic refractive index structures with a $1.6 \mu\text{m}$ pitch at viewing directions both normal and perpendicular to the writing beam, consistent with two-beam interference. Microscopic images of a grating that had been in near-contact with a $\Lambda_{pm} = 3.213 \mu\text{m}$ phase mask during fabrication [91] revealed a complex refractive index structure consistent with multiple-beam interference featuring phase jumps across the fibre core that have been associated with Talbot imaging [95, 97] as discussed in section 3.1.2. The existence of complex refractive index structures in the core of phase-mask-written fibre gratings has interesting spectral consequences which will be explored in this thesis.

1.6 Scope of thesis

As has been introduced in earlier sections, a previously unexpected and complex refractive index structure has been observed in the core of a type I FBG using DIC microscopy. This complex structure has been attributed to the multiple-beam interference patterns that can be induced through the use of the phase mask fabrication technique. FBGs fabricated with phase masks are generally considered to have been formed by two-beam interference of the $\pm 1^{\text{st}}$ diffraction orders of the phase mask. The observed refractive index structures suggest that small contributions from the zeroth and higher diffraction orders of the phase mask can have a significant effect on the

refractive index structure induced in the core of FBGs during fabrication. The observed complex refractive index structure raises four main questions regarding the structure of FBGs; and also the influence of the phase mask properties on the structure and subsequent performance of FBG-based devices:

1. Is there a correlation between the complex refractive index structure and the observed optical spectra of FBGs?
2. Can the structure or its interaction with the fibre type be used to alter the spectral characteristics?
3. How do the spectral characteristics evolve during fabrication?
4. Can such FBGs offer improved sensing capabilities?

This thesis seeks to understand the refractive index structure of various types of FBGs and the effect the phase mask diffraction orders have on the induced structure. Furthermore, this thesis seeks to understand the spectral consequences of the induced refractive index structure; in particular the origins and growth of spectral features during fabrication and also the possible implications in the field of sensing. DIC microscopy was used in this thesis to investigate the structures produced under different fabrication conditions. The effects of multiple-beam interference were investigated using the phase mask fabrication technique and two-beam interference conditions were investigated using a prism interferometer.

In Chapter 1, the literature is reviewed and presented with the key theory relevant to the thesis. In Chapter 2, the techniques used for the fabrication of the FBG samples investigated in this work are described. In the beginning of Chapter 3, the expected intensity distributions and the techniques used for DIC imaging have been described. Chapter 3 then presents the results of DIC imaging experiments performed on various FBGs and compares the observed structures with the predicted intensity distributions.

In addition to the DIC images which provide detailed information on the structure of various FBGs, the effect of different fabrication conditions were

investigated spectrally. In Chapters 4, 5 and 6, an analysis of the spectral consequences of the observed structures are presented. As discussed in section 1.5.5, the phase mask fabrication technique has been found to give rise to spectral features at wavelengths other than the expected harmonic reflections of the FBG. In particular, spectral features at two-thirds and two-fifths of the design Bragg wavelength, λ_B , would not occur if the FBG had been produced as a result of pure two-beam interference. Such reflections have been observed previously only for type II FBGs and were attributed to the damage associated with these grating types.

In Chapter 4, the observation of spectral features at $2/5 \lambda_B$ and $2/3 \lambda_B$ is investigated in type I and IIA FBGs. Spectral features at λ_B and $2/3 \lambda_B$ were compared under singlemode and multimode conditions with a theoretical analysis of the predicted fundamental mode field patterns at the respective wavelengths. The spectral properties of FBGs written with standard zeroth-order nulled phase masks were compared with FBGs written with a custom-made mask; designed to provide equal contributions from the $\pm 1^{\text{st}}$ and $\pm 2^{\text{nd}}$ diffraction orders. In Chapter 5, the growth with increasing fluence of spectral features at λ_B and $2/3 \lambda_B$ are compared with a theoretical model for two periods of interest in the core of the FBG. This analysis is aimed at understanding the origins and growth of the spectral features of interest.

Reflections at wavelengths other than the Bragg wavelength have been used as the basis of simultaneous axial strain and temperature sensors. In order to contribute to the knowledge in this field and, hopefully, help pave the way for improved sensors, the axial strain and temperature characteristics of reflections due to the complex refractive index structure of phase-mask-written FBGs are investigated in Chapter 6. The combination of spectral shifts at these wavelengths with the relatively strain independent fluorescence intensity ratio (FIR) technique is also investigated and evaluated. The conclusions and key findings of the thesis are summarised in Chapter 7 along with suggestions for future work.

Chapter 2:

Fibre Bragg Grating Fabrication

Fibre Bragg gratings are most commonly fabricated by transverse exposure to an interference pattern of UV radiation. As discussed in section 1.5.5, images of the core of a phase-mask-written FBG have revealed a complex refractive index structure. The complex structure was attributed to multiple-beam interference produced by the phase mask technique and in particular, the observed structure was attributed to the interference of the $\pm 1^{\text{st}}$ and $\pm 2^{\text{nd}}$ diffraction orders. The effect of the nature of the interference pattern used in fabrication on the microscopic and spectral properties of FBGs in various fibre types is the subject of the next three chapters. This chapter details the fabrication conditions of the two techniques used in this thesis for the generation of UV interference patterns, namely the multiple-beam phase mask and the two-beam prism interferometer techniques.

2.1 Writing fluence

Fabrication conditions for FBGs can be characterised by the total UV fluence to which the fibre is exposed, usually expressed in kJ/cm^2 . For continuous wave (CW) laser sources, the beam power density and the exposure time are used to calculate the total fluence. The beam power density is given by the power of the beam divided by the cross-sectional area of the focused beam when a lens is used for focusing. The focused beam waist diameter, w_q , is given by:

$$w_q = f \theta_d$$

Equation 2-1

where f is the focal length of the focusing lens and θ_d is the full divergence angle of the beam. The focused power density is then given by:

$$P_f = \frac{P_o}{w_q l} \quad \text{Equation 2-2}$$

where P_o is the output power of the laser and l is the diameter of the beam. The diameter of the beam effectively defines the grating length when a stationary beam is used for writing. The fabrication parameters can be easily adjusted for a scanning beam technique. The writing power density, P_w , can then be calculated from an estimation of the ratio of the beam waist to the fibre diameter, called d , and is given by:

$$P_w = P_f \times d. \quad \text{Equation 2-3}$$

The ratio d can be estimated during fabrication from the image of the fibre shadow and beam waist on a screen placed behind fibre. The total fluence in kJ/cm^2 is then given by the writing power density multiplied by the exposure time:

$$F_T = P_w t = \frac{P_o}{f \theta_d l} \times d \times \alpha t \quad \text{Equation 2-4}$$

where P_w is in W/cm^2 , t is in seconds and α is an estimated loss factor due to filtering, absorption and reflections from optical components in the experimental arrangements used. The experimental uncertainties associated with the total fluence were calculated using standard error analysis [98]:

$$\left(\frac{\Delta F_T}{F_T}\right)^2 = \left(\frac{\Delta P_o}{P_o}\right)^2 + \left(\frac{\Delta f}{f}\right)^2 + \left(\frac{\Delta \theta_d}{\theta_d}\right)^2 + \left(\frac{\Delta l}{l}\right)^2 + \left(\frac{\Delta d}{d}\right)^2 + \left(\frac{\Delta \alpha}{\alpha}\right)^2 + \left(\frac{\Delta t}{t}\right)^2 \quad \text{Equation 2-5}$$

2.2 Laser sources

Two UV laser sources were used for the fabrication of samples in this thesis which are summarised in Table 2-1.

Laser label	Manufacturer/Model	Operating λ (nm)	θ_d (mrad)	Mode	Peak Power (mW)
UV-1	Coherent™ Innova FreD Ar Ion	244	1 ± 0.1	CW	120
UV-2	Coherent™ Sabre FreD Ar Ion	244	1 ± 0.1	CW	250

Table 2-1. UV laser sources used in this work.

2.3 Phase mask technique

2.3.1 Standard phase mask

A number of standard, commercially-produced phase masks were used to fabricate FBG samples for this work; the details of which are listed in Table 2-2. The phase masks labelled SM-1 and SM-2 were used with laser UV-1 in the experimental arrangement shown in Figure 2-1, located in the Optical Technology Research Laboratory at Victoria University, Melbourne. The average relative diffraction order efficiencies listed in Table 2-2 were measured using the arrangement in Figure 2-1 by placing an optical detector at a fixed distance behind the phase mask in the absence of a fibre.

Mask label	Manufacturer	Λ_{pm} (μm)	Average diffraction order efficiencies (%)				
			0 th	$\pm 1^{\text{st}}$	$\pm 2^{\text{nd}}$	$\pm 3^{\text{rd}}$	$\pm 4^{\text{th}}$
SM-1	Lasiris™	1.059	0.9	38.1	4.2	3.8	3.4
SM-2		1.0668	1.8	39	3.5	3.3	3.3
SM-3		1.0768	≤ 3	≥ 33	≈ 15.5		
SM-4		1.0703	≤ 3	≥ 33	≈ 15.5		

Table 2-2. Details of the standard phase masks used in this work. Images of the phase mask profiles are not included since these are not available from the manufacturer.

The power density of the unconditioned output laser beam is not suitable to photoinduce adequate refractive index changes for practical gratings so various UV-grade optics were used to condition and focus the writing beam onto the fibre with sufficient power density to fabricate the required FBG types [51]. The width of the focused beam on the fibre determines the grating length, l , which was controlled using various optical components as shown in Figure 2-1. A negative convex lens with a focal length of -50 mm was used to expand the laser beam. The expanded beam then passed through a circular aperture that was used to shape and filter the beam. The filtered beam was then incident on a collimating lens with a focal length of $+300$ mm. The output beam divergence was set to approximately (1 ± 0.1) mrad by adjusting the relative positioning of the two lenses. The beam was then reflected from two steering mirrors and directed to a cylindrical lens of focal length (150 ± 0.5) mm. A second circular aperture was used to shape and filter the focused beam. The factor, α , accounting for loss due to filtering, absorption and reflections from the components in the system was estimated from comparative measurements between the laser output and beam power before the phase mask. Three different apertures setting were used for beam filtering before the phase mask, which resulted in three different loss factors: (1) no aperture, $\alpha = 0.77 \pm 0.08$; (2) 8 mm aperture, $\alpha = 0.47 \pm 0.05$ and (3) 5 mm aperture, $\alpha = 0.22 \pm 0.02$.

The various fibre types used in this work are detailed in Table 2-4. Hydrogen loaded samples were photosensitised using the method described in section 2.6. Fibre samples were prepared by mechanical stripping of ~ 3 cm of the acrylate coating to expose the bare fibre. The bare fibre section was then cleaned thoroughly with isopropanol, mounted in a holder and positioned parallel to the phase mask within approximately 150 ± 50 μm .

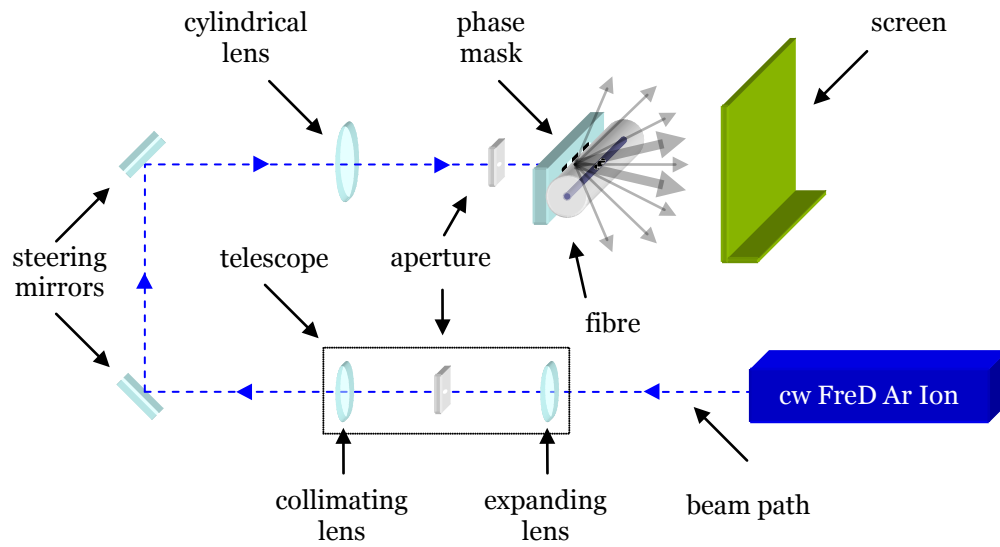


Figure 2-1. Schematic diagram of the experimental arrangement used for grating fabrication using phase masks SM-1 and SM-2.

A white screen was positioned behind the fibre to view the fluorescence diffraction pattern from the fibre when the phase mask was illuminated. The shadow in the pattern on the screen corresponds to strong absorption of the UV light by the fibre. The focusing of the beam on the fibre was optimised by adjustment of the cylindrical lens according to the shadow of the fibre on the screen, which was also used to estimate the ratio of the beam waist to the fibre diameter, d . The UV exposure was controlled by blocking and unblocking the laser beam and the exposure time was monitored using a stopwatch.

The details of additional phase masks used in this work, labelled SM-3 and SM-4, are listed in Table 2-2 with their specified diffraction order efficiencies [99]. These phase masks were used in the experimental arrangement shown in Figure 2-2, located at the FiGFab facility at Swinburne University, Melbourne [100]. The ex-commercial system uses a continuous wave (CW) Coherent[®] Sabre[®] frequency doubled argon ion laser operating at 244 nm and incorporates sophisticated electronics and automated programming to ensure optimally controlled and repeatable fabrication conditions.

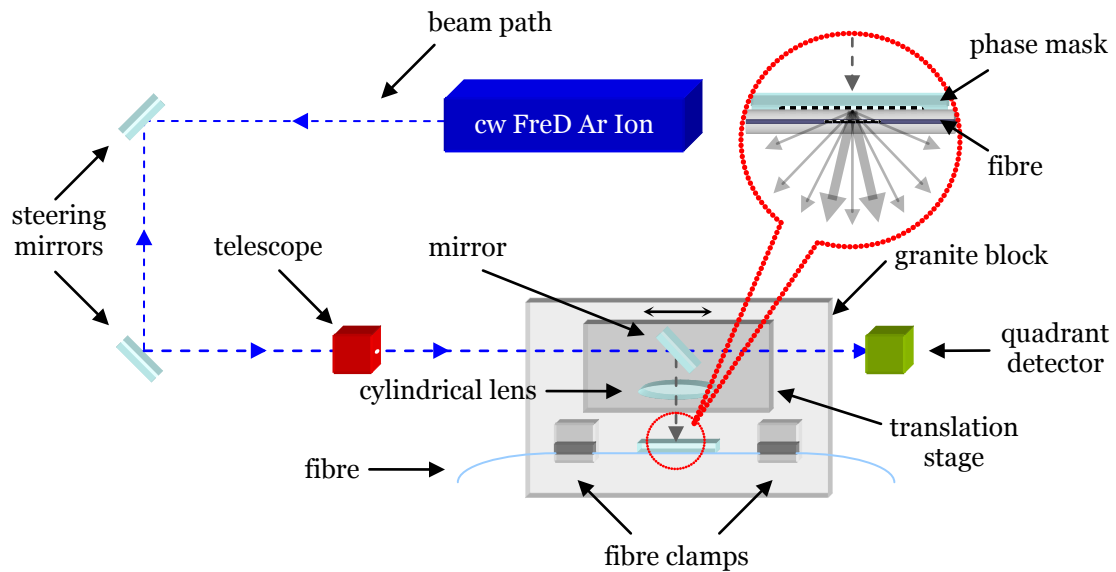


Figure 2-2. Schematic diagram of the experimental arrangement used for grating fabrication using phase masks SM-3 and SM-4.

As shown in Figure 2-2, a telescope adjusts the beam height which is monitored with feedback by a quadrant detector. Fibre gratings are written by scanning the laser beam across the phase mask at a rate determined by the user; a slower scan rate will give a longer exposure time and relatively stronger grating reflectance. The tension placed on the fibre, the grating length and the apodisation profile are also controlled by the user. Fibre gratings are apodised by dithering the beam (moving it back and forth at a high speed) to tailor the shape of the reflection peak [101]. Given the controlled nature of the fabrication system, the ratio of the fibre shadow to the beam height was assumed to be the same for all samples and was measured as $d = 0.33$. The loss factor due to filtering, absorption and reflections from the components in the system was estimated from comparative measurements between the laser output and beam power before the phase mask to be $\alpha = 0.62 \pm 0.02$. A uniform strain of 80 g was placed on the fibres and a Blackman-Harris [102] apodisation profile of order 0.5 was used during fabrication.

2.3.2 Custom-made phase mask

Standard phase masks generally provide contributions of about 40% from the $\pm 1^{\text{st}}$ orders and less than 5% from the $\pm 2^{\text{nd}}$ orders. In order to investigate the effect of different relative intensities in the orders produced by the phase mask, custom-made phase masks were sought from Ibsen Photonics™ in Denmark.

Mask label	Manufacturer	Λ_{pm} (μm)	Average diffraction order efficiencies (%)				
			0 th	$\pm 1^{\text{st}}$	$\pm 2^{\text{nd}}$	$\pm 3^{\text{rd}}$	$\pm 4^{\text{th}}$
CM-1	Ibsen Photonics™	1.07	30	5.1	25.8	1.9	2.3
CM-2		1.07	3.2	15	19.6	13.5	0.4

Table 2-3. Details of the custom-made phase masks used in this work. Images of the phase mask profiles are not included since these are not available from the manufacturer.

The details of the custom-made masks are listed in Table 2-3. A first mask, labelled CM-1, was designed to maximise the contributions of $\pm 2^{\text{nd}}$ diffraction orders. However, attempts at grating fabrication using this mask proved unsuccessful which is most likely due to an inadequate contribution from the $\pm 1^{\text{st}}$ orders of only 4.8% and too large a contribution from the 0th order. A second mask, labelled CM-2, was designed to transmit approximately equal contributions from each of the $\pm 1^{\text{st}}$ and $\pm 2^{\text{nd}}$ orders, while keeping the 0th order low. The average diffraction order efficiencies were measured the same way as described above for the standard masks.

A photograph taken during grating fabrication with mask CM-2 is shown in Figure 2-3. Fluorescence from the 0th, $\pm 1^{\text{st}}$ and $\pm 2^{\text{nd}}$ diffraction orders on the screen placed behind the illuminated mask and fibre illustrates the relative efficiencies between the diffraction orders. Although the -2^{nd} diffraction order is clipped slightly by the screen on the left hand side, the intensity of the $\pm 2^{\text{nd}}$ orders can be seen in the photograph to be slightly greater than the $\pm 1^{\text{st}}$ orders, as confirmed in Table 2-3 for mask CM-2.

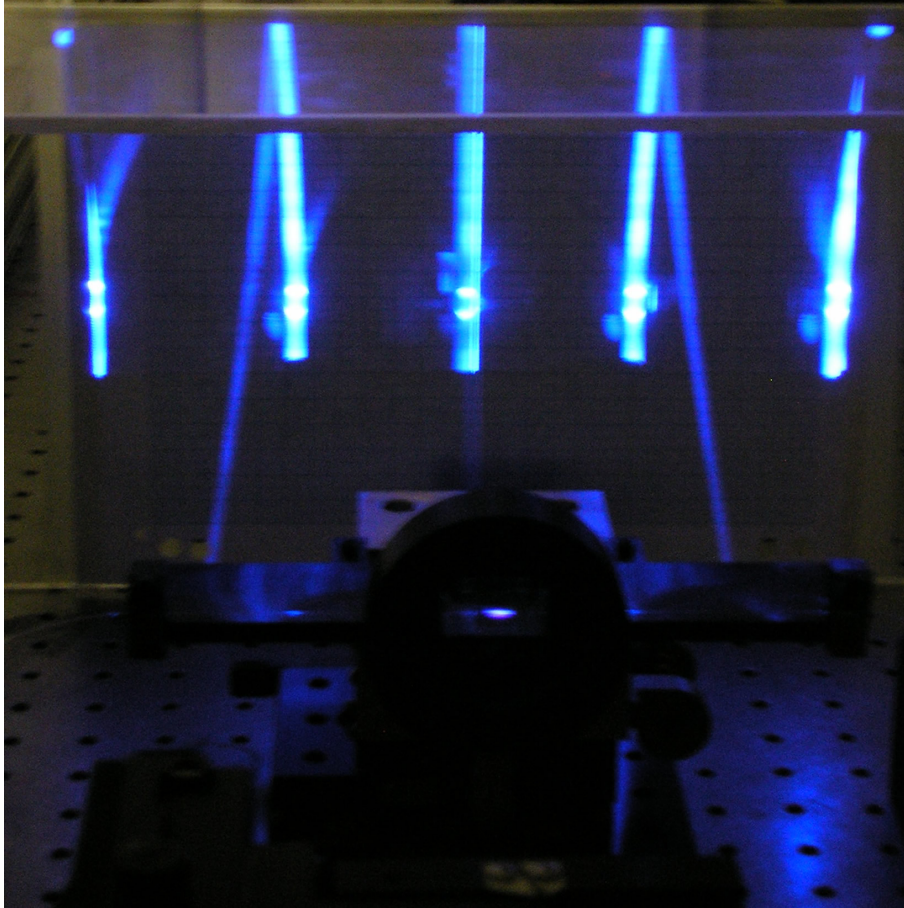


Figure 2-3. Photograph taken during grating fabrication with the custom made phase mask CM-2. The bright, vertical blue lines on the screen behind the mask and fibre from left to right are due to fluorescence from the -2^{nd} (clipped slightly), -1^{st} , 0^{th} , $+1^{\text{st}}$ and $+2^{\text{nd}}$ diffracted orders of the UV illuminated phase mask. The fibre shadow is also visible in the centre of the beam spot near the base of the blue vertical lines. The curved blue lines either side of the $\pm 1^{\text{st}}$ orders are due to reflections from the Perspex guard above the screen.

2.4 Prism interferometer technique

A prism interferometer was employed in this thesis in order to compare the spectral and microscopic properties of FBGs fabricated using two-beam interference with FBGs fabricated with multiple-beam interference, i.e. using a phase mask. The prism interferometer arrangement, shown in Figure 2-4(a), used the same laser and optical components as the arrangement shown in Figure 2-1, but used a 45° silica prism instead of a phase mask. In addition to this, the arrangement used a 4 mm slit before the cylindrical lens rather than an aperture after it. After passing through the slit, the 4 mm wide, collimated beam was focused onto the prism using the cylindrical lens.

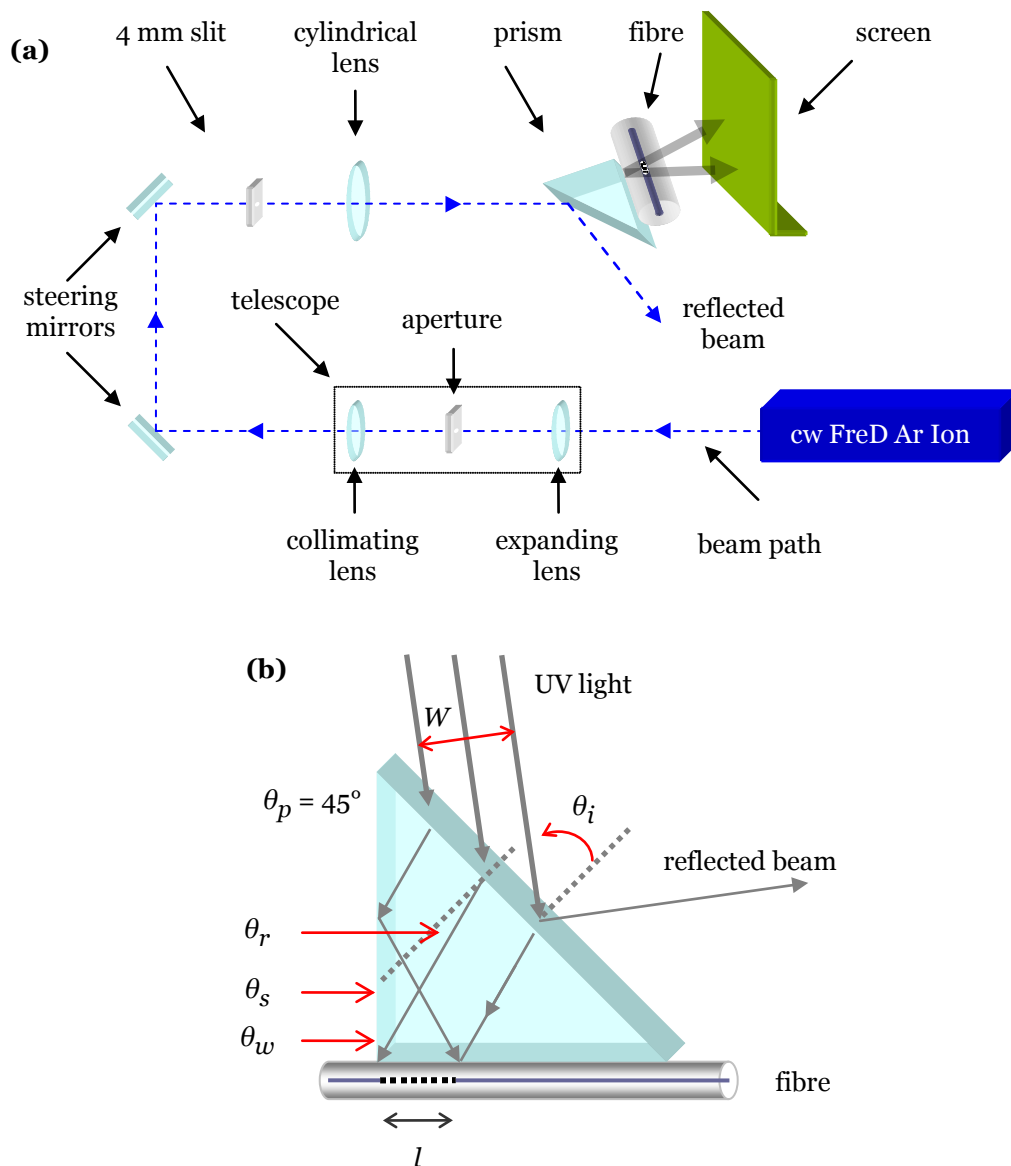


Figure 2-4. Schematic diagram of the experimental arrangement used for grating fabrication using a prism interferometer ((a)) and (b) the alignment of beam, prism and fibre.

The prism was mounted on a rotation stage which was used to set the pitch of the interfering beams and determine the Bragg wavelength. By rotating the prism, the beam reflected from the hypotenuse was used to set the angle of incidence according to a calibrated scale in the far field for the desired Bragg wavelength. After optimising the arrangement with dummy fibre, the stripped and cleaned sample fibre was mounted in a holder which was aligned parallel and as close as possible to the right-angled face of the prism. The focusing of

the beam on the fibre was optimised by adjustment of the cylindrical lens according to the shadow of the fibre on the screen, which was also used to estimate the ratio of the beam waist to the fibre diameter, d . The UV exposure was controlled by blocking and unblocking the laser beam and the exposure time was monitored using a stopwatch. The loss factor, α , due to components in the experimental arrangement was estimated to be 0.15 ± 0.02 .

The alignment of the beam, the prism and the fibre in the interferometer is shown in Figure 2-4(b). When the laser beam is incident on the hypotenuse of the prism, the refracted beam is bisected by the right-angled vertex. Half of the beam is totally internally reflected from one prism face and an interference pattern is formed on the prism face adjacent to the fibre which is imprinted in the photosensitive core. The length, l , of the grating produced using the prism interferometer method is given by:

$$l = \frac{W}{2 \cos \theta_i} \left[\sin \theta_p + \cos \theta_p \tan(\theta_w) \right], \quad \text{Equation 2-6}$$

where W is the beam width, θ_p is the prism apex angle, θ_i is the angle of incidence and θ_w is the writing angle [42]. An incident angle of $\theta_i = 63^\circ$ was chosen to produce gratings with a Bragg wavelength of approximately 1550 nm and to prevent clipping of the UV beam. Referring to Figure 2-4(b), the angle of refraction of the incident beam at the hypotenuse-air interface, θ_r , was calculated as $\sim 36.1^\circ$ using Snell's law and the known refractive index of silica, $n = 1.51086$ at the writing wavelength of 244 nm. The writing angle θ_w was determined using the geometry illustrated in Figure 2-4(b), where θ_s is the supplement of θ_p . According to Equation 2-6, an incident angle $\theta_i = 63 \pm 2^\circ$, an estimated beam width of $W = 4 \pm 2$ mm and writing angle $\theta_w = 8.9 \pm 1^\circ$ produces gratings which are approximately 3.6 ± 0.5 mm in length.

2.5 Fibre types

Fibre grating samples were fabricated in a number of different optical fibres, the details of which are summarised in Table 2-4. Most of these fibres are commercially available and have Ge or Ge:B doped silica cores. Fibre F-5 was produced at a custom fibre fabrication facility at LPMC in Nice, France, using a modified chemical vapour deposition and solution doping technique [103]. This fibre was doped to achieve $\text{Er}^{3+}:\text{Yb}^{3+}$ ion concentrations in the fibre core of 3000:3000 ppm, respectively, and a core composition of Si:Ge:P:Al.

Fibre label	Manufacturer /Name	Core dopants	λ_{cutoff} (nm)	Core diameter (μm)	Cladding diameter (μm)	Δn	NA
F-1	Optix™	Ge	~1300	7.4	125	8.6×10^{-3}	0.12
F-2	Fibrecore™	Ge:B	1260	8	125	0.40%	0.13
F-3	Corning™ HI1060	Ge	930 ± 40	3.6	125	1%	0.2
F-4	Corning™ SMF28	Ge	1260	8.2	125	0.36%	0.14
F-5	LPMC, Nice, France	$\text{Er}^{3+}:\text{Yb}^{3+}$	~1300	4.4	125	1.5×10^{-2}	0.2

Table 2-4. Details of the fibres used in this work. λ_{cutoff} is the singlemode cutoff wavelength, Δn is the refractive index difference between the core and the cladding and NA is the fibre numerical aperture.

2.6 Hydrogen loading

Hydrogen loading was used in this work to enhance the photosensitivity of all fibres except F-2, which is highly photosensitive without hydrogenation. Prior to UV exposure, the fibres were placed in a chamber which was filled with hydrogen gas and held under sufficient pressure and temperature conditions to achieve saturation of hydrogen molecules into fibre core. The pressure, temperature and length of time required to achieve saturation were determined using the following equations.

The equilibrium hydrogen solubility, or saturated hydrogen concentration in ppm, is given by [5, 104]:

$$C_{sat} = 3.3481 P e^{\left(\frac{8670 \text{ J/mol}}{RT}\right)}, \quad \text{Equation 2-7}$$

where P is the pressure in atm, $R = 8.311 \text{ J/K-mol}$ is the gas constant and T is the temperature in Kelvin. Here, 1 ppm is defined as 10^{-6} moles of H_2 per mole of SiO_2 . The diffusivity of hydrogen molecules in silica, D , is given by [42, 104]:

$$D = 2.83 \times 10^{-4} e^{\left(\frac{-4019 \text{ J/mol}}{RT}\right)}. \quad \text{Equation 2-8}$$

The concentration of hydrogen molecules in the fibre, in ppm, was calculated by solving the diffusion equation in cylindrical coordinates [5]:

$$C = C_{sat} \left\{ 1 - 2 \sum_{n=1}^{\infty} \frac{1}{\beta_n J_1(\beta_n)} \exp\left[-\beta_n^2 \frac{Dt}{r^2}\right] \right\}, \quad \text{Equation 2-9}$$

where β_n is the n^{th} zero of the zeroth-order Bessel function, $J_1(\beta_n)$ is the first-order Bessel function, r is the radius of the fibre in metres and t is the time in seconds. The diffusion of hydrogen molecules into the fibre over time at a gas pressure of 80 atm is shown in Figure 2-5 for various temperatures. The H_2 loaded fibres used in this work were typically exposed to ~ 80 atm pressure of H_2 and held at a temperature of ~ 60 °C for at least 2 days to ensure saturation of hydrogen molecules into fibre core. These conditions typically resulted in hydrogen concentrations in the core of approximately 6000 ppm or 6×10^{-3} moles of H_2 per mole of SiO_2 . Care was taken to minimise out-gasing of hydrogen by fabricating gratings soon after the fibre was removed from the pressurised chamber. The H_2 concentrations at the time of fabrication for the samples studied in this work were calculated using Equation 2-9 for $n = 1$ to 30 and are listed in Table 2-5 with their associated uncertainties. The uncertainties were estimated from the difference between the calculated maximum and minimum concentrations using the experimental uncertainties

$\Delta P = 5$ atm, $\Delta T = 2$ °C for $T = 20$ °C, $\Delta T = 5$ °C for $T > 20$ °C, $\Delta t = 1$ hour for $t \leq 3$ days and $\Delta t = 5$ hours for $t > 3$ days.

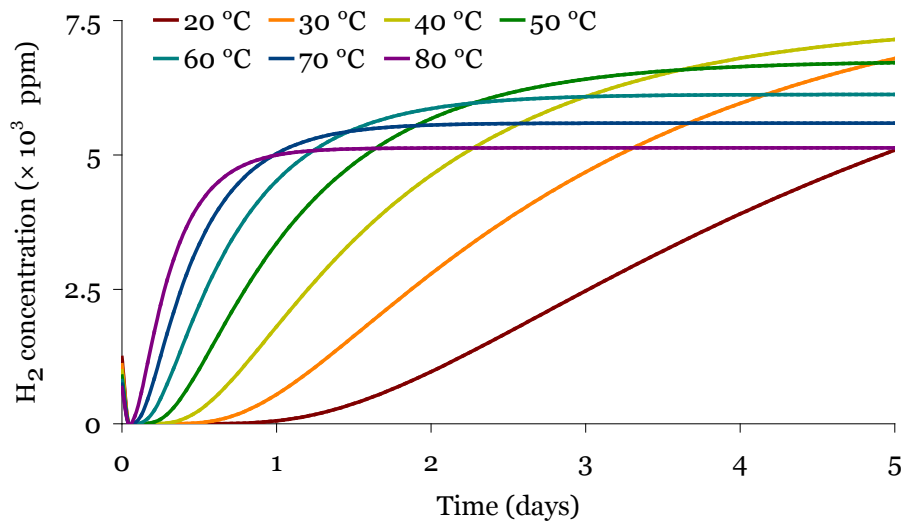


Figure 2-5. Diffusion of hydrogen molecules into the fibre over time at a gas pressure of 80 atm for various temperatures.

2.7 Sample details

The fabrication parameters and properties for the fibre gratings studied in this thesis are summarised in Table 2-5 in the order they are discussed in Chapters 3 and 4.

Sample	Fibre	H ₂ load	H ₂ conc. (ppm)	Type	Mask/prism	P ₀ (mW)	d (± 0.05)	l (mm)	α	t (sec)	F _T (kJ/cm ²)	~λ _B (nm)	~R _B (%)
Ip-1	F-4	yes	10500 ± 400	I	prism	96 ± 1	0.90	3.6 ± 0.5	0.15 ± 0.02	1430 ± 5	2.9 ± 0.6	1541.7	99.94
IIAp-1	F-2	no	-	IIA	prism	110 ± 2	0.90	3.6 ± 0.5	0.15 ± 0.02	18310 ± 10	50 ± 9	1536.8	98.90
IIA-1	F-2	no	-	IIA	SM-2	98 ± 5	0.80	8.0 ± 0.5	0.47 ± 0.05	19440 ± 10	60 ± 13	1544.5	99.93
I-1	F-1	yes	6200 ± 90	I	SM-2	91 ± 2	0.80	5.0 ± 0.5	0.22 ± 0.02	8510 ± 10	18 ± 3	1546.3	99.99
I-2	F-3	yes	6600 ± 70	I	SM-2	69 ± 1	0.90	8.0 ± 0.5	0.47 ± 0.05	2060 ± 10	5 ± 1	1546.8	99.99
I-3	F-1	yes	6200 ± 90	I	CM-2	99 ± 4	0.80	4.8 ± 0.5	0.22 ± 0.02	12780 ± 10	31 ± 6	1551.1	95.80
I-4	F-3	yes	5900 ± 100	I	CM-2	101 ± 1	0.90	12.0 ± 0.5	0.77 ± 0.08	2490 ± 10	10 ± 2	1551.2	99.99
I-5	F-1	yes	5300 ± 100	I	SM-1	107 ± 1	0.80	8.0 ± 0.5	0.47 ± 0.05	1121 ± 1	3.8 ± 0.7	1534.4	95.00
IIA-2	F-2	no	-	IIA	SM-1	98 ± 1	0.80	8.0 ± 0.5	0.47 ± 0.05	4800 ± 1	15 ± 3	1534.8	84.10
I-6	F-2	no	-	I	SM-1	67 ± 1	0.80	5.0 ± 0.5	0.22 ± 0.02	1020 ± 1	1.6 ± 0.3	1534.1	89.00
I-7	F-3	yes	9700 ± 2000	I	SM-3	263 ± 5	0.33	2.0 ± 0.1	0.62 ± 0.02	160 ± 1	4.7 ± 0.6	1561.8	99.60
I-8	F-3	yes	9700 ± 2000	I	SM-3	263 ± 5	0.33	2.0 ± 0.1	0.62 ± 0.02	240 ± 1	7.0 ± 0.9	1561.9	99.95
I-9	F-3	yes	9700 ± 2000	I	SM-3	263 ± 5	0.33	2.0 ± 0.1	0.62 ± 0.02	343 ± 1	10 ± 1	1562.0	99.98
I-10	F-1	yes	10700 ± 2000	I	SM-4	223 ± 2	0.33	5.0 ± 0.1	0.62 ± 0.02	600 ± 1	15 ± 2	1548.4	99.98
I-11	F-5	yes	6300 ± 100	I	SM-2	91 ± 1	0.85	12.0 ± 0.5	0.77 ± 0.08	198 ± 2	0.7 ± 0.1	1539.1	96.45

Table 2-5. Fabrication details and properties of the FBGs studied in this thesis. The parameters d and α are dimensionless as described in the text.

Chapter 3:

Microscopic Characterisation

A number of techniques exist to investigate the refractive index structure induced in the core of a FBG; these were discussed in section 1.5.6. These techniques all differ in their acquisition capabilities and effect on the state of the sample. The Differential Interference Contrast (DIC) microscopy technique has been adopted in this thesis both for its powerful detection capabilities and also for the non-destructive effect on the sample. In this chapter, DIC microscopy is used to investigate the refractive index structures of the FBGs described in Chapter 2 which were fabricated using a prism interferometer and both standard and custom-made phase masks. The chapter begins with a discussion of the predicted intensity distributions formed during fabrication of the FBGs to enable comparison with the structures observed in the DIC images. Following this, the experimental techniques used for DIC imaging are described along with the techniques used for image analysis. The results of imaging experiments are then presented and compared with the predicted intensity distributions. The spectral consequences of the observed refractive index structures will be discussed in Chapters 4 and 5.

3.1 Predicted intensity distributions

3.1.1 Prism Interferometer

The prism interferometer fabrication technique was employed in this thesis to investigate the spectral and microscopic characteristics of gratings formed by two-beam interference. As discussed in section 2.4, an incident angle of $\theta_i = 63^\circ$ was chosen to fabricate gratings resulting in a Bragg wavelength of

approximately 1550 nm. Using Equation 1-4, a Bragg wavelength of 1550 nm results from a grating period, Λ , of approximately 0.54 μm when n_{eff} of the LP_{01} mode is approximated as the refractive index of silica, $n = 1.44402$ (from Equation 1-6).

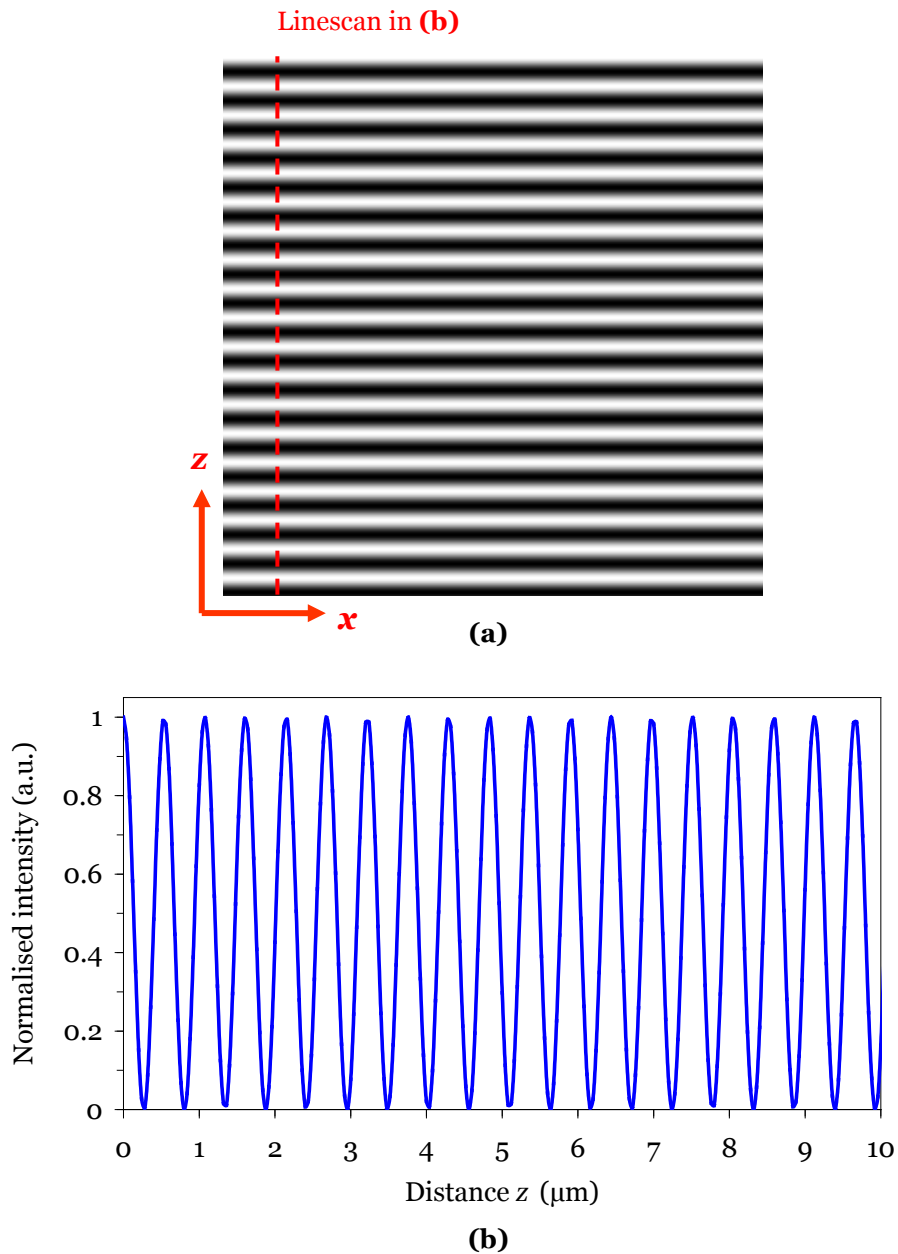


Figure 3-1. Predicted intensity distribution at the output face of the prism interferometer due to two-beam interference **(a)** with a fringe spacing of $\Lambda \approx 0.54 \mu\text{m}$. The image represents a physical area of $10 \times 10 \mu\text{m}$. **(b)** Linescan along z , corresponding to the direction parallel to both the output face of the prism and the axis of the fibre.

Assuming that FBGs are produced as a result of two-beam interference at the output face of the prism as illustrated in Figure 2-4(b), the image in Figure 3-1(a) shows the predicted intensity distribution during fabrication with a fringe spacing of $\Lambda \approx 0.54 \mu\text{m}$. The resulting intensity pattern is expected to be uniformly distributed along the fibre axis, z , as shown in Figure 3-1(b). Additionally, when only two beams are present, the interference fringes are expected to be uniformly distributed across x and exhibit no Talbot beating (see discussion in the next section).

3.1.2 Phase masks and Talbot diffraction

The field distributions in free space behind an illuminated phase mask have been imaged [95] and revealed the existence of Talbot diffraction patterns, as first observed by Talbot [105] in 1836. Talbot discovered that the pattern formed close to a phase diffraction grating can, under certain conditions, replicate the pattern of the original grating at periodic distances from its surface, subject to diffraction limits. Rayleigh [106], in 1881, first deduced the repeat length of the pattern, known as the Talbot length.

If the pattern behind the phase mask was formed by first-order diffraction alone, the two symmetrically crossing components within the Fresnel region would generate uniform fringes with half the period of the phase mask and would display no Talbot beating. Nulling of the higher diffraction orders is, however, nontrivial. Phase masks for FBG fabrication have been designed to induce a π phase-shift in the incident beam and cause a nulling of the zeroth diffraction order to power fractions as low as 1-2% with higher orders present also [95].

Near-field optical probe scans taken by Mills *et al.* [95] of the region near a π -phase shift mask yielded a Talbot length that agreed well with the result of a calculation for the interaction between the first and second diffraction orders. Scans were taken in a region corresponding to $\sim 50\text{-}60 \mu\text{m}$ from the phase mask, because this is where the fibre core would normally lie during fabrication due to the thickness of the cladding. The use of a very narrow beam, $\sim 50 \mu\text{m}$, made the second-order interaction negligible. Consequently

the beating between the first-order and the weak zeroth-order became apparent and the experimental Talbot length compared well with that which was calculated. The use of larger beam-widths in grating fabrication, which can be two orders of magnitude larger than the beam used by Mills *et al.*, and the use of UV wavelengths means that higher-order interactions are not negligible.

In 1881, Rayleigh deduced that assuming $\lambda \ll \Lambda_{pm}$, i.e. the wavelength of the incident radiation is much smaller than the period of the phase mask, the Talbot length, Z_T , is given by:

$$Z_T = \frac{2(\Lambda_{pm})^2}{\lambda}. \quad \text{Equation 3-1}$$

When $\lambda \sim \Lambda_{pm}$, the Talbot pattern does not reproduce the pattern of the original grating and the number of diffraction orders is small. In the production of fibre gratings, each diffraction order becomes significant and has associated with it a characteristic repeating pattern relating to its interaction with each and every other diffraction order. As the distance from the phase mask is increased, complex patterns that undergo regions of change can emerge because the spreading diffracted beams have finite width and therefore limited interaction.

The Talbot pattern for a phase mask illuminated normally by a plane wave can be described by a scalar electric field [107]:

$$E(x, z) = \sum_m C_m \exp(i m \mathbf{G} x) \exp(i \mathbf{k}_m z) \quad \text{Equation 3-2}$$

where C_m is the amplitude of the electric field of the diffracted order m , $\mathbf{k}_m = (\mathbf{k}^2 - m^2 \mathbf{G}^2)^{1/2}$, $\mathbf{k} = (2\pi n_w / \lambda_w)$, n_w is the refractive index of the medium behind the phase mask at the writing wavelength λ_w and $\mathbf{G} = (2\pi / \Lambda_{pm})$ is the unit reciprocal lattice vector of the phase mask. When the

number of diffraction orders is small, Rayleigh's approximation for the Talbot length becomes:

$$Z_T(m,n) = \frac{2\pi}{\left(\mathbf{k}^2 - m^2\mathbf{G}^2\right)^{1/2} - \left(\mathbf{k}^2 - n^2\mathbf{G}^2\right)^{1/2}} \quad \text{Equation 3-3}$$

where m and n are integers representing diffraction orders and Z_T is the Talbot length of a repeating pattern resulting from the interaction of two chosen orders. The greatest repeat length is for $m = 0$ and $n = 1$.

The diffraction patterns generated by phase masks used in this work have been modelled to enable interpretation of the spectral and microscopic properties of the fabricated samples. The diffraction patterns produced behind a phase mask during the fabrication of FBGs are formed by interference between the orders of the phase mask that overlap coherently, as discussed in section 1.4.3. Each diffraction order produced by the phase mask possesses a finite distance over which it overlaps coherently with another order.

In order to predict the refractive index patterns imprinted in the core of phase-mask-written FBGs, the measured diffraction efficiencies were used by colleague Betty Kouskousis to model the expected interference patterns [108]. Under the fabrication conditions used in this work, the fibre was typically placed within 150 μm of the phase mask, so that the photosensitive core lay within 250 μm of the phase mask during fabrication. The diffracted orders considered in this investigation include those up to ± 2 , since the contributions from other orders would be incoherent within the fibre core [109].

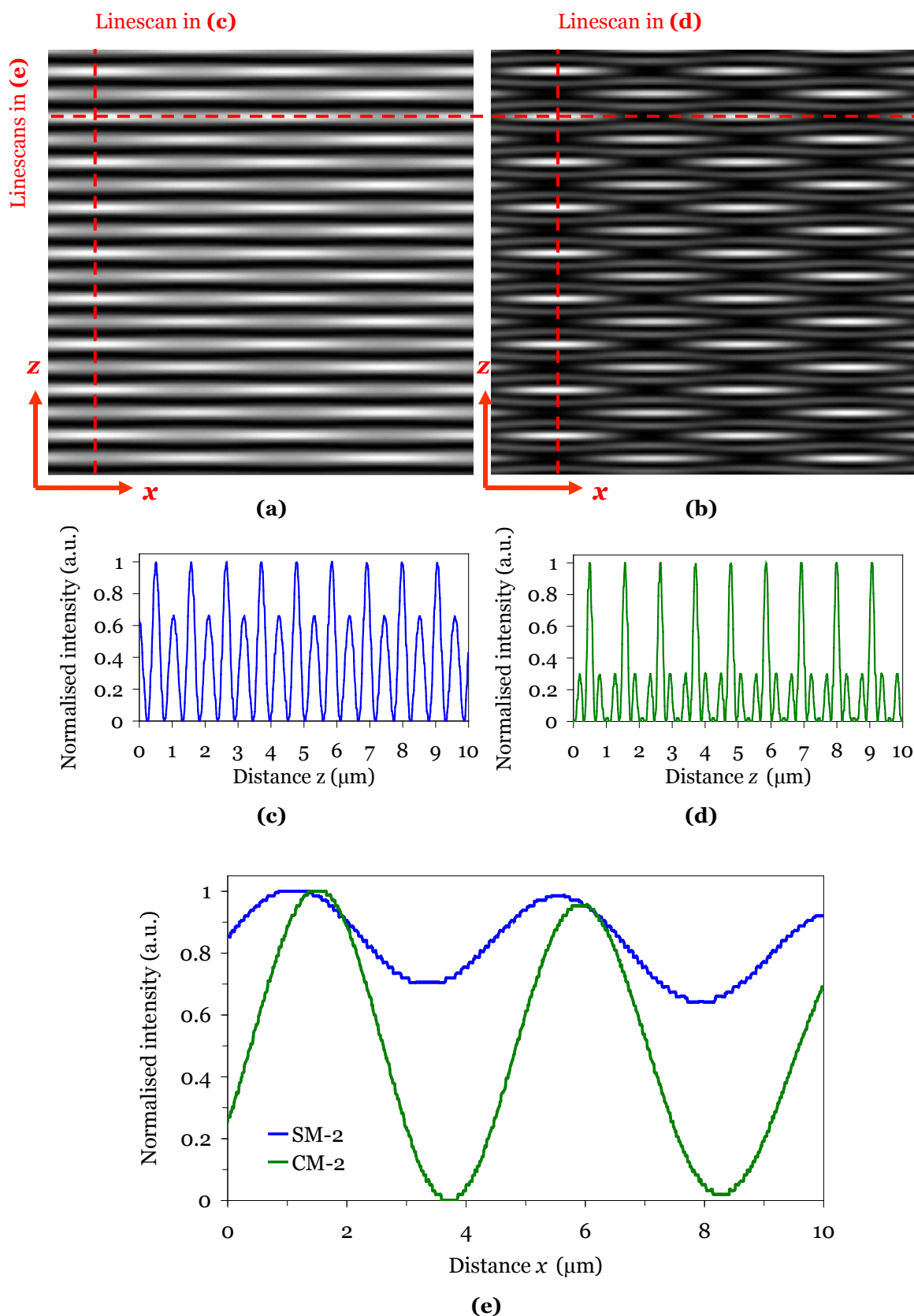


Figure 3-2. Simulated intensity distributions behind UV irradiated phase masks in the region the fibre core lies during grating fabrication: **(a)** SM-2 and **(b)** CM-2. The images represent a physical area of $10 \times 10 \mu\text{m}$. Linescans through the maximum intensity parallel to the phase mask in z for **(c)** SM-2 and **(d)** CM-2. **(e)** Linescans through the maximum intensity perpendicular to the phase mask in x for masks SM-2 and CM-2.

In this study, the patterns generated by the standard zeroth-order-nulled phase mask (labelled SM-2) will be compared with those formed by the custom-made phase mask (labelled CM-2). The model for the predicted diffraction patterns used Equation 3-2 with a writing wavelength $\lambda_w = 244$ nm, in a medium with index $n_w = 1.511$ (the index of silica at λ_w) and included the relative contributions of the 0th, $\pm 1^{\text{st}}$ and $\pm 2^{\text{nd}}$ diffracted orders of the phase masks and Λ_{pm} for masks SM-2 and CM-2 as listed in Table 2-2 and Table 2-3, respectively. In practice, the index of the fibre core is slightly higher than the index of silica which will cause small variations in the Talbot lengths observed in FBG images.

The simulated multiple-beam interference patterns of the phase masks SM-2 and CM-2 are shown in Figure 3-2(a) and (b), respectively. As expected, the images reveal complex, interleaving regions of constructive and destructive interference due to beating between the multiple orders of the phase masks. The plots featured in Figure 3-2(c) and (d) are linescans along the direction parallel to the phase mask (z) through a region containing a maximum in the normalised intensity of the simulated images in Figure 3-2(a) and (b), respectively. Fast Fourier Transforms (FFTs) of these z -linescans reveal a number of spectral components which are summarised in Table 3-1 along with the relative strengths of each component in the FFT power spectrum. The dominant period in the standard phase mask image in Figure 3-2(a) is clearly half of the phase mask period ($\Lambda_{pm}/2 \approx 0.53 \mu\text{m}$); this is confirmed by the 92.5% relative strength of this period from the FFT of the z data.

The most dominant periods in the intensity pattern produced behind the custom-made phase mask are $\Lambda_{pm}/3$ and Λ_{pm} . As can be seen in Figure 3-2(d), the features in the custom-made phase mask image with a period of approximately $0.36 \mu\text{m}$ (corresponding to $\Lambda_{pm}/3$) are 70% less intense than features with a period equal to Λ_{pm} , consequently they are not expected to dominate in the refractive index structure induced in a fibre core. The increased contributions of the 0th and $\pm 2^{\text{nd}}$ diffraction orders of the custom-made phase mask have evidently caused the phase mask period Λ_{pm} to

dominate the interference pattern produced behind the mask. This result is consistent with the work of Dyer *et al.* [52], which reported that even small contributions from either of the 0th or 2nd diffraction orders can cause Λ_{pm} features to dominate over $\Lambda_{pm}/2$ features.

Mask label	Λ_{pm} (μm)	Period in z ($\pm 0.01 \mu\text{m}$)	Fraction of Λ_{pm}	Normalised z FFT strength (%)	Period in x ($\pm 0.01 \mu\text{m}$)
SM-2	1.0668	0.53	$\sim 1/2$	92.5	4.57
		1.11	~ 1	4.5	
		0.36	$\sim 1/3$	3	
CM-2	1.07	0.36	$\sim 1/3$	41.9	4.49
		1.11	~ 1	36.9	
		0.25	$\sim 1/4$	13.1	
		0.53	$\sim 1/2$	8.1	

Table 3-1. Spectral components of the simulated diffraction pattern for the standard phase mask SM-2 and custom-made phase mask CM-2.

m	n	Z_T of SM-2 ($\pm 0.05 \mu\text{m}$)	Z_T of CM-2 ($\pm 0.05 \mu\text{m}$)
0	1	14.01	14.10
0	2	3.44	3.46
0	3	1.48	1.49
0	4	0.79	0.80
1	2	4.56	4.59
1	3	1.66	1.67
1	4	0.84	0.84
2	3	2.60	2.62
2	4	1.03	1.03

Table 3-2. Calculated Talbot lengths of the diffraction patterns produced by the standard phase mask SM-2 and custom-made phase mask CM-2 in a medium with index $n_w = 1.511$ and with $\lambda_w = 244 \text{ nm}$.

The Talbot lengths of the simulated phase mask diffraction patterns in Figure 3-2(a) and (b) were found from the peak-to-peak distances in the x -linescans in Figure 3-2(e) and are listed in Table 3-1. The Talbot lengths of the simulated patterns are in good agreement with the Talbot lengths calculated from Equation 3-3, listed in Table 3-2, for the interaction between the 1st and

2nd orders of each phase mask illuminated with $\lambda_w = 244$ nm in a medium of index $n_w = 1.511$. The differing diffraction efficiencies between the standard and custom phase masks have not significantly affected the Talbot lengths of the simulated interference patterns. However, the lower 1st order and higher 0th and 2nd orders of the custom-made phase mask have affected the dominance of the periods present in the z -axis, which corresponds to the direction of propagation along a FBG that would be produced using the phase mask. The dominance of the Λ_{pm} period over the $\Lambda_{pm}/2$ period is expected to affect the strength of harmonic reflectances from these periods in the core of FBGs.

3.2 Differential interference contrast microscopy

A modified form of DIC microscopy was used in this thesis and a schematic diagram of the experimental arrangement is shown in Figure 3-3. An inverted Olympus IX FL microscope in the Optical Technology Research Laboratory (OTRL) at Victoria University was used. The microscope is infinity-corrected, equipped with high-resolution Nomarski optics and has an argon-ion laser operating at a wavelength of 488 nm as the light source.

Referring to Figure 3-3, the beam from the light source is first linearly polarised, split in two by the sliding Wollaston prism and then focused by the objective to two spots separated by a lateral shear of 0.58 ± 0.01 μm for the system used [109]. This value defines the resolution limit of the imaging system. The two beams are then focused onto the sample by the objective and any refractive index changes encountered by either beam as they pass through the sample will result in different optical paths between the beams. The second Wollaston prism recombines the two beams into a single beam that then passes through a second polariser, known as the analyser. The beam is then scanned in the plane perpendicular to the optical axis of the imaging system. Optical path differences between the beams manifest themselves as intensity variations in the scan. As a result, the intensity recorded within a DIC image may therefore be related to the gradient of the phase function of

the object and can be approximated as the square of the differential of the optical path-length through the specimen [96].

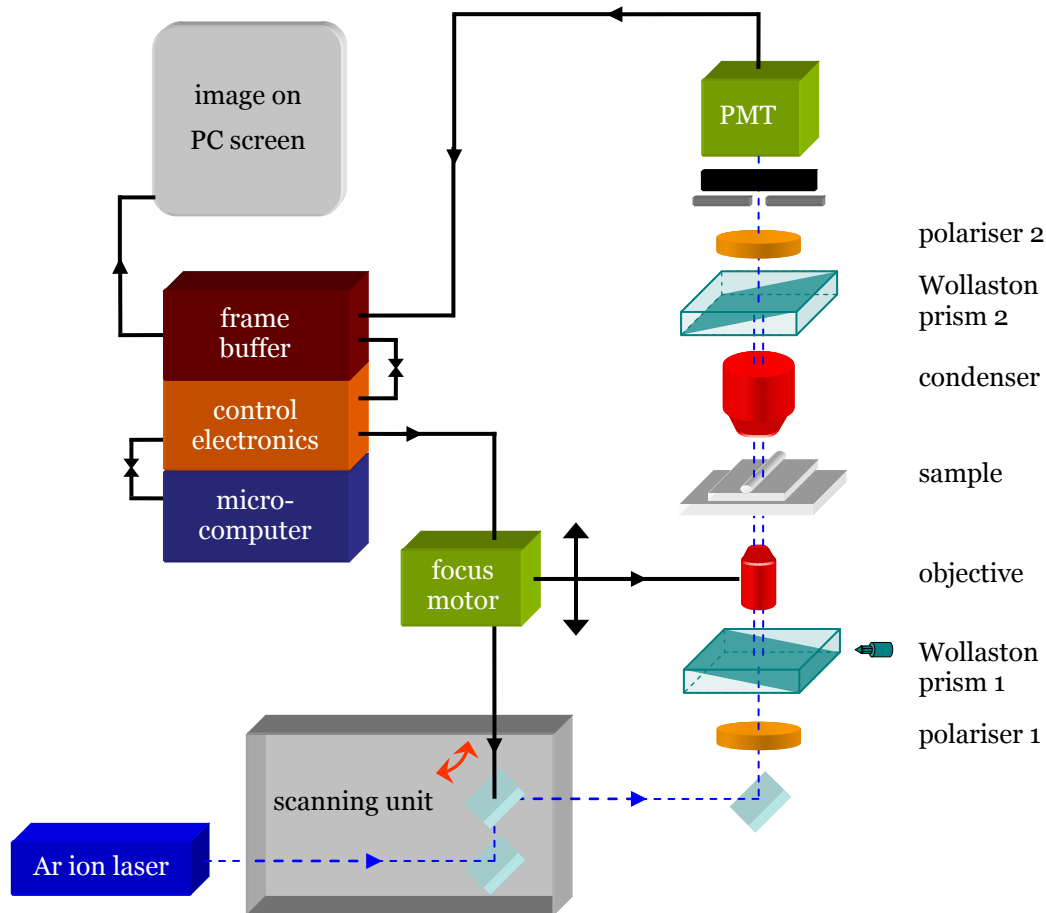


Figure 3-3. Schematic diagram of the modified form of Differential Interference Contrast microscopy used in this work.

The argon-ion laser was allowed time to stabilise before image acquisition so that intensity fluctuations were kept to a minimum. The images in this thesis were recorded using an Olympus UPlanApo 40× infinity-corrected objective which is corrected for the 0.17 mm thick cover slips. The glass cover slips used were $22 \times 22 \times 0.170$ mm and the glass cover slides were $22 \times 22 \times 1$ mm. Once the sample was mounted and located through the microscope oculars, the centring of the condenser and the extinction of the two polarisers were optimised. The focus conditions for each image were determined qualitatively by adjusting the objective lens height until the sharpest edges at the core or cladding boundaries were obtained. The sample was scanned and the images

were recorded using FluoView software by Olympus. The setting of the sliding Wollaston prism is discussed below.

3.2.1 Wollaston prism bias

The core components of the DIC system are the two birefringent Wollaston prisms as depicted in Figure 3-3; the first of these allows control of the phase bias between the two emerging beams via a rotating knob. With crossed polarisers and in the absence of a specimen, the expected relation between the phase bias, φ_b , and intensity, i , in a DIC image is [110]:

$$i \propto (1 - \cos \varphi_b). \quad \text{Equation 3-4}$$

The slider prism used in this thesis was calibrated in terms of the phase bias, φ_b , by Betty Kouskousis using an apparent empty volume containing an oil of $n=1.464$ at 26°C [108]. The calibration involved measurement of the intensity for the entire range of possible prism positions and the results are shown in Figure 3-4. The measured data were then fitted (also shown in Figure 3-4) using the following expression obtained from Equation 3-4 where τ is the number of clockwise turns of the prism:

$$i = p_1 \left(1 - \cos \left(\frac{\tau + p_2}{p_3} \right) \right) + p_4. \quad \text{Equation 3-5}$$

The parameters p_2 and p_3 are scaling factors which are fixed for a given microscope; they relate τ to φ_b . The parameters p_1 and p_4 depend on the illumination and the PMT gain and offset. An interactive method was used to find the values of the fitting parameters that minimise the mean square error between the measured and fitted data to be $p_1 = 1425.74$, $p_2 = 0.22$, $p_3 = 0.35$ and $p_4 = 20.9$.

The phase bias as a function of prism position was inferred from Equation 3-4 and the fit to Equation 3-5. As can be seen from Figure 3-4, the relationship between the phase bias and the measured intensity can be approximated as

linear for bias settings of $\pi/2$ which is most crucial when phase information is to be extracted from measured images. However, in this thesis DIC microscopy has been used as a tool for visualising the refractive index changes in the core of FBGs and as such the bias setting was chosen to maximise contrast in the images. A setting of $\tau \sim 2.08$ turns or $\varphi_b \sim 0.9\pi$ radians (as indicated by the red dotted line in Figure 3-4) was found to provide the best contrast in the images so this was used for all of the imaging experiments.

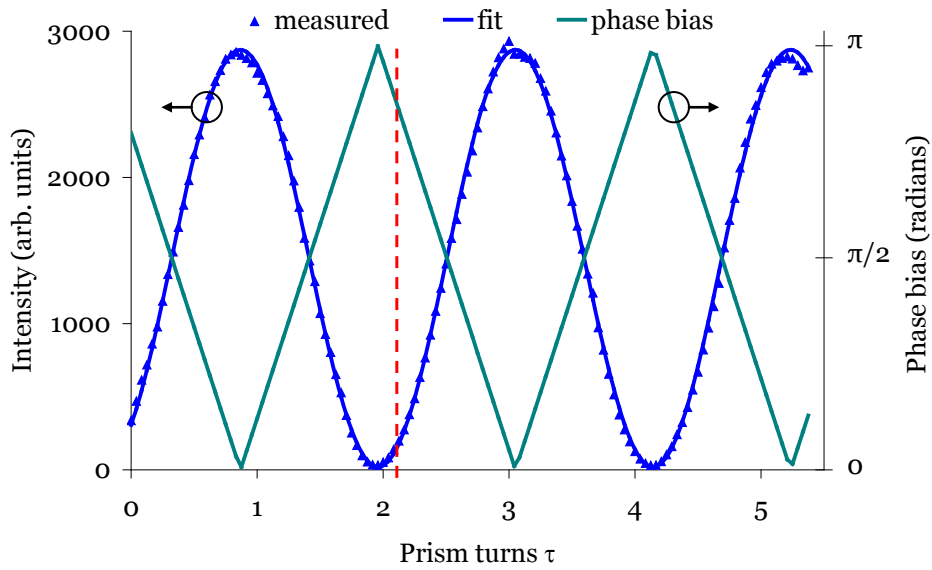


Figure 3-4. Wollaston prism phase bias calibration: measured and fitted intensities as well as calculated phase bias as a function of prism position. The red, dotted line indicates the chosen setting for the work in this thesis for optimum image contrast.

3.2.2 Sample preparation

In order to achieve the optimal contrast in DIC images of the fibre core region, a high level of index-matching is required between the immersion oil and the cladding of the fibre sample. A Cargille Series AA oil was used which was specified as having a refractive index of 1.4580 ± 0.0002 at 25°C . The temperature dependence of the refractive index of the oil was specified as $-3.73 \times 10^{-4}/^\circ\text{C}$. Immersed samples were mounted on a temperature-controlled rotation stage on the microscope to maintain index-matching during imaging. The optimal index-matching conditions for the various fibres used were determined, as discussed in section 3.2.3, and the oil and all

components were heated to the required temperature prior to mounting the sample.

The preparation process for the DIC imaging of samples in this thesis is illustrated in Figure 3-5 for the DIC system described in Figure 3-3. The sample to be imaged was placed on a cover slip along with extra pieces of the same fibre (called spacers) placed either side of the test sample in order to form a 'well' with the index-matching oil and also to prevent tilting in the microscope slide that is then placed on top of the sample. Prepared samples were mounted in the central groove of the temperature controlled rotation stage and one end of the fibre was fastened to allow the acquisition of DIC images at different rotational orientations about the fibre axis. The rotating column was connected to a mechanical stepper so that fibre rotation was controlled electronically with a precision of 0.01° .

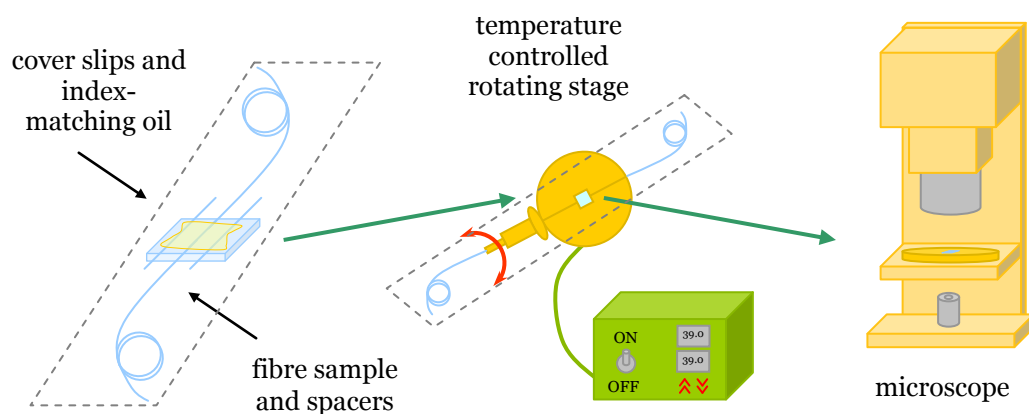


Figure 3-5. Schematic illustration of sample preparation and positioning used for DIC imaging of fibres at different rotational orientations.

3.2.3 Fibre properties and index-matching

To ensure optimal contrast in the DIC images, the index matching conditions were determined for each of the fibres F-1, F-2, F-3 and F-4; the properties of which summarised in Table 2-4. Plain, non-UV exposed samples of these fibres (with the acrylate coating removed) were immersed in the index-matching oil and mounted separately with their spacers on the temperature-controlled rotating stage as illustrated in Figure 3-5. DIC images of the four

fibres are shown in Figure 3-6. The images are the result of the raw DIC images with background images subtracted, which were recorded by moving the sample just out of the field of view.

The two standard telecommunications fibres used in this work are labelled as F1 and F4, and have core diameters of 7.4 and 8.2 μm , respectively. Both fibres were designed for singlemode operation at 1550 nm with cutoff wavelengths of approximately 1300 nm. DIC images of fibres F-1 and F-4 are featured in Figure 3-6(a) and (d), respectively. The fibre chosen in this work to examine type IIA fibre gratings is labelled F-2 and is Ge:B co-doped for enhanced photosensitivity. A DIC image of fibre F-2 is shown in Figure 3-6(b). Fibre F-2 has a core diameter of 8 μm and was designed for singlemode operation at 1550 nm with cutoff wavelength of approximately 1300 nm. The fibre chosen in this work to examine spectral features in the 1030 nm region under singlemode conditions is labelled F-3 and has a cutoff wavelength of 930 nm. A DIC image of fibre F-3 is shown in Figure 3-6(c) with a core diameter of 3.6 μm as estimated from DIC images.

All four fibres in Figure 3-6 have cladding diameters of approximately 125 μm of which the outer edges are visible in the images. The core of each fibre is clearly visible in the centre of the images and the depressed cladding boundaries of each fibre are also visible faintly in the images on either side of the core. The depressed claddings are most visible in the images of fibres F-2 and F-3. Depressed claddings are usually introduced using boron or fluorine during manufacture to lower the refractive index surrounding the core and reduce bending losses [42, 111]. The use of boron in particular has been shown to reduce losses to cladding modes of FBGs [85]. As can be seen in Figure 3-6, fibres F-2 and F-4 both have a refractive index dip visible in the ridge running through the centre of the core. Refractive index dips are the result of certain manufacturing processes, particularly in germanosilicate fibres as a result of the high temperatures required to collapse the preform when using the chemical vapour deposition technique [112]. The refractive index of the fibre core can be controlled by adjusting the concentration of germanium or

fluorine dopants in the different core layers, where fluorine can decrease the refractive index and germanium can increase the refractive index [113].

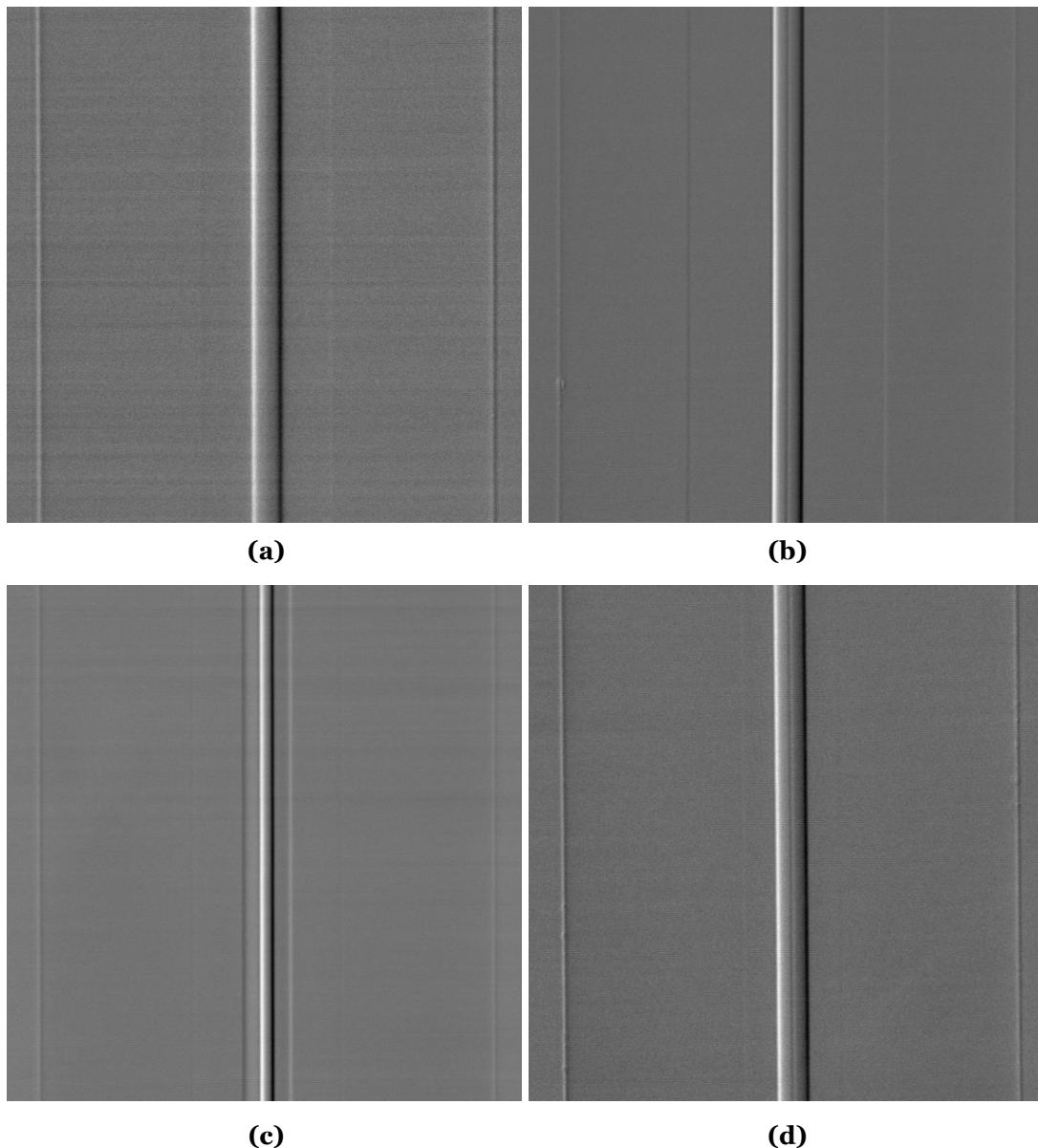


Figure 3-6. DIC images of the different fibres used in this work with the background subtracted: **(a)** F1, **(b)** F2, **(c)** F3 and **(d)** F4. The dimensions of each image are approximately $140 \times 140 \mu\text{m}$.

The optimum index-matching conditions for the fibres used in this work were determined by examining the intensity difference between the index-matching oil and fibre cladding from averaged line profiles across images measured at various temperatures. Index-matching is optimised when the cladding boundary is no longer distinguishable in the image, i.e. when the intensity

difference is zero between the boundaries and the oil. Linear fits were applied to the variation of intensity extrema at the cladding boundaries for each temperature to determine the zero intercept. To remove all sources of unwanted intensity variation from the imaging system, background images, with the fibre sample moved just out of the field of view, were measured at each temperature and subtracted from each corresponding fibre image.

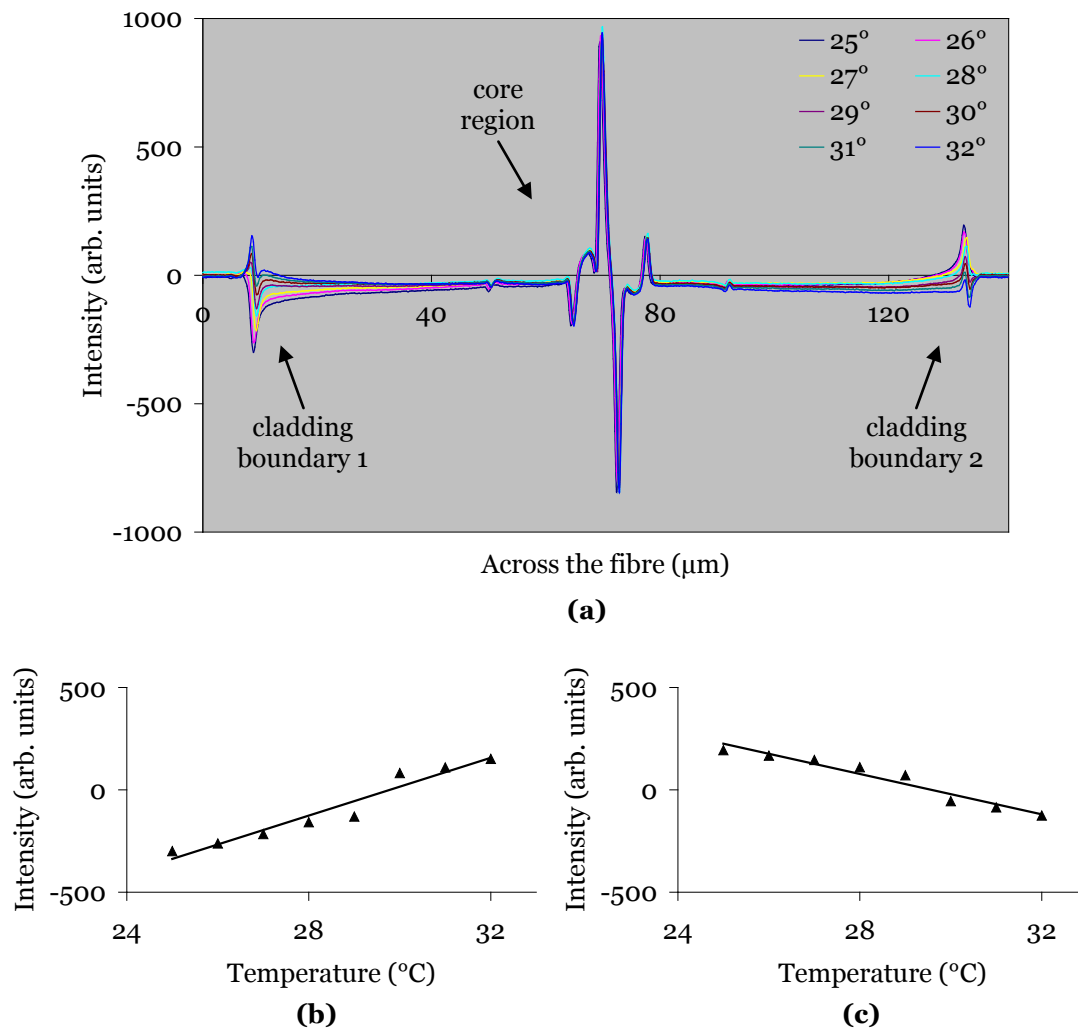


Figure 3-7. DIC measurements of intensity variation with temperature across **(a)** fibre F-3. Intensity versus temperature at **(b)** cladding boundary 1 and **(c)** cladding boundary 2, as indicated in **(a)** with linear fits applied as discussed in the text. The uncertainties associated with both the intensity and temperature values are not shown as they are smaller than the data points.

Images were recorded of fibre F-3 after stabilisation was reached at various temperatures from 25 to 32 $^{\circ}\text{C}$ in 1 $^{\circ}\text{C}$ increments. Background images were subtracted and averaged line profiles across the resulting images are shown in

Figure 3-7(a). The depressed cladding boundaries of fibre F-3 are visible in the core region of the line profile. The variation in detected intensity with temperature at the left and right cladding boundaries are shown in Figure 3-7(b) and (c), respectively. Linear fits applied to the data indicated that the detected intensity difference between the oil and the cladding of fibre F-3 was predicted to be zero at an average temperature of 29.7 ± 0.1 °C. This process was repeated for the other three fibres; the tested temperature ranges and measured optimal temperatures are listed in Table 3-3. The variations in optimal temperatures for each of the fibres is expected to be due to slight variations in cladding refractive index.

Fibre	F-1	F-2	F-3	F-4
T range (°C)	24 to 31	23 to 32	25 to 32	23 to 31
T (± 0.1 °C)	26.4	28.2	29.7	28.3

Table 3-3. Measured temperature ranges and optimal index-matching temperatures of the fibres used in this work.

3.2.4 Rotational analysis

As discussed in section 1.5.6, a complex refractive index structure has been observed using DIC microscopy in the core of type I FBG written with a phase mask. From various images recorded at different rotational orientations about the fibre axis, the images corresponding to orientations parallel and perpendicular to the UV beam used in fabrication were identified due to the distinct difference between the observed structures, as illustrated in Figure 3-8(a). Because the diffraction pattern generated behind the phase mask repeats in the direction of the UV writing beam and because a DIC image is an optical slice of the sample, an image which reveals a Talbot diffraction pattern in the core corresponds to the image plane parallel to the UV writing beam. An image recorded in the image plane perpendicular to the UV writing beam direction therefore reveals a uniform period since the image is an optical slice through one plane of the repeating diffraction pattern.

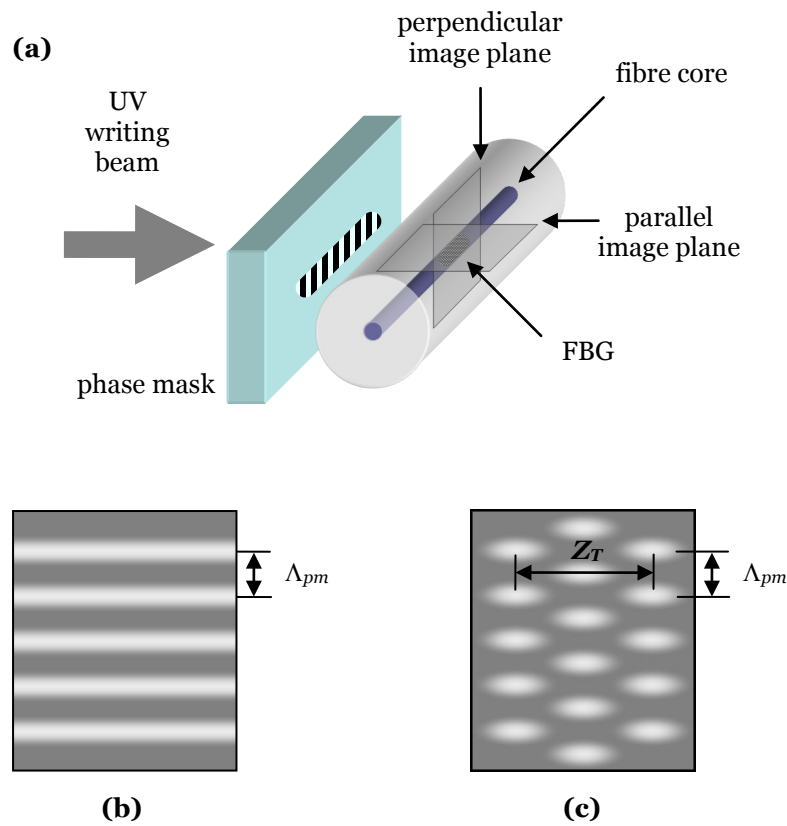


Figure 3-8. Schematic diagram identifying DIC imaging planes and fibre orientations corresponding to perpendicular and parallel to the UV writing beam (a) during fabrication. Schematic diagrams of expected FBG structure in images recorded in (b) the perpendicular image plane and (c) the parallel image plane.

DIC microscopy is used in this thesis to identify and compare the images of FBGs which reveal the sample orientations corresponding to perpendicular and parallel to the UV writing beam. In order to identify these two orthogonal images for each sample, the grating was firstly located with the microscope and the sample mounting was tested by checking that the expected structure changes were observed when the sample was rotated at a fixed image depth. Once correct mounting was verified, images were recorded in a fixed plane after the sample was rotated in 5° increments from 0 to 360° (unless otherwise specified). Background images, i.e. with the sample moved just out of the field of view, were measured and subtracted from each image to remove unwanted sources of intensity variation. The resulting set of images was analysed to identify the best two orthogonal images of which one exhibited uniform parallel lines (Figure 3-8(b)) and the other a Talbot diffraction pattern (Figure 3-8(c)). Due to the increment size, the precision with which

the respective orientations of the two images were identified was estimated as $\pm 5^\circ$. The tomography and quantification of the refractive index perturbations inside FBGs is the subject of other work [108] and beyond the scope of this thesis.

3.2.5 Analysis of periodic features

In order to determine the period of imaged grating features, sinusoidal fits were applied to linescans from the images. Linescans were averaged over a particular image area and normalised with respect to the maximum and minimum intensity values. The intensity I was modelled by applying fits of the form:

$$I = A \sin(\omega z + \varphi) + I_{off} + \delta z \quad \text{Equation 3-6}$$

where A is the amplitude, $\omega = 2\pi/\lambda$ is the angular frequency, φ is the phase and I_{off} is the intensity offset. The intensity gradient factor, δ , accounted for linear intensity gradients exhibited across some images. After subtraction of a background image, a residual intensity gradient can result from slight differences in imaging conditions during measurement of the FBG and background images.

The period of observed refractive index perturbations along the fibre, Λ , was determined by fitting the function in Equation 3-6 to linescans taken through periodic image features. Where specified, the periodicities of intensity variations in the images were also determined by applying Fast Fourier Transforms (FFTs) to the data to extract the Fourier components.

The observed repeat lengths of refractive index perturbations extending across the fibre, or Talbot length Z_T , were compared with sinusoidal functions as in Equation 3-6 with periods equal to the expected Talbot lengths. As detailed in Table 3-2, the Talbot lengths arising from beating between various orders range from approximately 0.8 to 14 μm . A Talbot length of approximately 4.6 μm is expected to result from beating between the $\pm 1^{\text{st}}$ and $\pm 2^{\text{nd}}$ orders of

each phase mask. The next shorter Talbot length of approximately $3.5 \mu\text{m}$ would be expected for beating between the 0^{th} and $\pm 2^{\text{nd}}$ orders, while the next longer Talbot length of approximately $14 \mu\text{m}$ would result from beating between the 0^{th} and $\pm 1^{\text{st}}$ orders.

3.3 Prism interferometer FBGs

A type I FBG (sample Ip-1) and a type IIA FBG (sample IIAp-1) were fabricated using the prism interferometer method described in section 2.4. The samples were each prepared for imaging using the procedure described in section 3.2.2 and imaged using the technique described in section 3.2.3. The details of the samples and the imaging experiments are shown in Table 3-4.

Sample	Fibre	Core diameter (μm)	Type	Optimal temperature ($\pm 0.1 \text{ }^\circ\text{C}$)	Imaging rotation range	Imaging rotation increment
Ip-1	F-4	7.4	I	28.2	$0^\circ - 360^\circ$	5°
IIAp-1	F-2	8	IIA	28.3	-	-

Table 3-4. Summary of the prism FBG imaging experiments.

3.3.1 Type I

Various images selected from the data set measured for sample Ip-1 are shown in Figure 3-9. The corresponding linescans taken lengthwise along the core of the images are shown in Figure 3-10. Figure 3-9(a) to (f) show the images of the prism interferometer FBG which were recorded at relative fibre axial orientations from 0° to 225° in 45° increments, respectively. The linescans in Figure 3-10 were averaged over the $30 \times 2 \mu\text{m}$ region illustrated in Figure 3-10(g) and normalised with respect to the maximum and minimum intensity values. The images and linescans reveal a complex refractive index structure and do not exhibit rotational symmetry. As emphasised in the inset of Figure 3-9(e), the images feature regions of index perturbation which appear to be blazed in alternating directions and bear no resemblance to the structure expected from two-beam interference (see Figure 3-1). As discussed in section

3.1.1, FBGs fabricated using the prism interferometer are expected to possess a sinusoidal refractive index structure with a period of approximately $0.54\ \mu\text{m}$, which is uniformly distributed along and across the core.

On each of the left and right hand sides, Figure 3-9 provides a set of three images which represent a span of 180° in 90° increments. The images of phase mask FBGs are expected to provide clear evidence of refractive index structures which are orthogonally distinct, i.e. at fibre orientations which are parallel and perpendicular to the direction of the writing beam during fabrication. In contrast to the expected images of phase mask FBGs, the images of the prism FBG show no evidence of orthogonal distinction nor do they reveal Talbot beating across the core, as expected.

The linescans in Figure 3-10 generally consist of 14 to 15 peaks over the $30\ \mu\text{m}$ range along the fibre in the z direction. However, anomalies are exhibited between 10 and $20\ \mu\text{m}$ in Figure 3-10(a), (b) and (c). These anomalies could be due to a number of factors including the resolution limit of the imaging system (lateral shear of $0.58\ \mu\text{m}$ – see section 3.2) and the FBG structure itself. FFTs of the linescans in Figure 3-10 revealed a number of spectral components; the periods corresponding to the peaks of interest are summarised in Table 3-5. The determined periods of the linescans in Figure 3-10(a), (b) and (c) were affected by the anomalies mentioned above. The periods measured from the images in Figure 3-10(d), (e) and (f) at 135° , 180° and 225° , respectively, were found to be $2.5 \pm 0.05\ \mu\text{m}$. The periods of the linescans taken from the images are in very poor agreement with the expected period for two-beam interference of $0.54\ \mu\text{m}$.

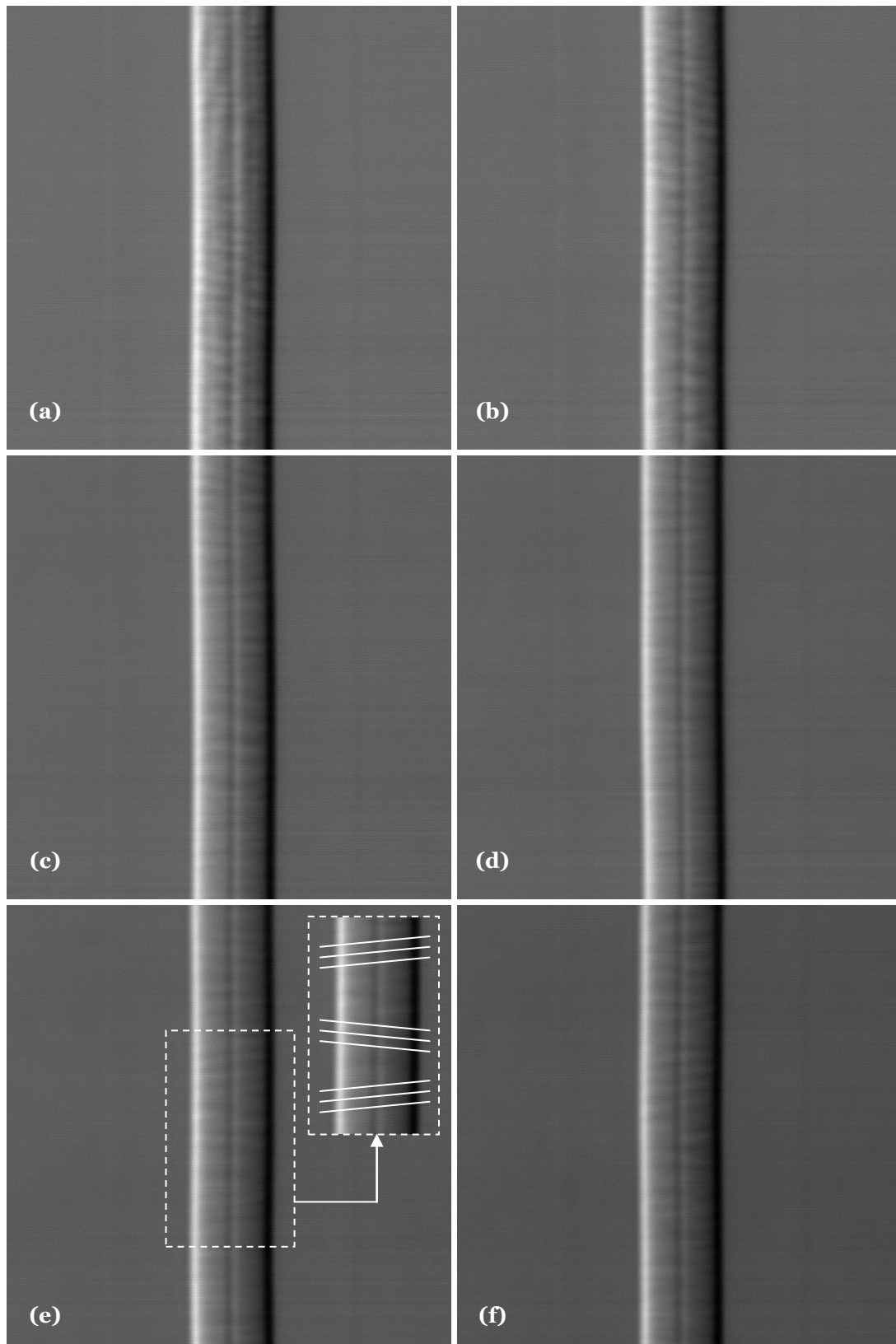


Figure 3-9. DIC images of a type I FBG written with a prism interferometer recorded at relative fibre orientations of **(a)** 0°, **(b)** 45°, **(c)** 90°, **(d)** 135°, **(e)** 180° and **(f)** 225°. The dimensions of each image are approximately $47 \times 47 \mu\text{m}$. The inset of **(e)** emphasises an apparent blazing in alternate directions which are visible in the electronic version but may be not be visible in the printed version of this thesis.

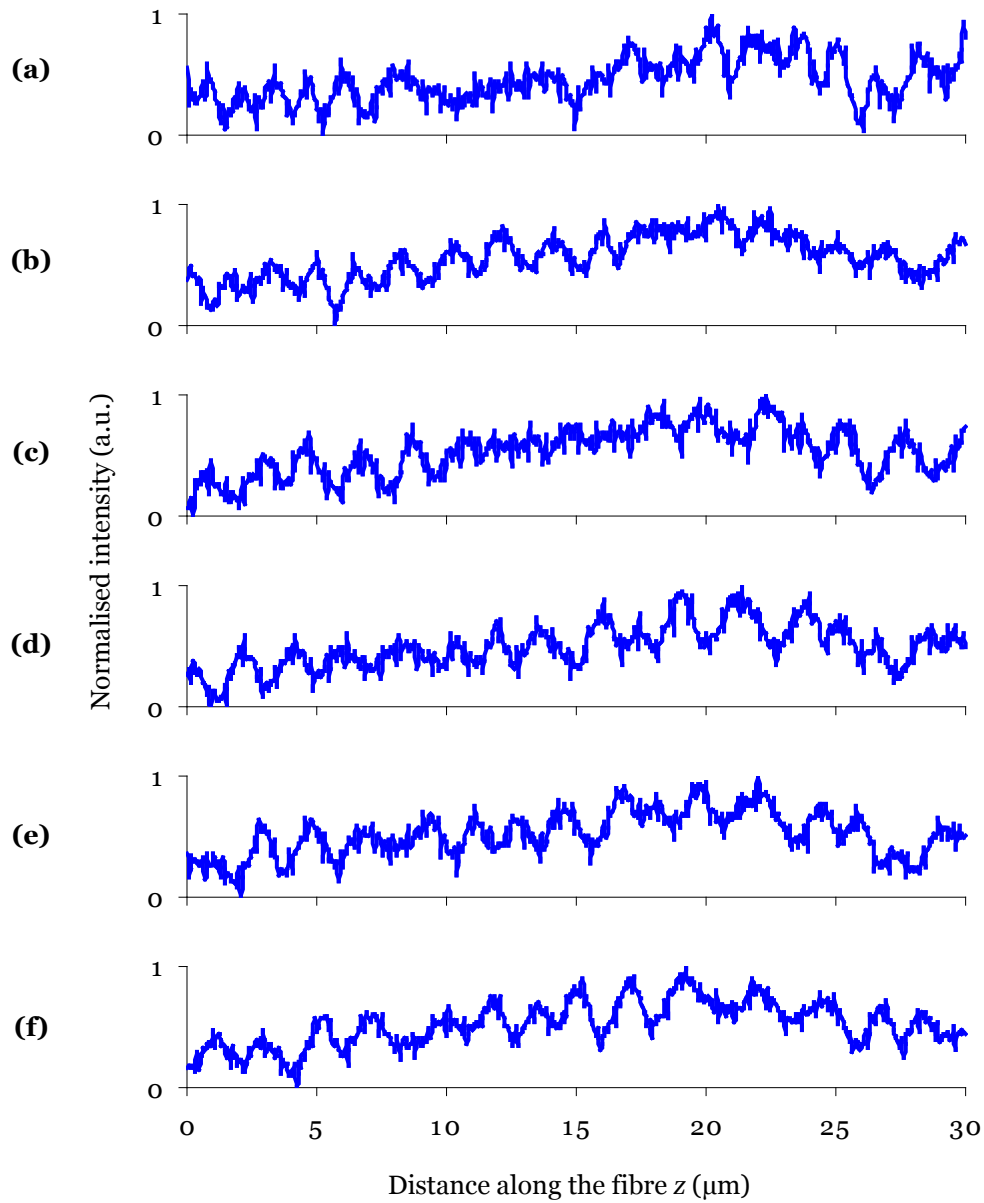


Figure 3-10. Intensity linescans taken along the fibre axis in the corresponding images in Figure 3-9(a) to (f), averaged over the region illustrated in (g).

Orientation	0°	45°	90°	135°	180°	225°
Period in z (± 0.05 µm)	1.58	1.76	1.87	2.5	2.5	2.5

Table 3-5. Periods determined by FFTs of the linescans in Figure 3-10 from the images in Figure 3-9 recorded at different fibre orientations.

Since a wavelength of 488 nm was used to record the DIC images, the expected FBG period of 0.54 µm is approaching the diffraction limit of the imaging system and in fact below the lateral shear of 0.58 µm. As a result, it is likely that the actual FBG period has not been resolved in the images in Figure 3-9. In contrast, the resolution limit of the imaging system is not expected to prevent the resolution of periodic features for the phase mask FBGs since the expected periods are around 1 µm. Furthermore, sample Ip-1 exhibited a Bragg wavelength of 1541.7 nm, as was shown in Table 2-5. According to Equation 1-3 and assuming that $n_{eff} = 1.44$, light in the region of 1541.7 nm would not be efficiently reflected from a grating period of 2.5 µm. This observation provides further evidence that the observed period of 2.5 µm is not the actual period of the FBG. The refractive index structure revealed in the images of the prism interferometer FBGs remains unexplained due the resolution limitation of the imaging system.

3.3.2 Type IIA

The refractive index structure in the core of sample IIAp-1 was difficult to distinguish in the DIC images; consequently rotational analysis was not performed. Various images of sample IIAp-1 are shown in Figure 3-11, and it can be seen that the refractive index perturbations are not apparent. To examine the features of the FBG more clearly, the non-exposed fibre image in Figure 3-11(c) was subtracted from image of the FBG in Figure 3-11(b). The result, shown in Figure 3-11(d), shows weak intensity variations but does not reveal any significant information about the structure of the sample. As shown in Table 2-5, sample IIAp-1 exhibited a Bragg wavelength of 1536.8 nm with a reflectance of approximately 98.9% (or -19.4 dB) despite being exposed to a

much larger fluence than sample Ip-1 which had a reflectance of approximately 99.94%. It is likely that the refractive index changes in the core resulting from the type IIA growth phase of sample IIAp-1 were not strong enough to be detected in the images. In general for prism and standard phase mask FBGs, reflectances higher than 99.9% (or -30 dB) were required for the refractive index changes to be detected in the DIC images.

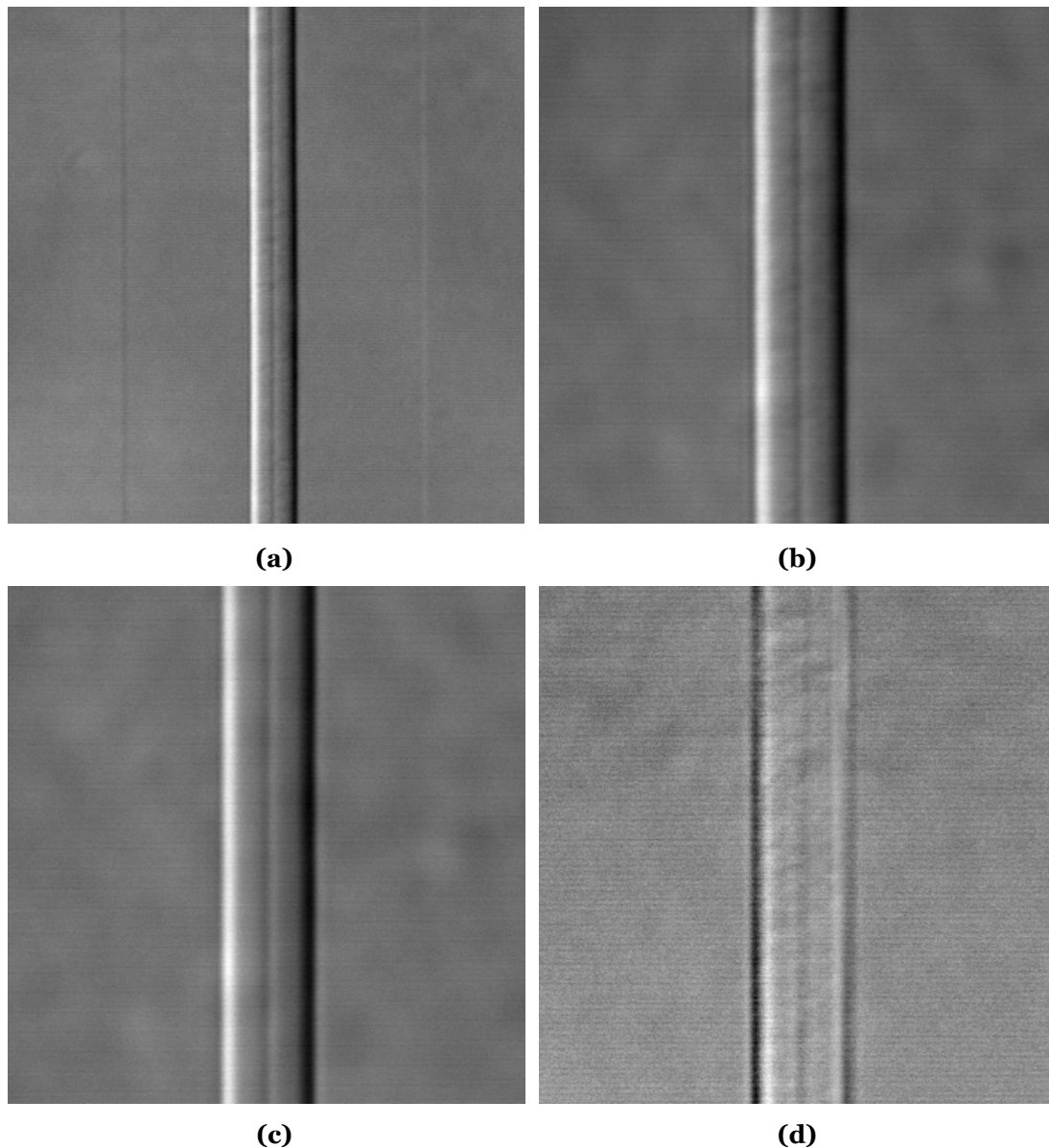


Figure 3-11. DIC images of a type IIA FBG written with a prism interferometer with dimensions **(a)** $93 \times 93 \mu\text{m}$ and **(b)** $47 \times 47 \mu\text{m}$. **(c)** non-exposed region of fibre F-2 ($47 \times 47 \mu\text{m}$); **(d)** Resulting image after (c) was subtracted from (b).

3.4 Standard phase mask FBGs

The following sections present the results and analysis of DIC imaging experiments for various gratings produced with standard phase mask SM-2 under the fabrication conditions presented in Chapter 2 and whose spectral characteristics are detailed in Chapter 4. The samples were prepared for imaging using the technique described in section 3.2.2 and imaged at the required temperatures as determined in section 3.2.3. Rotational analysis of the samples was performed and the images corresponding to parallel and perpendicular to the UV writing beam were identified as described in section 3.2.3. In order to examine the image features which are due to the FBG more closely, a non-exposed fibre image was subtracted from cropped regions of each of the images. The details of the samples and the imaging experiments are shown in Table 3-6.

Sample	Fibre	Core diameter (μm)	Type	Oil temperature (± 0.1 °C)	Imaging rotation range	Imaging rotation increment
IIA-1	F-2	8	IIA	28.2	0° - 360°	5°
I-1	F-1	7.4	I	26.4	0° - 360°	5°
I-2	F-3	3.6	I	29.7	0° - 360°	10°

Table 3-6. Summary of the standard phase mask FBG imaging experiments.

3.4.1 Type IIA

As will be discussed in section 4.2.2, sample IIA-1 exhibited clear type IIA growth characteristics. A strong transmission dip was observed at λ_B and small dips were observed in the region of $2/3 \lambda_B$, as shown in Figure 4-5. The images in Figure 3-12(a) and (b) were recorded at orthogonal fibre orientations and were identified as having been recorded in the planes corresponding to perpendicular (0°) and parallel (90°) to the writing beam, respectively. The non-exposed fibre image in Figure 3-12(c) was subtracted from cropped regions of each of the images in Figure 3-12(a) and (b), to produce the images shown in Figure 3-12(d) and (e), respectively.

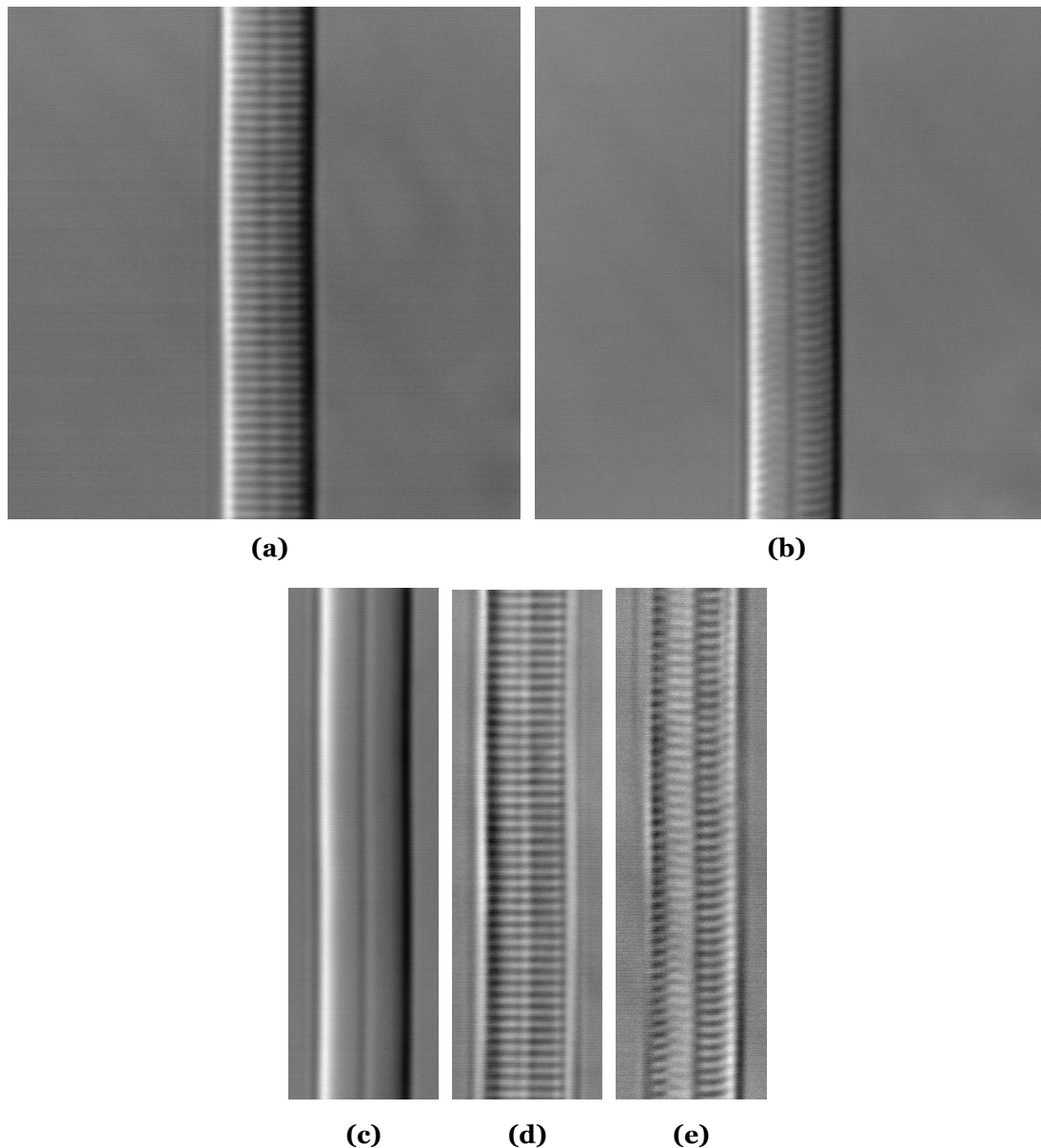


Figure 3-12. DIC images of a type IIA FBG written with a standard phase mask: sample IIA-1 recorded at fibre orientations **(a)** Image 1: 0° and **(b)** Image 2: 90° . The dimensions of each image are approximately $47 \times 47 \mu\text{m}$. **(c)** DIC image of sample IIA-1 recorded in a non-exposed region of fibre. **(d)** Result of Image 1 after subtraction of non-exposed fibre image in **(c)**; **(e)** result of Image 2 after subtraction of non-exposed fibre image in **(c)**. The images in **(c)** to **(e)** are approximately $47 \times 14 \mu\text{m}$.

The refractive index dip in the centre of the fibre core (as discussed in section 3.2.3) is clearly visible in Figure 3-12(a) and (b). If the refractive index dip is ignored, the refractive index variations along the fibre in Figure 3-12(a) and the corresponding processed image in Figure 3-12(d) are distributed uniformly across the core. As discussed in section 3.2.3, this structure is consistent with the assertion that the image was recorded at a fibre orientation corresponding to perpendicular to the direction of the UV beam during

fabrication. The refractive index structure in the images in Figure 3-12(b) and (e), however, reveals a complex refractive index structure that is expected for an image recorded at a fibre orientation corresponding to parallel to the direction of the UV beam during fabrication. The images in Figure 3-12 provide clear evidence of an orthogonally distinguishable refractive index structure, as expected for gratings written with a phase mask.

The linescans in Figure 3-13(a) and (b) were taken along the fibre axis from the perpendicular image in Figure 3-12(d) and averaged over the two adjacent $30 \times 2 \mu\text{m}$ regions illustrated on the right of the figure. As can be seen in the linescans, the periodic features on either side of the core are in phase, which was verified by the approximately 0 radian phase shift determined by fitting the data with the function in Equation 3-6.

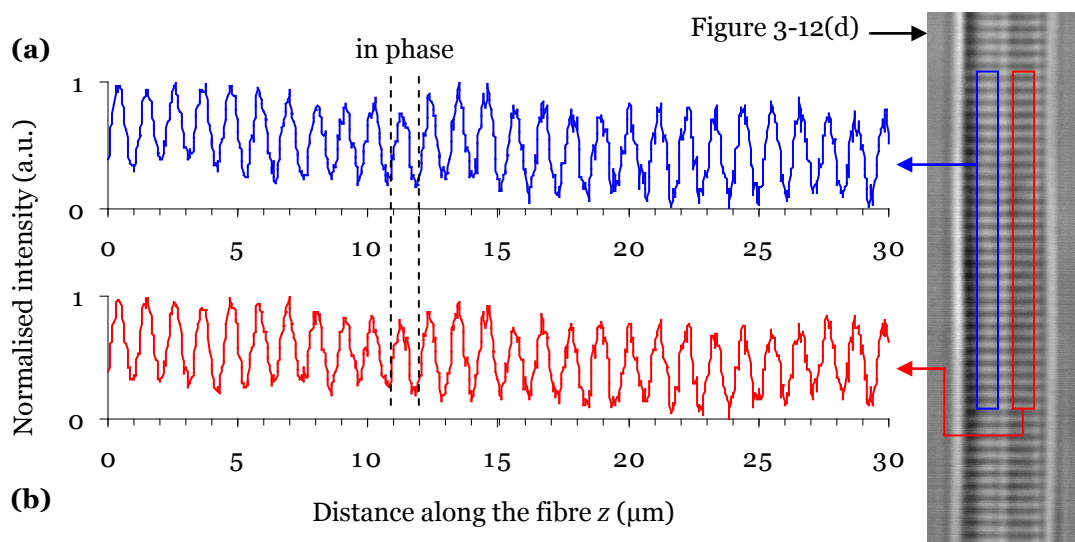


Figure 3-13. Analysis of perpendicular image features of a type II-A FBG: normalised average of linescans along the fibre axis from the DIC image of sample IIA-1 in Figure 3-12(d), taken from two adjacent regions as illustrated: **(a)** the left side of the core and **(b)** the right side of the core.

The linescans in Figure 3-14(a) and (b) were taken along the fibre axis from the parallel image in Figure 3-12(e) and averaged over the two adjacent $30 \times 2 \mu\text{m}$ regions illustrated on the right of the figure. As can be seen in Figure 3-14, the periodic features on either side of the core are out of phase by approximately half a period, i.e. π radians. The phase shift was determined as $(1.02 \pm 0.02)\pi$ radians by fitting the data with the function in Equation 3-6.

The average period of each of the four linescans in Figure 3-13 and Figure 3-14(a) to (b) was determined (by fitting with Equation 3-6) to be $1.09 \pm 0.05 \mu\text{m}$, which is in excellent agreement with the known period of the phase mask used in fabrication, $1.0668 \mu\text{m}$.

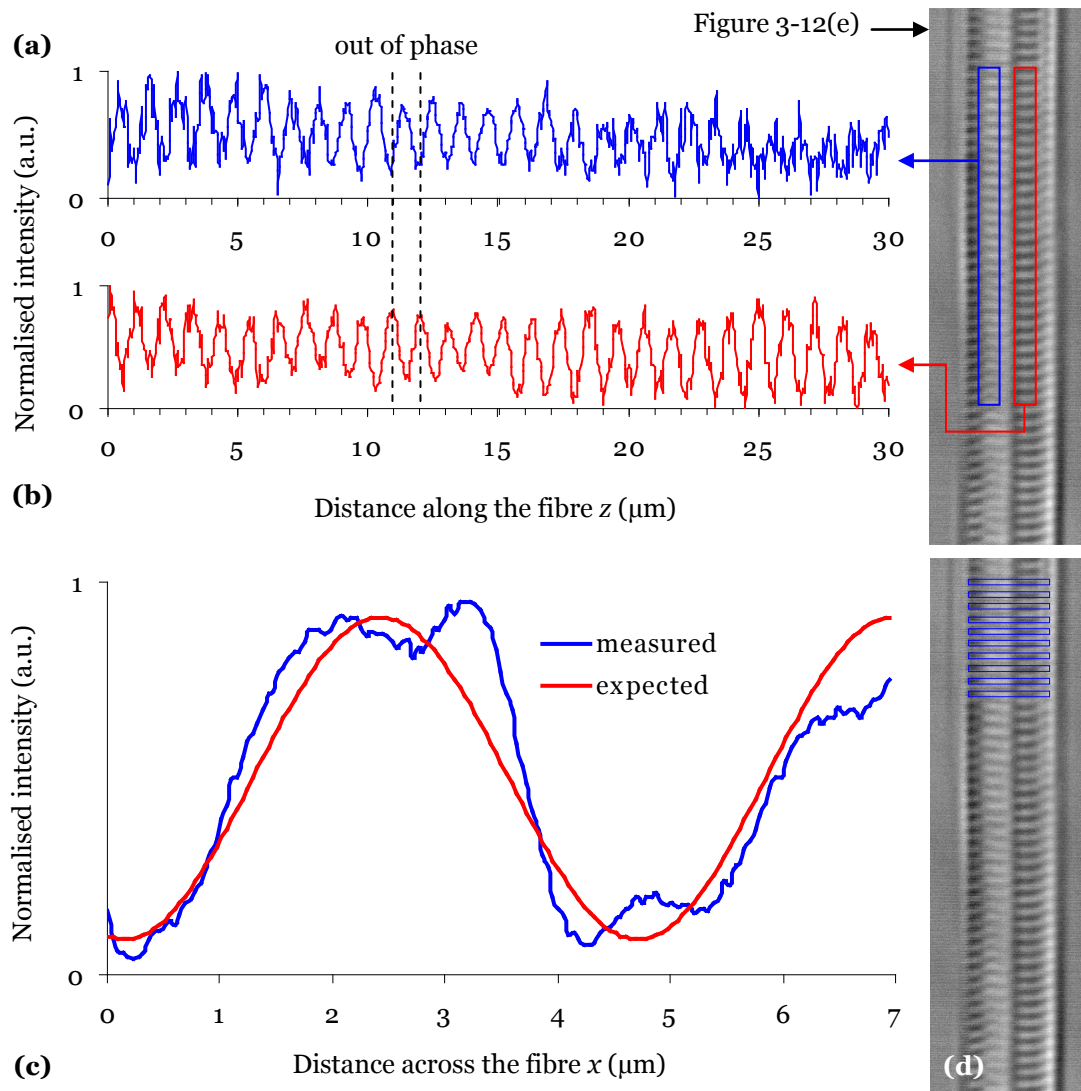


Figure 3-14. Analysis of parallel image features of a type II-A FBG: normalised average of linescans along the fibre axis from the DIC image of sample IIA-1 in Figure 3-12(e), taken from two adjacent positions as illustrated; **(a)** the left side of the core and **(b)** the right side of the core. **(c)** Comparison between the expected and measured Talbot profiles from linescans averaged over the ten regions in Figure 3-12(e) as illustrated in **(d)**. Note: the apparent superposition of two frequency components in **(c)** is likely to have resulted from misalignments during subtraction of the background image.

In order to analyse the Talbot length of the pattern extending across the core, linescans were taken across the fibre axis from the parallel image in Figure 3-12(e) and averaged over the ten $0.5 \times 7 \mu\text{m}$ regions illustrated in Figure

3-14(d). Ideally the subtraction of the non-exposed fibre image would remove the refractive index dip in the centre of the fibre and result in smooth, sinusoidal linescans; however this was difficult to achieve in practice, possibly due to slight misalignments during image subtraction. Consequently, the centre refractive index dip is still present in the images and the linescans across the fibre core. A sinusoidal function given by Equation 3-6 with a period of $4.56 \mu\text{m}$ (the calculated Talbot length for the SM-2 phase mask) is shown in red for comparison with the measured data. The observed Talbot length is estimated as $4.6 \pm 0.5 \mu\text{m}$ and, clearly, is in excellent agreement with the Talbot length expected for beating between the $\pm 1^{\text{st}}$ and $\pm 2^{\text{nd}}$ orders of the SM-2 phase mask, as detailed in Table 3-2.

3.4.2 Standard telecommunications fibre

Sample I-1 exhibited clear type I growth characteristics, as will be discussed in section 4.3.3. A strong transmission dip was observed at λ_B and smaller dips were observed in the region of $2/3 \lambda_B$ as shown in Figure 4-8(a) and (b), respectively. The DIC images in Figure 3-15(a) and (b) were recorded at orthogonal fibre orientations and were identified as having been recorded in the planes corresponding to perpendicular (0°) and parallel (90°) to the writing beam, respectively. The image in Figure 3-15(a), clearly exhibits a grating which is written uniformly across the core as expected for the image plane perpendicular to the writing beam. The image in Figure 3-15(b) shows evidence of a Talbot diffraction pattern which is consistent with the image plane parallel to the writing beam. The non-exposed fibre image in Figure 3-15(c) was subtracted from cropped regions of each of the images in Figure 3-15(a) and (b); the resulting images are shown in Figure 3-15(d) and (e), respectively.

The refractive index variations in the DIC image in Figure 3-15(a) and the corresponding processed image in Figure 3-15(d) are distributed uniformly across the core. As discussed in section 3.2.3, this structure is consistent with the assertion that the image was recorded at a fibre orientation corresponding to perpendicular to direction of the UV beam during fabrication. The

refractive index structure in the images in Figure 3-15(b) and (e), however, reveals a complex refractive index structure that is expected for an image recorded at a fibre orientation corresponding to parallel to direction of the UV beam during fabrication. The images in Figure 3-15 provide clear evidence of an orthogonally distinguishable refractive index structure, as expected for gratings written with a phase mask.

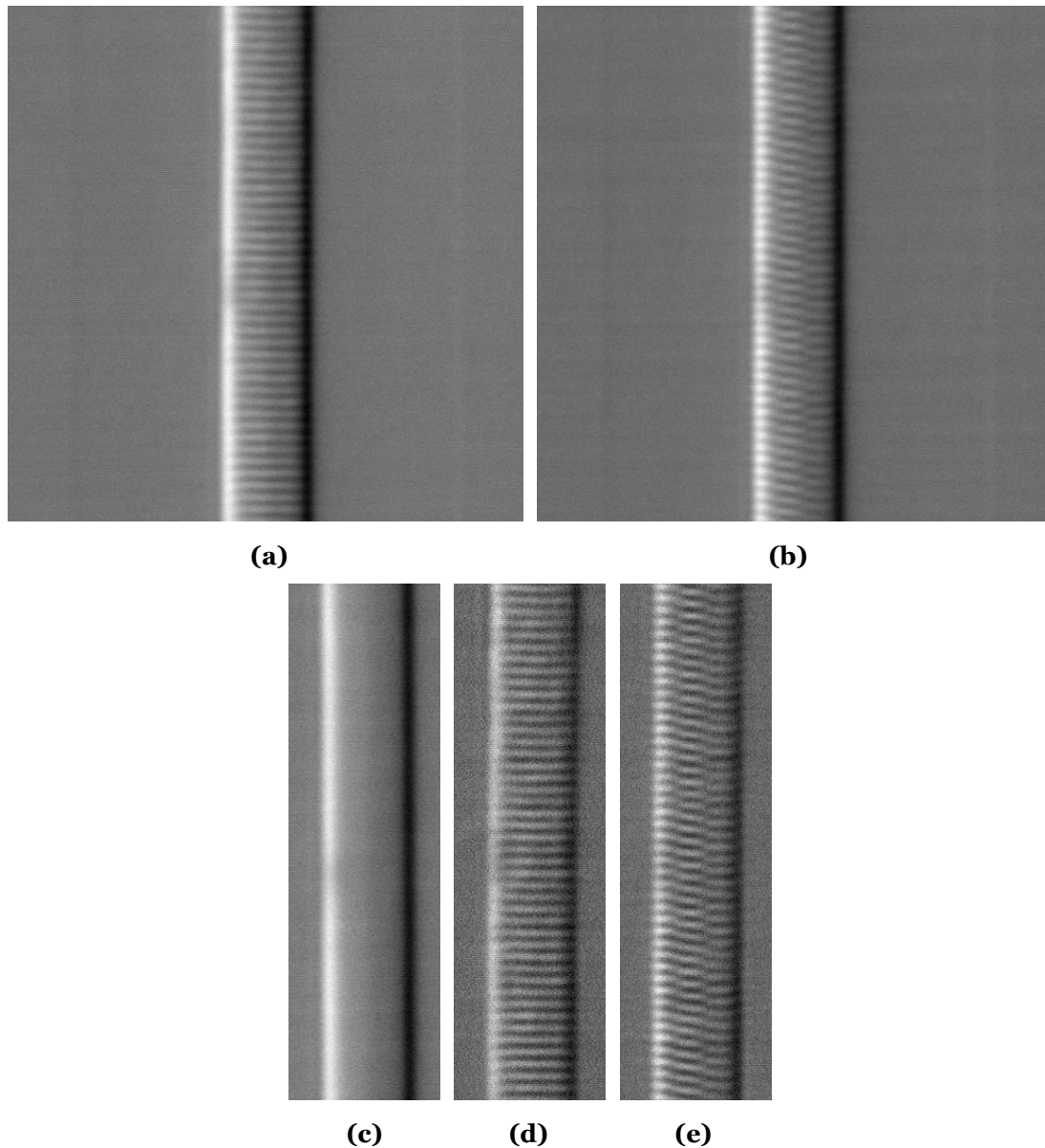


Figure 3-15. DIC images of a type I FBG written with a standard phase mask in standard fibre: sample I-1 recorded at fibre orientations **(a)** Image 1: 0° and **(b)** Image 2: 90° . The dimensions of each image are approximately $47 \times 47 \mu\text{m}$. **(c)** DIC image of sample I-1 recorded in a non-exposed region of fibre. **(d)** Result of Image 1 after subtraction of non-exposed fibre image in (c); **(e)** result of Image 2 after subtraction of non-exposed fibre image in (c). The images in (c) to (e) are approximately $47 \times 14 \mu\text{m}$.

The linescans in Figure 3-16(a) and (b) were taken along the fibre axis from the perpendicular image in Figure 3-15(d) and averaged over the two adjacent $30 \times 2 \mu\text{m}$ regions illustrated on the right of the figure. It can be seen that the periodic features on either side of the core are in phase, which was verified with a negligible phase shift of 0.02π radians, as determined by fitting the data with the function in Equation 3-6.

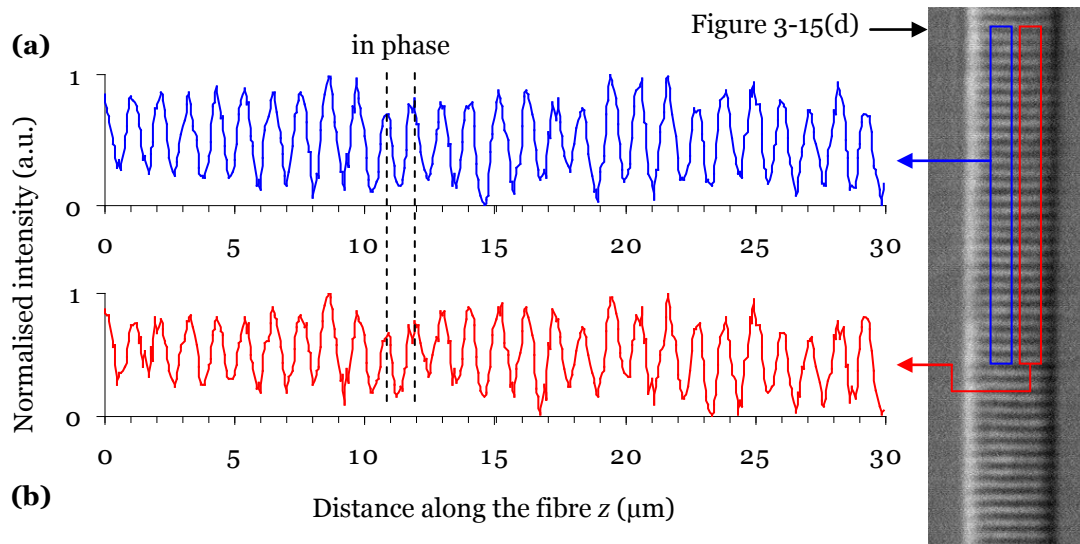


Figure 3-16. Analysis of perpendicular image features of a type I FBG: normalised average of linescans along the fibre axis from the DIC image of sample I-1 in Figure 3-15(d), taken from two adjacent regions as illustrated: **(a)** the left side of the core and **(b)** the right side of the core.

The linescans in Figure 3-17(a) and (b) were taken along the fibre axis from the parallel image in Figure 3-15(e) and averaged over the two adjacent $30 \times 2 \mu\text{m}$ regions illustrated on the right of the figure. It can be seen that the periodic features in both regions are out of phase by approximately half a period, i.e. π radians. The phase shift was determined as $(1.0 \pm 0.1)\pi$ radians by fitting the data with the function in Equation 3-6. The period of each of the four linescans in Figure 3-16 and Figure 3-17(a) to (b) was determined to be $1.08 \pm 0.05 \mu\text{m}$, which is in excellent agreement with the period of the phase mask used in fabrication, $1.0668 \mu\text{m}$.

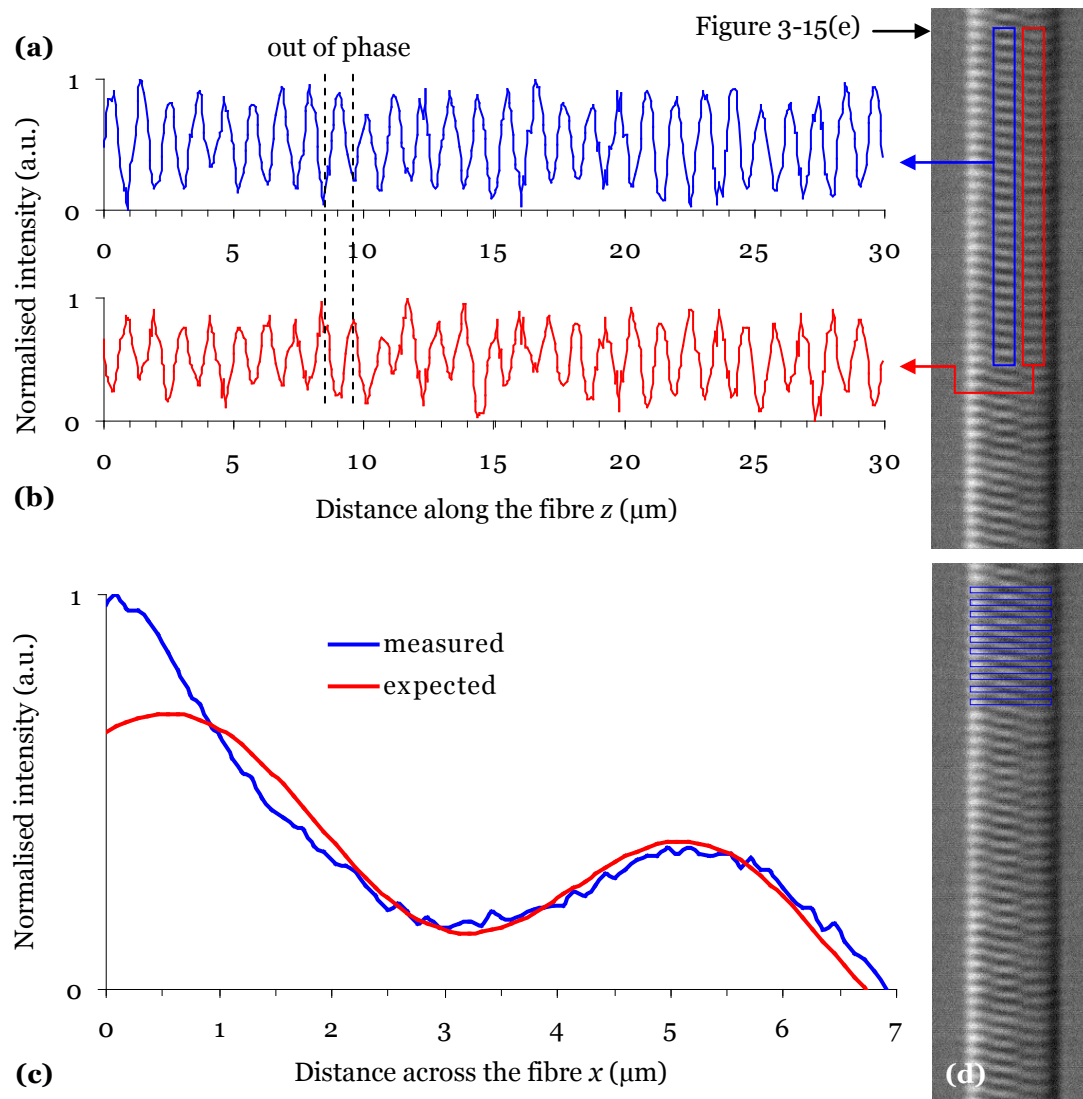


Figure 3-17. Analysis of parallel image features of a type I FBG: normalised average of linescans along the fibre axis from the DIC image of sample I-1 in Figure 3-15(e), taken from two adjacent positions as illustrated: **(a)** centre of the core and **(b)** the right side of the core. **(c)** Comparison between the expected and measured Talbot profiles from linescans averaged over the ten regions in Figure 3-15(e) as illustrated in **(d)**.

In order to analyse the Talbot length of the pattern extending across the core of sample I-1, linescans were taken across the fibre axis from the parallel image in Figure 3-15(e) and averaged over the ten $0.5 \times 7 \mu\text{m}$ regions illustrated in Figure 3-17(d). The linescans were then normalised and averaged to provide the data shown in blue in Figure 3-17(c). The apparent tilt in the measured data is due to a residual intensity gradient which is likely to have resulted from slight differences in imaging conditions during measurement of the FBG image and the background image which was subtracted. A sinusoidal function with a negative linear gradient

corresponding to the intensity gradient has been plotted in red for comparison with the data in Figure 3-17(c). The tilted sinusoidal function with a period equal to the expected Talbot length of $4.56\ \mu\text{m}$ compares well with the data. The data shows a period ($\sim 5\ \mu\text{m}$) which is slightly longer than the expected Talbot length; this is likely to have arisen from a difficulty distinguishing the Talbot patterns from the large intensity differences at the edges of the core. Considering this source of error, the measured Talbot length is in qualitative agreement with the expected $4.56\ \mu\text{m}$ for beating between the $\pm 1^{\text{st}}$ and $\pm 2^{\text{nd}}$ orders of the SM-2 phase mask, as detailed in Table 3-2.

3.4.3 Smaller core fibre

Sample I-2 exhibited clear type I growth characteristics and strong transmission dips at both λ_B and $2/3\ \lambda_B$ as will be shown in Figure 4-8(e) and (f), respectively. The images in Figure 3-18(a) and (b) were recorded at orthogonal fibre orientations and were identified as having been recorded in the planes corresponding to perpendicular (0°) and parallel (90°) to the writing beam, respectively, using the reasoning described in section 3.2.3. The image in Figure 3-18(a), clearly exhibits a grating which is written uniformly across the core as expected for the image plane perpendicular to the writing beam. The image in Figure 3-18(b) shows evidence of a Talbot diffraction pattern which is consistent with the image plane parallel to the writing beam. The non-exposed fibre image in Figure 3-18(c) was subtracted from cropped regions of each of the images in Figure 3-18(a) and (b); the resulting images are shown in Figure 3-18(d) and (e), respectively.

The refractive index variations in the DIC image in Figure 3-18(a) and the corresponding processed image in Figure 3-18(d) are distributed uniformly across the core with evidence of a slight tilt in the grating planes. The apparent non-uniformity of the grating planes at the edges of the core in Figure 3-18(d) is likely to be the result of misalignment during image subtraction. As discussed in section 3.2.3, the imaged structure is consistent with a fibre orientation corresponding to perpendicular to direction of the UV beam during fabrication. The refractive index structure in the images in Figure

3-18(b) and (e), however, reveals a complex refractive index structure that is expected for an image recorded at a fibre orientation corresponding to parallel to direction of the UV beam during fabrication. The images in Figure 3-18 provide clear evidence of an orthogonally distinguishable refractive index structure, as expected for gratings written with a phase mask.

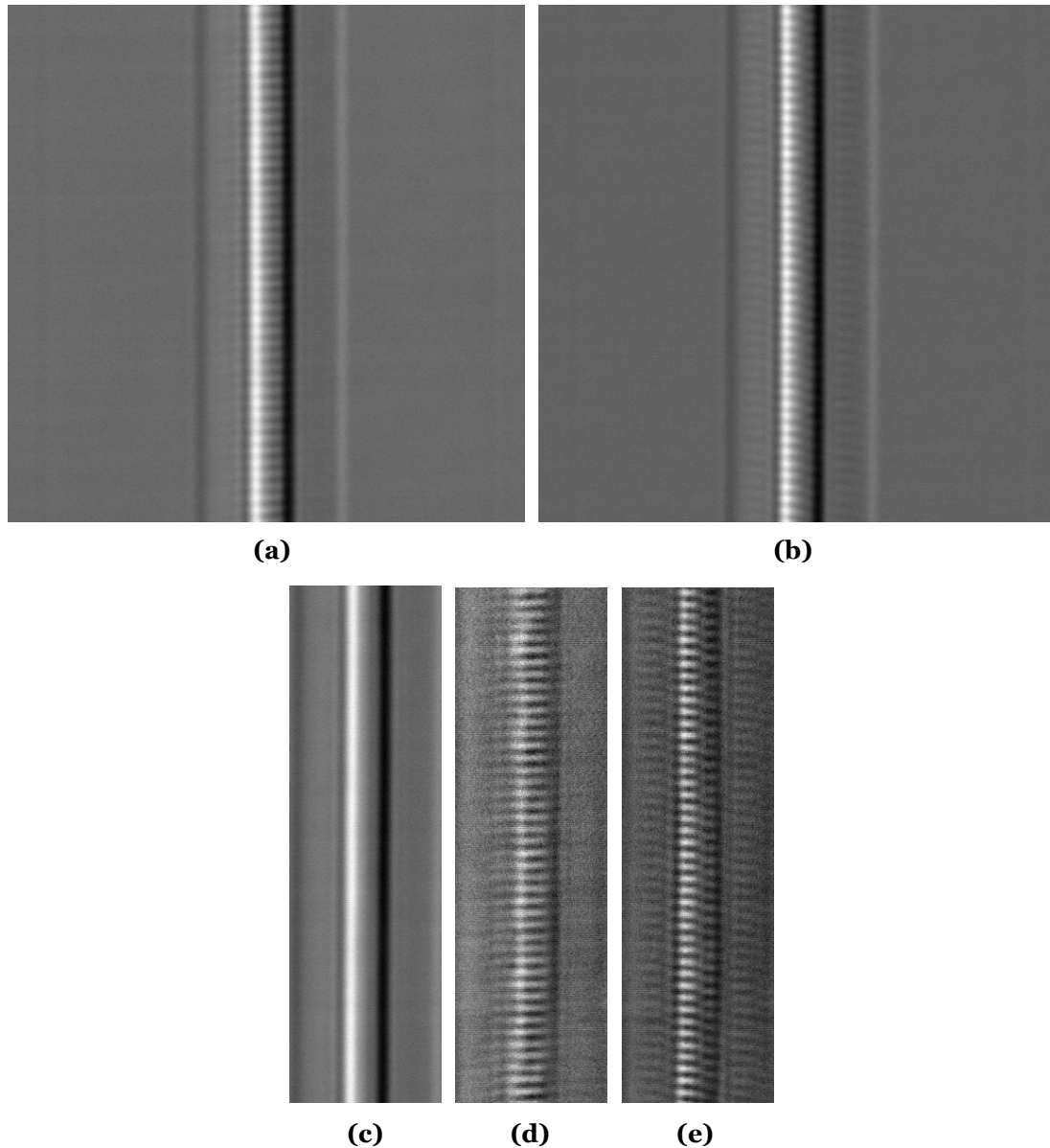


Figure 3-18. DIC images of a type I FBG written with a standard phase mask in small-core fibre: sample I-2 recorded at fibre orientations **(a)** Image 1: 0° and **(b)** Image 2: 90° . The dimensions of each image are approximately $47 \times 47 \mu\text{m}$. **(c)** DIC image of sample I-2 recorded in a non-exposed region of fibre. **(d)** Result of Image 1 after subtraction of non-exposed fibre image in (c); **(e)** result of Image 2 after subtraction of non-exposed fibre image in (c). The images in (c) to (e) are approximately $47 \times 14 \mu\text{m}$.

Refractive index perturbations are evident in the depressed cladding on either side of the central core region in Figure 3-18(b) and more clearly in Figure 3-18(e). As discussed in section 3.2.3, the depressed cladding region either side of the core of fibre F-3 was most likely formed by introducing fluorine or boron during fabrication to lower the refractive index. The weak perturbations evident either side of the core of sample I-2 are expected to be due to UV-induced refractive index changes as a result of low concentrations of germanium or the presence of fluorine/boron in the depressed cladding region [85]. Photosensitivity in depressed claddings has been previously reported to lower cladding mode losses [85, 114, 115]. Whatever the dopants are in the depressed cladding region of fibre F-3, the core region must be more photosensitive; giving rise to higher refractive index changes which are apparent from the larger intensity perturbations measured in the core region of the DIC images than in the depressed cladding.

The linescans in Figure 3-19(a) and (b) were taken along the fibre axis from the perpendicular image in Figure 3-18(d) and averaged over the two adjacent $30 \times 1 \mu\text{m}$ regions illustrated on the right of the figure. It can be seen that the periodic features on either side of the core are in phase, which was verified with a negligible phase shift of 0.04π radians, as determined by fitting the data with the function in Equation 3-6.

The linescans in Figure 3-20(a) and (b) were taken along the fibre axis from the parallel image in Figure 3-18(e) and averaged over the two adjacent $30 \times 1 \mu\text{m}$ regions illustrated on the right of the figure. It can be seen that the periodic features in both regions are out of phase by approximately half a period, i.e. π radians. The phase shift was determined as $(1.0 \pm 0.1)\pi$ radians by fitting the data with the function in Equation 3-6. The periods of the four linescans in Figure 3-19 and Figure 3-20(a) to (b) were determined to be $1.09 \pm 0.05 \mu\text{m}$, which is in excellent agreement with the period of the phase mask used in fabrication, $1.0668 \mu\text{m}$.

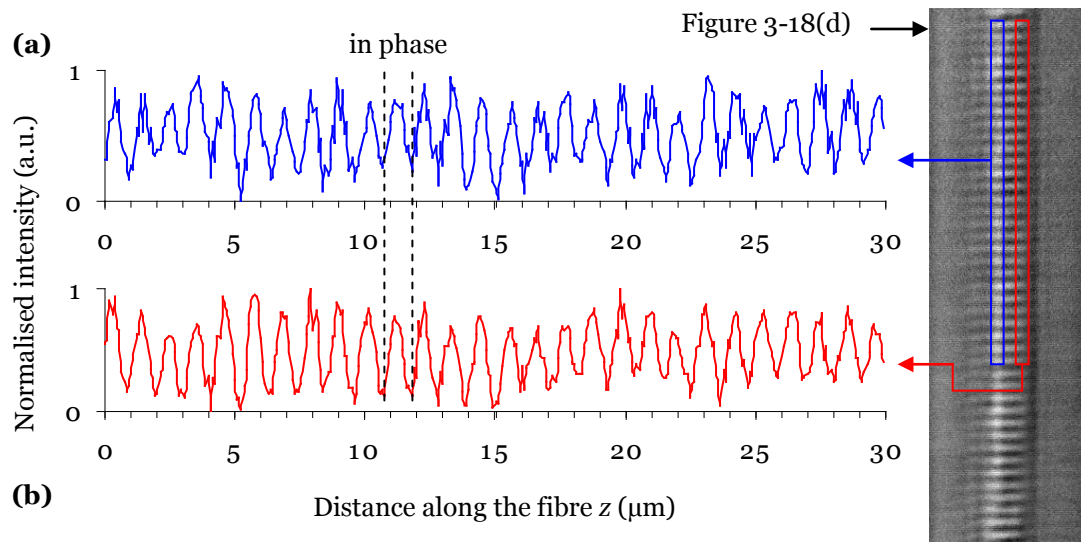


Figure 3-19. Analysis of perpendicular image features of a type I FBG: normalised average of linescans along the fibre axis from the DIC image of sample I-2 in Figure 3-18(d), taken from two adjacent regions as illustrated: **(a)** the left side of the core and **(b)** the right side of the core.

Fibre F-3 has a core diameter of $3.6 \mu\text{m}$, which prevents the measurement of a full period of the expected Talbot length of $4.56 \mu\text{m}$. Consequently, linescans were averaged over the ten regions illustrated in Figure 3-20(d), which each cover approximately $0.4 \times 12 \mu\text{m}$ to include the core and depressed cladding regions. The linescans were then averaged and normalised to provide the profile (blue) in Figure 3-20(c). The large differences in measured intensities due to the index perturbations in the core and depressed cladding regions also make it difficult to measure the Talbot length. The maximum and minimum intensities occurring at approximately $4.5 \mu\text{m}$ and $7 \mu\text{m}$, respectively, in the blue plot in Figure 3-20(c) are very different to the intensity levels observed in the cladding due to the higher UV-induced refractive index perturbations in the more photosensitive core. The intensity dip at approximately $8.6 \mu\text{m}$ is due to the ridge running down the right hand side of the core in Figure 3-18(e) which is likely to be the result of a misalignment during the subtraction of the non-exposed fibre image. The subtraction process involves a pixel by pixel subtraction of the intensity values and consequently small deviations from parallel alignment between the fibres in the two images can have a significant impact on the resulting image.

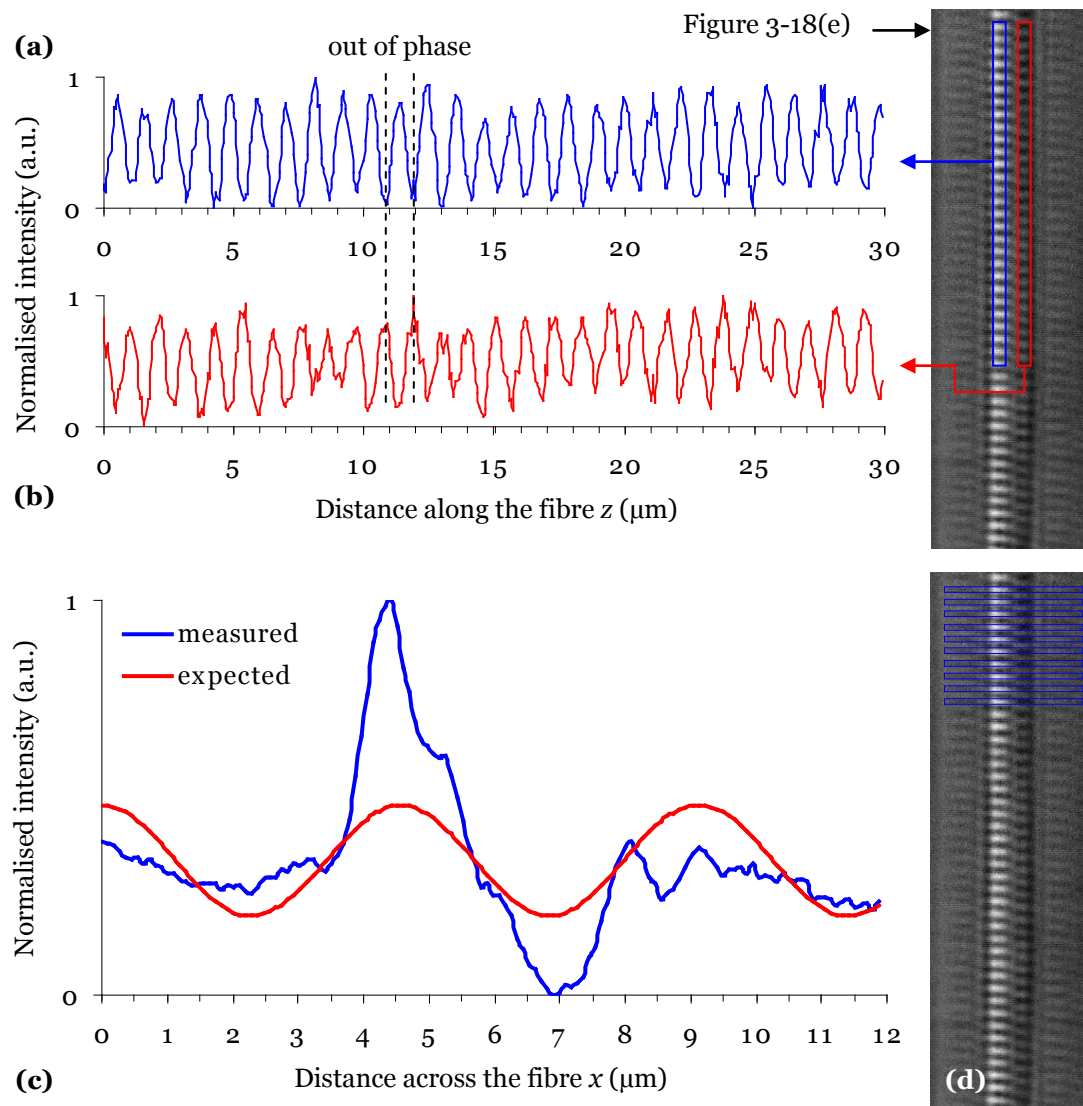


Figure 3-20. Analysis of parallel image features of a type I FBG: normalised average of linescans along the fibre axis from the DIC image of sample I-2 in Figure 3-18(e), taken from two adjacent positions as illustrated: **(a)** the left side of the core and **(b)** the right side of the core. **(c)** Comparison between the expected and measured Talbot profiles from linescans averaged over the ten regions in Figure 3-18(e) as illustrated in **(d)**.

Despite the large differences between the detected intensity levels of the refractive index perturbations in the core compared with those in the depressed cladding regions, the interleaving fringes of bright and dark regions can be seen to extend across the fibre in Figure 3-18(e). The sinusoidal function with a period equal to the expected Talbot length of $4.56 \mu\text{m}$ (shown in red) compares well with the period of the data in Figure 3-20(c). The observed Talbot length is estimated as $4.6 \pm 0.5 \mu\text{m}$ indicating that the observed refractive index patterns are likely to have formed as a result of

beating between the $\pm 1^{\text{st}}$ and $\pm 2^{\text{nd}}$ orders of the SM-2 phase mask, as detailed in Table 3-2.

3.5 Custom-made phase mask FBGs

The following sections present the results and analysis of DIC imaging experiments for various fibre gratings produced with a custom-made phase mask under the fabrication conditions presented in Chapter 2 and whose spectral characteristics are detailed in Chapter 4. The samples were prepared and analysed using the same techniques that were used for the standard phase mask samples.

In order to investigate the effect of different relative intensities in the orders produced by the phase mask, samples were fabricated using custom-made phase mask CM-2 with the properties discussed in section 2.3.2. As detailed in Table 2-5, samples I-3 and I-4 were fabricated using mask CM-2 in the hydrogen loaded fibres F-1 and F-3, respectively, with total fluences of approximately 31 and 10 kJ/cm², respectively. Fibre F-1 is singlemode in the region of λ_B but multimode in the region of $2/3 \lambda_B$, whereas fibre F-3 is singlemode in both regions. The details of the samples and the imaging experiments are shown in Table 3-7.

Sample	Fibre	Core diameter (μm)	Type	Oil temperature (± 0.1 °C)	Imaging rotation range	Imaging rotation increment
I-3	F-1	7.4	I	26.4	0° - 360°	5°
I-4	F-3	3.6	I	29.7	0° - 360°	5°

Table 3-7. Summary of the standard phase mask FBG imaging experiments.

3.5.1 Standard telecommunications fibre

As will be discussed in section 4.3.4, sample I-3 exhibited clear type I growth characteristics. A strong transmission dip was observed at λ_B and smaller dips

were observed in the region of $2/3 \lambda_B$ as shown in Figure 4-9(a) and (b), respectively.

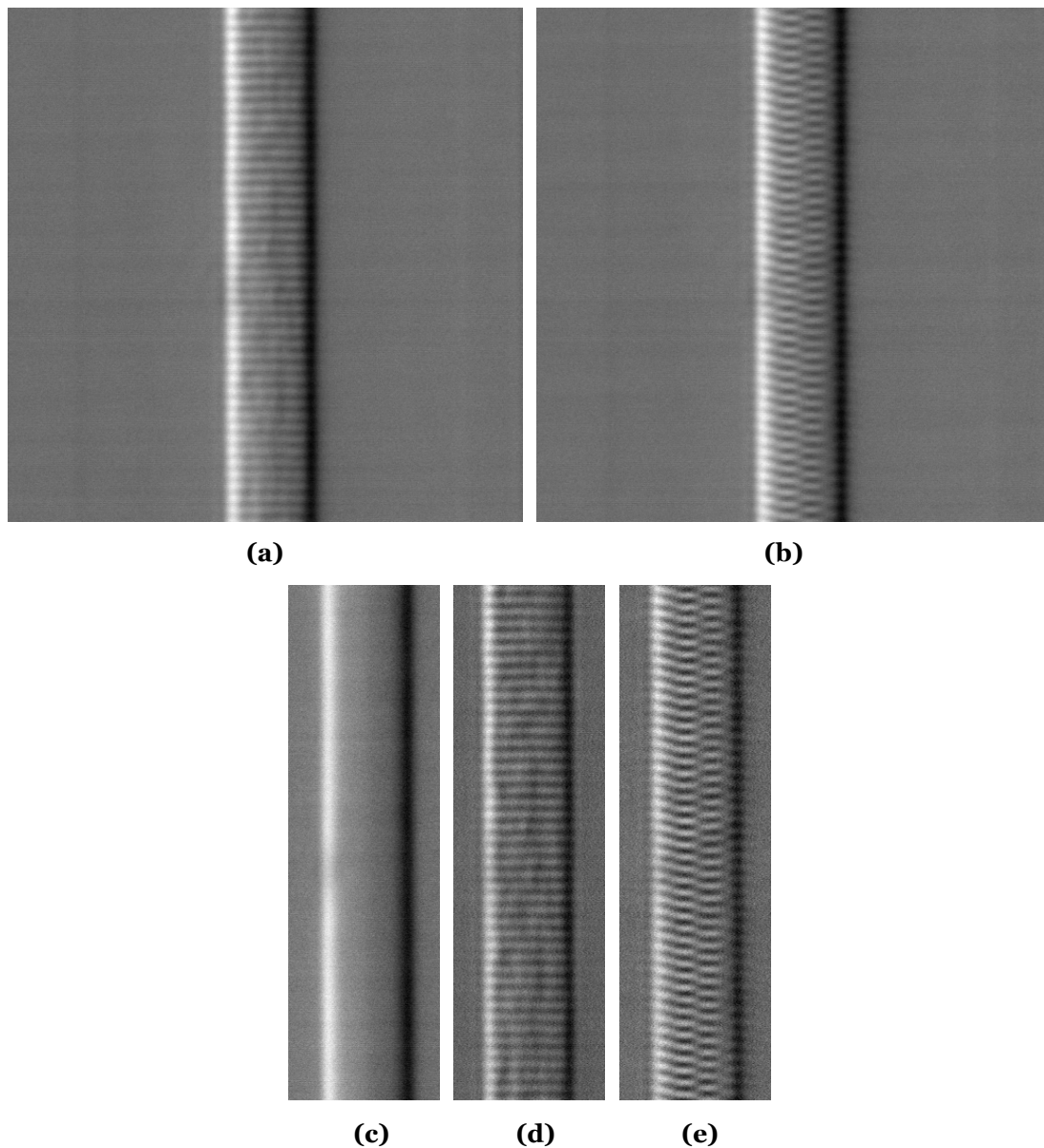


Figure 3-21. DIC images of a type I FBG written with a custom-made phase mask in standard fibre: sample I-3 recorded at fibre orientations **(a)** Image 1: 0° and **(b)** Image 2: 90° . The dimensions of each image are approximately $47 \times 47 \mu\text{m}$. **(c)** DIC image of sample I-3 recorded in a non-exposed region of fibre. **(d)** Result of Image 1 after subtraction of non-exposed fibre image in (c); **(e)** result of Image 2 after subtraction of non-exposed fibre image in (c). The images in (c) to (e) are approximately $47 \times 14 \mu\text{m}$.

The DIC images in Figure 3-21(a) and (b) were recorded at orthogonal fibre orientations and were identified as having been recorded in the planes corresponding to perpendicular (0°) and parallel (90°) to the writing beam, respectively. The image in Figure 3-21(a), clearly exhibits a grating which is

written uniformly across the core, as expected for the image plane perpendicular to the writing beam. The image in Figure 3-21(b) shows evidence of a Talbot diffraction pattern which is consistent with the image plane parallel to the writing beam. The non-exposed fibre image in Figure 3-21(c) was subtracted from each of the images in Figure 3-21(a) and (b); the resulting images are shown in Figure 3-21(d) and (e), respectively. The images in Figure 3-21 provide clear evidence of an orthogonally distinguishable refractive index structure in the core of sample I-3, as expected for gratings written with a phase mask.

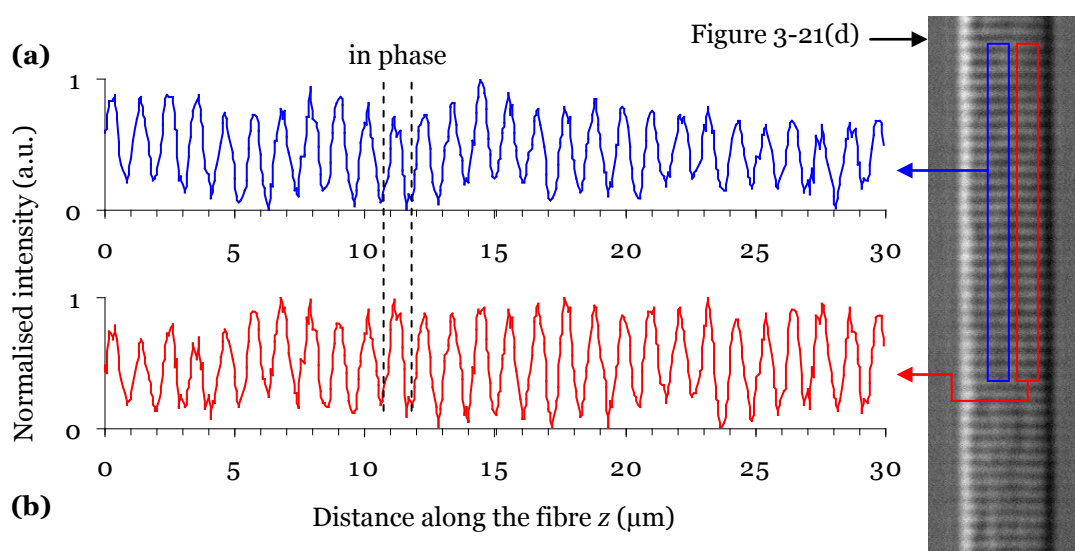


Figure 3-22. Analysis of perpendicular image features of a type I FBG: normalised average of linescans along the fibre axis from the DIC image of sample I-3 in Figure 3-21(d), taken from two adjacent regions as illustrated: **(a)** the left side of the core and **(b)** the right side of the core.

The linescans in Figure 3-22(a) and (b) were taken along the fibre axis from the perpendicular image in Figure 3-21(d) and averaged over the two adjacent $30 \times 2 \mu\text{m}$ regions illustrated on the right of the figure. As can be seen in the linescans, the periodic features on either side of the core are in phase, which was verified with a negligible phase shift of $(0.00 \pm 0.01)\pi$ radians as determined by fitting the data with the function in Equation 3-6.

The linescans in Figure 3-23(a) and (b) were taken along the fibre axis from the parallel image in Figure 3-21(e) and averaged over the two adjacent

$30 \times 2 \mu\text{m}$ regions illustrated on the right of the figure. As can be seen in Figure 3-23, the periodic features in both regions are out of phase by approximately half a period, i.e. π radians. The phase shift was determined as $(1.03 \pm 0.01)\pi$ radians by fitting the data with the function in Equation 3-6. The period of each of the four linescans in Figure 3-22 and Figure 3-23(a) to (b) was determined to be $1.09 \pm 0.05 \mu\text{m}$, which is in excellent agreement with the known period of the phase mask used in fabrication, $1.07 \mu\text{m}$.

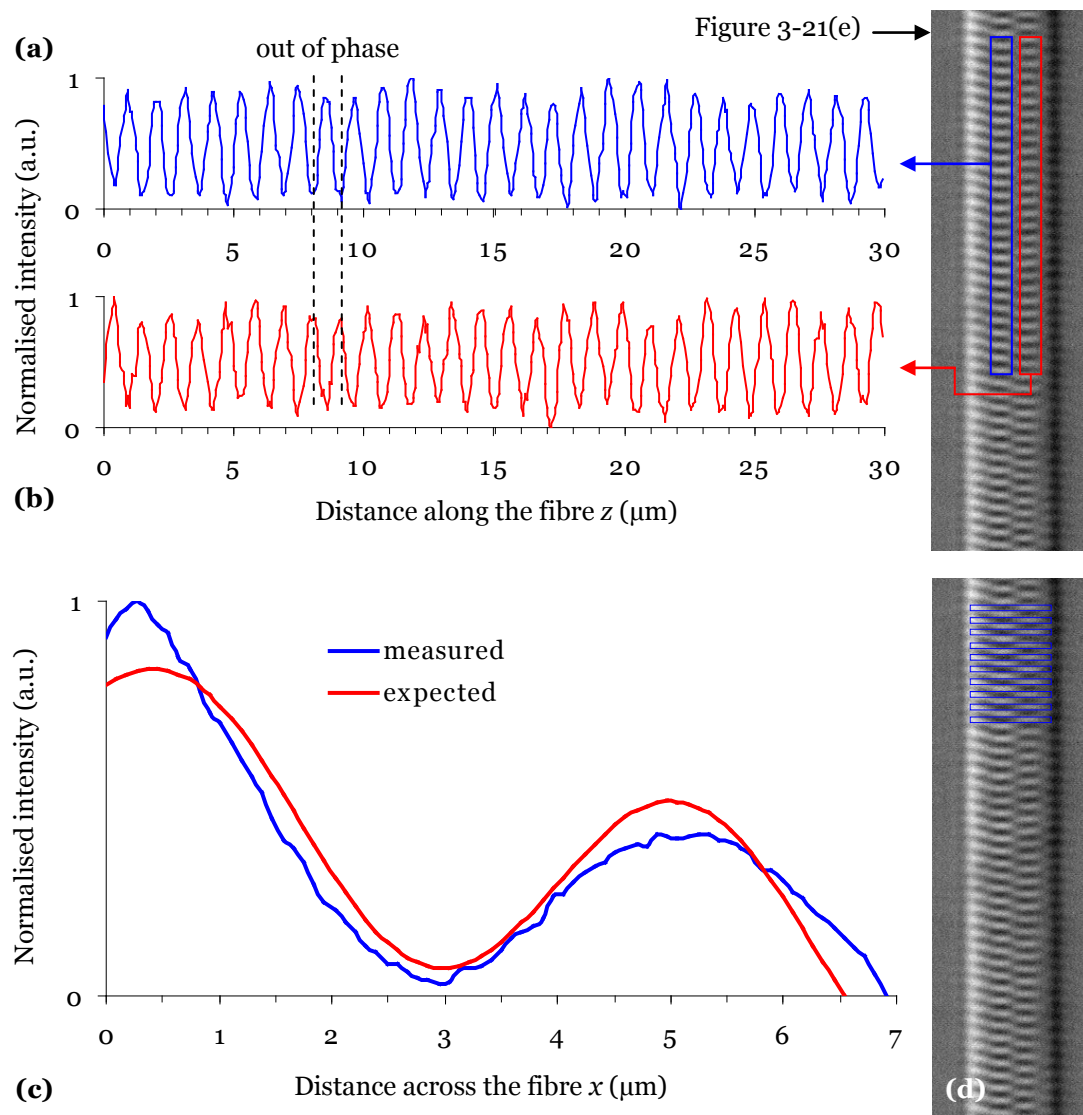


Figure 3-23. Analysis of parallel image features of a type I FBG: normalised average of linescans along the fibre axis from the DIC image of sample I-3 in Figure 3-21(e), taken from two adjacent positions as illustrated: **(a)** centre of the core and **(b)** the right side of the core. **(c)** Comparison between the expected and measured Talbot profiles from linescans averaged over the ten regions in Figure 3-21(e) as illustrated in **(d)**.

In order to analyse the Talbot length of the pattern extending across the core of sample I-3, linescans were averaged over the ten regions illustrated in Figure 3-23(d), which each covered approximately $0.5 \times 7 \mu\text{m}$. The linescans were then normalised and averaged to provide the blue plot in Figure 3-23(c). The apparent tilt in the data is possibly due to a residual intensity gradient as discussed previously. A sinusoidal function with a negative linear gradient corresponding to the intensity gradient has been plotted in red with the data in Figure 3-23(c) for comparison. The tilted sinusoidal function with a period equal to the expected Talbot length of $4.59 \mu\text{m}$ compares well with the data. However, the measured data shows period ($\sim 5 \mu\text{m}$) which is slightly longer than the expected Talbot length; likely to arise from a difficulty distinguishing the Talbot patterns from the large intensity differences at the edges of the core. Considering this source of error, the measured Talbot length is estimated as $4.6 \pm 0.5 \mu\text{m}$ indicating that the grating was formed as a result of beating between the $\pm 1^{\text{st}}$ and $\pm 2^{\text{nd}}$ orders of the CM-2 phase mask, as detailed in Table 3-2.

3.5.2 Smaller core fibre

Sample I-4 exhibited clear type I growth characteristics and strong transmission dips at both λ_B and $2/3 \lambda_B$ as will be shown in Figure 4-9(e) and (f), respectively. The DIC images in Figure 3-24(a) and (b) were recorded at orthogonal fibre orientations and were identified as having been recorded in the planes corresponding to perpendicular (0°) and parallel (90°) to the writing beam, respectively, using the reasoning described in section 3.2.3. The image in Figure 3-24(a), clearly exhibits a grating which is written uniformly across the core, as expected for the image plane perpendicular to the writing beam. The image in Figure 3-24(b) shows evidence of a Talbot diffraction pattern, which is consistent with the image plane parallel to the writing beam.

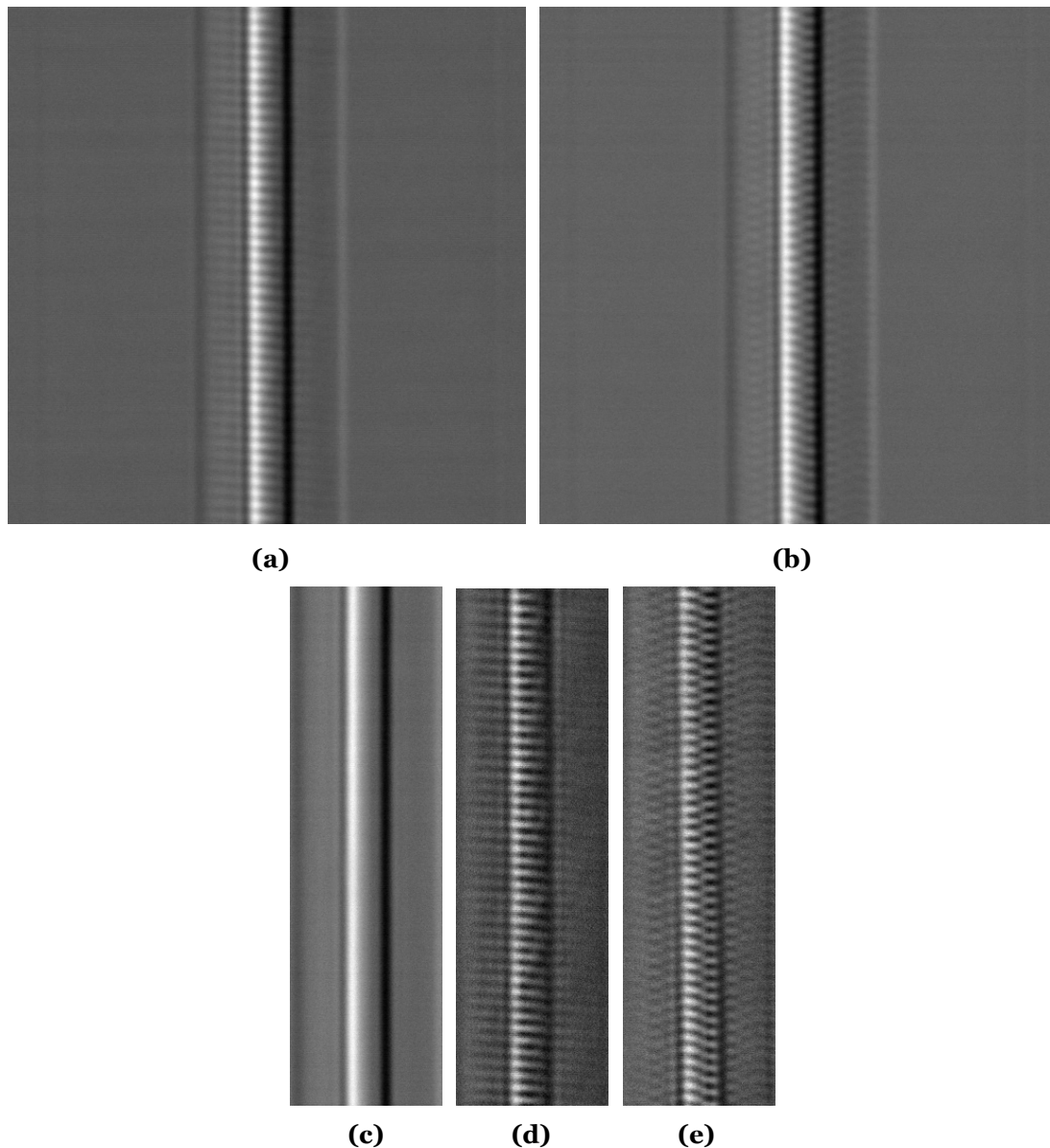


Figure 3-24. DIC images of a type I FBG written with a custom-made phase mask in small-core fibre: sample I-4 recorded at fibre orientations **(a)** Image 1: 0° and **(b)** Image 2: 90° . The dimensions of each image are approximately $47 \times 47 \mu\text{m}$. **(c)** DIC image of sample I-4 recorded in a non-exposed region of fibre. **(d)** Result of Image 1 after subtraction of non-exposed fibre image in (c); **(e)** result of Image 2 after subtraction of non-exposed fibre image in (c). The images in (c) to (e) are approximately $47 \times 14 \mu\text{m}$.

The non-exposed fibre image in Figure 3-24(c) was subtracted from each of the images in Figure 3-24(a) and (b); the resulting images are shown in Figure 3-24(d) and (e), respectively. The refractive index variations in the DIC image in Figure 3-24(a) and the corresponding processed image in Figure 3-24(d) are distributed uniformly across the core with evidence of a slight tilt in the grating planes. The grating tilt of approximately 3° is likely to be due to a slight rotational misalignment of the phase mask relative to the fibre during

fabrication. As discussed in section 3.2.3, the imaged structure is consistent with a fibre orientation corresponding to perpendicular to the direction of the UV beam during fabrication. The refractive index structure in the images in Figure 3-24(b) and (e), however, reveals a complex refractive index structure that is expected for an image recorded at a fibre orientation corresponding to parallel to direction of the UV beam during fabrication.

As was also observed for sample I-2 which was written in fibre F-3, refractive index perturbations are evident in the depressed cladding on either side of the central core region in Figure 3-24(b) and more clearly in Figure 3-24(e). As was discussed for sample I-2, the weak perturbations evident on either side of the core of sample I-4 are expected to be due to UV-induced refractive index changes as a result of low concentrations of germanium or the presence of fluorine/boron in the depressed cladding region. As was also observed for sample I-2, larger intensity perturbations were measured in the more photosensitive core region of sample I-4 than in the depressed cladding.

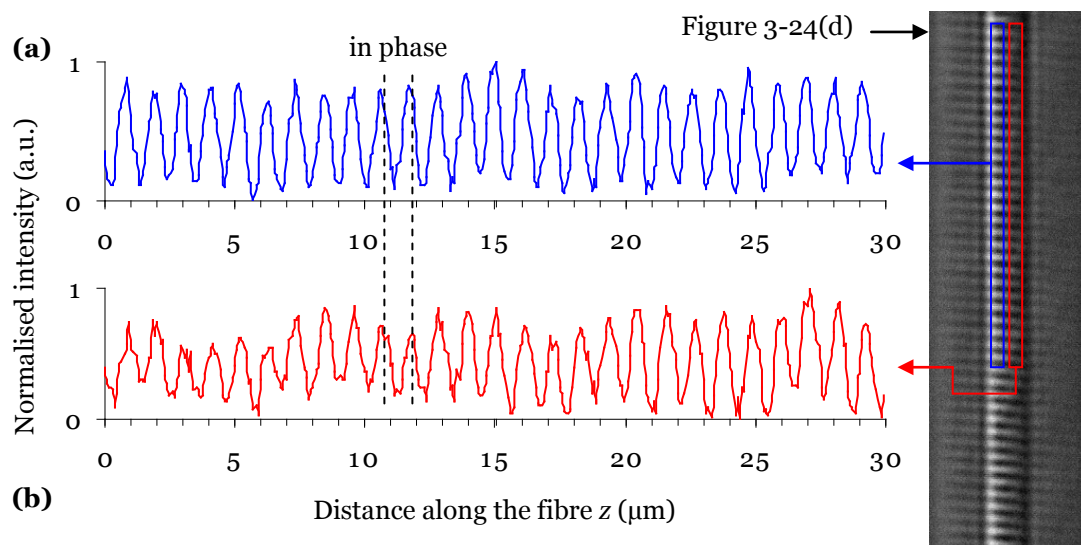


Figure 3-25. Analysis of perpendicular image features of a type I FBG: normalised average of linescans along the fibre axis from the DIC image of sample I-4 in Figure 3-24(d), taken from two adjacent regions as illustrated: **(a)** the left side of the core and **(b)** the right side of the core.

The linescans in Figure 3-25 were taken along the fibre axis from the image in Figure 3-24(d). The linescans were averaged over the two adjacent $30 \times 1 \mu\text{m}$

regions illustrated in Figure 3-25 and then normalised to the maximum and minimum intensity values. As can be seen in Figure 3-25, the periodic features in both regions are in phase, which was verified with a negligible phase shift of 0.01π radians as determined by fitting the data with the function in Equation 3-6.

The linescans in Figure 3-26 were taken along the fibre axis from the image in Figure 3-24(e). The linescans were averaged over the two adjacent $30 \times 1 \mu\text{m}$ regions illustrated in Figure 3-26 and then normalised to the maximum and minimum intensity values. As can be seen in Figure 3-26, the periodic features in both regions are out of phase by approximately half a period, i.e. π radians. The phase shift was determined as $(1.0 \pm 0.1)\pi$ radians by fitting the data with the function in Equation 3-6. The period of each of the four linescans in Figure 3-25 and Figure 3-26(a) to (b) was determined to be $1.09 \pm 0.05 \mu\text{m}$, which is in excellent agreement with the period of the phase mask used in fabrication, $1.07 \mu\text{m}$.

Fibre F-3 has a core diameter of $3.6 \mu\text{m}$ which prevents the measurement of a full period of the expected Talbot length of $4.59 \mu\text{m}$. As was done for previous samples, the linescans from the regions illustrated in Figure 3-26(d) were averaged and normalised to provide the plot in Figure 3-26(c). The large differences in measured intensities due to the index perturbations in the core and depressed cladding regions also make it difficult to measure the Talbot length. The maximum and minimum intensities occurring at approximately $4.5 \mu\text{m}$ and $6.9 \mu\text{m}$, respectively, are likely to be due to the higher UV-induced changes in the more photosensitive core. The intensity dip at approximately $10 \mu\text{m}$ is due to the dark ridge running down the right hand side of the core in Figure 3-24(e) which is likely to be the result of a misalignment during the subtraction of the non-exposed fibre image.

The sinusoidal function with a period equal to the expected Talbot length of $4.59 \mu\text{m}$ (shown in red) compares well with the data in Figure 3-26(c). However, the data shows a slightly longer period than the expected Talbot length which is likely to arise from a difficulty distinguishing the Talbot

patterns from the large intensity differences at the edges of the core. Considering this source of error, the measured Talbot length is estimated as $4.6 \pm 0.5 \mu\text{m}$ indicating that the grating was formed as a result of beating between the $\pm 1^{\text{st}}$ and $\pm 2^{\text{nd}}$ orders of the CM-2 phase mask, as detailed in Table 3-2.

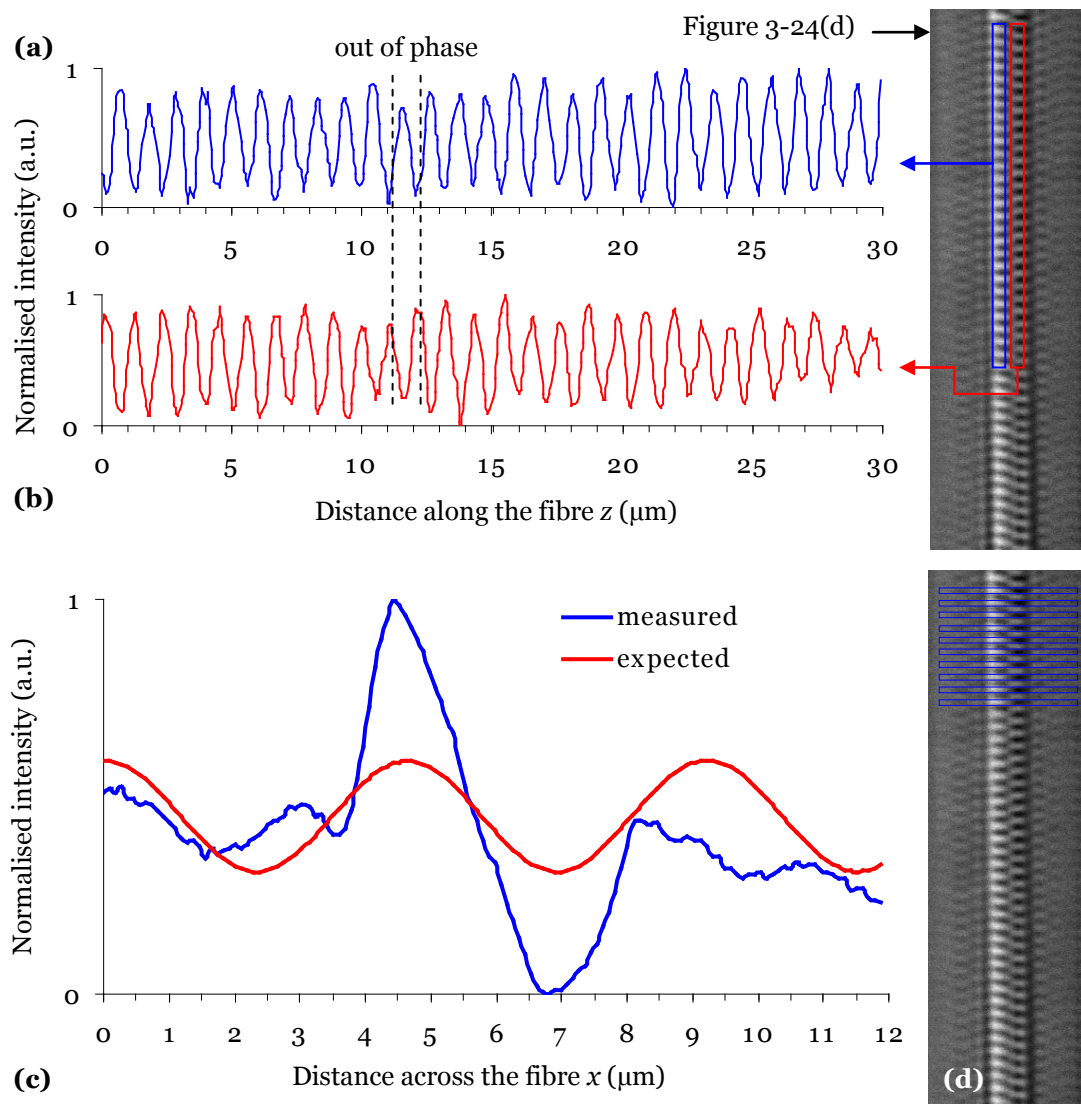


Figure 3-26. Analysis of parallel image features of a type I FBG: normalised average of linescans along the fibre axis from the DIC image of sample I-4 in Figure 3-24(e), taken from two adjacent positions as illustrated: **(a)** the left side of the core and **(b)** the right side of the core. **(c)** Comparison between the expected and measured Talbot profiles from linescans averaged over the ten regions in Figure 3-24(e) as illustrated in **(d)**.

3.6 Conclusions

The results of DIC imaging experiments performed on various FBG samples that were presented and analysed in this chapter are summarised in Table 3-8. The refractive index structure of the type I and IIA FBGs written with a prism interferometer (samples Ip-1 and IIAp-1) were imaged. The refractive index structure of phase-mask-written FBGs were also investigated, including a type IIA FBG (sample IIA-1). Additionally, type I FBGs (samples I-1 to I-4) fabricated in standard and smaller core fibres with the standard and custom-made phase masks were investigated.

Sample	Fibre	Core diameter (μm)	Type	Fabrication Details (mask pitch)	FBG period Λ ($\pm 0.05 \mu\text{m}$)	Parallel image phase shift (rad)	Talbot length Z_T ($\pm 0.5 \mu\text{m}$)
Ip-1	F-4	7.4	I	prism	2.50	-	-
IIAp-1	F-2	8	IIA		-	-	-
IIA-1	F-2	8	IIA	SM-2: 1.0668 μm	1.09	$(1.02 \pm 0.02) \pi$	4.6
I-1	F-1	7.4	I		1.08	$(1.0 \pm 0.1) \pi$	
I-2	F-3	3.6	I		1.09	$(1.0 \pm 0.1) \pi$	
I-3	F-1	7.4	I	CM-2: 1.07 μm	1.09	$(1.03 \pm 0.01) \pi$	4.6
I-4	F-3	3.6	I		1.09	$(1.0 \pm 0.1) \pi$	

Table 3-8. Summary of the imaging experiments and results.

The images of type I and IIA FBGs written with a prism interferometer were presented in sections 3.3.1 and 3.3.2, respectively. The expected structures for pure two-beam interference patterns could not be resolved in the images. The observed structures were complex but Talbot beating was not observed in the images. FFTs of features in the type I prism FBG images revealed much larger periods than the expected pitch of approximately $0.54 \mu\text{m}$ for two-beam interference. Three out of the six images presented for sample Ip-1 revealed grating features with a period of $2.50 \pm 0.05 \mu\text{m}$ which is inconsistent with the spectral results for the sample which demonstrated strong grating reflections at approximately 1541.7 nm. According to Equation 1-3 and assuming that $n_{\text{eff}} = 1.44$, light in the region of 1541.7 nm would not be reflected efficiently

from a grating period of $2.5 \mu\text{m}$. The observed features with a period of $2.5 \pm 0.05 \mu\text{m}$ are therefore likely to be an artefact. The prism-written fibre gratings are believed to possess a period closer to $0.54 \mu\text{m}$ which could not be resolved in the images due to the resolution limit of $0.58 \mu\text{m}$ of the microscope system. This limit did not prevent resolution of phase mask FBG features since the periods were around $1 \mu\text{m}$.

The images identified as having been measured in the parallel and perpendicular planes of the type I and type IIA FBGs written with either the standard or custom-made phase masks were presented in sections 3.4 and 3.5. The images recorded in the plane parallel to the direction of the UV writing beam all revealed index perturbations which were distributed uniformly across the core as expected. The images recorded in the perpendicular plane all revealed the existence of π phase-shifted gratings with a period consistent with the period of the phase mask used in fabrication. The measured Talbot lengths of the refractive index patterns extending across the core in the perpendicular images of the standard and custom-made phase mask FBGs were all consistent with the respective Talbot lengths expected for beating between the $\pm 1^{\text{st}}$ and $\pm 2^{\text{nd}}$ orders of each mask, as detailed in Table 3-2.

The imaged structures of the larger core FBGs written with the standard and custom phase masks, presented in sections 3.4.2 and 3.5.1, respectively, revealed full periods of the Talbot diffraction patterns in the core. However, the imaged structures of the smaller core FBGs written with the standard and custom phase masks, presented in sections 3.4.3 and 3.5.2, respectively, highlighted the size discrepancies between the core diameters and the expected Talbot lengths. The core diameter of the smaller core fibre prevents a full Talbot length from being formed across the core. This is expected to affect the spectral properties of FBGs written in this fibre, which will be investigated in Chapter 4.

Considering the differences in generated interference patterns and exposure fluences between the standard and custom made phase mask samples, it is difficult to compare the effect that each phase mask has on the images of the

resulting FBGs. Additionally, the measured intensity variations in the images were normalised for each sample and cannot be used to determine relative refractive index changes. While the intensity variations in the custom made phase mask images (samples I-3 and I-4) appear stronger than those in the standard phase mask images (samples I-1 and I-2), it is possible that this qualitative observation is due to the larger exposure fluences required to obtain high reflectances in the custom made phase mask samples. The effect of the higher order contributions of the custom made phase mask on the spectral properties of these FBGs will be investigated in Chapters 4 and 5.

Chapter 4:

Spectral Characterisation

This chapter investigates the effect of the phase mask and prism interferometer techniques on the spectral properties of the different types of gratings which were discussed in Chapters 2 and 3. The Bragg wavelength and other spectral regions are investigated where reflections are expected due to the complex refractive index structure.

The techniques used for obtaining optical spectra are described and the spectra of type I and IIA FBGs are then investigated and compared. The transmission spectra measured after fabrication of FBGs written using standard and custom-made phase mask techniques are compared in different spectral regions under multimode and singlemode propagation. The spectral consequences of the π phase-shifted gratings observed in the DIC images are then discussed and, finally, the spectral properties of prism interferometer FBGs are investigated.

4.1 Spectral measurements

Optical spectra of FBGs provide detailed information about their performance at various wavelengths and can be obtained in reflection or transmission mode. In this work, transmission spectra alone were used to compare the various FBG samples. The transmission spectra were measured in the arrangement illustrated in Figure 4-1 using an appropriate light source and one of a number of optical spectrum analysers (OSAs) as detailed in Tables 4-1 and 4-2, respectively. Reference traces were recorded in the absence of a grating and have been subtracted from the presented spectra to ensure that observed spectral features are due to the fibre grating itself and are not affected by fibre or light source wavelength variations. The peak reflectance

growths and wavelength shifts of specific spectral features with UV exposure time were inferred from transmission spectra measured during fabrication. The presented transmission spectra were measured after fabrication.

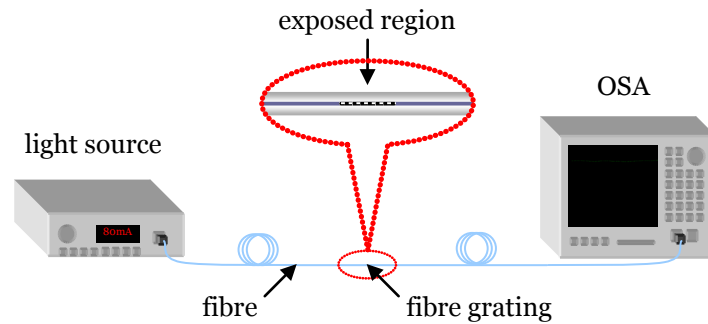


Figure 4-1. Schematic diagram of the experimental arrangement used for the measurement of transmission spectra.

Source label	λ range (nm)	Manufacturer	Details
LS-1	600-1600	Ando™	AQ-4303B white light source
LS-2	1520-1580	Er ³⁺ doped fibre and Newport™ laser diode	Er ³⁺ doped fibre ASE with 980 nm laser diode pump
LS-3	1520-1580	MPB Technologies™	EBS-7210 Er ³⁺ dual-band broadband source
LS-4	1010-1060	INO™ fibre and Newport™ laser diode	Yb ³⁺ doped fibre ASE with 980 nm laser diode pump
LS-5	1000-1100	QPhotonics™	QSDM-1050-2 1050 nm super luminescent diode

Table 4-1. Light sources used for the measurement of optical spectra; ASE: Amplified Spontaneous Emission.

OSA label	λ range (nm)	Model	Resolution range (nm)
OSA-1	400-1750	Ando™ AQ-6310B	0.1-1
OSA-2	350-1750	Ando™ AQ-6315E	0.05-1
OSA-3	600-1750	Ando™ AQ-6317B	0.01-1

Table 4-2. Optical spectrum analysers used in this work.

4.2 Type I and type IIA FBGs

In the following sections, the effect of the phase mask technique on the spectral properties of different types of gratings will be investigated.

4.2.1 The Bragg wavelength

A type I sample (labelled I-5 in Table 2-5) was fabricated under the same conditions as the FBG in which a complex refractive index structure was observed, as discussed in section 1.5.6. Sample I-5 was fabricated in hydrogen-loaded standard telecommunications fibre using phase mask SM-1 (in Table 2-2) using the experimental arrangement illustrated in Figure 2-1. As shown in Figure 4-2(a), the transmission spectra measured after fabrication at λ_B of sample I-5 exhibited a final reflectance of ~95% at ~1534.4 nm. Sample I-5 demonstrated a monotonic increase in reflectance at λ_B with UV fluence as shown in Figure 4-2(c), indicative of type I grating characteristics as discussed in section 1.4.5. The expected linear shift of λ_B to longer wavelengths with increasing fluence of sample I-5 is shown clearly in Figure 4-2(e).

Another sample, IIA-2, was written using the same phase mask and experimental arrangement as sample I-5 except non-hydrogen loaded, Fibrecore™ B-Ge co-doped fibre was used. As shown in Figure 4-2(b), the transmission spectra measured after fabrication at λ_B of sample IIA-2 exhibited a final reflectance of ~84% at ~1534.8 nm. The peak reflectance growth at λ_B with increasing fluence of sample IIA-2 is shown in Figure 4-2(d); the initial increase, partial erasure and subsequent regrowth clearly substantiate the designation of the sample as type IIA. The final spectra of the type IIA sample in Figure 4-2(b) shows a split transmission dip. This spectral feature was initially a single dip which split after approximately 10 kJ/cm² of UV exposure during the second phase of type IIA growth as illustrated in Figure 4-2(d) and (f). The shift of λ_B was observed to be non-linear during the first phase of type IIA growth. During the second growth phase, both minima of the split transmission dip shifted to shorter wavelengths as expected for type IIA FBGs. It should be noted that this sample's apparent "double-dip

structure” is not attributed to the same mechanisms to be discussed in section 4.4. It is unclear why splitting occurred for this type IIA FBG transmission dip; it is possibly due to a slight misalignment caused by an interruption during this phase of fabrication.

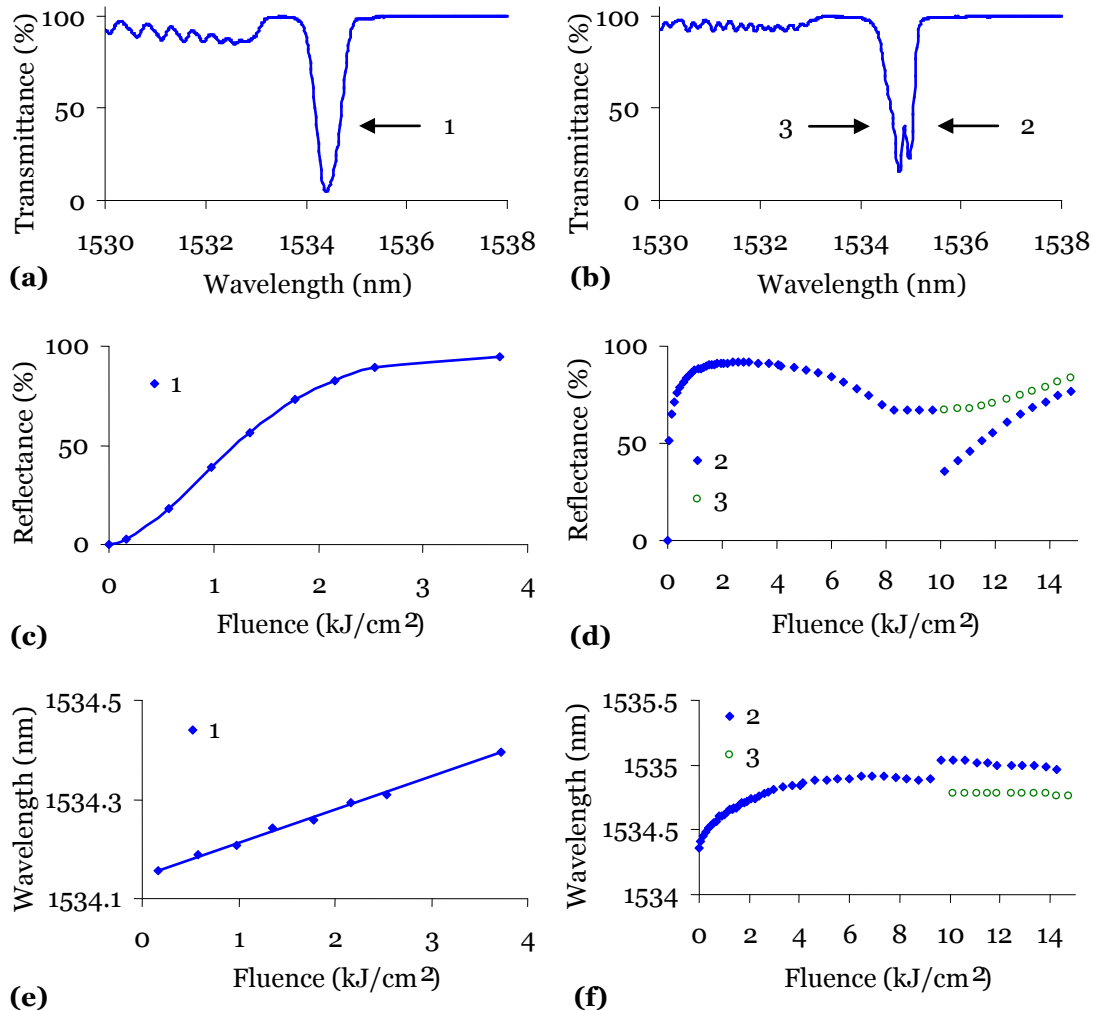


Figure 4-2. Spectral behaviour at λ_B of type I and IIA gratings. Transmission spectra measured after fabrication of samples (a) I-5 and (b) IIA-2. Peak reflectance growth of the numbered exposure features with increasing exposure fluence of samples (c) I-5 and (d) IIA-2. Wavelength shift of the numbered features of samples (e) I-5 and (f) IIA-2.

4.2.2 Other harmonic wavelengths

Images of the core of a phase-mask-written FBG have revealed the existence of two periods, namely one equal to the period of phase mask used in fabrication, Λ_{pm} , and one period equal to half of the phase mask period, $\Lambda_{pm}/2$, as

discussed in section 1.5.5. If these two periods do exist in the grating core, the grating will have two sets of harmonic reflections as predicted by Equation 1-3. Listed in Table 4-3 are the expected reflected wavelengths of modes with an effective index of $n_{eff} = 1.4485$ from two grating periods, Λ_{pm} and $\Lambda_{pm}/2$ for a phase mask of period $\Lambda_{pm} = 1.06 \mu\text{m}$. The wavelengths in Table 4-3 are approximate since n_{eff} varies with the wavelength λ . It can be noted that reflections in the regions of 1023 nm and 614 nm would not be apparent if the grating period was purely $0.53 \mu\text{m}$, as would be the case if the FBG was induced only by interference of the $\pm 1^{\text{st}}$ orders of the phase mask [116].

Harmonic m	λ_m (nm)	
	0.53 μm ($\Lambda_{pm}/2$)	1.06 μm (Λ_{pm})
1	1535	3070
2	768	1535
3	512	1023
4	384	768
5	307	614

Table 4-3. Approximate values of expected harmonic wavelengths of two grating periods [116].

Referring to Table 4-3, the reflection at $\lambda_B = 1535 \text{ nm}$ corresponds to the fundamental harmonic ($m = 1$) of a $0.53 \mu\text{m}$ period grating and the 2nd harmonic ($m = 2$) of a $1.06 \mu\text{m}$ period grating. The fundamental reflection of a grating period of $1.06 \mu\text{m}$ would occur at $3.07 \mu\text{m}$ but the high absorption of silica in this region prevents measurement at this wavelength. Consequently, the 2nd harmonic of $\Lambda_{pm}/2 = 0.53 \mu\text{m}$ and the 3rd, 4th and 5th harmonics of $\Lambda_{pm} = 1.06 \mu\text{m}$ were investigated. The wavelength values in Table 4-3 were used as a guide for the spectral measurements. Since the variation in n_{eff} causes wavelength variations of less than 5 nm in the measured regions, broad spectra were measured in order to locate the harmonic spectral features of the FBGs.

Transmission spectra in the 1030 nm region, corresponding to $2/3 \lambda_B$, were measured using OSA-1 from Table 4-2 operating with a resolution of 0.1 nm and light source LS-4 from Table 4-1. Transmission spectra in the 768 nm ($1/2 \lambda_B$) and 614 nm ($2/5 \lambda_B$) regions were measured using light source LS-1 and OSA-1 operating with a resolution of 0.2 nm. When small OSA resolutions are used, fine spectral detail can be measured but this comes at the expense of detectable light levels. When light levels are too low, it becomes difficult to distinguish spectral features from the noise in the signal. Consequently, the operating OSA resolution was chosen depending on the light levels achievable in the fibre. Figure 4-3 illustrates the features observed in the transmission spectra of the type I and type IIA samples at various harmonic wavelengths and Table 4-4 summarises these observations and respective reflectances. The circled spectral features were prominent in broader spectral measurements which allowed their distinction from background noise; however, narrow spectral regions are shown in Figure 4-3.

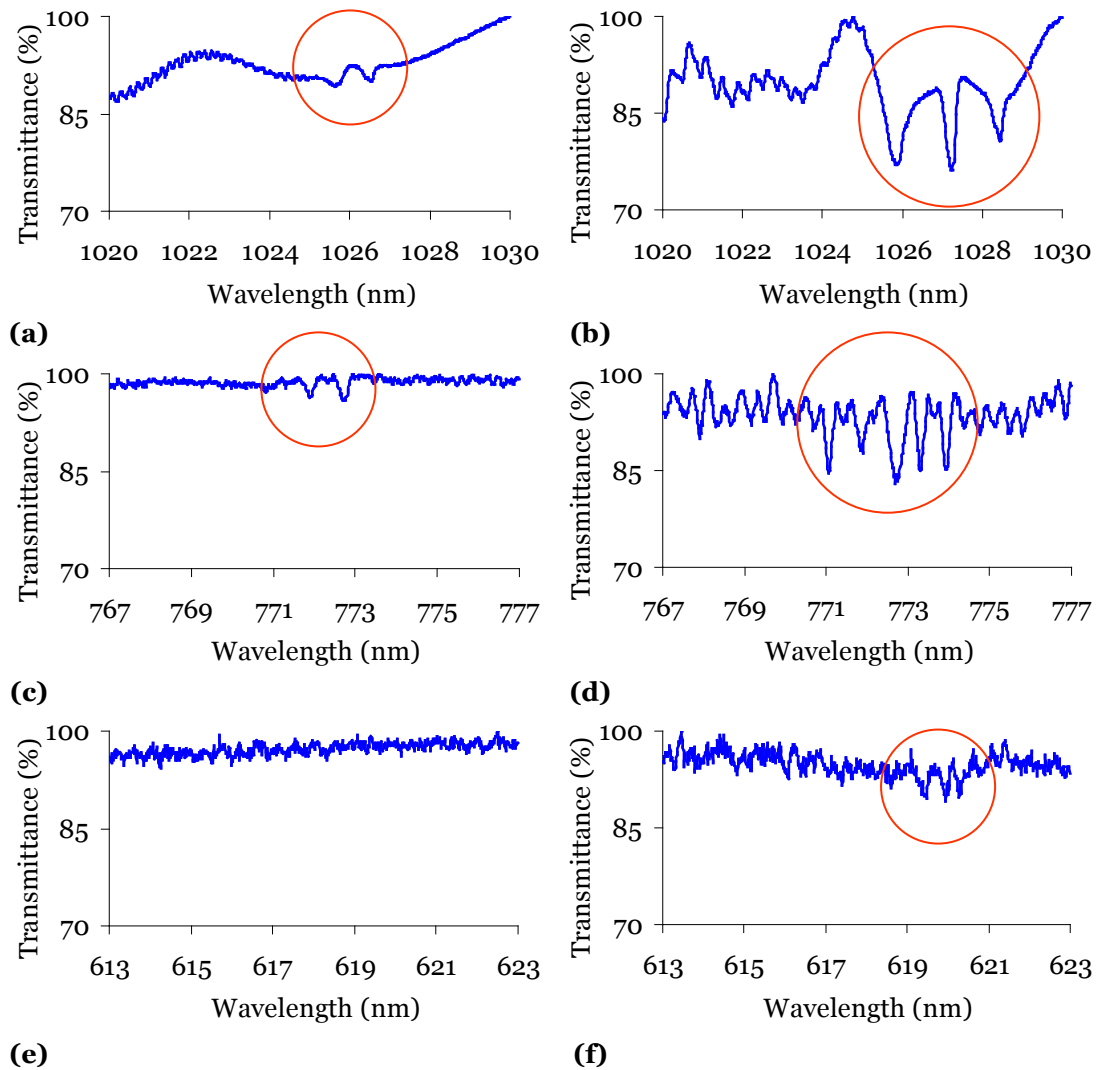


Figure 4-3. Spectral properties at other harmonic reflections of type I and IIA gratings. Transmission spectra measured after fabrication at $2/3 \lambda_B$ of samples (a) I-5 and (b) IIA-2; at $1/2 \lambda_B$ of samples (c) I-5 and (d) IIA-2 and at $2/5 \lambda_B$ of samples (e) I-5 and (f) IIA-2.

It can be noted in Table 4-4 that the peak reflected wavelengths are not precise integer ratios of λ_B ; this is due to the non-linear dependence of n_{eff} on wavelength. It can also be noted that the magnitude of reflectances at wavelengths lower than λ_B are small in comparison to reflectances at λ_B . This is likely to be due to the multimoded nature of the fibre at wavelengths smaller than the cutoff wavelength of ~ 1300 nm, which will be discussed further in section 4.3.

Sample	Harmonic m of a $1.06 \mu\text{m}$ grating	Wavelength ($\pm 0.1 \text{ nm}$)	Reflectance (%)
I-5	1	~ 3070	NM
	2	1534.4	95.0 ± 0.5
	3	1025.6	2.2 ± 0.5
		1026.5	2.8 ± 0.5
	4	771.9	4 ± 2
		772.7	6 ± 2
5	~ 614	ND	
IIA-2	1	~ 3070	NM
	2	1534.8	79.7 ± 0.5
	3	1025.9	14 ± 1
		1027.3	15 ± 1
		1028.5	10 ± 1
	4	771.1	8 ± 3
		771.9	7 ± 3
		772.7	11 ± 3
		773.3	9 ± 3
		773.9	8 ± 3
	5	619.4	5 ± 2
		620.0	5 ± 2
623.0		5 ± 2	

Table 4-4. Reflection peaks in various wavelength regions of type I and type IIA gratings. NM denotes 'not measured' and ND denotes 'not detected'. [116]

The transmission spectra of the type I sample in the 1030 nm wavelength region shows two dips (Figure 4-3(a)). Two dips were also observed at $1/2 \lambda_B$ ($\sim 772 \text{ nm}$) for this grating (Figure 4-3(c)), but no clear dips were observed in the $2/5 \lambda_B$ region around 614 nm (Figure 4-3(e)), possibly due to OSA resolution and noise level limitations. Figure 4-3(b) shows the transmission of the type IIA sample in the $2/3 \lambda_B$ region near 1030 nm, in which three distinct dips are seen. Five dips were observed in the 772 nm spectral region of the type IIA sample (Figure 4-3(d)) and three dips were observed around 620 nm (Figure 4-3(f)); there are possibly more dips that were not apparent due to noise. The observation of spectral features near 1030 nm and 614 nm are attributed to the existence of grating features with a period equal to the phase mask ($\sim 1.06 \mu\text{m}$).

The observation of multiple reflections at wavelengths lower than λ_B has been reported previously and was attributed to the presence of higher order modes since the fibre is not singlemode at wavelengths lower than the cutoff wavelength [86, 117]. The observation of multiple transmission dips could also be due to inefficient back reflections from the FBG (cladding mode losses) or destructive interference due to phase shifted gratings (to be discussed in section 4.4.1).

Comparison of transmittance spectra shows that the strength of minima near 1030 nm is greater for the type IIA sample than for the type I sample. This is consistent with reports that the magnitude of reflectances due to other harmonics of λ_B will depend upon the level of the saturation of the refractive index variation [83]. As shown in Figure 4-2(d), the type IIA sample reached saturation at a reflectance of approximately 90% prior to exhibiting partial erasure and subsequent regrowth. The type I sample may not have reached the same induced refractive index which may account for the lower reflectances at other harmonic wavelengths. As detailed in Table 2-5, sample IIA-2 was exposed to a UV fluence of 15 kJ/cm² while sample I-5 was exposed to only 3.8 kJ/cm². The much greater fluence of the type IIA FBG will have resulted in a much higher induced refractive index changes which may also account for the higher reflectances at other harmonic wavelengths.

Another sample, labelled I-6, was written under the same conditions as sample IIA-2 except that the exposure was ceased prior to the second phase of type IIA growth at a fluence of approximately 1.6 kJ/cm². The growth dynamics at λ_B of sample I-6, featured in Figure 4-4(a) and (b), were measured using LS-2 and OSA-1 operating with a resolution of 0.1 nm. Data were not recorded after about 0.7 kJ/cm², consequently the last data points in Figure 4-4(a) and (b) were measured after UV exposure. The drop in the wavelength of λ_B from ~1534.5 nm at ~0.7 kJ/cm² to ~1534.1 nm at ~1.6 kJ/cm² in Figure 4-4(b) is due to the removal of the slight tension placed on the fibre during fabrication and natural settling to shorter wavelengths which occurs when the UV exposure is ceased and local temperatures drop.

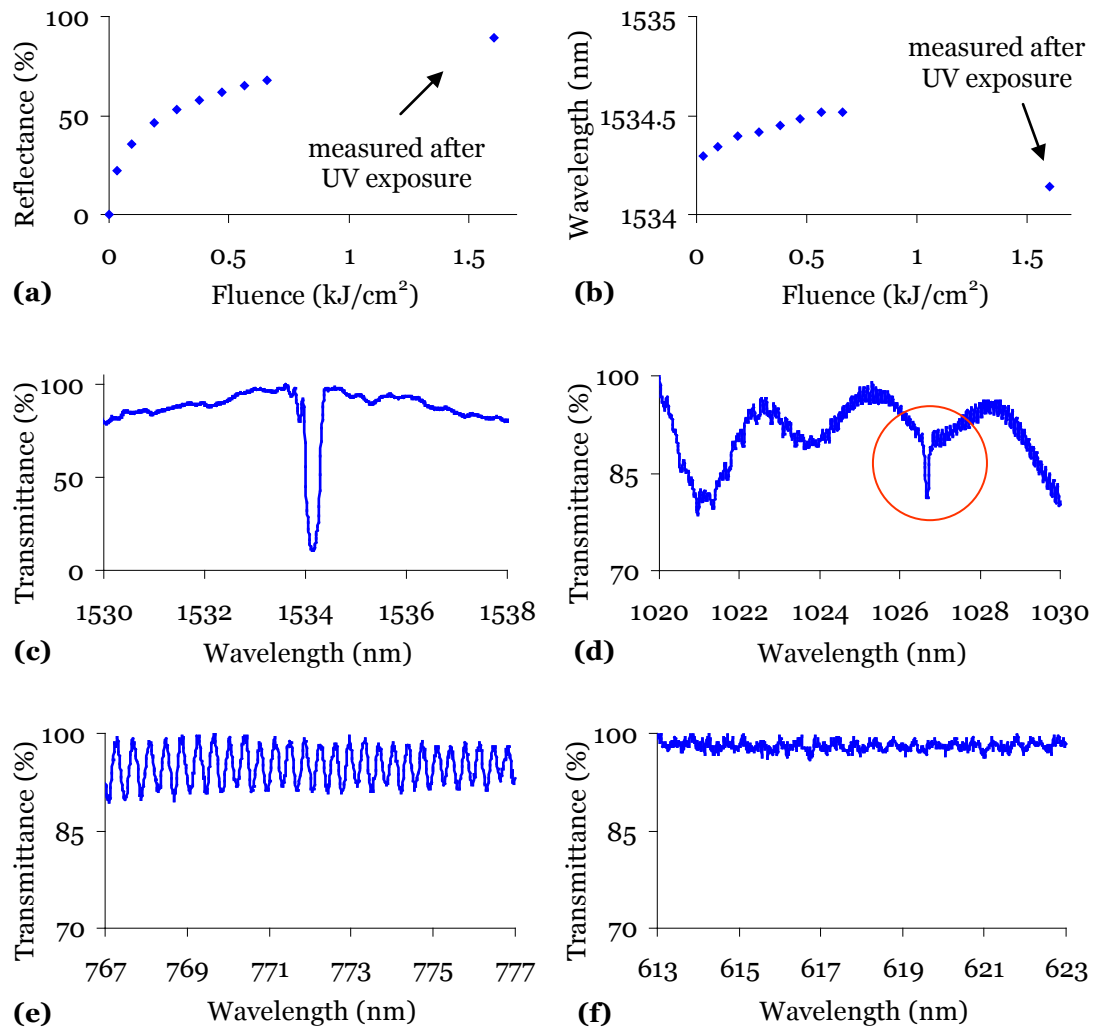


Figure 4-4. Spectral characteristics of a type I sample prior to type IIA growth. Growth of sample I-6 at λ_B : **(a)** peak reflectance and **(b)** wavelength shift with increasing UV exposure. Transmission spectra measured after exposure at **(c)** λ_B , **(d)** $2/3 \lambda_B$, **(e)** $1/2 \lambda_B$, and **(f)** $2/5 \lambda_B$.

The transmission spectrum at λ_B of sample I-6 (Figure 4-4(c)) was measured after exposure using OSA-2 operating at a resolution of 0.05 nm. The transmission spectra in the $1/2 \lambda_B$ and $2/5 \lambda_B$ regions are shown in Figure 4-4(e) and (f) and were measured after fabrication using LS-1 and OSA-1 operating with a resolution of 0.2 nm, as used for sample IIA-2. As can be seen, sample I-6 did not show any transmission dips in these regions which may be due to resolution and noise level limitations. Spectra measured at 0.2 nm resolution in the 1025 nm region also revealed no spectral features. However measurement with LS-5 and OSA-3 with a resolution of 0.01 nm

(Figure 4-4(d)) revealed a single transmission dip at about 1026.7 nm with a FWHM of approximately 0.1 nm and reflectance of about 9%. This is in contrast to the 1025 nm spectra of sample IIA-2 shown in Figure 4-3(b), which features three prominent transmission dips corresponding to approximately 14, 15 and 10% reflectance. The strength of reflectances in the harmonic spectra of the type I sample in Ge:B fibre are lower than the type IIA counterpart and these observations are consistent with the reports of Xie *et al.* [83] in that the Bragg reflectance peak may have not reached saturation in the case of the type I sample.

4.2.3 Further type IIA results

As presented and discussed in section 3.4.1, images of a phase-mask-written type IIA sample revealed a similarly complex refractive structure to the structure revealed for type I FBGs. The images presented in section 3.4.1 revealed a Talbot diffraction pattern consistent with beating between the $\pm 1^{\text{st}}$ and $\pm 2^{\text{nd}}$ orders of the phase mask. The images revealed the existence of π -shifted gratings with a period consistent with the period of the phase mask used in fabrication.

As detailed in Table 2-5, sample IIA-1 was written in fibre F-2 with standard phase mask SM-2 using the arrangement shown in Figure 2-1. As can be seen in Figure 4-5, the sample exhibited clear type IIA growth characteristics with the (a) regrowth phase and accompanying blue shift in the Bragg wavelength (in Figure 4-5(b)). The transmission spectra measured after fabrication in Figure 4-5(c) and (d) shows a strong dip ($\sim 99.9\%$) at λ_B and small dips ($\sim 5\%$) at approximately 1034 nm (in the region of $2/3 \lambda_B$), respectively. The observation of spectral features in the region of $2/3 \lambda_B$ for sample IIA-1 are consistent with the observed refractive index structure in the images of this sample shown in Figure 3-12.

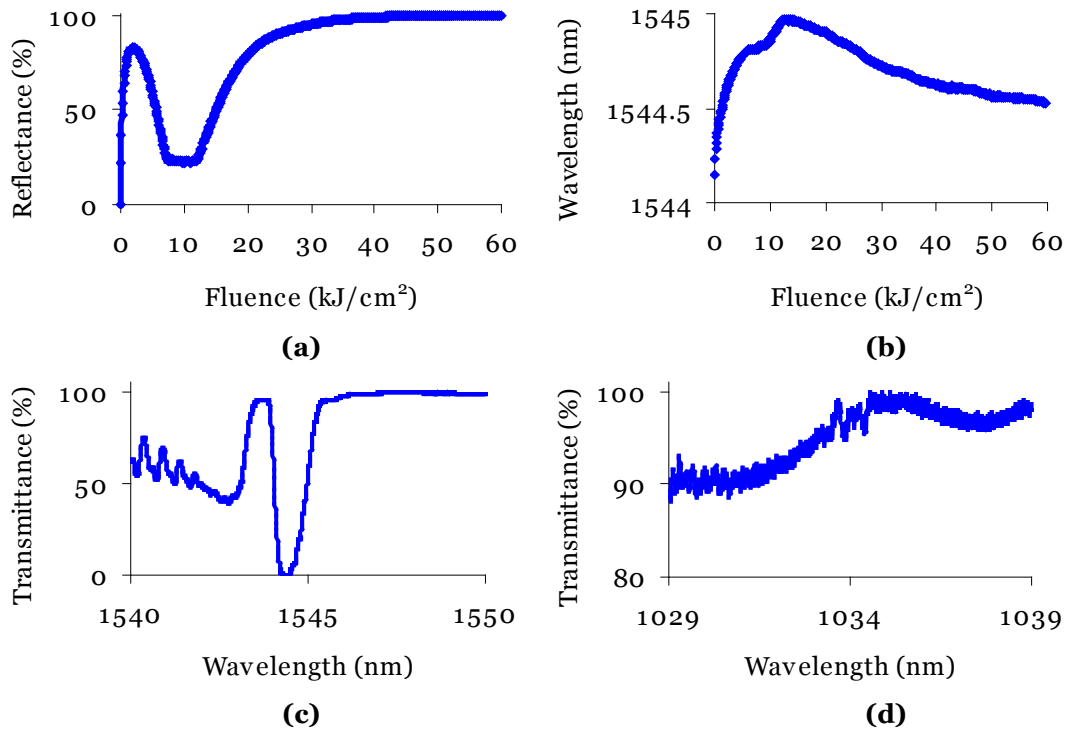


Figure 4-5. Growth of sample IIA-1 at λ_B : **(a)** peak reflectance and **(b)** wavelength shift with increasing UV fluence. Transmission spectra measured after fabrication of sample IIA-1 at **(c)** λ_B and **(d)** $2/3 \lambda_B$.

4.3 Multimode versus singlemode conditions

The occurrence of multiple transmission dips at higher harmonic reflections has been attributed to the multimoded nature of the fibre [86, 117]. To investigate this further, spectral features in the region of λ_B and $2/3 \lambda_B$ are compared here under multimode and singlemode conditions. In order to understand how light propagating under singlemode and multimode conditions interacts with the gratings written in the core, the simulated distribution of the fundamental mode at the two wavelengths in two different fibres are presented in the first subsection.

FBGs written with standard and custom-made phase masks are analysed to investigate the effect of different intensities in the 0th, 1st and 2nd diffracted orders on spectral features propagating under singlemode and multimode conditions. The samples to be analysed here are labelled I-1 through I-4 and their fabrication parameters are summarised in Table 2-5. The peak

reflectance and wavelength shifts during fabrication of features in the regions of λ_B and $2/3 \lambda_B$ were measured simultaneously for comparison. The changes in reflectance during writing are described and analysed in more detail in Chapter 5.

4.3.1 Predicted modal distributions

As detailed in Table 2-4, fibre F-1 has a cutoff wavelength of ~ 1300 nm so that it is singlemode in the region of $\lambda_B \sim 1550$ nm but multimode in the region of $2/3 \lambda_B$. Fibre F-3 was chosen due to its cutoff wavelength of ~ 930 nm so that light would propagate under singlemode conditions in both spectral regions of interest. The properties of these fibres at the two wavelengths of interest are summarised in Table 4-5. The V parameters were calculated using Equation 1-10 and as discussed in section 1.5.3, fibre F-1 at 1035 nm is clearly seen to be multimode since $V > 2.405$ [45]. In order to analyse adequately the spectral properties of FBGs at different wavelengths in these fibres, an understanding of the predicted distributions of the fundamental mode is required.

Fibre	F-1 1550 nm	F-1 1035 nm	F-3 1550 nm	F-3 1035 nm
ρ (μm)	3.7	3.7	1.8	1.8
d (μm)	125	125	125	125
Δn_{co} ($\times 10^{-3}$)	8.551	8.551	14.44	14.5
n_{cl}	1.44402	1.44998	1.44402	1.44998
n_{co}	1.45258	1.45853	1.45846	1.46448
V	2.36	3.54	1.49	2.25
$\eta(\lambda)$	0.8	0.9	0.5	0.7

Table 4-5. Simulation parameters for large and small core fibres F-1 and F-3.

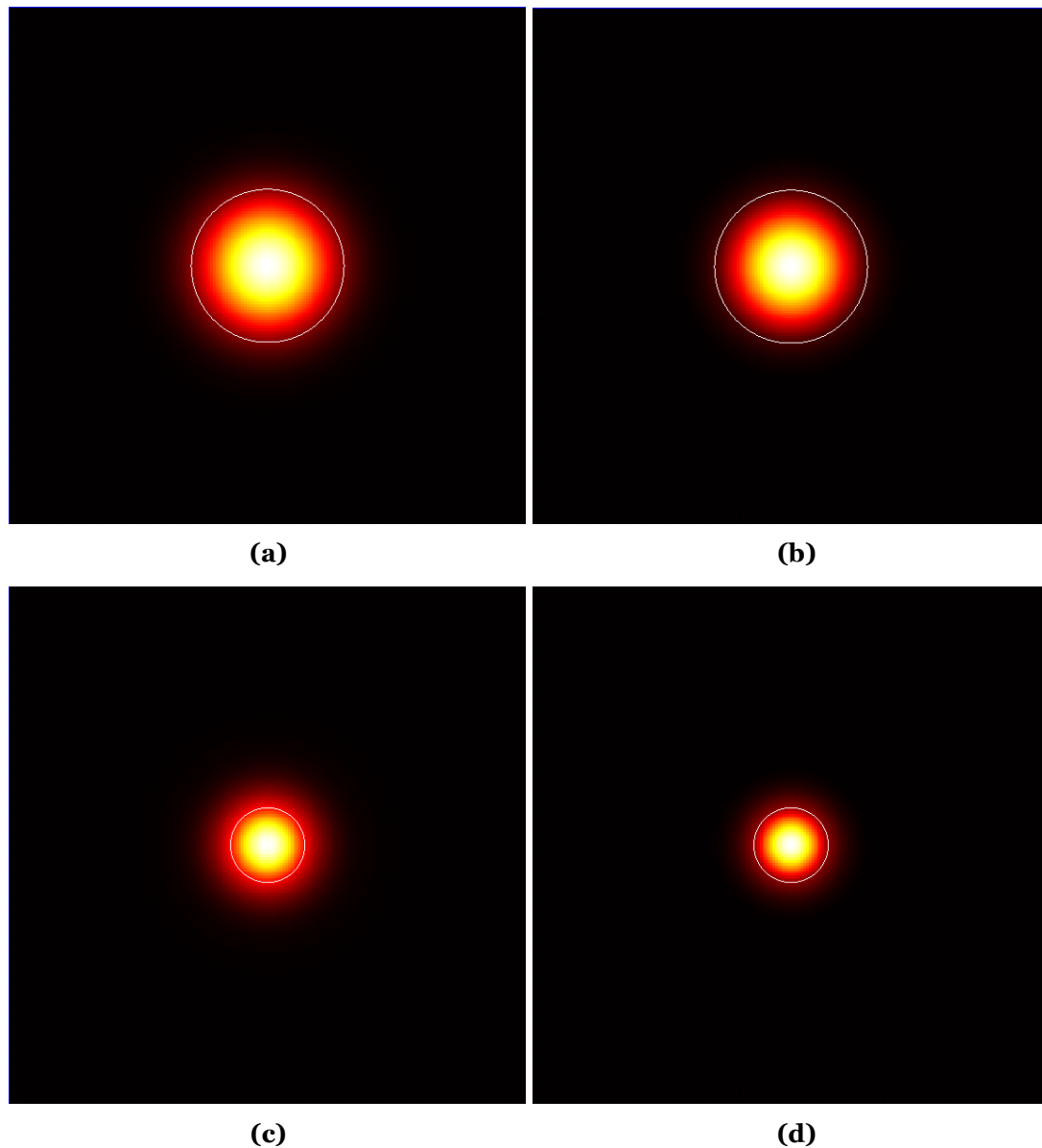


Figure 4-6. Calculated intensity distributions of the LP_{01} mode in fibre F1 at **(a)** $\lambda = 1550$ nm and **(b)** $\lambda = 1035$ nm and in fibre F3 at **(c)** $\lambda = 1550$ nm and **(d)** $\lambda = 1035$ nm. The size of each image is $25 \times 25 \mu\text{m}$ and the white ring marks the core/cladding boundary.

The intensity distributions of the LP_{01} (fundamental) modes in fibres F1 and F3 at 1550 nm and 1035 nm (shown in Figure 4-6) were calculated using Fimmwave software from Photon Design, UK. Fimmwave's vectorial fibre solver models fibres using a rigorous solution to the vectorial wave equation in cylindrical co-ordinates, assuming isotropic media with a perfect electrical conductor as the outer boundary condition. The model assumed step-index fibres with the known fibre diameter d , core radius ρ and refractive index

difference Δn_{co} as summarised in Table 4-5. The core and cladding indices, n_{co} and n_{cl} , at 1550 nm and 1035 nm were calculated using Equation 1-5 and Equation 1-6. The overlap between the fundamental mode and the core, $\eta(\lambda)$, was calculated as the filling fraction of the core region in Fimmwave, which calculates the ratio of power flux contained in the core to the power flux contained in the waveguide. For high values of $\eta(\lambda)$, both the high intensity central portion of the mode and low intensity evanescent tails are tightly confined to the core. Conversely, for low values of $\eta(\lambda)$, the mode profile is more spread out over the core so that higher intensities fill the core and the low intensity evanescent tails propagate in the cladding.

The two-dimensional intensity distributions of the LP_{01} modes at 1550 nm and 1035 nm for fibre F-1 are shown in Figure 4-6(a) and (b), respectively, and for fibre F-3 in Figure 4-6(c) and (d), respectively. As can be seen in Figure 4-6, the manner in which the fundamental mode fills the core of both fibres is different at 1550 nm and 1035 nm because of the size of the mode. In the larger core fibre F-1, the fundamental mode at 1550 nm has a lower value of $\eta(\lambda)$ meaning that the mode is more spread over the core than at 1035 nm. In the smaller core fibre F-3, the fundamental modes at both wavelengths have lower values of $\eta(\lambda)$ than in fibre F-1. Since propagating modes are more spread over the core under singlemode conditions, it is expected that higher intensities will fill the core and interact with the grating leading to higher reflectances. As can be seen in Table 4-5, $\eta(\lambda)$ is greater in Fibre F-1 at the multimode wavelength 1035 nm meaning the modal power is more tightly confined to the centre of the core. Thus, higher values of $\eta(\lambda)$ are expected to lead to reduced intensities interacting with the grating across the core and lower peak reflectances.

4.3.2 Simultaneous spectral measurements

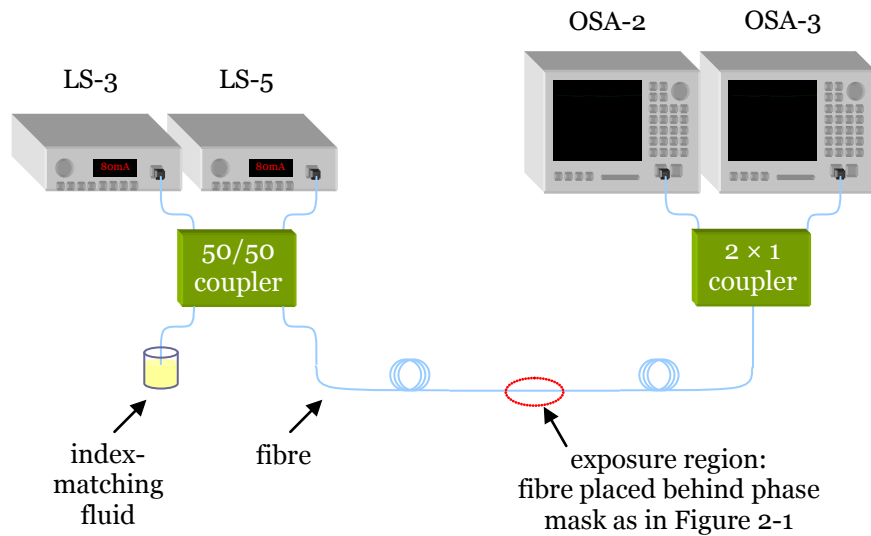


Figure 4-7. Schematic diagram of the experimental arrangement used for the simultaneous measurement of transmission spectra at λ_B and $2/3 \lambda_B$ during fabrication.

In order to further understand the relative growth dynamics of spectral features in the region of $2/3 \lambda_B$ and λ_B , the experimental arrangement shown in Figure 4-7 was used to enable simultaneous measurement in both spectral regions during fabrication. The arrangement coupled light from sources LS-3 and LS-5 with central wavelengths of 1550 and 1040 nm, respectively, into the sample fibre using a 50:50 coupler. The unused arm of the coupler was placed in index-matching fluid to prevent spurious back-reflections. The output arm of the 50:50 coupler was fusion spliced to the sample fibre, which was placed in the phase mask fabrication arrangement as shown in Figure 2-1. The output end of the exposed fibre sample was fusion spliced to a 2×1 coupler to separate the two wavelengths which were recorded during fabrication by OSA-2 and OSA-3 with the optimum device resolutions of 0.05 and 0.01 nm, respectively.

4.3.3 Standard phase mask

As detailed in Table 2-5, samples I-1 and I-2 were fabricated using standard phase mask SM-2 in the hydrogen loaded fibres F-1 and F-3, respectively, with

total fluences of approximately 18 and 5.0 kJ/cm², respectively. The images of samples I-1 and I-2, presented in sections 3.4.2 and 3.4.3, respectively, revealed a Talbot diffraction pattern consistent with beating between the $\pm 1^{\text{st}}$ and $\pm 2^{\text{nd}}$ orders of the phase mask. The images revealed the existence of π phase-shifted gratings with a period consistent with the period of the phase mask used in fabrication.

The transmission spectra measured after fabrication at λ_B and $2/3 \lambda_B$ of sample I-1 are shown in Figure 4-8(a) and (b), respectively. The spectra at λ_B shows a strong dip with $R = 99.99\%$ centred at ~ 1546.3 nm (labelled as 1) that is accompanied by prominent cladding mode losses on the short wavelength side. The main transmission dip is quite saturated; evident in the broad dip and flat region at $\sim 0\%$ transmittance. The spectra in the region of $2/3 \lambda_B$ shows three smaller dips (labelled as 2, 3 and 4) with peak reflectances of approximately 33, 25 and 11.5% at approximately 1033.1, 1034.1 and 1035.1 nm, respectively. The wavelength shifts during fabrication of the labelled spectral features are evident in Figure 4-8(c) and (d) to be clearly linear towards longer wavelengths, as expected for type I FBGs. The changes in reflectance during writing for samples I-1 and I-2 are described in more detail in sections 5.2.1 and 5.2.2, respectively.

Both samples I-1 and I-2 are singlemode in the spectral region of λ_B , while sample I-1 is multimode in the region of $2/3 \lambda_B$. The transmission spectra measured after fabrication at λ_B and $2/3 \lambda_B$ of sample I-2 are shown in Figure 4-8(e) and (f), respectively. The spectra of sample I-2 at λ_B shows a strong dip with $R = 99.99\%$ centred at ~ 1546.8 nm (labelled as 5) that is accompanied by strong cladding mode losses but they are not as strong as for sample I-1.

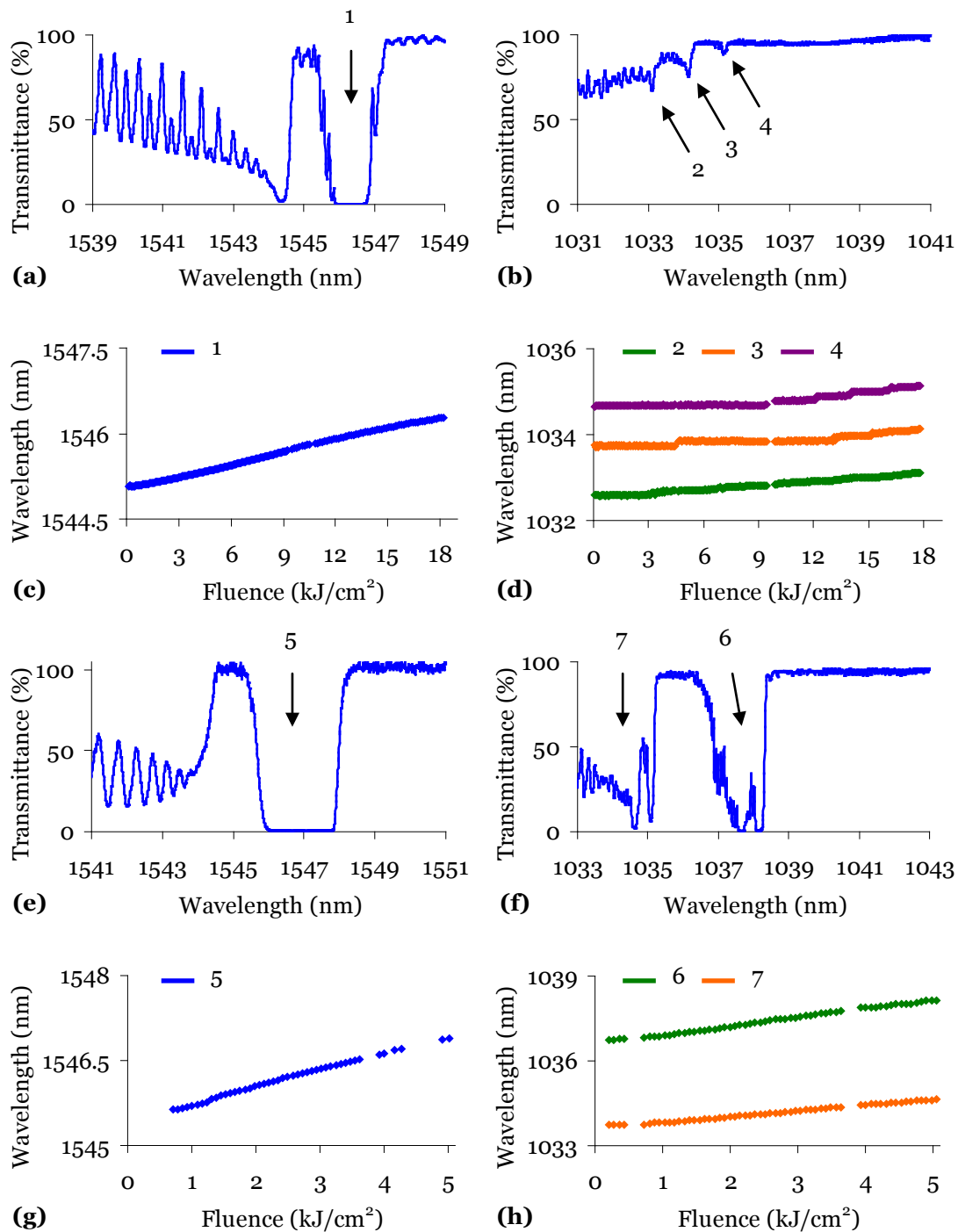


Figure 4-8. Spectral properties of multimode and singlemode FBGs fabricated using a standard phase mask. Transmission spectra measured after fabrication of sample I-1: (a) at λ_B and (b) at $2/3 \lambda_B$. The spectral shift of dips during fabrication of sample I-1 at (c) λ_B and (d) $2/3 \lambda_B$. Transmission spectra measured after fabrication of sample I-2: (e) at λ_B and (f) at $2/3 \lambda_B$. The spectral shift of dips during fabrication of sample I-2 at (g) λ_B and (h) $2/3 \lambda_B$.

The transmission dip at λ_B of sample I-2 is almost double the spectral width of the dip at λ_B of sample I-1, despite being exposed to a much lower total UV

fluence. As will be shown in the reflectance versus fluence plots in sections 5.2.1 and 5.2.2, the reflectance at λ_B of sample I-1 began to saturate after an exposure fluence of approximately 7 kJ/cm^2 , whereas the reflectance at λ_B of sample I-2 began to saturate after only 2 kJ/cm^2 . The lower fluence required for saturation and hence broader spectral widths at λ_B and $2/3 \lambda_B$ of the smaller core fibre sample I-2 is possibly due to a number of factors. It is possible that fibre F-3 has a higher Ge content in the core leading to higher photosensitivity than fibre F-1. Additionally, sample I-2 was fabricated with a longer grating length ($\sim 8 \text{ mm}$) than sample I-1 ($\sim 5 \text{ mm}$) in order to obtain adequate reflectance strengths in the different fibre types at both wavelengths of interest. Since the data has not been normalised to the grating length l , the larger length of sample I-2 is expected to produce stronger back reflections than from the shorter sample I-1. The broader spectral widths of sample I-2 are also possibly due to the respective modal overlaps discussed in 4.3.1. Since the fundamental modes at both wavelengths are more tightly confined to the core in fibre F-3 than in fibre F-1, there is greater interaction between the grating and the fundamental modes at each wavelength leading to lower saturation fluences.

The cladding mode losses on the short wavelength side of λ_B of the less-saturated sample I-1 are stronger than the cladding mode losses of sample I-2. This is possibly due to the higher total UV fluence, longer grating length or a slight tilt in the phase mask during fabrication [118]. The spectra in the region of $2/3 \lambda_B$ shows two prominent features (labelled as 6 and 7) with peak reflectances of approximately 99.7 and 98% at approximately 1038.1 and 1034.633 nm, respectively. The wavelength shifts during fabrication of the labelled spectral features can be seen in Figure 4-8(g) and (h) to also be clearly linear towards longer wavelengths as expected for type I FBGs. The spectral features labelled 6 and 7 in Figure 4-8(f) both exhibit a double transmission dip structure; however feature 7 is likely to be due to cladding modes and feature 6 has become saturated due to prolonged exposure. The evolution and possible origins of double-dip structures in the region of $2/3 \lambda_B$ will be discussed further in section 4.4.1.

The spectral features at $2/3 \lambda_B$ are much stronger in sample I-2 when the fibre is singlemode than those for sample I-1 when the fibre is multimode. This is possibly due to the larger grating length l but will also be due to the different propagation conditions of the two samples at $2/3 \lambda_B$. Under singlemode conditions, the fundamental mode is much more tightly confined to the core. Consequently, a greater fraction of the propagating optical power interacts with the refractive index structure in the core and stronger reflectances occur than in multimode fibre. As will be discussed further in section 5.2, this attribution is supported by the observation that, when features in both spectral regions are under singlemode conditions, the peak reflectances demonstrate similar growth characteristics. In contrast, when features at $2/3 \lambda_B$ are propagating under multimode conditions, the peak reflectance growth is much slower than the singlemode features at λ_B .

4.3.4 Custom-made phase mask

In order to investigate the effect of different relative intensities in the orders produced by the phase mask, samples were fabricated using custom-made phase mask CM-2 with the properties discussed in section 2.3.2. As detailed in Table 2-5, samples I-3 and I-4 were fabricated using mask CM-2 in the hydrogen loaded fibres F-1 and F-3, respectively, with total fluences of approximately 31 and 10 kJ/cm², respectively. The images of samples I-3 and I-4, presented in sections 3.5.1 and 3.5.2, respectively, revealed a Talbot diffraction pattern consistent with beating between the $\pm 1^{\text{st}}$ and $\pm 2^{\text{nd}}$ orders of the phase mask. The images revealed the existence of π -shifted gratings with a period consistent with the period of the phase mask used in fabrication.

As discussed above, fibre F-1 is singlemode in the region of λ_B but multimode in the region of $2/3 \lambda_B$ whereas fibre F-3 is singlemode in both regions. To reach similar levels of saturation, the custom-made phase mask FBGs required exposure to approximately double the fluences of the standard phase mask FBGs since the custom-made phase mask provided approximately half the 1st order contribution of the standard phase mask.

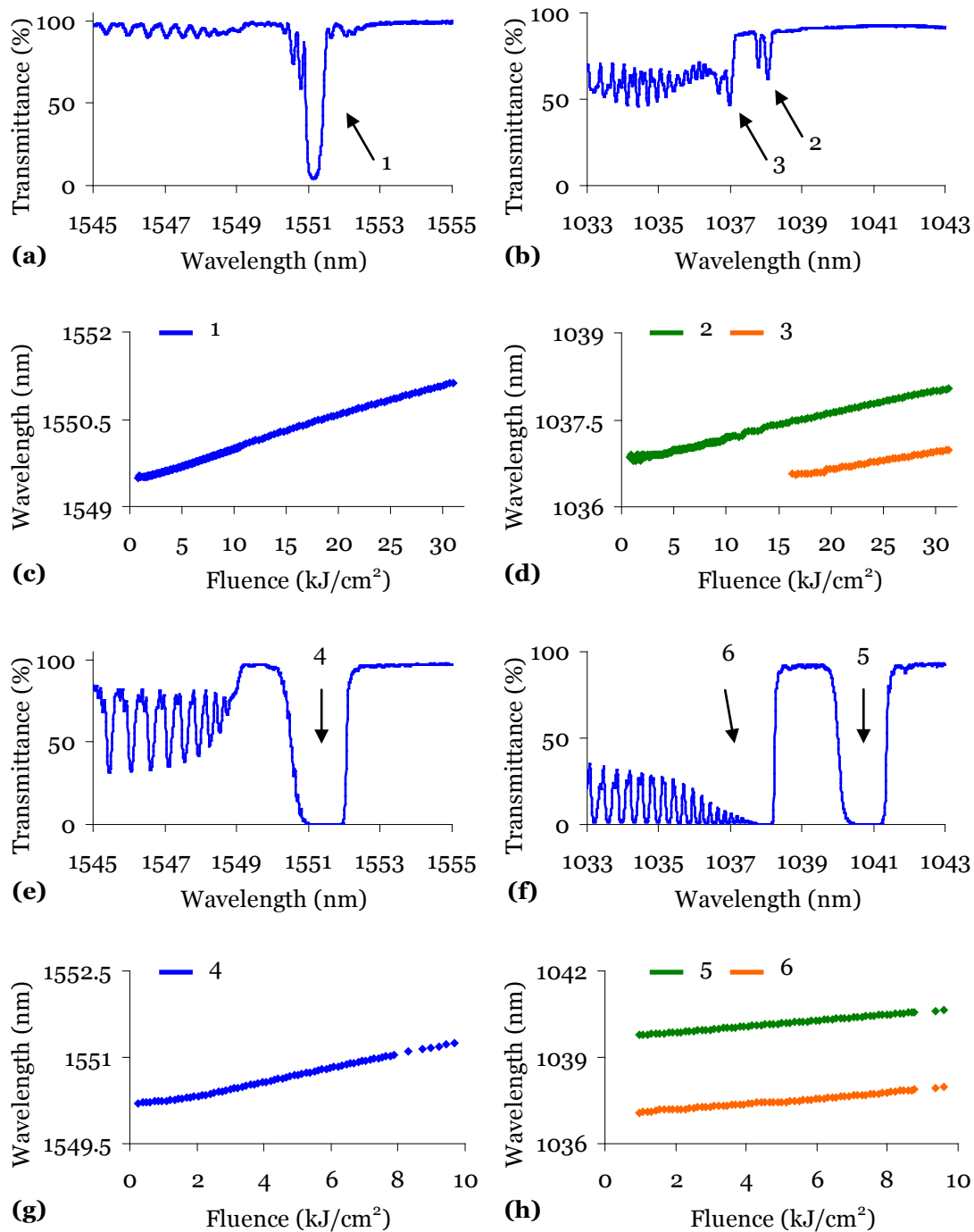


Figure 4-9. Spectral properties of multimode and singlemode FBGs fabricated using a custom-made phase mask. Transmission spectra measured after fabrication of sample I-3: **(a)** at λ_B and **(b)** at $2/3 \lambda_B$. The spectral shift during fabrication of sample I-3 at **(c)** λ_B and **(d)** $2/3 \lambda_B$. Transmission spectra measured after fabrication of sample I-4: **(e)** at λ_B and **(f)** at $2/3 \lambda_B$. The spectral shift during fabrication of sample I-4 at **(g)** λ_B and **(h)** $2/3 \lambda_B$.

The transmission spectra measured after fabrication at λ_B and $2/3 \lambda_B$ of sample I-3 are shown in Figure 4-9(a) and (b), respectively. The spectra at λ_B

shows a strong dip with $R = 95.8\%$ centred at ~ 1551.1 nm (labelled as 1) that is accompanied by almost no cladding-mode losses on the short wavelength side. The low cladding mode losses may be indicative of less inefficient reflections from this FBG. The main transmission dip is quite narrow indicating minimal saturation. The spectra in the region of $2/3 \lambda_B$ shows two sets of double-dip structures (labelled as 2 and 3) with peak reflectances of approximately 38 and 54% at approximately 1038 and 1037 nm, respectively. The possible origins of the observed double-dip structures in the region of $2/3 \lambda_B$ will be discussed further in section 4.4.1. The peak wavelength shifts during fabrication of the labelled spectral features are shown in Figure 4-9(c) and (d) and are linear towards longer wavelengths, as expected for normal type I growth. As will be discussed further in section 5.3, sample I-3 exhibited two phases of reflectance growth that was most likely caused by an interruption to the UV exposure conditions during fabrication. This assumption is supported by the normal type I growth evident in the measured wavelength shift of the sample.

The transmission spectra measured after fabrication in the two singlemode regions at λ_B and $2/3 \lambda_B$ of sample I-4 are shown in Figure 4-9(e) and (f), respectively. The spectra at λ_B shows a strong dip with $R = 99.99\%$ centred at ~ 1551.2 nm (labelled as 4) that is accompanied by much stronger cladding mode losses than sample I-3 at λ_B . The main transmission dip at λ_B of sample I-4 is much more saturated than that of sample I-3 with more than double the spectral width. The spectra at $2/3 \lambda_B$ shows the main dip with $R = 99.99\%$ centred at ~ 1040.6 nm (labelled as 5) that is accompanied by very strong cladding mode losses on the short wavelength side (labelled as 6). The main transmission dip at $2/3 \lambda_B$ of sample I-4 is almost as broad as the dip at λ_B . The wavelength shifts during fabrication of the labelled spectral features are shown in Figure 4-9(g) and (h) and are clearly linear towards longer wavelengths, as expected for type I FBGs.

Samples I-3 and I-4 were also fabricated with different lengths (~ 12 mm for sample I-4 and ~ 5 mm for sample I-3) in order to obtain adequate reflectance

strengths in the different fibre types at both wavelengths of interest. The stronger cladding mode losses at both $2/3 \lambda_B$ and λ_B of sample I-4 are possibly due to the longer grating length (compared with sample I-3) or a slight tilt in the phase mask during fabrication. The transmission dip at λ_B of sample I-4 is much broader than the dip at λ_B of sample I-3, despite being exposed to a much lower UV fluence. As previously discussed for samples I-1 and I-2, this is likely to be due to greater reflectance saturation resulting from higher fibre photosensitivity, longer grating length and higher modal confinement to the core in sample I-4.

The spectral features at $2/3 \lambda_B$ are much stronger in sample I-4 when the fibre is singlemode than those for sample I-3 when the fibre is multimode. As previously discussed, this is possibly due to the larger grating length l of sample I-4 but will also be due to the different propagation conditions of the two samples at $2/3 \lambda_B$. Under singlemode conditions, the fundamental mode is much more tightly confined to the core leading to greater interaction with the grating and stronger reflectances. As discussed above, this attribution is similarly supported by the observed growth characteristics for these samples which are analysed in Chapter 5.

In comparison to the standard phase mask, the custom-made phase mask provided a reduced contribution from the $\pm 1^{\text{st}}$ orders and a higher contribution from the 0^{th} and $\pm 2^{\text{nd}}$ orders. As discussed in section 3.1, the intensity patterns formed behind the standard phase mask is expected to be dominated by features with a period equal to the half the phase mask ($\Lambda_{pm}/2$) whereas the pattern formed behind the custom-made phase mask is expected to be dominated by features with a period equal to the phase mask (Λ_{pm}). Both phase masks were expected to exhibit a Talbot length, Z_T , of approximately $4.6 \mu\text{m}$.

On comparison of spectra from samples I-1 and I-3 written with the standard and custom-made phase masks, respectively, the use of the custom-made phase mask appears to have produced stronger reflectances in the multimode

region of $2/3 \lambda_B$. A peak reflectance of 33% was observed in the region of $2/3 \lambda_B$ for the standard mask sample I-1 (Figure 4-8(b)), whereas a peak reflectance of 54% was observed for the custom-made mask sample I-3 (Figure 4-9(b)). Spectral features in the region of $2/3 \lambda_B$ correspond to the 3rd harmonic reflections from a grating with a period of Λ_{pm} . The observed increase in peak reflectance at $2/3 \lambda_B$ can therefore be attributed to dominance of the period Λ_{pm} due to the higher contributions from the 0th and $\pm 2^{\text{nd}}$ orders from the custom-made phase mask.

On comparison of the singlemode samples I-2 and I-4 written with the standard and custom-made phase masks, respectively, the use of the custom made phase mask also appears to have produced stronger reflections in the region of $2/3 \lambda_B$. In fact, the spectral features at $2/3 \lambda_B$ for sample I-4 are approximately 10 dB stronger than the features for sample I-2 (dB data not shown). The spectral features at $2/3 \lambda_B$ are much more saturated for sample I-4, indicating that larger refractive index changes have been induced in the core due to the use of the custom-made phase mask. The repeat length, Z_T , of the intensity patterns formed perpendicular to the phase masks is $\sim 4.6 \mu\text{m}$ but the diameter of the fibre core of the singlemode samples is only $\sim 4 \mu\text{m}$. It is conceivable that the core of the singlemode fibre is not large enough to allow the $\Lambda_{pm}/2$ period to dominate the structure imprinted in the fibre core leading to similar reflectances in the standard and custom-made mask samples. These spectral results are consistent with the observed Talbot lengths in the images of samples I-1 to I-4 which were presented in sections 3.4 and 3.5.

4.4 Double-Dip Structure at $2/3 \lambda_B$

Spectral features in the region of $2/3 \lambda_B$ correspond to $m = 3$ harmonic reflections from a grating with a period equal to that of the phase mask used in fabrication. As discussed in sections 4.2 and 4.3, the occurrence of multiple transmission dips at wavelengths less than the cutoff wavelength has previously been attributed to the multimoded nature of the fibre. When light is propagating under singlemode conditions, only a single transmission dip is

expected to appear corresponding to the reflection of the single mode propagating in the fibre core. However, complex spectral features have been observed under singlemode conditions in the particular region of $2/3 \lambda_B$ for various samples. The following subsections will discuss some possible origins of the observation of more than one transmission dip at $2/3 \lambda_B$ under singlemode conditions.

As discussed in section 4.3.3 and shown in Figure 4-8(f), the spectra in the region of $2/3 \lambda_B$ of sample I-2 shows a saturated double-dip structure in the main transmission dip, despite being under singlemode conditions. Various transmission spectra at λ_B and $2/3 \lambda_B$ recorded during fabrication of sample I-2 are shown in Figure 4-10(a) and (b), respectively. Only the main transmission dips are shown here, not the cladding mode losses on the short wavelength side of the main dip. The transmission spectra shown in Figure 4-8(f) also exhibits a double-dip structure in the cladding mode losses on the short wavelength side of the main dip; the possible origins of this will be discussed in section 4.4.1.

As can be seen in Figure 4-10(a), the main spectral feature at λ_B exhibits a single dip throughout the grating growth which broadens with increasing fluence. The spectra at $2/3 \lambda_B$ in Figure 4-10(b), however, demonstrates two transmission dips which grow almost simultaneously. The double-dip structure is therefore not likely to consist of a main dip accompanied by a cladding mode loss, since these losses generally begin to grow upon saturation of the main dip. The transmittance of the central notch between the two dips at $2/3 \lambda_B$ in Figure 4-10(b) can be seen to decrease from approximately 100% (at 0 fluence) during fabrication as the structure broadens with saturation. The possible origins of the double-dip structure at $2/3 \lambda_B$ under singlemode conditions will be discussed in the following section.

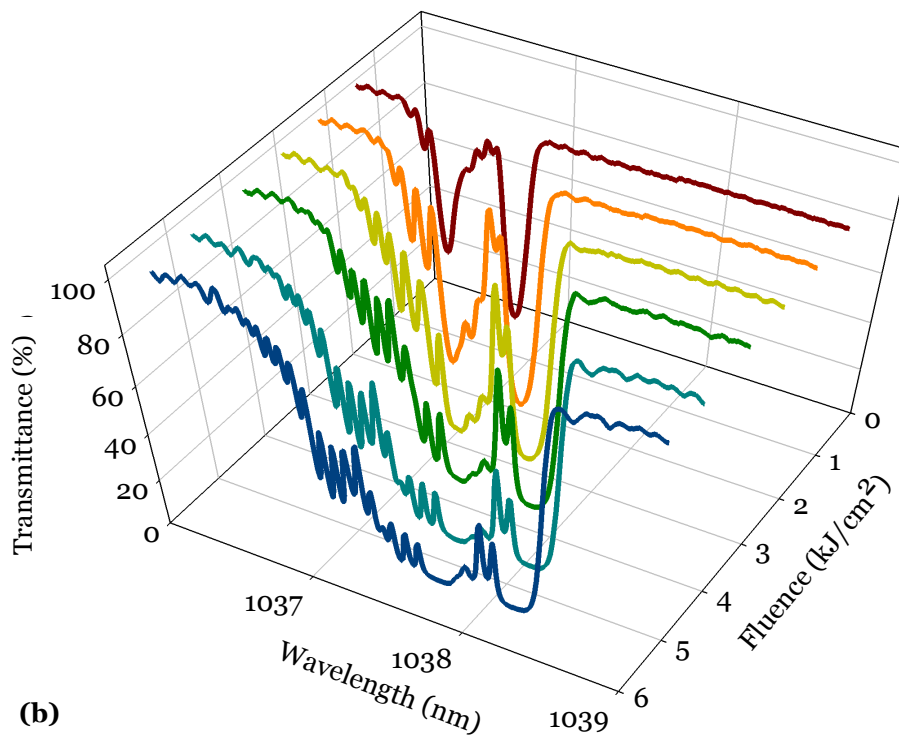
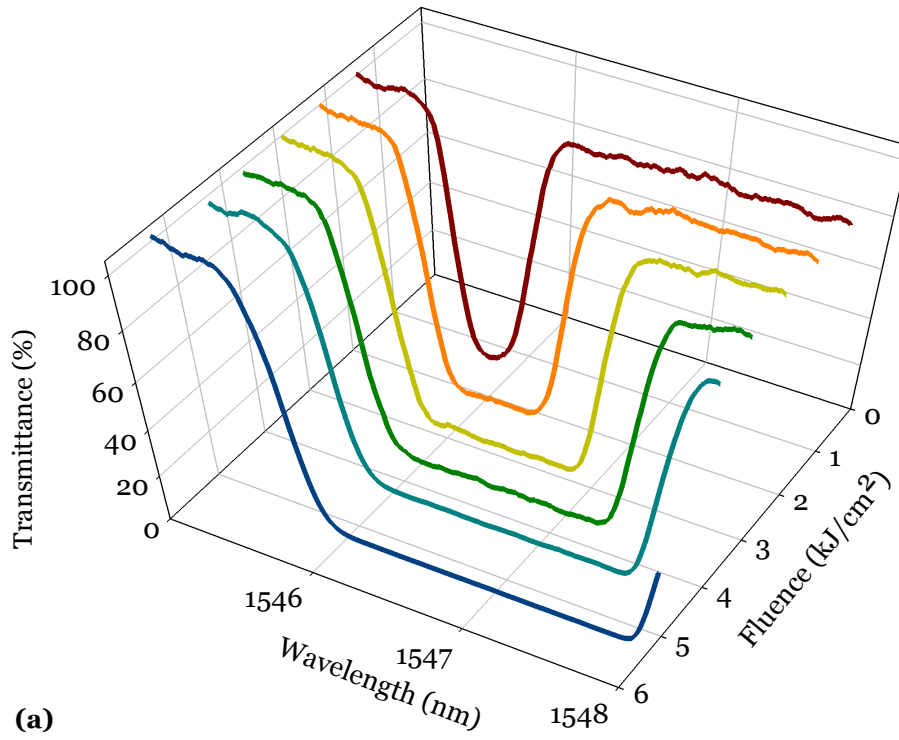


Figure 4-10. Evolution of spectral features of sample I-2: (a) at λ_B and (b) at $2/3 \lambda_B$.

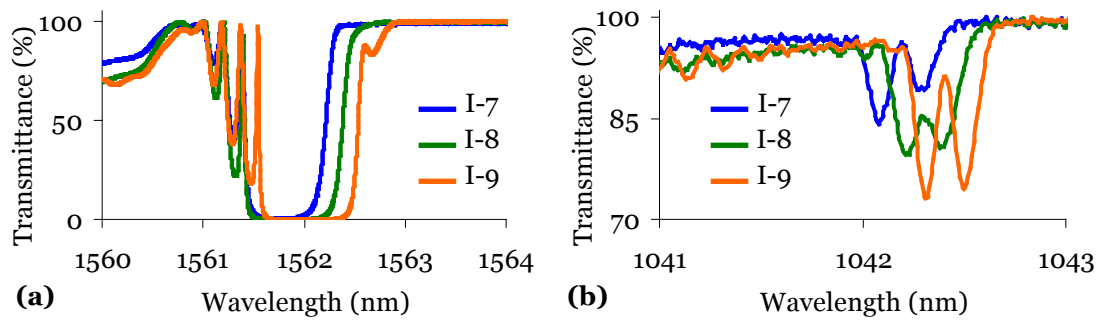


Figure 4-11. Transmission spectra measured after fabrication of samples I-7, I-8 and I-9 **(a)** at λ_B and **(b)** at $2/3 \lambda_B$.

As can be seen in Figure 4-11, a similar double-dip structure has also been observed in samples I-7, I-8 and I-9 which were written in fibre F-3 with standard phase mask SM-3 and the experimental arrangement shown in Figure 2-2. This phase mask and arrangement were different to those used for sample I-2 but the fibre type was the same. The three samples, I-7, I-8 and I-9, were fabricated under identical conditions as each other except the exposure fluences were 4.7, 7.0 and 10 kJ/cm², respectively. As shown in Figure 4-11, a single transmission dip was observed at λ_B and a double transmission dip structure was observed at $2/3 \lambda_B$ in the final spectra of all three samples. The transmittance of the central notch is greater for sample I-9 than for I-8. This is possibly due to the alignment of the fibre during fabrication with respect to the phase mask and the resulting Talbot diffraction pattern imprinted in the core. It is possible that the alignment of sample I-9 has allowed the features with a period equal to the phase mask to dominate the imprinted FBG resulting in more efficient destructive interference from the π phase-shifted grating planes, as will be discussed in the following section.

4.4.1 Phase-shifted FBGs

Phase-shifted gratings can be produced by the superposition of two interference patterns as discussed in section 1.4.5. The DIC microscopy of phase-mask-written FBGs presented in Chapter 3 has revealed the existence of interleaving planes of periodic refractive index modulations, which are

essentially two gratings with a period equal to the phase mask with a π phase-shift between them along the fibre. Consequently, some reflections of the phase mask period are expected to exhibit the central notch in spectral features as is characteristic of π phase-shifted gratings. It is likely that double-dip structures observed in the region of $2/3 \lambda_B$ are the result of π phase-shifted gratings induced by the multiple-beam interference produced by phase masks [119, 120].

As discussed in section 4.4, various grating samples written with phase masks exhibit a single transmission dip at λ_B and two transmission dips at $2/3 \lambda_B$ when the fibre is singlemode in both wavelength regions. As discussed in section 4.2.2, features at λ_B and $2/3 \lambda_B$ can be attributed to the $m = 2$ and $m = 3$ harmonic reflections, respectively, from a grating with a period equal to the phase mask, Λ_{pm} .

These observations are consistent with recent work that reported a split feature at $2 \lambda_B \approx 1552$ nm and a single feature at $\lambda_B \approx 785$ nm in both the reflection and transmission spectra of an FBG [119, 121]. The phase mask used in fabrication possessed a pitch of $\Lambda_{pm} = 0.536$ μm for a design wavelength 785 nm. The observed spectral features at $2 \lambda_B$ and λ_B correspond to the $m = 1$ and $m = 2$ reflections, respectively, from a grating with a period equal to the phase mask. Due to the presence of diffraction orders other than the first, the phase mask is likely to have induced a complex refractive index structure in the fibre core consisting of π phase-shifted gratings each with a period of 0.536 μm . The direct influence of other phase mask orders on spectral characteristics was verified which observed no grating reflections at $2 \lambda_B$ when all except the $\pm 1^{\text{st}}$ orders were removed [122]. Pure two-beam interference of the $\pm 1^{\text{st}}$ orders of this phase mask will produce a grating period equal to $\Lambda_{pm}/2$. Since reflections at $2 \lambda_B$ would be due to the $m = 1$ reflection from a period $\Lambda = \Lambda_{pm}$, the absence of such reflections verifies that the period equal to the phase mask is not induced in the fibre core when the zeroth and higher orders of the phase mask are removed.

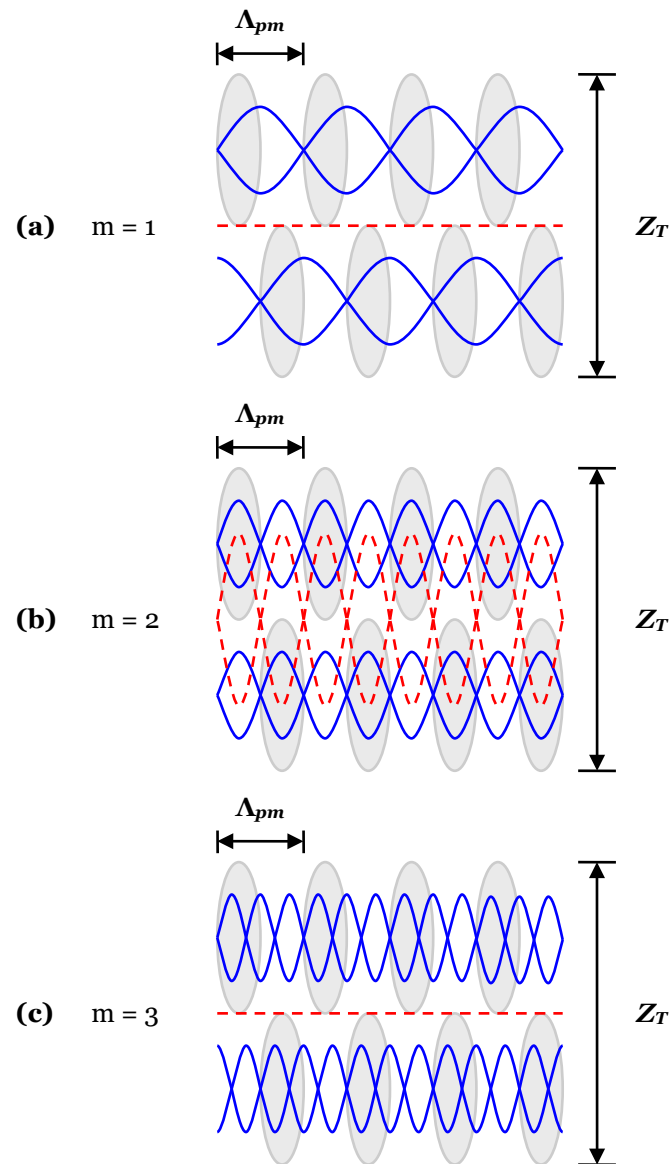


Figure 4-12. Schematic illustration of harmonic reflections from π phase-shifted Bragg gratings: the superposition (red lines) of standing waves (blue lines) formed by forward and backward propagating reflections from π phase-shifted gratings with period Λ_{pm} and repeat length Z_T induced by the phase mask fabrication technique.

The observation of single transmission dips at even harmonics ($m = 2$) and split dips at odd harmonics ($m = 1$ and $m = 3$) is consistent with the existence of π phase-shifted gratings in the fibre core each with a period equal to the phase mask, as illustrated in Figure 4-12. The standing waves generated by forward and backward propagating reflections from the face of the refractive index perturbations in the grating are illustrated with the blue lines. The

superposition of the standing waves formed by each of the interleaved gratings is illustrated with the red dotted lines. The standing waves formed by the π phase-shifted gratings are out of phase for odd harmonic reflections (Figure 4-12(a) and (c)) but in phase for even harmonic reflections (Figure 4-12(b)). Odd harmonic reflections are therefore expected to exhibit the central spectral notch due to destructive interference of the π phase-shifted reflections whereas even harmonic reflections are expected to exhibit no notch due to constructive interference. Hence at $2/3 \lambda_B$, a double-dip structure is observed in the spectra which is consistent with modelling of π phase-shifted FBGs [120].

4.5 Prism interferometer FBGs

The prism interferometer technique uses two-beam interference to fabricate FBGs as discussed in section 1.4.2. The DIC images of prism-written FBGs, presented in section 3.3, did not reveal refractive index structures that would give rise to reflections at $2/3 \lambda_B$. To investigate the spectral properties of FBGs written using two-beam interference, type I and type IIA samples were fabricated using a prism interferometer technique as described in section 2.4. The spectra at λ_B were measured using LS-3 and OSA-3 with a resolution of 0.01 nm.

The reflectance growth and wavelength shift at λ_B during fabrication of sample I-7 are shown in Figure 4-13(a) and (b), respectively, to be consistent with type I growth. The transmission spectra measured after fabrication at λ_B , shown in Figure 4-13(c), features a broad dip with $R = 99.99\%$ centred at ~ 1541.5 nm. Since the prism fabrication technique uses two-beam interference, the refractive index structure of prism FBGs are not expected to be as complex as those fabricated with a phase mask. If such a complex structure did exist in the core of this prism-written FBG, spectral features corresponding to $2/3 \lambda_B$ would lie around 1026 nm. Consequently, spectra were measured using LS-5 and OSA-3 over a broad wavelength range in this region. Figure 4-13(d) shows the transmittance of sample I-8 over a 20 nm range measured with an OSA resolution of 0.01 nm. The spectra in the region

of $2/3 \lambda_B$ shows periodic features that are most likely due to Fabry-Perot effects from fusion splices between the fibre containing the sample and the fibre coupled light source. No sharp features characteristic of reflections due to an FBG were observed in the spectral region near $2/3 \lambda_B$ of the prism-fabricated type I sample.

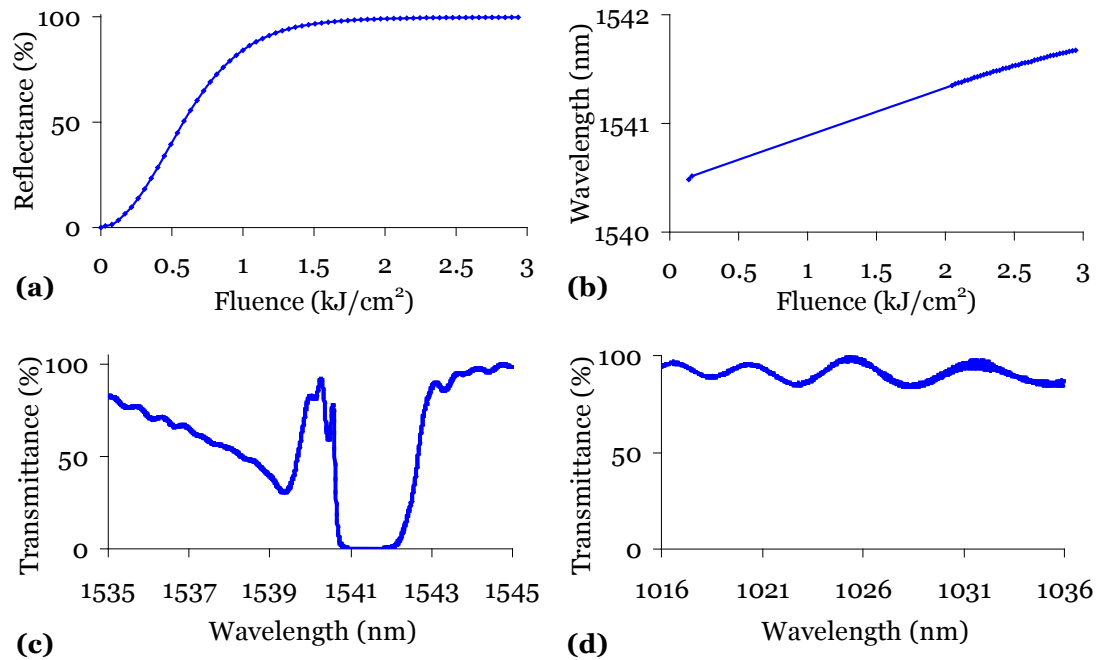


Figure 4-13. Spectral properties of a type I FBG fabricated using a prism interferometer: **(a)** reflectance growth and **(b)** spectral shift at λ_B during fabrication. Transmission spectra measured after fabrication at **(c)** λ_B and **(d)** $2/3 \lambda_B$.

As discussed in section 4.2.2, a grating period of approximately $1.07 \mu\text{m}$ is required to efficiently reflect wavelengths in the region of $2/3 \lambda_B$ ($\sim 1030 \text{ nm}$). FFTs of features in the type I prism FBG images presented in section 3.3.1 revealed much larger periods than $1.07 \mu\text{m}$. The lack of spectral features at $2/3 \lambda_B$ is consistent with the images of the sample which did not reveal the period required to cause reflections in this region. Furthermore, most images of sample Ip-1 indicated the presence of grating features with a period of $2.5 \pm 0.05 \mu\text{m}$. According to Equation 1-3 and assuming that $n_{eff} = 1.44$, light in the region of 1541.5 nm would not be efficiently reflected from a grating period of $2.5 \mu\text{m}$, but light in the region of 1030 nm would. The observation of

strong spectral features at λ_B and the lack of significant features at $2/3 \lambda_B$ provide evidence that the observed grating period of $2.5 \mu\text{m}$ does not actually exist in the FBG core but is rather an image artefact due to image resolution limitations. These spectral observations are consistent with the existence of a single period grating as formed by pure two-beam interference which could not be resolved in the DIC images.

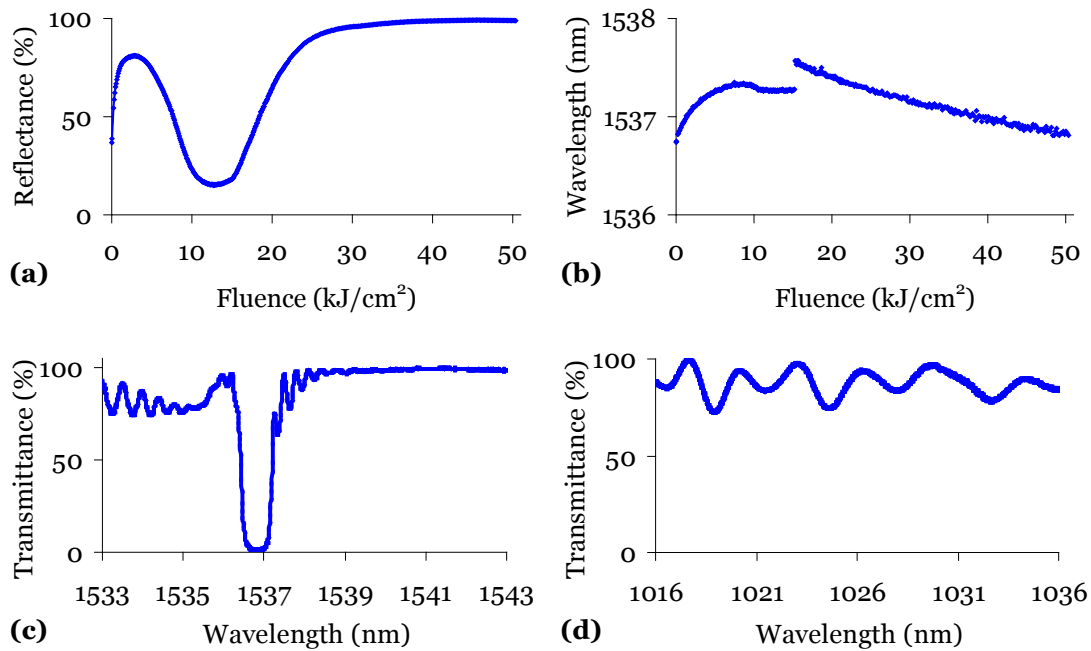


Figure 4-14. Spectral properties of a type IIA FBG fabricated using a prism interferometer: **(a)** reflectance growth and **(b)** spectral shift at λ_B during fabrication. Transmission spectra measured after fabrication at **(c)** λ_B and **(d)** $2/3 \lambda_B$.

The reflectance growth and wavelength shift at λ_B during fabrication of sample IIAp-1 are shown in Figure 4-14(a) and (b), respectively, to be consistent with type IIA growth. The transmission spectra measured after fabrication at λ_B , shown in Figure 4-14(c), features a strong dip with $R = 98.9\%$ centred at $\sim 1536.8 \text{ nm}$. Figure 4-14(d) shows the transmittance of sample IIAp-1 over a 20 nm range measured with LS-5 and OSA-3 with a resolution of 0.01 nm. The spectra in the region of $2/3 \lambda_B$ also shows periodic features that are most likely due to fusion splices between the sample and the fibre coupled light source.

No sharp features characteristic of reflections due to an FBG were observed in the spectral region near $2/3 \lambda_B$ of the prism-fabricated type IIA sample.

The absence of spectral features at $2/3 \lambda_B$ in these prism interferometer gratings are consistent with other work in which harmonic reflections of the phase mask period were not observed when only the $\pm 1^{\text{st}}$ orders were present during fabrication [122]. When all phase mask orders were present, spectral features were observed in the regions corresponding to $m = 1$ and 2 of a grating with a period $\Lambda_{pm} = 0.536 \mu\text{m}$ at approximately $2 \lambda_B = 1552 \text{ nm}$ and $\lambda_B = 785 \text{ nm}$, respectively. However, when the zeroth and higher orders were removed by a blocker and mirror arrangement so that the interference pattern was formed by only the $\pm 1^{\text{st}}$ orders, the resulting fibre grating had a period equal to $\Lambda_{pm}/2$ and consequently could not reflect light in the region of $2 \lambda_B$.

4.6 Conclusions

The spectral characteristics of various FBG samples have been analysed in this chapter. As discussed in section 4.2, spectral features in the region of $2/3 \lambda_B$ and $2/5 \lambda_B$ have been observed in type I and IIA FBGs written with a phase mask, consistent with the images in Chapter 3 which revealed gratings imprinted in the core with a period equal to the phase mask.

Spectral features in the region of $2/3 \lambda_B$ and $2/5 \lambda_B$ have been observed previously by Malo *et al.* [51] for a type II grating written using a phase mask and a single, high-fluence UV pulse. These reflections were attributed to grating features with a period equal to the phase mask since reflections at $2/3 \lambda_B$ ($\sim 1030 \text{ nm}$) and $2/5 \lambda_B$ ($\sim 620 \text{ nm}$) are not harmonics of a grating period equal to half the phase mask as expected from pure two-beam interference of the $\pm 1^{\text{st}}$ orders. Malo *et al.* attributed the formation of a grating with the phase mask period to the damaging nature of the single, high-fluence pulse used to fabricate the type II FBG. However, the observation of spectral features in the regions of $2/3 \lambda_B$ and $2/5 \lambda_B$ in type I and IIA FBGs in this work, provides evidence for the existence of a refractive index structure in

the core resulting from the Talbot diffraction pattern formed behind a phase mask during fabrication.

Multiple reflections have been observed at wavelengths other than the designed wavelength, λ_B , in type I and IIA FBGs, as discussed in section 4.2. This has also been reported previously and was explained as being due to presence of higher order modes as the fibre may not be singlemoded at lower wavelengths [86]. The type IIA FBG written with a standard phase mask exhibited stronger reflections at $2/3 \lambda_B$ than the type I FBG, which has been attributed to either the lower exposure fluence of the type I FBG or the greater saturation of the type IIA FBG. It may be expected that the magnitude of the reflectance due to other harmonics of the fundamental Bragg wavelength will depend upon the level of saturation of the refractive index variation [83].

In section 4.3, the reflectance strengths of spectral features at λ_B and $2/3 \lambda_B$ were compared in various FBGs written with phase masks. FBGs written in two different fibre types with two different phase masks were investigated. The larger core fibre exhibited singlemode propagation at λ_B but multimode propagation at $2/3 \lambda_B$, whereas the smaller core fibre exhibited singlemode propagation at both wavelengths. One phase mask was a standard, 0th order-nulled phase mask whereas the other was custom designed to provide a higher 0th order contribution and approximately equal contributions from both of the $\pm 1^{\text{st}}$ and $\pm 2^{\text{nd}}$ orders.

In comparison to the reflectance strength at λ_B , the strengths of features at $2/3 \lambda_B$ of both the standard and custom phase mask FBGs were observed to be low when propagating under multimode conditions and higher when under singlemode conditions. These observations are consistent with the modal overlaps in the two fibres at respective wavelength as discussed in section 4.3.1. In the larger core fibre, the fundamental mode at 1550 nm fills a greater fraction of the core than at 1035 nm. In the smaller core fibre, the fundamental modes at both wavelengths fill a larger fraction of the core than in the larger core fibre. Since propagating modes fill a greater fraction of the

core under singlemode conditions, it is expected that a higher fraction of power will interact with the grating and lead to higher reflectances.

Fibre Bragg gratings written with the custom phase mask (which provided higher 0th and $\pm 2^{\text{nd}}$ orders) exhibited stronger reflections at $2/3 \lambda_B$ than FBGs written with a standard, 0th order nulled phase mask. Although the exposure fluences of the custom and standard phase mask samples cannot be compared directly, the exposure fluences of the custom-made phase mask samples were comparative to the standard phase mask samples since the fluence was approximately doubled to compensate for the lower contribution from the $\pm 1^{\text{st}}$ diffraction orders. Consequently, the observation of stronger reflectance strengths at $2/3 \lambda_B$ for the custom phase mask FBGs is consistent with the dominance of grating features with a period equal to the phase mask. This is consistent with the diffraction pattern formed behind the custom-made phase mask, as discussed in section 3.1.2.

As discussed in section 4.4, the observation of single transmission dips at even harmonics ($m = 2$) and split dips at odd harmonics ($m = 1$ and $m = 3$) is consistent with the existence of π phase-shifted gratings in the fibre core each with a period equal to the phase mask. Odd harmonic reflections are expected to exhibit a central spectral notch due to destructive interference of the π phase-shifted forward and backward propagating reflections whereas even harmonic reflections are expected to exhibit no notch due to constructive interference.

Type I and IIA FBGs written with a prism interferometer did not exhibit spectral features at $2/3 \lambda_B$. These observations are consistent with the existence of a single period grating as formed by pure two-beam interference (discussed in section 3.1.1). FBGs with such a refractive index structure will exhibit first-order reflections at λ_B and no reflections at $2/3 \lambda_B$.

Chapter 5:

Harmonic Reflectance Growth

The observation of spectral features at $2/3 \lambda_B$ for the phase-mask-written samples I-1 to I-4 in section 4.3 is consistent with the refractive index structures observed in the images of these samples. The images of all four samples, presented in sections 3.4 and 3.5, revealed the existence of π phase-shifted gratings with a period equal to the period of the phase mask used in fabrication, which would give rise to harmonic reflections in the region of $2/3 \lambda_B$. In addition to the phase mask period, a period equal to half the phase mask period has been observed to exist in the core of phase mask FBGs as a result of averaging across the Talbot diffraction pattern, as illustrated in Figure 1-9(d).

As discussed in section 4.2.2, spectral features at $2/3 \lambda_B$ occur only as a third harmonic reflection from a grating with a period equal to the phase mask, Λ_{pm} . Spectral features at λ_B , however, are harmonic reflections of both periods expected to be present in the FBG, Λ_{pm} and $\Lambda_{pm}/2$. It is therefore possible that spectral features at λ_B are caused by harmonic reflections from either of the gratings inside the FBG or a combination of both. In order to further understand the origins of these spectral features, the growth with increasing fluence of spectral features at λ_B and $2/3 \lambda_B$ is compared with a theoretical model in this chapter.

The induced refractive index change at different harmonic wavelengths of a type I fibre grating was reported by Xie *et al.* [83] to exhibit a saturated exponential dependence on the UV fluence. This chapter begins by presenting the theory of the Xie *et al.* model, which is used in the remainder of the

chapter to analyse the spectral growth of harmonic reflections of type I FBGs. To compare the measured reflectance growth in the $2/3 \lambda_B$ spectral region with the measured growth at λ_B , the multimode and singlemode samples discussed in section 4.3 will be analysed here in terms of the Xie *et al.* model for reflectance growth as a function of fluence.

5.1 The Xie model

As described in section 1.5.3, the reflectance of a FBG at a wavelength λ_m is given by [5]:

$$R_m(l, \lambda_m) = \tanh^2 \left(\frac{\pi \Delta n_m l \eta(\lambda_m)}{\lambda_m} \right) \quad \text{Equation 1-11}$$

where l is the grating length and $\eta(\lambda_m)$ is the overlap between the fundamental mode and the index modulation at λ_m and Δn_m is the amplitude of the induced refractive index at λ_m .

As described in section 1.5.4, the contributions of higher order components can be determined from a Fourier expansion of the induced refractive index profile. Assuming that the index change profile of a FBG has a constant period Λ and is only a function of the distance along the fibre z , the contributions of higher order components to the induced refractive index profile can be described by [83]:

$$\begin{aligned} \Delta n(z) = & \Delta n_o + \Delta n_1 \cos \left(\frac{2\pi z}{\Lambda} + \varphi_1 \right) + \Delta n_2 \cos \left(\frac{4\pi z}{\Lambda} + \varphi_2 \right) \\ & + \Delta n_3 \cos \left(\frac{6\pi z}{\Lambda} + \varphi_3 \right) \dots, \quad 0 \leq z \leq l, \\ \Delta n(z) = & 0, \quad z > l \text{ and } z < 0, \end{aligned} \quad \text{Equation 1-14}$$

where Δn_o is determined experimentally using Equation 1-13, l is the grating length and $(\varphi_1, \varphi_2, \varphi_3)$ and $(\Delta n_1, \Delta n_2, \Delta n_3)$ represent the first three terms of the Fourier phase and amplitude spectra, respectively.

The growth of the induced refractive index change during the fabrication of gratings in germanium-doped silica fibre without hydrogen or deuterium-presensitisation can be described by a power law of the form $\Delta n \propto t^\alpha$, where α increases with power density [50, 123]. Fibres that are presensitised with hydrogen or deuterium however, normally follow a saturating exponential time t dependence of the form $\Delta n \propto 1 - \exp(-t/\tau)$ [124], where τ is a fitting parameter. The mechanisms for grating growth in the two fibre types are almost certainly different [53], with saturated exponential growth most likely related to the absorption of one UV photon while power law growth is most likely related to multiple photon absorption.

Xie *et al.* [83] reported that the growths of first and second-order reflectances from a Bragg grating are described well by a model in which the photoinduced index change $\Delta n(z, N)$ depends upon the number N of laser pulses and upon the local fluence of the beam impinging on the fibre, as follows:

$$\Delta n(z, N) = \Delta n_o \left(1 - e^{-k N \left(1 + \cos\left(\frac{2\pi z}{\Lambda}\right)\right)} \right) \quad \text{Equation 5-1}$$

where k is a fitting parameter that is proportional to the intensity of the writing beam. Assuming the Fourier phase components are zero, the Fourier amplitude spectra in Equation 1-14 can then be written as a function of z and N from the Fourier coefficients of Equation 5-1:

$$\Delta n_m(z, N) = \frac{2}{\Lambda} \int_0^\Lambda \Delta n_o \left(1 - e^{-k N \left(1 + \cos\left(\frac{2\pi z}{\Lambda}\right)\right)} \right) \times \cos\left(\frac{2m\pi z}{\Lambda}\right) dz,$$

for ($m = 1, 2, 3\dots$).

Equation 5-2

The solutions of Equation 5-2 are obtained numerically and when substituted into Equation 1-11, can be used to describe the growth with increasing fluence of harmonic reflectances from the FBG.

5.1.1 Data analysis

An iterative process which minimised the root mean square error (*RMSE*) was used to apply theoretical fits to the experimental data in this thesis. The *RMSE* (or standard error of estimate) between the measured value, y_m , and the estimated theoretical value, y_e , is given by [125]:

$$RMSE = \sqrt{\frac{\sum_{i=1}^n (y_{m,i} - y_{e,i})^2}{n}} \quad \text{Equation 5-3}$$

where n is the number of data points. The curves of best fit were determined numerically by varying fitting parameters until the minimum *RMSE* was obtained. The quality of each fit is assessed by calculating the square of the Pearson product moment correlation coefficient, r^2 , using the expression [125]:

$$r = \frac{\sum_{i=1}^n (y_{m,i} - \overline{y_m})(y_{e,i} - \overline{y_e})}{\sqrt{\sum_{i=1}^n (y_{m,i} - \overline{y_m})^2 \sum_{i=1}^n (y_{e,i} - \overline{y_e})^2}} \quad \text{Equation 5-4}$$

where $\overline{y_m}$ and $\overline{y_e}$ are the average of the measured and estimated data, respectively.

5.1.2 Model parameters

The Xie *et al.* model describes the growth of induced refractive indices due to different harmonic components in terms of N , the number of laser pulses that the fibre was exposed to during fabrication, and a dimensionless fitting parameter k . In this work, continuous wave (CW) laser radiation was used and exposure is described in terms of cumulative fluence, F in units of (kJ/cm²). In order to apply the model to the CW-laser-written samples in this work, FBG growth will be characterised in terms of fluence F with units of (kJ/cm²) and

fitting parameter k with units of (cm^2/kJ). The fitting parameter k is likely to be co-dependant on many factors involved in the fabrication process, including the photosensitivity of the fibre which was enhanced by hydrogen loading, the placement of the fibre behind the phase mask and the quality of the interference pattern formed behind the phase mask which is ultimately photo-imprinted in the fibre core.

As discussed in section 4.2.2, spectral features at $2/3 \lambda_B$ occur only as a third harmonic reflection from a grating with a period equal to the phase mask, Λ_{pm} . Consequently, the data for the growth of the peak reflectance at $2/3 \lambda_B$ with increasing fluence is analysed using Equation 1-11 and the Xie *et al.* model for $\Delta n_m(z, N)$ using the $m = 3$ solution of Equation 5-2 for $\Lambda = \Lambda_{pm}$. Spectral features at λ_B , however, are harmonic reflections of both periods expected to be present in the FBG, Λ_{pm} and $\Lambda_{pm}/2$. To investigate the origins of reflections at λ_B , the Xie *et al.* model is applied to the measured growth of the peak reflectance at λ_B for both possible cases: (a) for $m = 1$ of a grating with period $\Lambda = \Lambda_{pm}/2$ and (b) for $m = 2$ of a grating with period $\Lambda = \Lambda_{pm}$. Since growth at $2/3 \lambda_B$ can only be described by the $m = 3$ case for $\Lambda = \Lambda_{pm}$, the fits were optimised for this case by varying the parameter k for the lowest *RMSE* (Equation 5-3) between the calculated and the measured reflectances at $2/3 \lambda_B$.

Since spectral features at λ_B can result from the $m = 1$ reflection from a $\Lambda_{pm}/2$ grating or from the $m = 2$ reflection from a $\Lambda = \Lambda_{pm}$ grating, the two cases will first be analysed separately to investigate the contribution of each component. However, it is also possible that the measured growth at λ_B is due to a combination of reflectances from both grating periods. To investigate the combined contribution, the total induced refractive index change at λ_B will be considered as:

$$\Delta n_T = a \Delta n_1(\lambda_B) + b \Delta n_2(\lambda_B) \quad \text{Equation 5-5}$$

where a and b are the contribution factors of the Fourier amplitudes $\Delta n_1(\lambda_B)$ and $\Delta n_2(\lambda_B)$, respectively. The induced refractive index change at λ_B is assumed to be due only to these components such that the sum of the factors a and b is equal to 1 (or 100%). Since the Fourier amplitudes are coupled, the parameters a and b cannot be estimated independently but will be estimated from the measured data via fits to the measured reflectance growths. The measured reflectance growth at λ_B will then be analysed using a modified form of Equation 1-11:

$$R(l, \lambda_B) = \tanh^2 \left(\frac{\pi \Delta n_T l \eta(\lambda_B)}{\lambda_B} \right). \quad \text{Equation 5-6}$$

Sample	I-1	I-2	I-3	I-4
l (± 0.5 mm)	5.0	8.0	4.5	12.0
F_T (kJ/cm ²)	18 \pm 3	5 \pm 1	31 \pm 6	10 \pm 2
λ_B (± 0.05 nm)	1546.30	1546.80	1551.10	1551.20
$n_{cl}(\lambda_B)$ ($\pm 1 \times 10^{-5}$)	1.44407	1.44406	1.44401	1.44401
$n_{co}(\lambda_B)$ ($\pm 1 \times 10^{-5}$)	1.45262	1.45850	1.45256	1.45845
$V(\lambda_B)$ (± 0.01)	2.37	1.50	2.36	1.50
$\Delta\lambda_B$ (± 0.05 nm)	1.28	1.38	1.68	1.09
$n_{eff}(\lambda_B)$ ($\pm 1 \times 10^{-5}$)	1.44852	1.44732	1.44845	1.44724
$\eta(\lambda_B)$ (± 0.1)	0.8	0.5	0.8	0.5
$\Delta n_o(\lambda_B)$ ($\times 10^{-3}$)	1.49 \pm 0.04	2.6 \pm 0.3	1.97 \pm 0.05	2.1 \pm 0.2
λ_3 (± 0.05 nm)	1033.10	1038.10	1038.04	1040.64
$n_{cl}(\lambda_3)$ ($\pm 1 \times 10^{-5}$)	1.45001	1.44995	1.44995	1.44991
$n_{co}(\lambda_3)$ ($\pm 1 \times 10^{-5}$)	1.45856	1.46444	1.45850	1.46441
$V(\lambda_3)$ (± 0.01)	3.55	2.24	3.53	2.23
$\Delta\lambda_3$ (± 0.05 nm)	0.56	1.49	1.28	0.97
$n_{eff}(\lambda_3)$ ($\pm 1 \times 10^{-5}$)	1.45622	1.45700	1.45615	1.45695
$\eta(\lambda_3)$ (± 0.1)	0.9	0.7	0.9	0.7
$\Delta n_3(\lambda_3)$ ($\times 10^{-3}$)	0.87 \pm 0.01	3.0 \pm 0.4	1.99 \pm 0.03	1.9 \pm 0.2

Table 5-1. Measured and calculated parameters of the standard and custom-made phase mask FBGs studied in this work.

The sample parameters used in applying the Xie *et al.* model are summarised in Table 5-1. The listed parameters include grating length l and total UV fluence F_T . The Bragg wavelength, λ_B , is the wavelength of the peak reflectance inferred from transmission spectra measured after fabrication in section 4.3 and the wavelength shift $\Delta\lambda_B$, was inferred from $F = 0$ intercepts of linear fits applied to the evolution of λ_B with increasing fluence F . The main spectral features at $2/3 \lambda_B$ are here denoted λ_3 , and were also inferred from the relevant transmission spectra measured after fabrication in section 4.3. The wavelength shifts $\Delta\lambda_3$, were also inferred from $F = 0$ intercepts of linear fits applied to the evolution of λ_3 with increasing fluence F . The core and cladding indices were calculated using Equation 1-5 and the known fibre parameters in Table 2-4. The normalised frequencies $V(\lambda_B)$ and $V(\lambda_3)$ were calculated using Equation 1-10. The effective indices $n_{eff}(\lambda_B)$ and $n_{eff}(\lambda_3)$ and mode power fractions $\eta(\lambda_B)$ and $\eta(\lambda_3)$ were calculated using Fimmwave software, as described in section 4.3.1. The mean index changes $\Delta n_o(\lambda_B)$ and $\Delta n_o(\lambda_3)$ were inferred from the respective wavelength shifts using Equation 1-13.

5.2 Standard phase mask

5.2.1 Multimode conditions

The spectral properties at λ_B and $2/3 \lambda_B$ of sample I-1 were presented and discussed in section 4.3.3. The measured reflectance growth of the spectral features labelled 1 (at λ_B) and 2 (at $2/3 \lambda_B$) in Figure 4-8(a) and (b), respectively, are plotted in Figure 5-1 as blue diamonds and green squares, respectively. As was discussed in section 4.3.3, the growth of the reflectance peak at $2/3 \lambda_B$ was observed to be much slower than the growth of the reflectance peak at λ_B , which is attributed to the multimoded nature of the fibre at $2/3 \lambda_B$.

The growth of the reflectance peak at $2/3 \lambda_B$ was fitted with the Xie *et al.* model for $m = 3$ and $\Lambda = \Lambda_{pm}$, as shown by the solid green lines in Figure 5-1. The best fit was provided for $k = 0.114 \text{ cm}^2/\text{kJ}$ with a *RMSE* between the

measured and modelled reflectances of 0.03. The resulting fits for the growth of the reflectance peak at λ_B , firstly for $m = 1$ with $\Lambda = \Lambda_{pm}/2$ and secondly for $m = 2$ with $\Lambda = \Lambda_{pm}$ are shown in Figure 5-1(a) by the solid orange and purple lines, respectively.

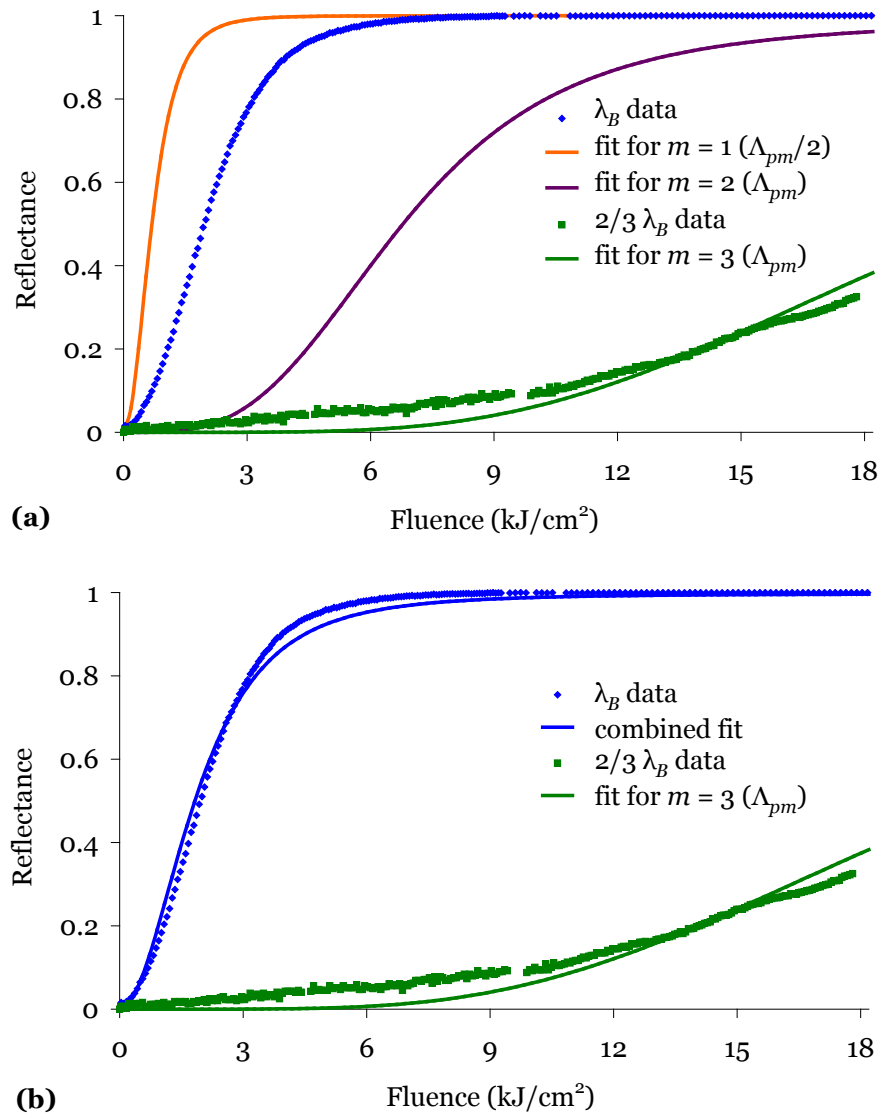


Figure 5-1. The measured and modelled reflectance growth of spectral features at λ_B and $2/3 \lambda_B$ of sample I-1: **(a)** with fits for λ_B as $m = 1$ of a $\Lambda_{pm}/2$ grating, for λ_B as $m = 2$ of a Λ_{pm} grating and for $2/3 \lambda_B$ as $m = 3$ of a Λ_{pm} grating; **(b)** with fits for λ_B as a combination of both harmonic components and for $2/3 \lambda_B$ as $m = 3$ of a Λ_{pm} grating.

As can be seen in Figure 5-1(a), the reflectance growth at λ_B is not described particularly well by either of the cases $m = 1$ (for $\Lambda_{pm}/2$) or $m = 2$ (for Λ_{pm})

alone. When the data were analysed as a combination of these components given by Equation 5-5, the factors $a = 39.5 \pm 0.5\%$ and $b = 60.5 \pm 0.5\%$ provided the fit with lowest *RMSE* (shown in Figure 5-1(b) by the solid blue line), indicating that a greater percentage contribution to the observed reflectance growth is provided by the $m = 2$ component of a grating with a period Λ_{pm} . The measured data shown in Figure 5-1(a) appears to be more closely described by the modelled growth of the $m = 1$ component of a grating with a period $\Lambda_{pm}/2$, which is due to the non-linear relationship between the reflectance and induced refractive index change. Since reflectance is proportional to \tanh^2 of the induced refractive index change, a higher contribution to the induced refractive index change in this case has resulted in an apparently smaller effect on the observed reflectance growth. Consequently, the fitting parameters a and b obtained for sample I-1 indicate that the observed reflectance growth at λ_B is due to approximately 60% contribution from the $m = 2$ (for Λ_{pm}) component approximately 40% contribution from the the $m = 1$ (for $\Lambda_{pm}/2$) component.

Variable	λ_B			$2/3 \lambda_B$
	1	2	1 and 2	3
m	1	2	1 and 2	3
Λ (μm)	$\Lambda_{pm}/2$	Λ_{pm}	$\Lambda_{pm}/2$ and Λ_{pm}	Λ_{pm}
<i>RMSE</i>	0.20	0.44	0.02	0.03
r^2	0.69	0.51	0.996	0.98

Table 5-2. Assessment of Xie *et al.* model application to measured harmonic reflectance growth of sample I-1.

The interference patterns generated behind the standard phase mask were expected to be dominated by features with a period equal to $\Lambda_{pm}/2$, as discussed in section 3.1.2. The modelling results for this sample suggest that the refractive index features inside the FBG with a period equal to $\Lambda_{pm}/2$ have a measurable effect on the observed reflectance growth at λ_B , but the growth is predominantly due to the second harmonic reflection from the FBG features with a period equal to the phase mask. The linescan through the expected

intensity distribution generated by the standard phase mask, shown in Figure 3-2(c), revealed intensity peaks with a period equal to Λ_{pm} and interleaving peaks forming the $\Lambda_{pm}/2$ period with intensities of approximately 60% of the Λ_{pm} period peaks. It is possible that the intensity of the interleaving peaks in the phase mask interference pattern are not strong enough to induce the required refractive index changes and enable the $\Lambda_{pm}/2$ period to dominate the structure inside the core, leading to the observed dominance of the Λ_{pm} period in the spectral results.

5.2.2 Singlemode conditions

The spectral properties at λ_B and $2/3 \lambda_B$ of standard phase mask sample I-2 were presented and discussed in section 4.3.3. The measured reflectance growth of the spectral features labelled 5 (at λ_B) and 6 (at $2/3 \lambda_B$) in Figure 4-8(e) and (f), respectively, are plotted in Figure 5-2 as blue diamonds and green squares, respectively. As was discussed in section 4.3.3, the observed growth of reflectance peak at $2/3 \lambda_B$ is similar to the growth of the reflectance peak at λ_B , which is attributed to the singlemoded nature of the fibre in both spectral regions.

The growth of the reflectance peak at $2/3 \lambda_B$ was fitted with the Xie *et al.* model for $m = 3$ and $\Lambda = \Lambda_{pm}$, as shown by the solid green line in Figure 5-2. The best fit was provided for $k = 0.94 \text{ cm}^2/\text{kJ}$ with a *RMSE* between the measured and modelled reflectances of 0.05. The resulting fits for the growth of the reflectance peak at λ_B firstly for $m = 1$ with $\Lambda = \Lambda_{pm}/2$ and secondly for $m = 2$ with $\Lambda = \Lambda_{pm}$ are shown in Figure 5-2(a) by the solid orange and purple lines, respectively.

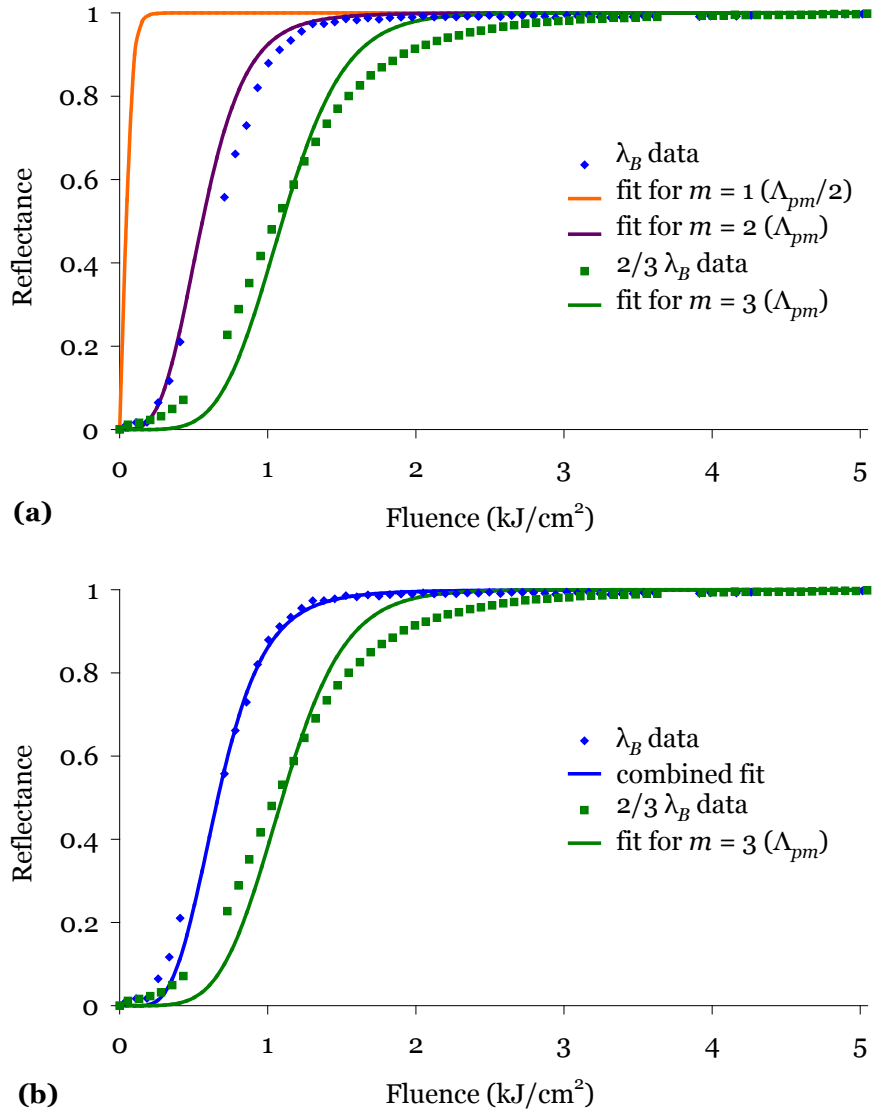


Figure 5-2. The measured and modelled reflectance growth of spectral features at λ_B and $2/3 \lambda_B$ of sample I-2: **(a)** with fits for λ_B as $m = 1$ of a $\Lambda_{pm}/2$ grating, for λ_B as $m = 2$ of a Λ_{pm} grating and for $2/3 \lambda_B$ as $m = 3$ of a Λ_{pm} grating; **(b)** with fits for λ_B as a combination of both harmonic components and for $2/3 \lambda_B$ as $m = 3$ of a Λ_{pm} grating.

Variable	λ_B			$2/3 \lambda_B$
	1	2	1 and 2	3
m	1	2	1 and 2	3
Λ (μm)	$\Lambda_{pm}/2$	Λ_{pm}	$\Lambda_{pm}/2$ and Λ_{pm}	Λ_{pm}
RMSE	0.30	0.04	0.02	0.05
r^2	0.29	0.99	0.998	0.99

Table 5-3. Assessment of Xie *et al.* model application to measured harmonic reflectance growth of sample I-2.

As can be seen in Figure 5-2, the data for sample I-2 are described well when the reflection at λ_B is considered as the second harmonic ($m = 2$) of a grating with a Λ_{pm} period. When the data were analysed as a combination of both components given by Equation 5-5, the factors $a = 3 \pm 0.5\%$ and $b = 97 \pm 0.5\%$ provided the fit with lowest *RMSE* which is shown in Figure 5-2(b) by the solid blue line. Considering the reflectance growth at λ_B as being due to a combination of both harmonic components provided only a slight improvement to the fit to the data over the case for $m = 2$ with $\Lambda = \Lambda_{pm}$ alone.

These results suggest that Λ_{pm} is the dominant period in the refractive index structure that exists in the smaller fibre core sample I-2. As discussed in section 4.3.3, the spectral characteristics of the singlemode, smaller core fibre samples also indicated that the gratings could be dominated by the Λ_{pm} period since the reflectances at $2/3 \lambda_B$ of both the standard and custom-made mask samples were much stronger than the multimode, larger core fibre samples. Although the predicted diffraction pattern of the standard phase mask is dominated by the $\Lambda_{pm}/2$ period, the spectral results indicate that the imprinted FBGs are instead dominated by the Λ_{pm} period since the measured reflectances are best described as harmonics of this period. The modelling suggests that the reflectance growth at λ_B of sample I-2 occurs predominantly as the second harmonic reflection of features with the Λ_{pm} period. This is possibly due to the smaller core of the fibre restricting the interaction area and preventing the interleaving fringes from forming the half period structure.

The data in Figure 5-2 are actually described quite well by the Xie *et al.* model for the 2nd and 3rd harmonics of a structure dominated by the Λ_{pm} period. Discrepancies between the data and the fits are seen mainly in the slopes of the reflectance growth prior to saturation which is reached at approximately $F = 2 \text{ kJ/cm}^2$ for λ_B and $F = 3 \text{ kJ/cm}^2$ for $2/3 \lambda_B$. The discrepancies in the slopes are most likely due to uncertainties associated with estimating the induced refractive index changes and other fitting parameters. These results indicate that when features in both spectral regions are under singlemode conditions, the peak reflectances demonstrate similar growth characteristics.

In contrast, when features at $2/3 \lambda_B$ are propagating under multimode conditions, as for sample I-1, the peak reflectance growth at $2/3 \lambda_B$ is much slower than the growth of singlemode features at λ_B .

5.3 Custom-made phase mask

5.3.1 Multimode conditions

The spectral properties at λ_B and $2/3 \lambda_B$ of the custom-made phase mask sample I-3 were presented and discussed in section 4.3.4. The measured reflectance growth of the spectral features labelled 1 (at λ_B) and 2 (at $2/3 \lambda_B$) in Figure 4-9(a) and (b), respectively, are plotted in Figure 5-3 as blue diamonds and green squares, respectively. The growth of both reflectance peaks of sample I-3 exhibited two phases of growth; one which slowed after $F \approx 9 \text{ kJ/cm}^2$ and began to grow again at around $F \approx 12 \text{ kJ/cm}^2$. Although reminiscent of type IIA growth, this is highly unlikely in this hydrogen-loaded standard telecommunications fibre since type IIA growth is typically only observed in high germanium and co-doped fibres. Normal type I growth was evident from the observed linear shifts in peak reflectance wavelengths (Figure 4-9(c) and (d)) so it is likely that this abnormal growth was caused by an interruption to the UV exposure conditions during fabrication. This was possibly due to a drop in the power of the UV laser or a disruption to the beam or fibre position. To simplify the analysis of this growth in terms of the Xie *et al.* model, the second growth phase of the reflectance peaks will be treated as normal type I growth.

The second growth phase of the reflectance peak at $2/3 \lambda_B$, from $F \approx 12 \text{ kJ/cm}^2$ onwards, was fitted with the Xie *et al.* model for $m = 3$ and $\Lambda = \Lambda_{pm}$, as shown by the solid green lines in Figure 5-3. The best fit was provided for $k = 0.044 \text{ cm}^2/\text{kJ}$ with a *RMSE* of 0.02. The resulting fits for the second growth phase of the reflectance peak at λ_B firstly for $m = 1$ with $\Lambda = \Lambda_{pm}/2$ and secondly for $m = 2$ with $\Lambda = \Lambda_{pm}$ are shown in Figure 5-3(a) by the solid orange and purple lines, respectively.

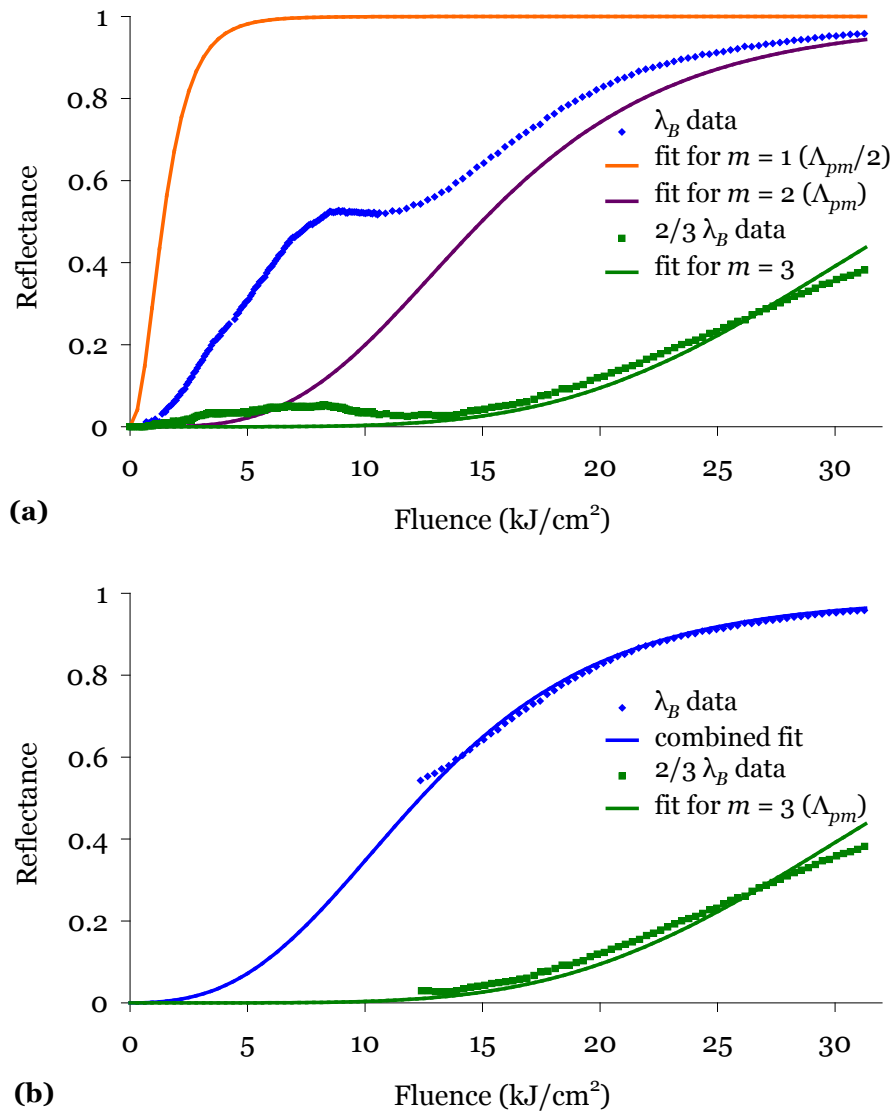


Figure 5-3. The measured and modelled reflectance growth of spectral features at λ_B and $2/3 \lambda_B$ of sample I-3: **(a)** with fits for λ_B as $m = 1$ of a $\Lambda_{pm}/2$ grating, for λ_B as $m = 2$ of a Λ_{pm} grating and for $2/3 \lambda_B$ as $m = 3$ of a Λ_{pm} grating; **(b)** with fits for λ_B as a combination of both harmonic components and for $2/3 \lambda_B$ as $m = 3$ of a Λ_{pm} grating (and early data omitted).

Variable	λ_B			$2/3 \lambda_B$
	1	2	1 and 2	3
m	1	2	1 and 2	3
Λ (μm)	$\Lambda_{pm}/2$	Λ_{pm}	$\Lambda_{pm}/2$ and Λ_{pm}	Λ_{pm}
RMSE	0.49	0.25	0.01	0.03
r^2	0.39	0.84	0.89	0.98

Table 5-4. Assessment of Xie *et al.* model application to measured harmonic reflectance growth of sample I-3.

As can be seen in Figure 5-3(a), the data for sample I-3 are described well when the reflection at λ_B is considered as the second harmonic ($m = 2$) of a grating with a Λ_{pm} period. When the data were analysed as a combination of both components given by Equation 5-5, the factors $a = 5 \pm 0.5\%$ and $b = 95 \pm 0.5\%$ provided the fit with lowest *RMSE*, which is shown in Figure 5-3(b) by the solid blue line. Considering the reflectance growth at λ_B as being due to a combination of both harmonic components provided only a slight improvement to the fit to the data over the case for $m = 2$ with $\Lambda = \Lambda_{pm}$ alone. The modelling indicates that the observed reflectance growth at λ_B for sample I-3 is predominantly due to second harmonic reflections from the Λ_{pm} period features which is consistent with the expected intensity distributions of the custom made phase mask.

The growth of the reflectance peak at $2/3 \lambda_B$ of this custom-made phase mask sample was observed to be slower than the growth of the reflectance peak at λ_B . A significant delay was also observed for the multimode sample I-1 between the growths at $2/3 \lambda_B$ and λ_B . However, the growth at both wavelengths was relatively faster for the custom-made phase mask, larger core fibre sample I-3. This is attributed to the dominance of the Λ_{pm} period in the pattern formed by the custom-made phase mask.

5.3.2 Singlemode conditions

The spectral properties at λ_B and $2/3 \lambda_B$ of the custom-made phase mask sample I-4 were presented and discussed in section 4.3.4. The measured reflectance growth of the spectral features labelled 4 (at λ_B) and 5 (at $2/3 \lambda_B$) in Figure 4-9(e) and (f), respectively, are plotted in Figure 5-4 as blue diamonds and green squares, respectively.

The growth of the reflectance peak at $2/3 \lambda_B$ was fitted with the Xie *et al.* model for $m = 3$ and $\Lambda = \Lambda_{pm}$, as shown by the solid green line in Figure 5-4. The best fit was provided for $k = 0.515 \text{ cm}^2/\text{kJ}$ with a *RMSE* of 0.03. The resulting fits for the growth of the reflectance peak at λ_B firstly for $m = 1$ with

$\Lambda = \Lambda_{pm}/2$ and secondly for $m = 2$ with $\Lambda = \Lambda_{pm}$ are shown Figure 5-4 by the solid orange and purple lines, respectively.

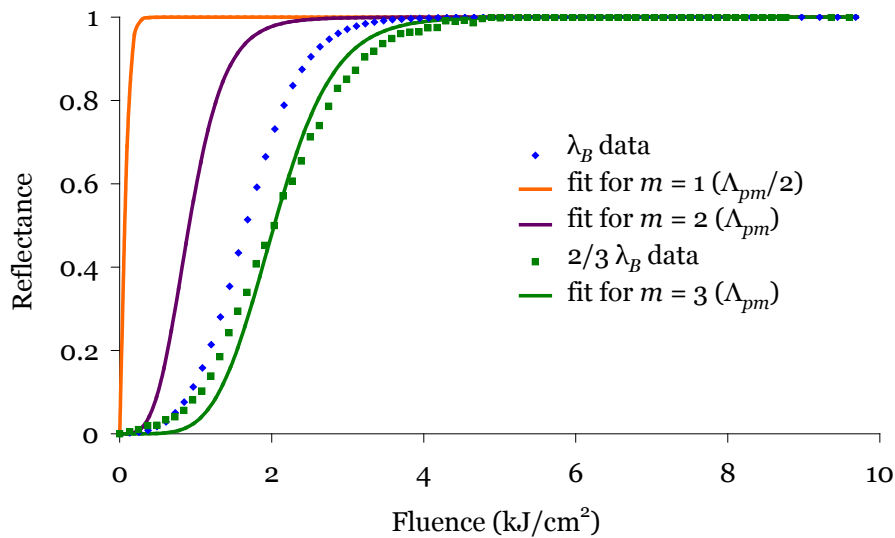


Figure 5-4. The measured and modelled reflectance growth of spectral features at λ_B and $2/3 \lambda_B$ of sample I-4: with fits for λ_B as $m = 1$ of a $\Lambda_{pm}/2$ grating, for λ_B as $m = 2$ of a Λ_{pm} grating and for $2/3 \lambda_B$ as $m = 3$ of a Λ_{pm} grating.

Variable	λ_B		$2/3 \lambda_B$
	1	2	3
m	1	2	3
Λ (μm)	$\Lambda_{pm}/2$	Λ_{pm}	Λ_{pm}
RMSE	0.38	0.18	0.03
r^2	0.10	0.80	0.99

Table 5-5. Assessment of Xie *et al.* model application to measured harmonic reflectance growth of sample I-4.

As can be seen in Figure 5-4, the best fit to the measured data for sample I-4 is provided when the reflection at λ_B is described as the second harmonic ($m = 2$) of a grating with a Λ_{pm} period. Considering the reflectance growth at λ_B as being due to a combination of both harmonic components, given by Equation 5-5, provided no improvement to the fit to the data over the case for

$m = 2$ with $\Lambda = \Lambda_{pm}$ alone. Hence the factors $a = 0\%$ and $b = 100\%$ provided the fit corresponding to the case for $m = 2$ with $\Lambda = \Lambda_{pm}$.

These results suggest that Λ_{pm} is the dominant period in the refractive index structure that exists in the core of sample I-4. As discussed in section 4.3.4, the spectral characteristics of the singlemode, smaller core fibre samples also indicated that these gratings could be dominated by the Λ_{pm} period since the reflectances at $2/3 \lambda_B$ of both the standard and custom-made mask samples were much stronger than the multimode, larger core fibre samples. The observed growths are also consistent with the predicted diffraction pattern of the custom-made phase mask which is dominated by the Λ_{pm} period.

The observed growths in the two spectral regions, however, are more similar than predicted by the Xie *et al.* model. The growth of reflectance peak at $2/3 \lambda_B$ was observed to be almost coincident with the growth of the reflectance peak at λ_B , which is attributed firstly to the singlemoded nature of the fibre at both wavelengths and secondly to the dominance of Λ_{pm} features in the pattern provided by the custom-made phase mask. The measured growth of λ_B of sample I-4 is actually slower than the predicted growth shown in Figure 5-4. As previously mentioned, the discrepancies in the slopes are most likely due to uncertainties associated with estimating the induced refractive index changes and other fitting parameters. This result for the custom-made phase mask indicates that when features in both spectral regions are under singlemode conditions, the peak reflectances demonstrate similar growth characteristics. In contrast, when features at $2/3 \lambda_B$ are propagating under multimode conditions, the peak reflectance growth is much slower than the singlemode features at λ_B .

5.4 Conclusions

The growth of the reflectance of spectral features at λ_B and $2/3 \lambda_B$ as a function of exposure fluence have been analysed in this chapter in terms of the model proposed by Xie *et al.* [83]. The type I FBGs fabricated in standard and

smaller core fibres with the standard and custom-made phase masks discussed in section 4.3 have been investigated. As discussed in section 4.2.2, spectral features at $2/3 \lambda_B$ occur only as a third harmonic reflection from a grating with a period equal to the phase mask, Λ_{pm} . Consequently, the data for the growth of the peak reflectance at $2/3 \lambda_B$ with increasing fluence were analysed using Equation 1-11 and the Xie *et al.* model for $\Delta n_m(z, N)$ using the $m = 3$ solution of Equation 5-2 for $\Lambda = \Lambda_{pm}$. Spectral features at λ_B , however, are harmonic reflections of both periods expected to be present in the FBG, Λ_{pm} and $\Lambda_{pm}/2$. To investigate the origins of reflections at λ_B , the Xie *et al.* model was applied to the measured growth of the peak reflectance at λ_B for both possible cases: (a) for $m = 1$ of a grating with period $\Lambda = \Lambda_{pm}/2$ and (b) for $m = 2$ of a grating with period $\Lambda = \Lambda_{pm}$.

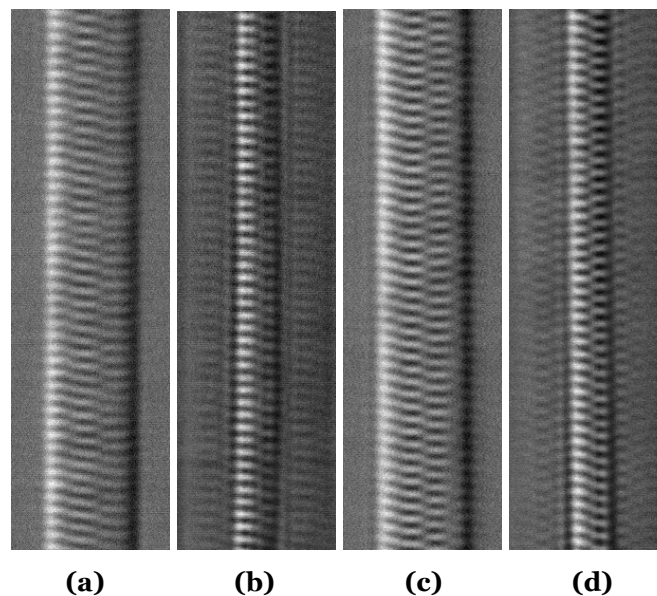


Figure 5-5. DIC images showing the imprinted Talbot diffraction patterns of type I FBGs as presented in sections 3.4 and 3.5: written with **(a)** standard phase mask in standard fibre (I-1); **(b)** standard phase mask in smaller core fibre (I-2); **(c)** custom made phase mask in standard fibre (I-3) and **(d)** custom made phase mask in smaller core fibre (I-4). The images are approximately $47 \times 14 \mu\text{m}$.

The images of samples I-1 to I-4 measured in the plane perpendicular to the writing beam were presented and analysed in sections 3.4 and 3.5. These images are shown again in Figure 5-5 to enable comparison of the imprinted Talbot diffraction patterns with the core sizes of the four samples. The Talbot

lengths measured in the images were consistent with the expected value of approximately $4.6 \mu\text{m}$. The core diameters of the standard and smaller core fibres are listed in Table 5-6. As can be seen in the images of the standard telecommunications fibre samples I-1 and I-3 in Figure 5-5(a) and (c), respectively, more than one full Talbot length ($\sim 1.6\times$) is imprinted in the core whereas approximately only 80% of one full Talbot length is imprinted in the core of the smaller core fibre samples (I-2 and I-4 in Figure 5-5(b) and (d), respectively).

The sample properties and the conclusions of the reflectance growth modelling carried out in this chapter are summarised in Table 5-6. As can be seen, the observed reflectance growth at λ_B of the standard phase mask, larger core FBG was attributed to significant contributions from each of the $m = 2$ (for Λ_{pm}) and $m = 1$ (for $\Lambda_{pm}/2$) components, as discussed in section 5.2.1. These results are not consistent with the interference pattern predicted to exist behind the standard phase mask (section 3.1.2) which is significantly dominated by features with a period equal to $\Lambda_{pm}/2$. The observed dominance of the Λ_{pm} period in the spectral results was attributed to a lack of sufficient intensities in the interference pattern generated by the standard phase mask, which would be required to enable the $\Lambda_{pm}/2$ period to dominate the structure inside the core.

Sample	Fibre	Core diameter (μm)	Phase mask pitch	Contribution from $m = 1$ of $\Lambda_{pm}/2$ a (%)	Contribution from $m = 2$ of Λ_{pm} b (%)
I-1	F-1	7.4	SM-2: 1.0668 μm	39.5	60.5
I-2	F-3	3.6		3	97
I-3	F-1	7.4	CM-2: 1.07 μm	5	95
I-4	F-3	3.6		0	100

Table 5-6. Summary of the sample properties and the modelled contributions of spectral components to the observed reflectance growth for spectral features at λ_B .

The observed reflectance growth of the standard phase mask, smaller core FBG was described well when the reflection at λ_B was considered as the second harmonic ($m = 2$) of a grating with a Λ_{pm} period, as discussed in section 5.2.2. Although the predicted diffraction pattern of the standard phase mask is dominated by the $\Lambda_{pm}/2$ period, the spectral results of the smaller core sample indicate that the photo-imprinted FBG is dominated by the Λ_{pm} period since the measured reflectances are best described as harmonics of this period. This observation was attributed to insufficient intensities in the phase mask interference pattern and the restriction of the interaction area in the smaller core fibre which prevented the interleaving fringes from forming the half period structure. The $\Lambda_{pm}/2$ period was observed to have a more significant effect on the reflectance growth at λ_B of the standard phase mask, larger core FBG than the growth of the standard phase mask, smaller core FBG. This is attributed to the larger core size allowing for more than one Talbot length to be imprinted in the core, causing the less dominant $\Lambda_{pm}/2$ period to have a greater effect on the reflections from the FBG.

The observed reflectance growth at λ_B of the custom phase mask, larger core FBG was described well as the $m = 2$ of a grating with period equal to the phase mask (Λ_{pm}), as discussed in section 5.3.1. The observed reflectance growth at λ_B of the custom made phase mask, smaller core FBG was also attributed to a larger contribution from the $m = 2$ component of a grating with a period equal to the phase mask (Λ_{pm}), as discussed in section 5.3.2. These results were attributed to the dominance of the Λ_{pm} period in the pattern formed by the custom-made phase mask, as discussed in section 3.1.2. The higher contributions of the custom-made phase mask orders other than the $\pm 1^{\text{st}}$ were found to cause the Λ_{pm} period features to dominate. Consequently, spectral features at λ_B are likely to originate as reflections from the Λ_{pm} period regardless of the fibre core size for the custom-made phase mask. The results of the reflectance growth modelling for samples I-1 to I-4 are consistent with the images presented in Figure 5-5, which show strong features with a period equal to the phase mask.

Chapter 6:

Temperature and Strain Characterisation

A number of grating samples, as discussed in Chapter 4, exhibit spectral features in the region of $2/3$ of the designed Bragg wavelength, λ_B . These are present as a result of the complex refractive index structure induced by the phase mask fabrication technique. This chapter presents investigations of the axial strain and temperature characteristics of these spectral features at $2/3 \lambda_B$ in type I and IIA gratings as the basis for dual wavelength simultaneous sensing of temperature and strain in combination with features at λ_B . The results are compared with those previously reported for dual wavelength sensors which use spectral features at λ_B and $1/2 \lambda_B$. The use of spectral features at $2/3 \lambda_B$ in combination with the strain independent fluorescence intensity ratio technique is also investigated for possible applications in simultaneous strain and temperature sensing.

6.1 Introduction

The axial (or longitudinal) strain response of FBGs arises due to both the physical elongation of the sensor (and corresponding fractional change in grating period), and the change in fibre index due to photoelastic effects. The thermal response arises due to the inherent thermal expansion of the fibre material and the temperature dependence of the refractive index. For FBGs, the wavelength dependence of the photoelastic and thermo-optic coefficients of the fibre glass causes a small variation in the ratio of responses of gratings written at different wavelengths. The shift in Bragg wavelength with strain and temperature can be expressed by [6]:

$$\Delta\lambda_B = 2n\Lambda \left(\left\{ 1 - \left(\frac{n^2}{2} \right) [P_{12} - \nu(P_{11} + P_{12})] \right\} \varepsilon + \left[\alpha + \frac{\left(\frac{dn}{dT} \right)}{n} \right] \Delta T \right)$$

Equation 6-1

where n is the effective refractive index of the fibre core, Λ is the period of the grating, ε is the applied strain, P_{ij} are the Pockel's (piezo) coefficients of the stress-optic tensor, ν is Poisson's ratio, α is the coefficient of thermal expansion of the fibre material (e.g., silica) and ΔT is the temperature change.

The factor $\left\{ \left(\frac{n^2}{2} \right) [P_{12} - \nu(P_{11} + P_{12})] \right\}$ has a value of ≈ 0.21 .

Although very attractive as sensors, FBGs suffer an inherent cross-sensitivity between temperature and strain which creates a problem for sensor systems designed to monitor strain for example, as temperature variations along the fibre path can lead to unrepresentative, thermal-apparent strain readings [6]. Some of the many schemes developed to overcome this cross-sensitivity were discussed in section 1.3. The use of two wavelengths from a single fibre sensor to measure strain and temperature simultaneously is a highly desirable and cost effective method for co-located point sensing.

Co-located sensing systems may consist of two sensor elements which have very different responses to strain ($K_{\varepsilon 1}, K_{\varepsilon 2}$) and temperature (K_{T1}, K_{T2}) located at the same point on the structure. The strain (ε) and temperature (T) can then be determined from measurements of two wavelength shifts via inversion of a transfer matrix equation [126]:

$$\begin{bmatrix} \Delta\lambda_1 \\ \Delta\lambda_2 \end{bmatrix} = \begin{bmatrix} K_{\varepsilon 1} & K_{T1} \\ K_{\varepsilon 2} & K_{T2} \end{bmatrix} \begin{bmatrix} \varepsilon \\ T \end{bmatrix}. \quad \text{Equation 6-2}$$

Successful application of the transfer matrix method requires a nonzero determinant of the response matrix, i.e. the ratio of the strain responses of the

two sensors must be different from the ratio of their temperature responses; so that the following condition is satisfied:

$$\frac{K_{\varepsilon 1}}{K_{\varepsilon 2}} \neq \frac{K_{T1}}{K_{T2}} . \quad \text{Equation 6-3}$$

If the condition in Equation 6-3 is satisfied by an amount greater than the experimental error, the sensor can in principle be used to measure temperature and strain simultaneously. The more dissimilar the ratios are, the better the capacity for discrimination between the two measurands. The ability of the sensor to discriminate between temperature and strain depends not only on the coefficients but also on the precision with which the wavelength shifts can be detected. For wavelength measurement uncertainties, a and b , in λ_1 and λ_2 , respectively, the measurement uncertainties for the sensor per pm error in the wavelength measurement can be found using [12]:

$$\Delta\varepsilon_{\max} = \pm \left(\left(\frac{K_{\varepsilon 1}^2}{a^2} + \frac{K_{\varepsilon 2}^2}{b^2} \right) - \frac{\left(\frac{K_{\varepsilon 1}K_{T1}}{a^2} + \frac{K_{\varepsilon 2}K_{T2}}{b^2} \right)^2}{\left(\frac{K_{T1}^2}{a^2} + \frac{K_{T2}^2}{b^2} \right)} \right)^{-\frac{1}{2}} , \quad \text{Equation 6-4}$$

$$\Delta T_{\max} = \pm \left(\left(\frac{K_{T1}^2}{a^2} + \frac{K_{T2}^2}{b^2} \right) - \frac{\left(\frac{K_{\varepsilon 1}K_{T1}}{a^2} + \frac{K_{\varepsilon 2}K_{T2}}{b^2} \right)^2}{\left(\frac{K_{\varepsilon 1}^2}{a^2} + \frac{K_{\varepsilon 2}^2}{b^2} \right)} \right)^{-\frac{1}{2}} . \quad \text{Equation 6-5}$$

Brady *et al.* [12] and Echevarria *et al.* [13] have reported simultaneous temperature and strain discrimination using a single grating written by interferometric and phase mask techniques respectively. These single grating sensors detect the peak reflectance shift with temperature and strain of the Bragg wavelength, λ_B , and a reflectance peak at $\sim 1/2 \lambda_B$, referred to by the authors as the first- and second-order diffraction wavelengths respectively.

The differences in responses to strain and temperature at the two different wavelengths for these sensors provide the basis for discrimination and simultaneous measurement. The reported coefficients and associated measurement uncertainties are listed in Table 6-1.

Parameter	Brady <i>et al.</i> [12]	Echevarria <i>et al.</i> [13]	Sivanesan <i>et al.</i> [14]	Xu <i>et al.</i> [8]	Shu <i>et al.</i> [18]	Kalli <i>et al.</i> [23]
λ_1 (nm)	1561	1535.85	1300	1298	1558 (IIA FBG)	1560 (IA FBG)
λ_2 (nm)	789	767.94	660	848	1558 (IA FBG)	1574 (I FBG)
λ_1/λ_2	1.978	2	1.97	1.53	1	0.99
$K_{\epsilon 1}$ (pm/ $\mu\epsilon$)	1.203	1.092	0.793*	0.96	1.074	0.818
$K_{\epsilon 2}$ (pm/ $\mu\epsilon$)	0.603	0.472	0.792*	0.59	1.075	0.828
K_{T1} (pm/ $^{\circ}\text{C}$)	11.877	9.70	6.675*	8.72	10.02	8.531
K_{T2} (pm/ $^{\circ}\text{C}$)	6.604	4.89	7.75*	6.3	7.37	7.403
$K_{\epsilon 1}/K_{\epsilon 2}$	1.995	2.314	1.001*	1.627	1.001	0.988
K_{T1}/K_{T2}	1.798	1.984	0.861*	1.384	1.36	1.152
Ratio difference (%)	10.9	16.6	16.3	17.6	36.1	16.6
Strain uncertainty ($\mu\epsilon/\text{pm}$)	± 17.44	± 14.27	$\pm 11.91^{**}$	$\pm 11.91^{**}$	± 4.4	± 11.2
Temperature uncertainty ($^{\circ}\text{C}/\text{pm}$)	± 1.72	± 1.56	$\pm 1.30^{**}$	$\pm 1.25^{**}$	± 0.54	± 1.15

Table 6-1. Axial strain and temperature characteristics of previously reported dual wavelength or dual grating sensors. * Estimated from graphs ** Calculated using the methodology of Brady *et al.* [12].

Sivanesan *et al.* [14] reported on the conditions for optimal wavelength pair selection for dual FBG simultaneous sensors of temperature and strain. It was found that the measurement precision of the sensor depended primarily on the temperature response of the fibre gratings at the respective wavelengths. Furthermore, the sensor performance is improved when the wavelength pair is made up of one wavelength above 1300 nm and one below 800 nm [14]. The numerical values of the sensing coefficients listed in Table 6-1 were not provided by the authors but were estimated from graphs for comparison with similar sensors. The associated measurement uncertainties were calculated

using the methodology of Brady *et al.* [12] and are low due to the almost identical strain responses at each wavelength.

The greatest difference between strain and temperature responses in dual grating sensors to date has been achieved using gratings in two different fibre diameters [127], however, these sensors are elaborate and more complex to manufacture on a large scale than single grating sensors. Xu *et al.* [8] demonstrated improved measurement uncertainties (see Table 6-1) through the use of two superimposed gratings in the same fibre. Shu *et al.* [18] reported very low measurement uncertainties (see Table 6-1) due to the large difference in temperature responses and almost identical strain responses of type IIA and IA fibre gratings. However the inscription of two gratings in series is also more complicated and costly for mass production than a single grating sensor.

In general, the sensors with the lowest measurement uncertainties in Table 6-1 owe their precision to the similarity in strain responses and dissimilarity in temperature responses. Also shown in Table 6-1 are the percentage differences between the ratios $K_{\epsilon_1}/K_{\epsilon_2}$ and K_{T_1}/K_{T_2} for the reported sensors. The improvements in measurement uncertainties are consistent with higher percentage differences between the ratios of the strain and temperature coefficients.

6.2 Experimental arrangement

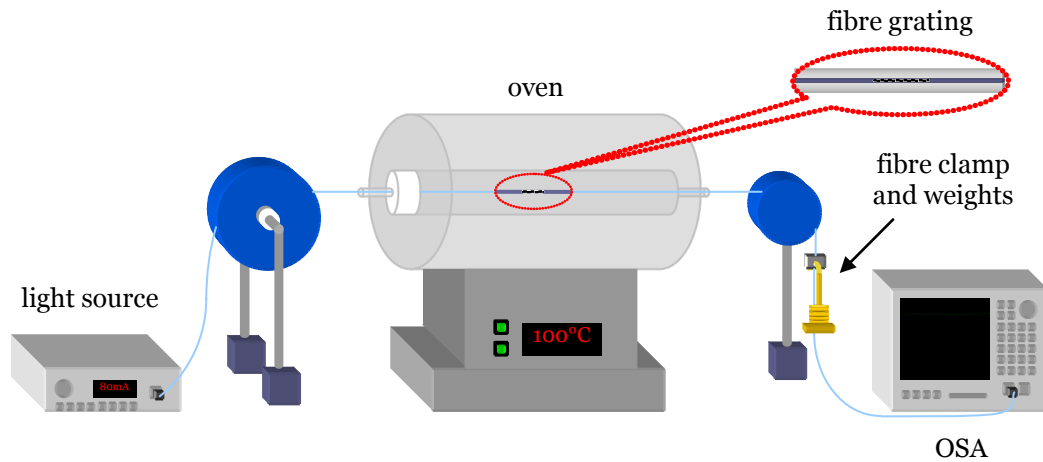


Figure 6-1. Experimental arrangement for axial strain and temperature testing.

The responses of various phase-mask-written samples to temperature and axial strain were investigated using a standard calibration technique [26] and the experimental arrangement pictured in Figure 6-1. The arrangement combined a Carbolite™ MTF 12/38/400 horizontal tube furnace for temperature control, various metal weights and a fibre clamp for applying various strains to the fibre. Strain values were calculated via Young's modulus for silica, $E = 68 \text{ GPa}$ [128]. The fibre sample was passed through a glass tube with the grating located in the centre of the oven. The sample was kept taut, static and out of contact with the tube having been fastened by spools at each end of the oven.

Transmission spectra were measured with the same method described in section 4.1 while grating samples were subjected to various strain and temperature conditions. Illumination of the FBG dip near 1539 nm was provided by the well-known fluorescence from Er^{3+} emitted when it is pumped by 800 nm light. The dip in the region of 1030 nm was illuminated by an Yb^{3+} -doped fibre ASE source. The transmission spectra were recorded at a resolution of 0.005 nm. The wavelength shifts were inferred from the minima of the spectral features of interest which were measured in dB to provide more detail. At least 2 trials of strain and temperature measurements were

completed for each wavelength and the experimental uncertainties were approximately $\pm 3.2\%$ in the strain measurements and ± 1 °C in temperature measurements.

6.3 Dual wavelength sensing

The strain and temperature responses of spectral features at λ_B and $2/3 \lambda_B$ of samples I-10 and IIA-2 were investigated separately using the experimental arrangement shown in Figure 6-1 [116, 129]. As detailed in Table 2-5, sample I-10 was fabricated in standard telecommunications fibre using a standard phase mask and the experimental arrangement shown in Figure 2-2. The transmission spectra measured after fabrication of sample I-10 in the regions of λ_B and $2/3 \lambda_B$ are shown in Figure 6-2(a) and (b), respectively. As discussed in section 4.2, sample IIA-2 was fabricated in non-hydrogen loaded, Fibrecore™ B-Ge co-doped fibre using a standard phase mask in the experimental arrangement illustrated in Figure 2-1. For comparison, the transmission spectra measured after fabrication of sample IIA-2 in the regions of λ_B and $2/3 \lambda_B$ are shown again in Figure 6-2(c) and (d), respectively.

For sample I-10, the shift in the strongest transmittance dips in Figure 6-2(a) and (b) at approximately 1548 nm and 1035 nm, respectively, were investigated and for sample IIA-2, the shift in the strongest transmittance dips in Figure 6-2(c) and (d) at approximately 1535.2 nm and 1027.4 nm, respectively, were investigated.

The results of the strain and temperature experiments for each sample are shown in Figure 6-3. The responses to temperature and strain of both transmission dips for both samples are linear as expected for the relatively small ranges of temperature and strain tested. Linear fits were applied to the data and the temperature and strain coefficients of each peak were determined from the gradients, which are listed in Table 6-2 along with the standard errors. The measured coefficients are of the order of those reported previously [12, 13] for reflectance peaks at $\sim 1/2 \lambda_B$ and λ_B , which were listed in Table 6-1.

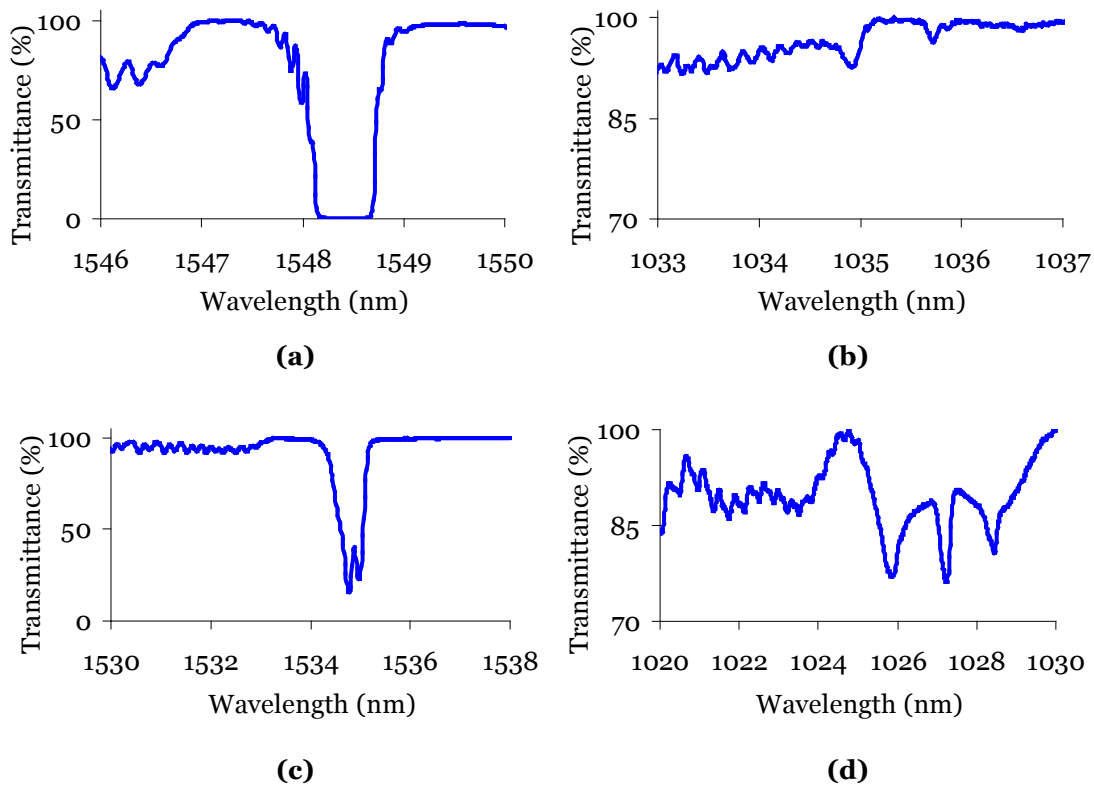


Figure 6-2. Transmission spectra measured after fabrication of type I and IIA gratings: sample I-10 at (a) λ_B and (b) $2/3 \lambda_B$ and for sample IIA-2 at (c) λ_B and (d) $2/3 \lambda_B$.

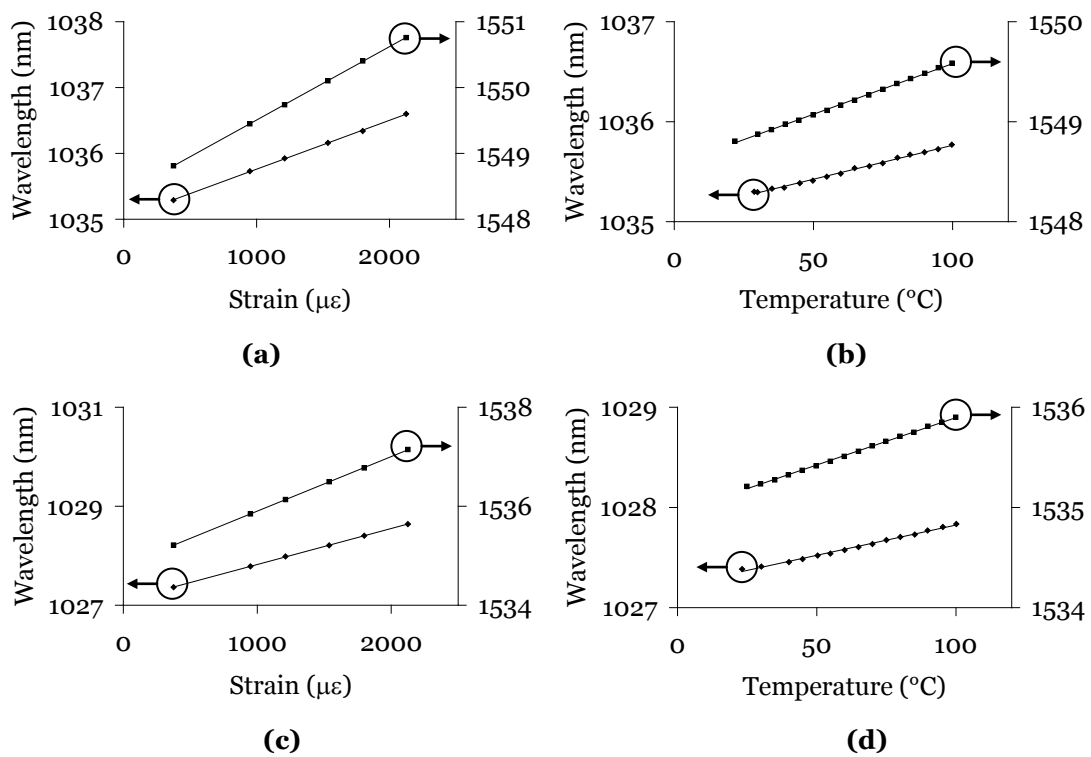


Figure 6-3. Responses of transmission dips at $2/3 \lambda_B$ and λ_B for sample I-10: (a) strain and (b) temperature and for sample IIA-2: (c) strain and (d) temperature.

Parameter	Sample I-10	Sample IIA-2	Yam <i>et al.</i> [121]
λ_1 (nm)	1548.9	1535.2	1553
λ_2 (nm)	1035.3	1027.4	785
λ_1/λ_2	1.496	1.494	1.978
$K_{\epsilon 1}$ (pm/ $\mu\epsilon$)	1.115 ± 0.003	1.101 ± 0.034	0.912 ± 0.004
$K_{\epsilon 2}$ (pm/ $\mu\epsilon$)	0.742 ± 0.007	0.728 ± 0.042	0.452 ± 0.004
K_{T1} (pm/ $^{\circ}\text{C}$)	10.148 ± 0.087	9.455 ± 0.092	10.96 ± 0.07
K_{T2} (pm/ $^{\circ}\text{C}$)	6.792 ± 0.116	6.032 ± 0.116	5.98 ± 0.06
$K_{\epsilon 1}/K_{\epsilon 2}$	1.502 ± 0.039	1.512 ± 0.007	2.018 ± 0.011
K_{T1}/K_{T2}	1.494 ± 0.043	1.568 ± 0.027	1.833 ± 0.018
Ratio difference (%)	0.6	3.6	10.1
Strain uncertainty ($\mu\epsilon/\text{pm}$)	± 324	± 46	± 25
Temperature uncertainty ($^{\circ}\text{C}/\text{pm}$)	± 36	± 5	± 2

Table 6-2. Axial strain and temperature characteristics of two different wavelengths for various samples.

The measurement uncertainties of samples I-10 and IIA-2 were calculated using Equation 6-4 and Equation 6-5 assuming measurement uncertainties in each wavelength of 1 pm, as were used by Brady *et al.* [12]. As can be seen in Table 6-2, the strain and temperature uncertainties for samples I-10 and IIA-2 at the two tested wavelengths are higher than those reported by Brady *et al.* and Echevarria *et al.* (see Table 6-1). This is likely to be due to the similarity in strain and temperature responses of the two wavelengths tested for the different sensors. The ratio of the wavelengths investigated by Brady *et al.*, Echevarria *et al.* and Sivanesan *et al.* was approximately 2 whereas the ratio of the wavelengths tested for samples I-10 and IIA-2 was approximately 1.5. It is expected that the measurement uncertainties of dual wavelength sensors will be improved if the ratio of the two test wavelengths is increased beyond 2 and if one of the wavelengths is shorter than 800 nm [14]. The measurement precision of a dual-grating sensor, in which both gratings are fabricated in the same fibre, has been shown to depend primarily on the temperature response of the fibre gratings at the respective wavelengths. Varying temperature

responses at different wavelengths result from the temperature-dependent refractive index in optical fibres [14].

Also shown in Table 6-2 are the percentage differences between the ratios $K_{\epsilon 1}/K_{\epsilon 2}$ and $K_{T 1}/K_{T 2}$ for each sample. As discussed in section 6.1, the more dissimilar the ratios of the strain and temperature coefficients, the better the capacity of the sensor to discriminate between the two measurands. Sample I-10 exhibited a small percentage difference between the ratios of the strain and temperature coefficients which has led to large measurement uncertainties. It can be noted that sample IIA-2 provides an improvement in measurement uncertainties over sample I-10 due to the larger difference between the strain and temperature coefficient ratios. The ratio of the temperature coefficients for sample IIA-2 was larger than the ratio of the strain coefficients by 3.6%, indicating that the sample was more sensitive to temperature changes than strain changes. This observation is consistent with other work which found that strain responses are generally similar between type I and IIA FBGs whereas temperature responses are generally higher for type IIA gratings [18, 130].

In related work, the strain and temperature responses of spectral features at $\lambda_B \approx 785$ nm and $2\lambda_B \approx 1552$ nm of a grating written with a $\Lambda_{pm} = 0.536$ μ m phase mask have been investigated [119, 121]. These spectral features occur as a result of 1st and 2nd order Bragg reflections from a grating with a period equal to the phase mask as discussed in section 4.4.1. The responses to temperature and strain of the spectral features at 785 nm and 1552 nm and the associated measurement uncertainties are listed in Table 6-2. These measurement uncertainties compare well with the work of Brady *et al.* [12] and Echevarria *et al.* [13] due to the similarity between the test wavelengths.

6.4 Dual wavelength sensing with FIR

Both wavelengths in a dual wavelength co-located sensor are sensitive to temperature and strain which gives rise to cross-sensitivity. As discussed in section 1.3, another method of co-located temperature and strain sensing

involves a fibre grating written in rare-earth-doped optical fibre. When rare-earth ions are excited by an optical pulse, the resultant fluorescent decay curve has a lifetime that depends strongly upon temperature and weakly upon strain [24]. The related fluorescence intensity ratio (FIR) technique [25], which also relies upon the decay of excited levels in rare-earth ions, has been shown to be essentially strain independent.

The strain and temperature responses of spectral features at λ_B and $2/3 \lambda_B$ as well as the FIR of sample I-11 were investigated using the experimental arrangement shown in Figure 6-1 [131]. As detailed in Table 2-5, sample I-11 was fabricated in $\text{Er}^{3+}:\text{Yb}^{3+}$ co-doped fibre using a standard phase mask and the experimental arrangement shown in Figure 2-1. The transmission spectra measured after fabrication of sample I-11 in Figure 6-4(a) and (b) show prominent transmission dips at $\lambda_B \approx 1539.2$ nm and $2/3 \lambda_B \approx 1030$ nm, respectively.

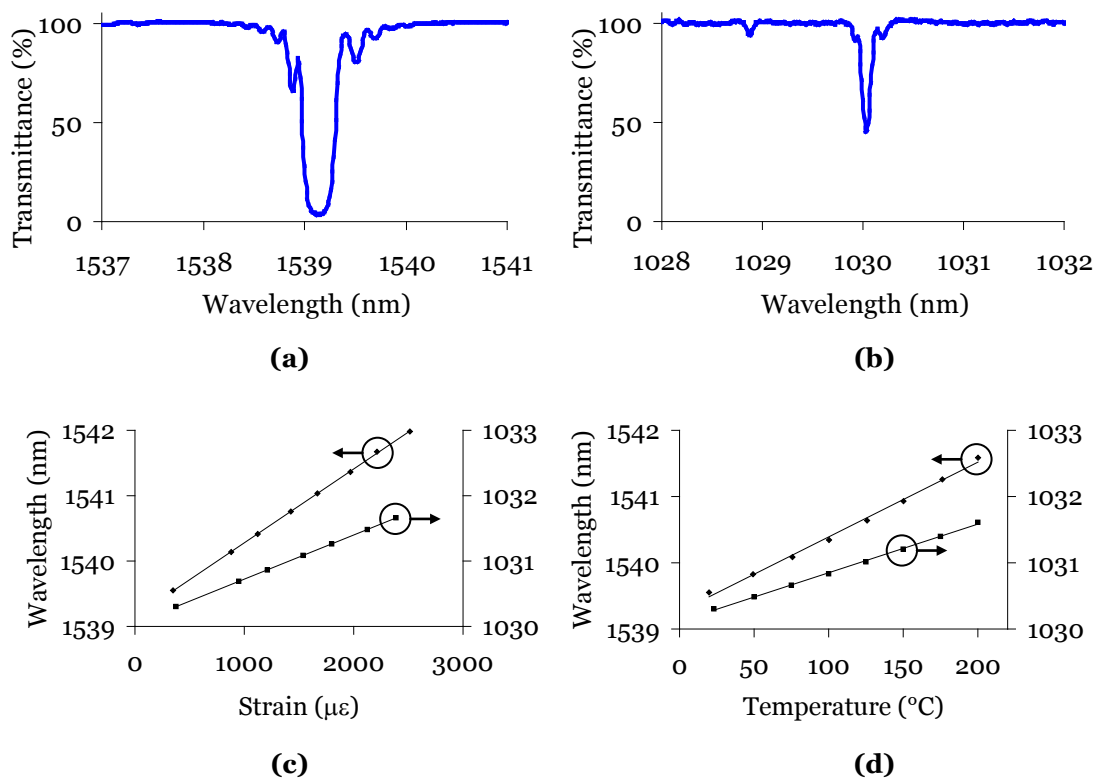


Figure 6-4. Transmission spectra measured after fabrication of sample I-11 (a) at λ_B and (b) at $2/3 \lambda_B$ and the response of the transmission dips to (c) strain and (d) temperature.

Spectral features at odd harmonic reflections of the phase mask period are expected to exhibit a central notch in the transmission dip, as discussed in section 4.4.1. The transmission dip at 1030 nm in Figure 6-4(b) appears as a single dip which is expected to be due to the smaller core of the fibre. As detailed in Table 2-4, the $\text{Er}^{3+}:\text{Yb}^{3+}$ co-doped fibre, F-5, has a core diameter of 4.4 μm which would not allow a full Talbot length of approximately 4.65 μm to be formed. As such, it is possible that a π phase-shifted pair of gratings has not been written in the core of the fibre which would cause a central notch due destructive interference for odd harmonic reflections.

Parameter	Sample I-11 λ_1 and λ_2	Parameter	Sample I-11 FIR and λ_1 or λ_2
λ_1 (nm)	1539.2	$K_{\varepsilon R} (\times 10^{-7} \%/ \mu\varepsilon)$	0.719 ± 1.3
λ_2 (nm)	1030	$K_{TR} (\times 10^{-3} \%/ ^\circ\text{C})$	1.199 ± 0.001
λ_1 / λ_2	1.494	$K_{\varepsilon 1} / K_{\varepsilon R}$	15689814
$K_{\varepsilon 1}$ (pm/ $\mu\varepsilon$)	1.129 ± 0.006	K_{T1} / K_{TR}	9403
$K_{\varepsilon 2}$ (pm/ $\mu\varepsilon$)	0.675 ± 0.001	$K_{\varepsilon 2} / K_{\varepsilon R}$	9381178
K_{T1} (pm/ $^\circ\text{C}$)	11.273 ± 0.297	K_{T2} / K_{TR}	6125
K_{T2} (pm/ $^\circ\text{C}$)	7.343 ± 0.111	Ratio difference λ_1 and FIR (%)	166754
$K_{\varepsilon 1} / K_{\varepsilon 2}$	1.672 ± 0.008	Ratio difference λ_2 and FIR (%)	153060
K_{T1} / K_{T2}	1.535 ± 0.038	Strain uncertainty λ_1 and FIR ($\mu\varepsilon/\text{pm}$)	± 1.216
Ratio difference λ_1 and λ_2 (%)	8.9	Temperature uncertainty λ_1 and FIR ($^\circ\text{C}/\text{pm}$)	± 0.083
Strain uncertainty λ_1 and λ_2 ($\mu\varepsilon/\text{pm}$)	± 19.77	Strain uncertainty λ_2 and FIR ($\mu\varepsilon/\text{pm}$)	± 1.738
Temperature uncertainty λ_1 and λ_2 ($^\circ\text{C}/\text{pm}$)	± 1.93	Temperature uncertainty λ_2 and FIR ($^\circ\text{C}/\text{pm}$)	± 0.083

Table 6-3. Axial strain and temperature characteristics of two different wavelengths and FIR for sample I-11.

The results of the strain and temperature experiments for sample I-11 at λ_1 and λ_2 are shown in Figure 6-4(c) and (d) for strain and temperature, respectively. The resulting coefficients are listed on the left hand side of Table 6-3 along with the standard errors. The measured strain and temperature coefficients for λ_1 and λ_2 are of the order of those reported previously [12, 13] for reflectance peaks at $\sim 1/2 \lambda_B$ and λ_B , which were listed in Table 6-1. Surprisingly for sample I-11, the measurement uncertainties for λ_1 and λ_2 are more comparable to those reported previously [12, 13] than sample I-10 and IIA-2 (listed in Table 6-2). This has been observed despite the smaller ratio of the test wavelengths and the fact that neither wavelength is shorter than 800 nm. The ratio of the strain coefficients for λ_1 and λ_2 is 8.9% larger than the ratio of the temperature coefficients for sample I-11. In comparison to the three samples presented in Table 6-2, sample I-11 has lower measurement uncertainties for temperature and strain using spectral features at $2/3 \lambda_B$ and λ_B . Combined with the essentially strain independent FIR technique, such sensors have high potential for accurate simultaneous measurement of temperature and strain.

To measure temperature and strain simultaneously using a single FBG which incorporates FIR with wavelength shifts at either 1539 nm or 1030 nm, there are two options via the transfer matrix method [26]. The first option combines the strain and temperature coefficients of the FIR and wavelength shifts at $\lambda_1 = 1539$ nm, while the second option combines the coefficients of the FIR with wavelength shifts at $\lambda_2 = 1030$ nm. The transfer matrix equations for the two options are given by Equation 6-6 and Equation 6-7, where ΔR is the variation in the FIR and $K_{\varepsilon R}$ and K_{TR} are the measured FIR strain and temperature coefficients, respectively.

$$\begin{bmatrix} \Delta\lambda_1 \\ \Delta R \end{bmatrix} = \begin{bmatrix} K_{\varepsilon 1} & K_{T1} \\ K_{\varepsilon R} & K_{TR} \end{bmatrix} \begin{bmatrix} \varepsilon \\ T \end{bmatrix} \quad \text{Equation 6-6}$$

$$\begin{bmatrix} \Delta\lambda_2 \\ \Delta R \end{bmatrix} = \begin{bmatrix} K_{\varepsilon 2} & K_{T2} \\ K_{\varepsilon R} & K_{TR} \end{bmatrix} \begin{bmatrix} \varepsilon \\ T \end{bmatrix} \quad \text{Equation 6-7}$$

The fluorescence spectra of Yb^{3+} is shown in Figure 6-5(a) and illustrates the different temperature dependences of the spectral regions I_1 (1040–1070 nm) and I_2 (880–970 nm) [27]. The variation in the ratio of fluorescence intensities in these two regions, ΔR , has been used in combination with FBG spectral shifts in $\text{Er}^{3+}:\text{Yb}^{3+}$ co-doped fibre for simultaneous sensing of temperature and strain [27]. Such FIR sensors use the fluorescence peaks emitted as a result of 800 nm illumination of the ${}^2\text{F}_{5/2}$ level in Yb^{3+} via energy transfer from Er^{3+} , the source of the well-known broad 1550 nm spectral fluorescence emission that can be used for FBG interrogation.

The FIR results for sample I-11 are shown in Figure 6-5(b) for strain and in Figure 6-5(c) for temperature. The resulting coefficients are listed on the right hand side of Table 6-3 along with the standard errors. The measurement uncertainties for the each of the options described above were calculated using Equation 6-4 and Equation 6-5 (with the matrix coefficients K_{eR} and K_{TR} in place of K_{e2} and K_{T2}), assuming wavelength uncertainties of $a = 1$ pm and ΔR uncertainties of $b = 1 \times 10^{-4}$ %. As expected, the ratios of the strain and temperature coefficients of the FIR combined with either of the wavelengths at $\lambda_1 = 1539$ nm or $\lambda_2 = 1030$ nm are very large; $>150,000$ %. The large differences between these ratios have lead to very small uncertainties of less than $\pm 2 \mu\epsilon/\text{pm}$ in strain measurements and less than ± 0.1 °C/pm in temperature measurements for the FIR with either λ_1 or λ_2 . These results indicate that FBGs written with standard phase masks in $\text{Er}^{3+}:\text{Yb}^{3+}$ co-doped fibre can be used to measure strain and temperature simultaneously with very high precision by incorporating FIR and spectral shifts at either λ_B or $2/3 \lambda_B$.

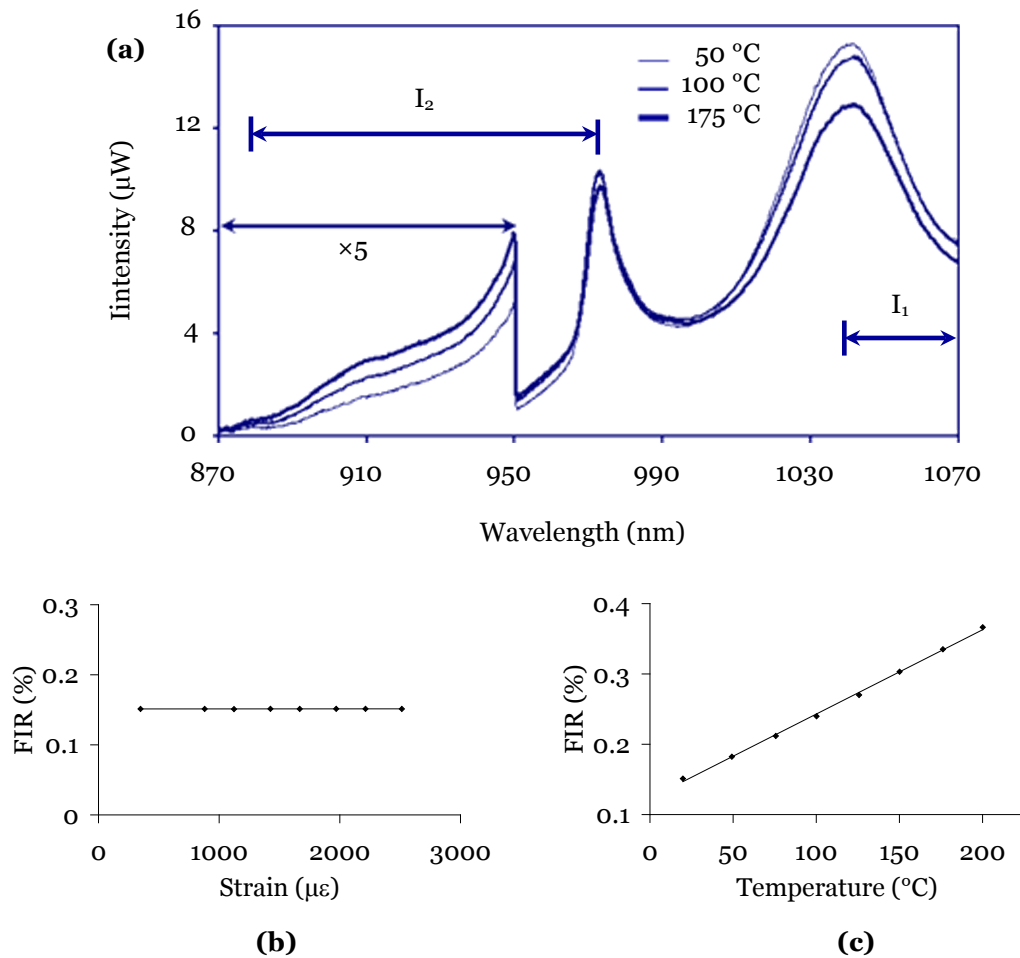


Figure 6-5. Fluorescence spectra of Yb^{3+} (a) illustrating the intensity decrease with temperature in region I_1 and the increase with temperature in region I_2 . Note: spectral region 870–950 nm has been magnified fivefold as a visual aid [27]. Response of the FIR of I_1 to I_2 to (b) strain and (c) temperature.

Another advantage of a single grating sensor in $\text{Er}^{3+}:\text{Yb}^{3+}$ -co-doped fibre is that only a single light source is required since fluorescence peaks from Yb^{3+} result from 800 nm illumination of the $^2F_{5/2}$ level in Yb^{3+} via energy transfer from the Er^{3+} [27]. Conveniently for this sensor, the resultant fluorescence peaks from Er^{3+} and Yb^{3+} are located in the vicinity of λ_B and $2/3 \lambda_B$, respectively. This sensor would only require a single light source to produce the fluorescence from $\text{Er}^{3+}:\text{Yb}^{3+}$ -co-doped fibre which in turn illuminates the two FBG wavelengths while populating relevant energy levels for FIR measurements.

6.5 Conclusions

The strain and temperature responses of spectral features at λ_B and $2/3 \lambda_B$ of type I and IIA fibre gratings were investigated for use in potential sensing applications. The spectral features at $2/3 \lambda_B$ are due to a complex refractive index structure induced in the core of phase-mask-written FBGs. Wavelength shifts of transmission dips in both spectral regions displayed linear behaviour with temperature and strain changes as expected. The measurement uncertainties of the proposed dual wavelength sensors were consistent with previous work [12, 13]. The type IIA sample demonstrated an improvement in measurement uncertainties over the type I sample due to a larger sensitivity to temperature changes. This observation is consistent with other work which has shown that strain responses are generally similar between type I and IIA FBGs whereas temperature responses are generally higher for type IIA gratings [18, 130].

Although the closeness of the λ_B and $2/3 \lambda_B$ pair of wavelengths reduces the ability of the sensor to discriminate between the measurands, the sensor does offer certain advantages by using the $2/3 \lambda_B$ dip instead of the dip at $1/2 \lambda_B$. The reduced optical attenuation in a fibre at ~ 1030 nm, compared with ~ 785 nm, would allow the sensor to be operated at a location much more distant from the instrumentation unit. Secondly, operation at $2/3 \lambda_B$, for fibre having a cut-off near 1300 nm, is less multi-mode than at $1/2 \lambda_B$. Furthermore, a much simpler arrangement is possible compared with other sensors as illumination of both the Bragg peaks, at ~ 1030 and 1550 nm, is possible through the use of a single $\text{Er}^{3+}:\text{Yb}^{3+}$ ASE light source.

This chapter also investigated the strain and temperature responses of spectral features at λ_B and $2/3 \lambda_B$ in combination with the FIR of a type I FBG written in $\text{Er}^{3+}:\text{Yb}^{3+}$ co-doped fibre using a standard phase mask. The dual wavelength sensor itself without FIR demonstrates measurement uncertainties which compare very well with those reported previously for λ_B and $1/2 \lambda_B$ [12, 13], despite a closer wavelength pair. When the essentially

strain independent FIR measurements are combined with measured wavelength shifts at either λ_B or $2/3 \lambda_B$, the single grating sensor demonstrates very small uncertainties of less than $\pm 2 \mu\epsilon/\text{pm}$ in strain measurements and less than $\pm 0.1 \text{ }^\circ\text{C}/\text{pm}$ in temperature measurements.

Such an arrangement could be used as a simple and compact sensor which records one axial strain and two temperature measurements simultaneously and requires only a single light source to monitor changes in the FIR or FBG wavelengths. Such a system could be pumped with a single light source in which the fluorescence from $\text{Er}^{3+}:\text{Yb}^{3+}$ -co-doped fibre is used to illuminate the two FBG wavelengths of interest as well as populate the relevant energy levels for FIR measurements.

Chapter 7:

Conclusions

This thesis sought to explore a number of questions raised by the complex refractive index structure observed to exist in the core of a phase-mask-written type I FBG. The investigations have shown the existence of similar complex structures in the core of other type I and type IIA FBGs using DIC microscopy. The phase mask fabrication technique has been shown to have a significant effect on the induced refractive index structures and optical spectra of various FBGs. An analysis of the growth of FBG spectral features during fabrication has indicated that the grating periods from which these features are reflected depends on the wavelength, the nature of the phase mask used in fabrication and core size of the fibre. Spectral features which arise from the observed complex refractive index structures have been found to exhibit the expected responses to axial strain and temperature with potential applications in dual-wavelength simultaneous sensing.

This thesis has addressed four main questions regarding the structure of similar and dissimilar FBGs; and also the influence of the phase mask properties on the structure and subsequent performance of FBG-based devices:

1. Is there a correlation between the complex refractive index structure and the observed optical spectra of FBGs?

The refractive index structures of different FBGs were investigated in Chapter 3 and the spectral consequences of the observed refractive index structures were investigated in Chapters 4, 5 and 6. The imaging results in this thesis have shown that the small contributions of the zeroth and $\pm 2^{\text{nd}}$ orders of standard phase masks are strong enough to induce periodic features in the

interference pattern with a period equal to the phase mask. The spectral results have shown that FBG periods equal to the phase mask give rise to harmonic reflections at $2/3 \lambda_B$ and $2/5 \lambda_B$ in phase-mask-written FBGs. Reflections at these wavelengths would not occur if the refractive index structure of the FBGs consisted of uniformly distributed perturbations with a period equal to half of the phase mask.

Using DIC microscopy, the effects on the structure of FBGs resulting from three different fabrication techniques were investigated, including the prism interferometer and two very different phase masks. In addition to the standard, zeroth-order nulled phase mask technique, the effects of contributions from phase mask diffraction orders other than the first were investigated using a custom-made phase mask.

The structures expected for pure two-beam interference could not be resolved in the images of type I and IIA FBGs written with a prism interferometer. The structures observed in the prism FBG images were non-uniform but did not reveal Talbot diffraction patterns which would result from multiple-beam interference during fabrication. The expected periods of the prism FBGs of approximately $0.5 \mu\text{m}$ could not be resolved in the images which is expected to be due to the resolution limit of the imaging system. The periods measured in the images of the prism FBGs were inconsistent with spectral results at the Bragg wavelength, providing further evidence that the observed image features were more likely to be artefacts due to poor resolution than an accurate representation of the FBG structures.

The images of phase-mask-written type I and IIA FBGs provided compelling evidence that the use of a phase mask for fabrication has a significant effect on the refractive index structures induced in the fibre core. Multiple-beam interference of the diffracted orders of the phase mask is expected to give rise to a structure consisting of interleaving grating planes with a period equal to the phase mask. The images of FBGs written with either the standard or custom-made phase masks indeed revealed the existence of π phase-shifted gratings with a period consistent with the period of the phase mask used in

fabrication. The observed Talbot lengths of the refractive index patterns extending across the core of the standard and custom-made phase mask FBGs were all consistent with the Talbot length expected for beating between the $\pm 1^{\text{st}}$ and $\pm 2^{\text{nd}}$ orders of each mask. Images of FBGs written in standard telecommunications fibre with standard or custom-made phase masks revealed at least one full period of the Talbot diffraction patterns extending across the core. However, images of FBGs written in fibre designed for singlemode operation at 1030 nm revealed that the core was too small for a full Talbot length to be formed across the fibre core.

Spectral features in the region of $2/3$ and $2/5$ of the design wavelength, λ_B , were observed for type I and IIA FBGs written with a phase mask. These results were consistent with the evidence in the DIC images that gratings with a period equal to the phase mask had been photo-imprinted in the core. Spectral features in the region of $2/3 \lambda_B$ and $2/5 \lambda_B$ had previously been observed for a type II FBG [51] and were attributed to the damaging nature of the single, high-fluence UV pulse used in fabrication. The imaging and spectral results in this thesis have shown that grating features with a period equal to the phase mask are produced under low-fluence, continuous wave laser conditions as a result of the multiple-beam interference patterns formed by phase masks.

2. Can the structure or its interaction with the fibre type be used to alter the spectral characteristics?

The reflectance strengths of spectral features at λ_B and $2/3 \lambda_B$ were compared in various FBGs written with phase masks. FBGs written in two different fibre types with two different phase masks were investigated and the spectral characteristics were shown to vary with fabrication conditions and fibre type. The first fibre type, standard telecommunications fibre, exhibits singlemode propagation at λ_B but multimode propagation at $2/3 \lambda_B$, whereas the second, smaller core fibre exhibits singlemode propagation in both wavelength regions. One phase mask was a standard, 0th order-nulled phase mask whereas the other was custom designed to provide a higher 0th order

contribution and approximately equal contributions from both of the $\pm 1^{\text{st}}$ and $\pm 2^{\text{nd}}$ orders.

In comparison to the reflectance strength at λ_B , the strengths of features at $2/3 \lambda_B$ of both the standard and custom-made phase mask FBGs were observed to be relatively low when propagating under multimode conditions and high when under singlemode conditions. These observations are consistent with the modal overlaps in the two fibres at the respective wavelengths. In the larger core standard telecommunications fibre, the fundamental mode at 1550 nm fills a greater fraction of the core than at 1035 nm. In the smaller core fibre, the fundamental modes at both wavelengths fill a larger fraction of the core than in the larger core fibre. Since propagating modes fill a greater fraction of the core under singlemode conditions, a higher fraction of power interacts with the grating leading to higher reflectances.

The contributions of different diffraction orders of the phase mask have been found to have a significant effect on the spectra of various FBGs. Samples written with the custom-made phase mask exhibited stronger reflections at $2/3 \lambda_B$ than FBGs written with the standard phase mask. This observation is consistent with the dominance of grating features with a period equal to the phase mask in the intensity pattern generated by the custom made phase mask.

As mentioned above, the expected period of grating features in type I and IIA FBGs written with a prism interferometer was not resolved in the DIC images due to the resolution limitations of the imaging system. The spectral results, however, were consistent with the existence of the grating period expected for pure two-beam interference. Neither the type I nor IIA FBG written with the prism interferometer exhibited spectral features at $2/3 \lambda_B$ as expected for a uniform period formed by two-beam interference with first-order reflections at λ_B .

For various phase-mask-written FBGs, single transmission dips were observed in the spectra at λ_B , whereas split transmission dips were observed at $2/3 \lambda_B$ when both wavelengths propagated under singlemode conditions. These observations have been attributed to the π phase-shifted gratings with a period equal to the phase mask which were revealed in the DIC images. At odd harmonic reflections, such as the third-order reflections at $2/3 \lambda_B$, the standing waves generated from the π phase-shifted gratings interfere destructively and cause a central notch in the transmission dip. However, at even harmonic reflections, such as the second-order reflections at λ_B , single transmission dips were observed as a result of constructive interference.

3. How do the spectral characteristics evolve during fabrication?

The simulated intensity patterns and recorded DIC images revealed the existence of two grating periods in the FBGs, i.e. Λ_{pm} and $\Lambda_{pm}/2$. Spectral features at $2/3 \lambda_B$ are likely to originate only as the third harmonic reflection of a Λ_{pm} grating, but features at λ_B could arise as separate or combined contributions from either the first harmonic reflection from a $\Lambda_{pm}/2$ grating or the second harmonic reflection from a Λ_{pm} grating. In order to understand the contribution each period makes to the observed reflections, the reflectance growth during fabrication was analysed in terms of separate Fourier components of a modified version of the model proposed by Xie *et al.* [83]. The contributions from each component to the reflections at λ_B of type I, phase-mask-written FBGs in standard and smaller core fibres were found to depend on the properties of the phase mask and also the size of the fibre core.

The observed reflectance growth at λ_B of the standard phase mask, larger core FBG was shown to result from significant contributions from each of the second-order component for a Λ_{pm} period grating and the first-order component for a $\Lambda_{pm}/2$ period grating. The interference patterns generated by the standard phase mask were expected to be dominated by the $\Lambda_{pm}/2$ period features, but the modelling results indicated that reflections at λ_B occur due to a larger contribution from the Λ_{pm} period features. This observation was

attributed to insufficient intensities in the phase mask interference pattern leading to refractive index changes in the fibre core which were not strong enough to allow the $\Lambda_{pm}/2$ period features to dominate. The significant contribution of the $\Lambda_{pm}/2$ period features to the observed reflectance growth was attributed to the core size of the standard telecommunications fibre allowing more than one Talbot length to be imprinted in the core and hence the propagating light would have a greater interaction with the less dominant $\Lambda_{pm}/2$ features. In the smaller core fibre however, the observed reflectance growth at λ_B of the standard phase mask FBG was better described as the second harmonic of a grating with a Λ_{pm} period with only a small contribution from the first harmonic reflection of a $\Lambda_{pm}/2$ period. The smaller contribution of $\Lambda_{pm}/2$ period features in the smaller core sample was attributed to the restricted interaction of propagating light with the less dominant half period structure.

The higher contributions of the zeroth and $\pm 2^{\text{nd}}$ orders of the custom-made phase mask have been shown to have a significant effect on the origins of harmonic Bragg reflections. The intensity pattern produced by the custom-made phase mask, with equal contributions from the $\pm 1^{\text{st}}$ and $\pm 2^{\text{nd}}$ orders and a higher zeroth-order than the standard mask, is expected to be dominated by Λ_{pm} period features. Accordingly, the observed reflectance growth at λ_B of the FBGs written with the custom phase mask in both the standard and smaller core fibres were described well as the second harmonic of the Λ_{pm} period.

4. Can such FBGs offer improved sensing capabilities?

The strain and temperature responses of spectral features at λ_B and $2/3 \lambda_B$ of type I and IIA fibre gratings were investigated in Chapter 6. Wavelength shifts of transmission dips in both spectral regions displayed linear behaviour with temperature and strain changes as expected. The measurement uncertainties of the proposed dual wavelength sensors were consistent with previous work [12, 13]. The type IIA sample demonstrated an improvement in measurement

uncertainties over the type I sample due to a larger sensitivity to temperature changes. This observation is consistent with other work which has shown that strain responses are generally similar between type I and IIA FBGs whereas temperature responses are generally higher for type IIA gratings [18, 130]. Although the closeness of the λ_B and $2/3 \lambda_B$ pair of wavelengths reduces the ability of the sensor to discriminate between temperature and strain, the sensor does offer certain advantages by using the $2/3 \lambda_B$ dip instead of the dip at $1/2 \lambda_B$. The reduced optical attenuation and smaller number of modes propagating in standard telecommunications a fibre at ~ 1030 nm, compared with ~ 785 nm, would allow the sensor to be operated at distant locations with greater reflectance strengths and easier detection.

This thesis also investigated the strain and temperature responses of spectral features at λ_B and $2/3 \lambda_B$ in combination with the fluorescence intensity ratio (FIR) of a type I FBG written in rare-earth doped fibre using a standard phase mask. The dual-wavelength sensor itself without FIR demonstrated measurement uncertainties which compare very well with those reported previously for λ_B and $1/2 \lambda_B$ [12, 13], despite a closer wavelength pair. When the essentially strain independent FIR measurements are combined with measured wavelength shifts at either λ_B or $2/3 \lambda_B$, the single grating sensor demonstrates very small uncertainties of less than $\pm 2 \mu\epsilon/\text{pm}$ in strain measurements and less than $\pm 0.1 \text{ }^\circ\text{C}/\text{pm}$ in temperature measurements. Since only a single light source is required to monitor changes in the FIR or FBG wavelengths, such an arrangement could be used as a simple and compact system capable of co-located detection of two axial strain (one from each FBG wavelength) and three temperature (FIR and two FBG wavelengths) measurements simultaneously with high precision.

7.1 Suggestions for future work

The investigations undertaken in this thesis have lead to a number of suggestions for future work. The studies undertaken have shown how the combination of DIC images and spectral measurements can provide valuable insight to the effect of fabrication conditions on the internal structure,

characteristics and performance of FBG-based, bulk waveguide and other optical devices.

A recent study has developed a tool for quantifying the refractive index changes induced in the core of FBGs using DIC microscopy [108]. This tool would be particularly useful for gaining further insight to the mechanisms responsible for the induced refractive index changes in the core of FBGs. Furthermore, refractive index profiling with DIC microscopy would be valuable for investigating the validity of the model used in this thesis for the growth of refractive index changes and reflectance strengths at different harmonic wavelengths of FBGs. The quantification of refractive index changes inside FBGs would also be valuable for characterising the precise effect of increased phase mask diffraction orders during fabrication. The intensity changes in DIC images recorded for FBGs written with the custom-made phase mask in this thesis appeared to be stronger than the standard phase mask FBGs; the extent of this effect could be better understood through refractive index profiling. This work could lead, for example, to a new generation of phase masks which, instead of suppressing the zeroth and higher orders, are optimised for new applications in FBG-based multiple wavelength fibre laser and sensor systems.

To further investigate the structures formed in prism interferometer FBGs using DIC microscopy, an imaging laser wavelength shorter than 488 nm could be used to decrease the diffraction limit and improve the resolving power of the imaging system. The lateral shear of approximately 0.58 μm with the 488 nm laser could be decreased to as low as 0.5 μm with a 405 nm laser which will enable resolution of smaller features. Alternatively, the prism interferometer technique could be varied such that the grating spacing is increased beyond 0.5 μm . Grating periods of around 0.65 μm may be easier to resolve using the current imaging system and will result in FBG operating wavelengths of approximately 1870 nm. At this wavelength, the fibre attenuation is comparable with that of the 1030 nm region meaning that signal detection should not be too difficult. The optical spectra of FBGs with

grating periods longer than approximately $0.7\ \mu\text{m}$ will be difficult to monitor due to the high absorption of silica glass at wavelengths longer than $2\ \mu\text{m}$.

The explanations offered for the various spectral features of FBGs presented in this thesis have described the data well. In order to verify the observed spectral features, it would be beneficial to use coupled mode theory and the predicted modal distributions from Fimmwave software (in section 4.3.1) to obtain spectra which can be compared with the experimental results. Furthermore, a mathematical characterisation of the complex refractive index modulations would enable analysis of all spectral characteristics of a grating based on the coupled mode theory, including how the phase-shift is induced, and the relative coupling strength at each harmonic wavelength. Such a characterisation would also be helpful for optimising the geometrical parameters of fibre and phase mask to achieve higher efficiency or desired properties.

A key problem in FBG fabrication is achieving the highest reflectivity with limited photosensitivity or grating length. The results in this thesis suggest that there might be an optimal core size for the highest reflectivity which is not affected by the multiple-beam interference patterns induced in the core via the phase mask fabrication method. A more detailed investigation into the interaction of fibre core size with the multiple-beam interference patterns of the phase mask technique is also suggested for future work. For example, the spectral characteristics of FBGs in larger core multimode fibres could be investigated. Additionally, since the quality (or fringe visibility) of the index modulation in an FBG is conventionally considered to be uniform across the core, an investigation into the effect of the observed non-uniform index modulations on the fringe visibility would be a useful extension to this thesis.

As discussed in this thesis, the microscopic and spectral characteristics of phase-mask-written FBGs are consistent with the existence of the π phase-shifted gratings in the core. The spectral properties of FBGs written with a $0.536\ \mu\text{m}$ pitch phase mask have been shown to compare very well with a model developed for conventional π phase-shifted FBGs [120]. For further

investigation of the FBGs studied in this thesis, the same modelling technique could be applied. Furthermore, Tomljenovic-Hanic and Love [132] have reported that identical gratings which are offset longitudinally by half a grating period can be used as mode selective reflection gratings. Such devices have enabled the design of more effective and compact wavelength add/drop devices [133, 134]. In relation to this thesis, the investigation of the mode selective capabilities of the π phase-shifted gratings observed to exist in the core of phase-mask-written FBGs is also suggested for future work.

The double-dip structure in the spectra of odd harmonic reflections from FBGs has been attributed to the existence of π phase-shifted gratings and described in this thesis using a model which considers light as discrete propagating waves. The investigation of a model which considers the incident light as propagating modes could offer better insight into the spectral consequences of π phase-shifted gratings.

The use of FBG spectral shifts at ~ 1030 nm and ~ 1550 nm were investigated in this thesis as the basis for dual-wavelength simultaneous sensing of temperature and axial strain. This wavelength pair does not exhibit the differences in temperature and strain responses required for accurate discrimination of the two measurands. As reported by Sivanesan *et al.* [14], differences in temperature and strain responses for dual-wavelength simultaneous sensing with a single FBG can be optimised when one of the wavelengths is in the range of 1300-1500 nm and the other wavelength is below 600 nm. In relation to this work, the complex refractive index structure induced by a phase mask with a period of around $0.536 \mu\text{m}$ would give rise to first, second and third harmonic reflections at approximately 1550 nm, 785 nm and 520 nm, respectively. The third harmonic reflections at 520 nm for a $0.536 \mu\text{m}$ pitch phase mask are expected to be as strong as the third harmonic reflections at 1030 nm for a $1 \mu\text{m}$ pitch phase mask which were investigated in this thesis. The utilisation of a single FBG with reflections at 1550 nm and 520 nm has potential for improved precision in simultaneous temperature and strain sensing over other single FBG dual-wavelength sensors.

It is hoped that the tools and methods developed in this thesis can assist in optimising the next generation of FBG-based and other diffractive optical devices.

Bibliography



1. Rogers, A.J., *Understanding optical fiber communications*. 2001, Boston, Mass; London: Artech House.
2. Dakin, J. and B. Culshaw, eds. *Optical fiber sensors. Applications, Analysis and Future Trends*. Vol. 4. 1997, Artech House: Boston.
3. Renaudier, J., O. Bertran-Pardo, G. Charlet, M. Salsi, H. Mardoyan, P. Tran, and S. Bigo, *8 Tb/s long haul transmission over low dispersion fibers using 100 Gb/s PDM-QPSK channels paired with coherent detection*. Bell Labs Technical Journal, 2010. 14(4): p. 27-46.
4. Weisenbach, L. *Fiber Optic Sensors*. 2005 [cited March 31, 2006]; Available from: <http://www.bccresearch.com/instrum/G116N.html>.
5. Othonos, A. and K. Kalli, *Fiber Bragg gratings: fundamentals and applications in telecommunications and sensing*. Artech House. 1999, Boston, Mass.; London: Artech House.
6. Kersey, A.D., M.A. Davis, H.J. Patrick, M. LeBlanc, K.P. Koo, C.G. Askins, M.A. Putnam, and E.J. Friebele, *Fiber grating sensors*. Journal of Lightwave Technology, 1997. 15(8): p. 1442-1463.
7. Lo, Y.-L., *Using in-fiber Bragg-grating sensors for measuring axial strain and temperature simultaneously on surfaces of structures*. Optical Engineering, 1998. 37(8): p. 2272-2276.
8. Xu, M.G., J.L. Archambault, L. Reekie, and J.P. Dakin, *Discrimination between strain and temperature effects using dual-wavelength fibre grating sensors*. Electronics Letters, 1994. 30(13): p. 1085-1087.
9. Kanellopoulos, S.E., V.A. Handerek, and A.J. Rogers, *Simultaneous strain and temperature sensing with photogenerated in-fiber gratings*. Optics Letters, 1995. 20(3): p. 333-335.
10. Bhatia, V. and A.M. Vengsarkar, *Optical fiber long-period grating sensors*. Optics Letters, 1996. 21(9): p. 692-694.

11. Kalli, K., G. Brady, D.J. Webb, D.A. Jackson, L. Zhang, and I. Bennion, *Possible approach for simultaneous measurement of strain and temperature with second harmonics in a fibre Bragg grating sensor*. Presented at OFS10 (Glasgow), postdeadline paper 2.1, 1994.
12. Brady, G.P., K. Kalli, D.J. Webb, D.A. Jackson, L. Reekie, and J.L. Archambault, *Simultaneous measurement of strain and temperature using the first- and second-order diffraction wavelengths of Bragg gratings*. IEE Proceedings-Optoelectronics, 1997. 144(3): p. 156-161.
13. Echevarria, J., A. Quintela, C. Jauregui, and J.M. Lopez-Higuera, *Uniform fiber Bragg grating first- and second-order diffraction wavelength experimental characterization for strain-temperature discrimination*. IEEE Photonics Technology Letters, 2001. 13(7): p. 696-698.
14. Sivanesan, P., J.S. Sirkis, Y. Murata, and S.G. Buckley, *Optimal wavelength pair selection and accuracy analysis of dual fiber grating sensors for simultaneously measuring strain and temperature*. Optical Engineering, 2002. 41(10): p. 2456-2463.
15. Chen, G., L. Liu, H. Jia, J. Yu, L. Xu, and W. Wang, *Simultaneous strain and temperature measurements with fiber Bragg grating written in novel Hi-Bi optical fiber*. IEEE Photonics Technology Letters, 2004. 16(1): p. 221-223.
16. Cavaleiro, P.M., F.M. Araujo, L.A. Ferreira, J.L. Santos, and F. Farahi, *Simultaneous measurement of strain and temperature using Bragg gratings written in germanosilicate and boron-codoped germanosilicate fibers*. IEEE Photonics Technology Letters, 1999. 11(12): p. 1635-1637.
17. Guan, B.-O., H.-Y. Tam, S.-L. Ho, W.-H. Chung, and X.-Y. Dong, *Simultaneous strain and temperature measurement using a single fibre Bragg grating*. Electronics Letters, 2000. 36(12): p. 1018-1019.
18. Shu, X., Y. Liu, D. Zhao, B. Gwandu, F. Floreani, Z. Lin, and I. Bennion, *Dependence of temperature and strain coefficients on fiber grating type and its application to simultaneous temperature and strain measurement*. Optics Letters, 2002. 27(9): p. 701-703.
19. Simpson, A.G., K. Kalli, K. Zhou, L. Zhang, and I. Bennion, *An idealised method for the fabrication of temperature invariant IA-I strain sensors*. Postdeadline session, OFS-16 Nara, Japan, PD4, 2003.
20. Frazao, O., *Simultaneous measurement of strain and temperature using type I and type IIA fibre Bragg gratings*. Journal of Optics A-Pure and Applied Optics, 2003. 5(3): p. 183-185.
21. Pal, S., J. Mandal, T. Sun, K.T.V. Grattan, M. Fokine, F. Carlsson, P.Y. Fonjallaz, S.A. Wade, and S.F. Collins, *Characteristics of potential fibre*

- Bragg grating sensor-based devices at elevated temperatures.* Measurement Science & Technology, 2003. 14(7): p. 1131-1136.
22. Pal, S., T. Sun, K.T.V. Grattan, S.A. Wade, S.F. Collins, G.W. Baxter, B. Dussardier, and G. Monnom, *Strain-independent temperature measurement using a type-I and type-IIA optical fiber Bragg grating combination.* Review of Scientific Instruments, 2004. 75(5 PART 1): p. 1327-1331.
 23. Kalli, K., A.G. Simpson, K. Zhou, L. Zhang, and I. Bennion, *Tailoring the temperature and strain coefficients of Type I and Type IA dual grating sensors - The impact of hydrogenation conditions.* Measurement Science and Technology, 2006. 17(5): p. 949-954.
 24. Forsyth, D.I., S.A. Wade, T. Sun, C. Xiaomei, and K.T.V. Grattan, *Dual temperature and strain measurement with the combined fluorescence lifetime and Bragg wavelength shift approach in doped optical fiber.* Applied Optics, 2002. 41(31): p. 6585-6592.
 25. Wade, S.A., S.F. Collins, and G.W. Baxter, *Fluorescence intensity ratio technique for optical fiber point temperature sensing.* Journal of Applied Physics, 2003. 94(8): p. 4743-4756.
 26. Trpkovski, S., S.A. Wade, G.W. Baxter, and S.F. Collins, *Dual temperature and strain sensor using a combined fiber Bragg grating and fluorescence intensity ratio technique in Er³⁺-doped fiber.* Review of Scientific Instruments, 2003. 74(5): p. 2880-2885.
 27. Trpkovski, S., S.A. Wade, S.F. Collins, and G.W. Baxter, *Er³⁺:Yb³⁺ doped fibre with embedded FBG for simultaneous measurement of temperature and longitudinal strain.* Measurement Science & Technology, 2005. 16(2): p. 488-496.
 28. Rao, Y.J., P.J. Henderson, D.A. Jackson, L. Zhang, and I. Bennion, *Simultaneous strain, temperature and vibration measurement using a multiplexed in-fibre-Bragg-grating/fibre-Fabry-Perot sensor system.* Electronics Letters, 1997. 33(24): p. 2063-2064.
 29. Kang, H.-K., H.-J. Bang, C.-S. Hong, and C.-G. Kim, *Simultaneous measurement of strain, temperature and vibration frequency using a fibre optic sensor.* Measurement Science & Technology, 2002. 13(8): p. 1191-1196.
 30. Gander, M.J., W.N. MacPherson, R. McBride, J.D.C. Jones, L. Zhang, I. Bennion, P.M. Blanchard, J.G. Burnett, and A.H. Greenaway, *Bend measurement using Bragg gratings in multicore fibre.* Electronics Letters, 2000. 36(2): p. 120-121.
 31. Flockhart, G.M.H., W.N. MacPherson, J.S. Barton, J.D.C. Jones, L. Zhang, and I. Bennion, *Two-axis bend measurement with Bragg gratings in multicore optical fiber.* Optics Letters, 2003. 28(6): p. 387-389.

32. Gwandu, B.A.L., X.W. Shu, Y. Liu, W. Zhang, L. Zhang, and I. Bennion, *Simultaneous measurement of strain, temperature and curvature using a sampled fibre Bragg grating*. 2002 15th Optical Fiber Sensors Conference Technical Digest. OFS 2002(Cat. No.02EX533), 2002: p. 79-82 vol.1.
33. Iadicicco, A., S. Campopiano, A. Cutolo, M. Giordano, and A. Cusano, *Nonuniform thinned fiber Bragg gratings for simultaneous refractive index and temperature measurements*. IEEE Photonics Technology Letters, 2005. 17(7): p. 1495-1497.
34. Zhu, T., Y.-J. Rao, and Q.-J. Mo, *Simultaneous measurement of refractive index and temperature using a single ultralong-period fiber grating*. IEEE Photonics Technology Letters, 2005. 17(12): p. 2700-2702.
35. Zhao, C.-L., X. Yang, M.S. Demokan, and W. Jin, *Simultaneous temperature and refractive index measurements using a 3 degrees slanted multimode fiber Bragg grating*. Journal of Lightwave Technology, 2006. 24(2): p. 879-883.
36. Wagreich, R.B., W.A. Atia, H. Singh, and J.S. Sirkis, *Effects of diametric load on fibre Bragg gratings fabricated in low birefringent fibre*. Electronics Letters, 1996. 32(13): p. 1223-1224.
37. Chi, H., T. Xiao-Ming, and Y. Dong-Xiao, *Simultaneous measurement of axial strain, temperature, and transverse load by a superstructure fiber grating*. Optics Letters, 2001. 26(24): p. 1949-1951.
38. Liu, Y., L. Zhang, and I. Bennion, *Fibre optic load sensors with high transverse strain sensitivity based on long-period gratings in B/Ge co-doped fibre*. Electronics Letters, 1999. 35(8): p. 661-663.
39. Udd, E., W.L. Schulz, J.M. Seim, D.V. Nelson, and A. Makino, *Transverse fiber grating strain sensors based on dual overlaid fiber gratings on polarization preserving fibers*. Proceedings of the SPIE - The International Society for Optical Engineering, 1998. 3330: p. 253-263.
40. Udd, E., W. Schulz, J. Seim, E. Haugse, A. Trego, P. Johnson, T.E. Bennett, D. Nelson, and A. Makino, *Multidimensional strain field measurements using fiber optic grating sensors*. Proceedings of the SPIE - The International Society for Optical Engineering, 2000. 3986: p. 254-262.
41. Chehura, E., Y. Chen-Chun, S.E. Staines, S.W. James, and R.P. Tatam, *Characterization of the response of fibre Bragg gratings fabricated in stress and geometrically induced high birefringence fibres to temperature and transverse load*. Smart Materials and Structures, 2004. 13(4): p. 888-895.

42. Kashyap, R., *Fiber Bragg gratings*. Optics and photonics. 1999, San Diego, London: Academic Press.
43. Hill, K.O., Y. Fujii, D.C. Johnson, and B.S. Kawasaki, *Photosensitivity in optical fibre waveguides: Application to reflection filter fabrication*. Applied Physics Letters, 1978. 32(10): p. 647-649.
44. Lam, D.K.W. and B.K. Garside, *Characterization of single-mode optical fiber filters*. Applied Optics, 1981. 20(3): p. 440-445.
45. Meltz, G., W.W. Morey, and W.H. Glenn, *Formation of Bragg gratings in optical fibers by a transverse holographic method*. Optics Letters, 1989. 14(15): p. 823-825.
46. Limberger, H.G., P.Y. Fonjallaz, P. Lambelet, R.P. Salathe, C. Zimmer, and H.H. Gilgen, *OLCR characterization of efficient Bragg gratings in optical fiber*. Proceedings of the SPIE - The International Society for Optical Engineering, 1993. 2044: p. 272-283.
47. Kashyap, R., J.R. Armitage, R. Wyatt, S.T. Davey, and D.L. Williams, *All-fibre narrowband reflection gratings at 1500 nm*. Electronics Letters, 1990. 26(11): p. 730-732.
48. Broer, M.M., R.L. Cone, and J.R. Simpson, *Ultraviolet-induced distributed-feedback gratings in Ce³⁺-doped silica optical fibers*. Optics Letters, 1991. 16(18): p. 1391-1393.
49. Hill, K.O., B. Malo, F. Bilodeau, D.C. Johnson, and J. Albert, *Bragg gratings fabricated in monomode photosensitive optical fiber by UV exposure through a phase mask*. Applied Physics Letters, 1993. 62(10): p. 1035-1037.
50. Anderson, D.Z., V. Mizrahi, T. Erdogan, and A.E. White, *Production of in-fibre gratings using a diffractive optical element*. Electronics Letters, 1993. 29(6): p. 566-568.
51. Malo, B., D.C. Johnson, F. Bilodeau, J. Albert, and K.O. Hill, *Single-excimer-pulse writing of fiber gratings by use of a zero-order nulled phase mask: grating spectral response and visualization of index perturbations*. Optics Letters, 1993. 18(15): p. 1277-1279.
52. Dyer, P.E., R.J. Farley, and R. Giedl, *Analysis of grating formation with excimer laser irradiated phase masks*. Optics Communications, 1995. 115(3-4): p. 327-334.
53. Poumellec, B. and F. Kherbouche, *The photorefractive Bragg gratings in the fibers for telecommunications*. Journal de Physique III, 1996. 6(12): p. 1595-1624.
54. Hosono, H., Y. Abe, D.L. Kinser, R.A. Weeks, K. Muta, and H. Kawazoe, *Nature and origin of the 5-eV band in SiO₂:GeO₂ glasses*. Physical Review B (Condensed Matter), 1992. 46(18): p. 11445-11451.

55. Nishii, J., K. Fukumi, H. Yamanaka, K. Kawamura, H. Hosono, and H. Kawazoe, *Photochemical reactions in GeO₂-SiO₂ glasses induced by ultraviolet irradiation: comparison between Hg lamp and excimer laser*. Physical Review B (Condensed Matter), 1995. 52(3): p. 1661-1665.
56. Russell, S.J.P., D.P. Hand, Y.T. Chow, and L.J. Poyntz-Wright, *Optically-induced creation, transformation and organisation of defects and colour-centres in optical fibres*. Proceedings of the SPIE - The International Society for Optical Engineering, 1992. 1516: p. 47-54.
57. Williams, D.L., B.J. Ainslie, R. Kashyap, G.D. Maxwell, J.R. Armitage, R.J. Campbell, and R. Wyatt, *Photosensitive index changes in germania doped silica glass fibres and waveguides*. Proceedings of the SPIE - The International Society for Optical Engineering, 1993. 2044: p. 55-68.
58. Limberger, H.G., P.Y. Fonjallaz, R.P. Salathe, and F. Cochet, *Compaction- and photoelastic-induced index changes in fiber Bragg gratings*. Applied Physics Letters, 1996. 68(22): p. 3069-3071.
59. Poumellec, B., P. Niay, M. Douay, and J.F. Bayon, *The UV-induced refractive index grating in Ge:SiO₂ preforms: Additional CW experiments and the macroscopic origin of the change in index*. Journal of Physics D (Applied Physics), 1996. 29(7): p. 1842-1856.
60. Liu, Y., J.A.R. Williams, L. Zhang, and I. Bennion, *Abnormal spectral evolution of fiber Bragg gratings in hydrogenated fibers*. Optics Letters, 2002. 27(8): p. 586-588.
61. Xie, W.X., P. Niay, P. Bernage, M. Douay, J.F. Bayon, T. Georges, M. Monerie, and B. Poumellec, *Experimental evidence of two types of photorefractive effects occurring during photoinscriptions of Bragg gratings within germanosilicate fibres*. Optics Communications, 1993. 104(1-3): p. 185-195.
62. Reid, D.C.J., C.M. Ragdale, I. Bennion, J. Buus, and W.J. Stewart, *Phase-shifted Moire grating fibre resonators*. Electronics Letters, 1990. 26(1): p. 10-12.
63. Legoubin, S., E. Fertein, M. Douay, P. Bernage, P. Niay, F. Bayon, and T. Georges, *Formation of moire grating in core of germanosilicate fibre by transverse holographic double exposure method*. Electronics Letters, 1991. 27(21): p. 1945-1947.
64. Canning, J. and M.G. Sceats, *π -phase-shifted periodic distributed structures in optical fibres by UV post-processing*. Electronics Letters, 1994. 30(16): p. 1344-1345.
65. Kashyap, R., P.F. McKee, and D. Armes, *UV written reflection grating structures in photosensitive optical fibres using phase-shifted phase masks*. Electronics Letters, 1994. 30(23): p. 1977-1978.

66. Martinez, C. and P. Ferdinand, *Phase-shifted fibre Bragg grating photo-writing using UV phase plate in modified Lloyd mirror configuration*. Electronics Letters, 1998. 34(17): p. 1687-1688.
67. Martinez, C. and P. Ferdinand, *Analysis of phase-shifted fiber Bragg gratings written with phase plates*. Applied Optics, 1999. 32(15): p. 3223-3228.
68. Cross, P.S. and R.V. Schmidt, *Coupled Surface-Acoustic-Wave Resonators*. Bell System Technical Journal, 1977. 56(8): p. 1447-1482.
69. Sekartedjo, K., N. Eda, K. Furuya, Y. Suematsu, F. Koyama, and T. Tanbun-ek, *1.5 μm phase-shifted DFB lasers for single-mode operation*. Electronics Letters, 1984. 20(2): p. 80-81.
70. Agrawal, G.P. and S. Radic, *Phase-shifted fiber Bragg gratings and their application for wavelength demultiplexing*. IEEE Photonics Technology Letters, 1994. 6(8): p. 995-997.
71. Lemaire, P.J., R.M. Atkins, V. Mizrahi, and W.A. Reed, *High pressure H_2 loading as a technique for achieving ultrahigh UV photosensitivity and thermal sensitivity in GeO_2 doped optical fibres*. Electronics Letters, 1993. 29(13): p. 1191-1193.
72. Bilodeau, F., B. Malo, J. Albert, D.C. Johnson, K.O. Hill, Y. Hibino, M. Abe, and M. Kawachi, *Photosensitization of optical fiber and silica-on-silicon/silica waveguides*. Optics Letters, 1993. 18(12): p. 953-955.
73. Hill, K.O., et al., *Photosensitivity in $\text{Eu}^{2+}:\text{Al}_2\text{O}_3$ doped core fibre: preliminary results and applications to mode converters*. Conference on Optical Fibre Communication, Technical Digest Series (Optical Society of America, Washington, DC), 1991. 16: p. 14-17.
74. Bilodeau, F., D.C. Johnson, B. Malo, K.A. Vineberg, K.O. Hill, T.F. Morse, A. Kilian, and L. Reinhart, *Ultraviolet-light photosensitivity in Er^{3+} -Ge-doped optical fiber*. Optics Letters, 1990. 15(20): p. 1138-1140.
75. Brambilla, G. and V. Pruneri, *Enhanced photorefractivity in tin-doped silica optical fibers (review)*. IEEE Journal of Selected Topics in Quantum Electronics, 2001. 7(3): p. 403-408.
76. Oh, K., P.S. Westbrook, R.M. Atkins, P. Reyes, R.S. Windeler, W.A. Reed, T.E. Stockert, D. Brownlow, and D. DiGiovanni, *Ultraviolet photosensitive response in an antimony-doped optical fiber*. Optics Letters, 2002. 27(7): p. 488-490.
77. Poignant, H., S. Boj, E. Delevaque, M. Monerie, T. Taunay, P. Niay, P. Bernage, and W.X. Xie, *Efficiency and thermal behaviour of cerium-doped fluorozirconate glass fibre Bragg gratings*. Electronics Letters, 1994. 30(16): p. 1339-1341.

78. Williams, D.L., B.J. Ainslie, J.R. Armitage, R. Kashyap, and R. Campbell, *Enhanced UV photosensitivity in boron codoped germanosilicate fibres*. Electronics Letters, 1993. 29(1): p. 45-47.
79. Born, M., E. Wolf, and A.B. Bhatia, *Principles of optics : electromagnetic theory of propagation, interference and diffraction of light*. 6th corr. ed. ed. 1986, Oxford ; Sydney :: Pergamon Press.
80. Erdogan, T., *Fiber grating spectra*. Journal of Lightwave Technology, 1997. 15(8): p. 1277-1294.
81. Malitson, I.H., *Interspecimen comparison of the refractive index of fused silica*. Journal of the Optical Society of America, 1965. 55(10): p. 1205-1209.
82. Sellmeier, *Zur Erklärung der abnormen Farbenfolge im Spectrum einiger Substanzen*. Annalen der Physik und Chemie, 1871. 219(6): p. 272-282.
83. Xie, W.X., M. Douay, P. Bernage, P. Niay, J.F. Bayon, and T. Georges, *Second order diffraction efficiency of Bragg gratings written within germanosilicate fibres*. Optics Communications, 1993. 101(1-2): p. 85-91.
84. Limberger, H.G., P.Y. Fonjallaz, and R.P. Salathe, *Spectral characterisation of photoinduced high efficiency Bragg gratings in standard telecommunication fibres*. Electronics Letters, 1993. 29(1): p. 47-49.
85. Dong, L., L. Reekie, J.L. Cruz, J.E. Caplen, J.P. deSandro, and D.N. Payne, *Optical fibers with depressed claddings for suppression of coupling into cladding modes in fiber Bragg gratings*. IEEE Photonics Technology Letters, 1997. 9(1): p. 64-66.
86. Hill, K.O. and G. Meltz, *Fiber Bragg grating technology fundamentals and overview*. Journal of Lightwave Technology, 1997. 15(8): p. 1263-1276.
87. Mihailov, S.J., C.W. Smelser, P. Lu, R.B. Walker, D. Grobnic, H. Ding, G. Henderson, and J. Unruh, *Fiber Bragg gratings made with a phase mask and 800-nm femtosecond radiation*. Optics Letters, 2003. 28(12): p. 995-997.
88. Mihailov, S.J., C.W. Smelser, D. Grobnic, R.B. Walker, L. Ping, D. Huimin, and J. Unruh, *Bragg gratings written in all-SiO₂ and Ge-doped core fibers with 800-nm femtosecond radiation and a phase mask*. Journal of Lightwave Technology, 2004. 22(1): p. 94-100.
89. Smelser, C.W., D. Grobnic, and S.J. Mihailov, *Generation of pure two-beam interference grating structures in an optical fiber with a femtosecond infrared source and a phase mask*. Optics Letters, 2004. 29(15): p. 1730-1732.

90. Smelser, C.W., S.J. Mihailov, D. Grobnic, L. Ping, R.B. Walker, D. Huimin, and D. Xiaoli, *Multiple-beam interference patterns in optical fiber generated with ultrafast pulses and a phase mask*. Optics Letters, 2004. 29(13): p. 1458-1460.
91. Grobnic, D., C.W. Smelser, S.J. Mihailov, R.B. Walker, and P. Lu, *Fiber Bragg gratings with suppressed cladding modes made in SMF-28 with a femtosecond IR laser and a phase mask*. IEEE Photonics Technology Letters, 2004. 16(8): p. 1864-1866.
92. Muriel, M.A., A. Carballar, and J. Azana, *Field distributions inside fiber gratings*. IEEE Journal of Quantum Electronics, 1999. 35(4): p. 548-558.
93. Mills, J.D., C.W.J. Hillman, W.S. Brocklesby, and B.H. Blott, *Evanescent field imaging of an optical fiber Bragg grating*. Applied Physics Letters, 1999. 75(26): p. 4058-4060.
94. El-Diasty, F., A. Heaney, and T. Erdogan, *Analysis of fiber Bragg gratings by a side-diffraction interference technique*. Applied Optics, 2001. 40(6): p. 890-896.
95. Mills, J.D., C.W.J. Hillman, B.H. Blott, and W.S. Brocklesby, *Imaging of free-space interference patterns used to manufacture fiber Bragg gratings*. Applied Optics, 2000. 39(33): p. 6128-6135.
96. Pluta, M., *Advanced light microscopy*. Vol. 2. 1989, Amsterdam: Elsevier.
97. Dragomir, N.M., C. Rollinson, S.A. Wade, A.J. Stevenson, S.F. Collins, G.W. Baxter, P.M. Farrell, and A. Roberts, *Nondestructive imaging of a type I optical fiber Bragg grating*. Optics Letters, 2003. 28(10): p. 789-791.
98. Taylor, J.R., *An Introduction to Error Analysis: The Study of Uncertainties in Physical Measurements*. 1982: University Science Books.
99. StockerYale. *Optical Components - Rectangular Phase Mask*. 2007 [cited 30 Nov 2009]; Available from: http://www.stockeryale.com/o/lasiris_pm/products/pm_rpm.pdf.
100. Stoddart, P.R., C. Davis, S. Wade, and A. Mazzolini, *FIGFAB: Fibre Bragg grating fabrication and collaborative research at Swinburne University*, in *1st Pacific International Conference on Applications of Lasers and Optics (PICALO)*. 2004: Melbourne, Victoria, Australia.
101. Albert, J., K.O. Hill, B. Malo, S. Theriault, F. Bilodeau, D.C. Johnson, and L.E. Erickson, *Apodisation of the spectral response of fibre Bragg gratings using a phase mask with variable diffraction efficiency*. Electronics Letters, 1995. 31(3): p. 222-223.

102. Van Trees, H.L., *Optimum Array Processing - Part IV, Detection, Estimation, and Modulation Theory*. 2002, John Wiley & Sons. p. 103.
103. Digonnet, M.J.F., *Rare earth doped fiber lasers and amplifiers*. Optical engineering, ed. B.J. Thompson. Vol. 37. 2001, New York: Marcel Dekker, Inc.
104. Lemaire, P.J., *Reliability of optical fibers exposed to hydrogen: prediction of long-term loss increases*. Optical Engineering, 1991. 30(6): p. 780-789.
105. Talbot, H., *Facts relating to optical science*. 1836. 9: p. 401-407.
106. Lord Rayleigh, *On the manufacture and theory of diffractrion grating*. 1881. 11: p. 196-205.
107. Kittel, C., *Introduction to solid state physics / Charles Kittel*. 5th ed. 1976, New York: Wiley.
108. Kouskousis, B., *Microscopic characterisation of fibre Bragg gratings*, PhD thesis, 2010, Victoria University: Melbourne, Australia.
109. Kouskousis, B.P., C.M. Rollinson, D.J. Kitcher, S.F. Collins, G.W. Baxter, S.A. Wade, N.M. Dragomir, and A. Roberts, *Quantitative investigation of the refractive-index modulation within the core of a fiber Bragg grating*. Optics Express, 2006. 14(22).
110. Dana, K.J., *Three Dimensional Reconstruction of the Tectorial Membrane: An Image Processing Method using Nomarski Differential Interference Contrast Microscopy*, Master of Science thesis, 1992, Massachusetts Institute of Technology: Boston, USA. p. 95.
111. Morey, W.W., G. Meltz, J.D. Love, and S.J. Hewlett, *Mode-coupling characteristics of UV-written Bragg gratings in depressed-cladding fiber*. Electronics Letters, 1994. 30(9): p. 730-732.
112. Pierson, H.O., *Handbook of chemical vapor deposition: principles, technology, and applications*. 1999, Noyes Publications: Norwich, N.Y. p. 420.
113. Jiang, X.Q., *Reverse dispersion fiber with depressed core-index profile for dispersion-managed fiber pairs*. Optics Communications, 2005. 255(4-6): p. 230-234.
114. Oh, K., M.S. Kim, H.S. Seo, U.C. Paek, and B.H. Choi, *Suppression of cladding mode coupling in Bragg grating using GeO₂-B₂O₃ codoped photosensitive cladding optical fibre*. Electronics Letters, 1999. 35(5): p. 423-424.
115. Kim, J.M., K. Oh, T.S. Park, C.S. Kim, and K. Jeong, *Suppression of cladding-mode coupling loss in fiber Bragg gratings by independent control of refractive index and photosensitive profiles in a single-mode*

- optical fiber*. Photonics Technology Letters, IEEE, 2000. 12(11): p. 1504-1506.
116. Rollinson, C.M., S.A. Wade, N.M. Dragomir, S.F. Collins, A. Roberts, and G.W. Baxter, *Reflections near 1030 nm from 1540 nm fibre Bragg gratings: Evidence of a complex refractive index structure*. Optics Communications, 2005. 256(4-6): p. 310-318.
 117. Mizunami, T., T.V. Djambova, T. Niiho, and S. Gupta, *Bragg gratings in multimode and few-mode optical fibers*. Journal of Lightwave Technology, 2000. 18(2): p. 230-235.
 118. Erdogan, T. and J.E. Sipe, *Radiation-mode coupling loss in tilted fiber phase gratings*. Optics Letters, 1995. 20(18): p. 1838-1840.
 119. Yam, S.P., Z. Brodzeli, B.P. Kouskousis, C.M. Rollinson, S.A. Wade, G.W. Baxter, and S.F. Collins, *Fabrication of a π -phase-shifted fiber Bragg grating at twice the Bragg wavelength with the standard phase mask technique*. Optics Letters, 2009. 34(13): p. 2021-2023.
 120. Yam, S.P., G.W. Baxter, S.A. Wade, and S.F. Collins, *Modelling of an alternative pi-phase-shifted fibre Bragg grating operating at twice the Bragg wavelength*. Proc. 35th Australian Conference on Optical Fibre Technology & 19th Australian Institute of Physics Congress (ACOFT/AIP), 2010: p. 659.
 121. Yam, S.P., Z. Brodzeli, S.A. Wade, C.M. Rollinson, G.W. Baxter, and S.F. Collins, *Use of first-order diffraction wavelengths corresponding to dual-grating periodicities in a single fibre Bragg grating for simultaneous temperature and strain measurement*. Measurement Science and Technology, 2009(3): p. 034008.
 122. Yam, S.P., Z. Brodzeli, S.A. Wade, G.W. Baxter, and S.F. Collins, *Occurrence of Features of Fiber Bragg Grating Spectra Having a Wavelength Corresponding to the Phase Mask Periodicity*. Journal of Electronic Science and Technology of China, 2008. 6(4): p. 458-461.
 123. Patrick, H. and S.L. Gilbert, *Growth of Bragg gratings produced by continuous-wave ultraviolet light in optical fiber*. Optics Letters, 1993. 18(18): p. 1484-1486.
 124. Strasser, T.A., T. Erdogan, A.E. White, V. Mizrahi, and P.J. Lemaire, *Ultraviolet laser fabrication of strong, nearly polarization-independent Bragg reflectors in*. Applied Physics Letters, 1994. 65(26): p. 3308.
 125. Spiegel, M.R., J.J. Schiller, and R.A. Srinivasan, *Probability and statistics*. 3rd ed. ed. 2009, New York: McGraw-Hill.
 126. Farahi, F., D.J. Webb, J.D.C. Jones, and D.A. Jackson, *Simultaneous measurement of temperature and strain: cross-sensitivity considerations*. Journal of Lightwave Technology, 1990. 8(2): p. 138-142.

127. James, S.W., *Simultaneous independent temperature and strain measurement using in-fibre Bragg grating sensors*. Electronics Letters, 1996. 32(12): p. 1133-1134.
128. MatWeb. *Online Materials Information Resource for Silica*. 2011 [cited 23 Mar 2011]; Available from: <http://www.matweb.com/search/DataSheet.aspx?MatGUID=a028dco9086e4e6f9885e90ae49ecc32>.
129. Rollinson, C.M., S.A. Wade, N.M. Dragomir, G.W. Baxter, and S.F. Collins, *Strain and temperature response of transmission dips at 2/3 of the Bragg wavelength in type I and IIA fiber Bragg gratings*. 17th International Conference on Optical Fibre Sensors, Pts 1 and 2, Proc. SPIE, 2005. 5855: p. 310-313.
130. Pal, S., T. Sun, K.T.V. Grattan, S.A. Wade, S.F. Collins, G.W. Baxter, B. Dussardier, and G. Monnom, *Bragg grating performance in Er-Sn-doped germanosilicate fiber for simultaneous measurement of wide range temperature (to 500 degrees C) and strain*. Review of Scientific Instruments, 2003. 74(11): p. 4858-4862.
131. Rollinson, C.M., S. Trpkovski, S.A. Wade, N.M. Dragomir, G.W. Baxter, and S.F. Collins, *Three parameter measurement using a single fiber Bragg grating inscribed in Er³⁺: Yb³⁺-codoped fiber*. 17th International Conference on Optical Fibre Sensors, Pts 1 and 2, Proc. SPIE, 2005. 5855: p. 134-137.
132. Tomljenovic-Hanic, S. and J.D. Love, *Symmetry-selective reflection gratings*. Journal of the Optical Society of America A-Optics Image Science and Vision, 2005. 22(8): p. 1615-1619.
133. Castro, J., D.F. Geraghty, S. Honkanen, C.M. Greiner, D. Iazikov, and T.W. Mossberg, *Demonstration of mode conversion using anti-symmetric waveguide Bragg gratings*. Opt. Express, 2005. 13(11): p. 4180-4184.
134. Castillo, J.E., J.M. Castro, R.K. Kostuk, and D.F. Geraghty, *Study of Multichannel Parallel Anti-Symmetric Waveguide Bragg Gratings for Telecom Applications*. Photonics Technology Letters, IEEE, 2007. 19(2): p. 85-87.

Appendix: List of Publications



A.1 Book chapters

1. Rollinson, C.M., S.T. Huntington, B.C. Gibson, and J. Canning, *Fractal fibre for enhanced throughput SNOM probes*, in *Trends in Photonics*, J. Canning, Editor. 2010, Transworld Research Network. p. 373-408.*

A.2 Journal articles

1. Dragomir, N.M., C. Rollinson, S.A. Wade, A.J. Stevenson, S.F. Collins, G.W. Baxter, P.M. Farrell, and A. Roberts, *Nondestructive imaging of a type I optical fiber Bragg grating*. *Optics Letters*, 2003. 28(10): p. 789-791.
2. Rollinson, C.M., S.A. Wade, N.M. Dragomir, S.F. Collins, A. Roberts, and G.W. Baxter, *Reflections near 1030 nm from 1540 nm fibre Bragg gratings: Evidence of a complex refractive index structure*. *Optics Communications*, 2005. 256(4-6): p. 310-318.
3. Kouskousis, B.P., C.M. Rollinson, D.J. Kitcher, S.F. Collins, G.W. Baxter, S.A. Wade, N.M. Dragomir, and A. Roberts, *Quantitative investigation of the refractive-index modulation within the core of a fiber Bragg grating*. *Optics Express*, 2006. 14(22).
4. Yam, S.P., Z. Brodzeli, B.P. Kouskousis, C.M. Rollinson, S.A. Wade, G.W. Baxter, and S.F. Collins, *Fabrication of a π -phase-shifted fiber Bragg grating at twice the Bragg wavelength with the standard phase mask technique*. *Optics Letters*, 2009. 34(13): p. 2021-2023.

5. Yam, S.P., Z. Brodzeli, S.A. Wade, C.M. Rollinson, G.W. Baxter, and S.F. Collins, *Use of first-order diffraction wavelengths corresponding to dual-grating periodicities in a single fibre Bragg grating for simultaneous temperature and strain measurement*. Measurement Science and Technology, 2009(3): p. 034008.
6. Rollinson, C.M., S.M. Orbons, S.T. Huntington, B.C. Gibson, J. Canning, J.D. Love, A. Roberts, and D.N. Jamieson, *Metal-free scanning optical microscopy with a fractal fiber probe*. Optics Express, 2009. 17(3): p. 1772-1780.*
7. Rollinson, C.M., B.C. Gibson, S.T. Huntington, S. Rubanov, and J. Canning, *Characterization of nanoscale features in tapered fractal and photonic crystal fibers*. Optics Express, 2011. 19(3): p. 1860-1865.*
8. Rollinson, C.M., S.A. Wade, B.P. Kouskousis, D.J. Kitcher, G.W. Baxter, and S.F. Collins, *Variations of the growth of harmonic reflections in fiber Bragg gratings fabricated using phase masks*. Journal of the Optical Society of America A (Optics, Image Science and Vision), 2012. 29(7): p. 1259-1268.

A.3 Conference proceedings

1. Rollinson, C.M., S.A. Wade, N.M. Dragomir, G.W. Baxter, and S.F. Collins, *Imaging of Fibre Bragg Gratings: Towards the realisation of better sensors*. Proc. Inaugural Australasian Workshop on Structural Health Monitoring, 2002.
2. Rollinson, C.M., S.A. Wade, N.M. Dragomir, A. Roberts, S.F. Collins, and G.W. Baxter, *Effect of the phase mask writing technique on higher order reflections of Type I and Type IIA fibre Bragg gratings*. Proc. Conference on the Optical Internet 2003 and 28th Australian Conference on Optical Fibre Technology (COIN/ACOFT), 2003: p. 411-414.
3. Rollinson, C., S.A. Wade, N.M. Dragomir, G.W. Baxter, S.F. Collins, and A. Roberts, *Evolution of reflectance peaks at wavelengths other than the expected harmonics of a fibre Bragg grating*. Proc. Australasian Conference on Optics, Lasers and Spectroscopy (ACOLS), 2003.
4. Kouskousis, B., N.M. Dragomir, C. Rollinson, S.A. Wade, S.F. Collins, G.W. Baxter, and A. Roberts, *A comparison between the modelled intensity distribution and the imaged refractive index modulation for a type-I fibre Bragg grating produced using the phase mask technique*. Proc. Australasian Conference on Optics, Lasers and Spectroscopy (ACOLS), 2003.
5. Wade, S.A., C. Rollinson, N.M. Dragomir, A. Roberts, S.F. Collins, and G.W. Baxter, *Toward a better understanding of optical fibre Bragg grating sensors*. Proc. 12th Conference on Sensors and their Applications, IOP Publishing, 2003: p. 435-441.

6. Dragomir, N.M., C. Rollinson, F. Sidiroglou, S.A. Wade, A. Roberts, S.F. Collins, and G.W. Baxter, *Evaluation of optical fiber sensors using differential interference contrast imaging techniques*. Proc. 16th International Optical Fiber Sensors Conference (OFS), 2003: p. 230-233.
7. Rollinson, C.M., S.A. Wade, S. Pal, J. Mandal, T. Sun, K.T.V. Grattan, W. Blanc, B. Dussardier, G. Monnom, G.W. Baxter, and S.F. Collins, *Photosensitivity of tin-doped aluminosilicate optical fibre*. Proc. 29th Australian Conference on Optical Fibre Technology (ACOFT/AOS), 2004. PO7.
8. Rollinson, C.M., S.A. Wade, N.M. Dragomir, A. Roberts, G.W. Baxter, and S.F. Collins, *Three Parameter Sensing With A Single Bragg Grating In Non-Birefringent Fiber*. Proc. Topical Meeting on Bragg Gratings, Poling, and Photosensitivity (BGPP/ACOFT), 2005: p. 92-94.
9. Rollinson, C.M., S.A. Wade, N.M. Dragomir, G.W. Baxter, and S.F. Collins, *Strain and temperature response of transmission dips at 2/3 of the Bragg wavelength in type I and IIA fiber Bragg gratings*. 17th International Conference on Optical Fibre Sensors, Pts 1 and 2, Proc. SPIE, 2005. 5855: p. 310-313.
10. Rollinson, C.M., S. Trpkovski, S.A. Wade, N.M. Dragomir, G.W. Baxter, and S.F. Collins, *Three parameter measurement using a single fiber Bragg grating inscribed in Er³⁺: Yb³⁺-codoped fiber*. 17th International Conference on Optical Fibre Sensors, Pts 1 and 2, Proc. SPIE, 2005. 5855: p. 134-137.
11. Yam, S.P., C.M. Rollinson, D.J. Kitcher, G.W. Baxter, and S.F. Collins, *Transverse Strain Response of Transmission Dips at 2/3 of the Bragg Wavelength in a Fiber Bragg Grating*. 18th International Conference on Optical Fibre Sensors, 2006: p. TuE47.
12. Kouskousis, B., N.M. Dragomir, C.M. Rollinson, S.A. Wade, D.J. Kitcher, S.F. Collins, A. Roberts, and G.W. Baxter, *Comparison between a simulated and measured image of a fibre Bragg grating*. Proc. 31st Australian Conference on Optical Fibre Technology (ACOFT/AOS), 2006: p. 81-83.
13. Yam, S.P., C.M. Rollinson, D.J. Kitcher, S.A. Wade, G.W. Baxter, and S.F. Collins, *Behavior of transmission dips at 2/3 of the Bragg wavelength in a fiber Bragg grating*. Proc. 5th International Conference on Optical Communications and Networks/ 2nd International Symposium on Advances and Trends in Fiber Optics and Applications (ICO CN/ATFO), 2006.
14. Yam, S.P., C.M. Rollinson, D.J. Kitcher, S.A. Wade, G.W. Baxter, and S.F. Collins, *Effects of transverse strain on dips at 2/3 of the Bragg wavelength in a non-birefringent fibre Bragg grating*. Proc. 17th Australian Institute of Physics (AIP) National Congress incorporating the Conference of the Australian Optical Society (AIP/AOS), 2006.

15. Gibson, B., C. Rollinson, S. Huntington, J. Canning, M. Stevenson, K. Lyytikainen, J. Love, and V. Steblina, *Ultra-high throughput optical probes based on Fractal Fibre*. Proc. Joint International on Optical Internet and The Australian Conference on Optical Fibre Technology (ACOFT), 2007: p. 293-295.*
16. Orbons, S.M., M. Milicevic, C.M. Rollinson, B. Gibson, S.T. Huntington, D.N. Jamieson, B. Luther-Davies, D. Freeman, M.I. Haftel, C. Schlockerman, T.J. Davis, and A. Roberts, *Plasmonic nanoresonant materials*. Proc. Photonics: Design, Technology, and Packaging III, 2008. 6801: p. 80101.*
17. Rollinson, C.M., S.T. Huntington, B.C. Gibson, S. Rubanov, and J. Canning, *Nanostructures in tapered air-silica fibres*. Proc. Joint Conference of the Opto-Electronics and Communications Conference and The Australian Conference on Optical Fibre Technology (OECC/ACOFT), 2008. 1 and 2: p. 245-246.*
18. Yam, S.P., Z. Brodzeli, B.P. Kouskousis, C.M. Rollinson, S.A. Wade, G.W. Baxter, and S.F. Collins, *A π -phase-shifted fiber Bragg grating fabricated using a single phase mask*. Proc. 14th OptoElectronics and Communications Conference (OECC), 2009.
19. Collins, S.F., S.P. Yam, H.K. Bal, B.P. Kouskousis, C.M. Rollinson, F. Sidirolou, Z. Brodzeli, S.A. Wade, and G.W. Baxter, *Fiber Bragg gratings at twice the Bragg wavelength: properties and sensor applications (invited paper)*. Proc. 2nd Asia-Pacific Optical Sensors Conference (APOS), 2010. TU15.

* Not related to this thesis.